

DISSERTATION

MESOSPHERIC MOMENTUM FLUX STUDIES
OVER FORT COLLINS CO (41N, 105W)

Submitted by

Phillip Edward Acott

Department of Physics

In partial fulfillment of the requirements

For the Degree of Doctor of Philosophy

Colorado State University

Fort Collins, Colorado

Spring 2009

UMI Number: 3374672

INFORMATION TO USERS

The quality of this reproduction is dependent upon the quality of the copy submitted. Broken or indistinct print, colored or poor quality illustrations and photographs, print bleed-through, substandard margins, and improper alignment can adversely affect reproduction.

In the unlikely event that the author did not send a complete manuscript and there are missing pages, these will be noted. Also, if unauthorized copyright material had to be removed, a note will indicate the deletion.

UMI[®]

UMI Microform 3374672
Copyright 2009 by ProQuest LLC
All rights reserved. This microform edition is protected against
unauthorized copying under Title 17, United States Code.

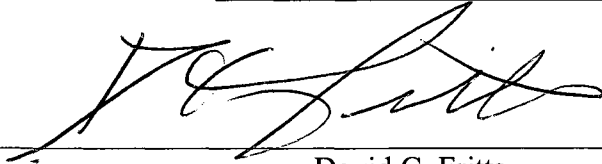
ProQuest LLC
789 East Eisenhower Parkway
P.O. Box 1346
Ann Arbor, MI 48106-1346

COLORADO STATE UNIVERSITY

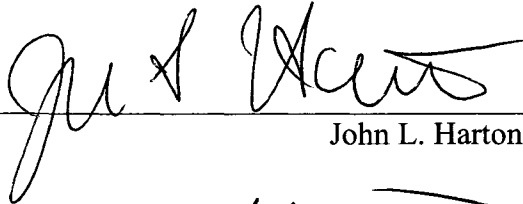
March 13, 2009

WE HEREBY RECOMMEND THAT THE DISSERTATION PREPARED UNDER OUR SUPERVISION BY PHILLIP EDWARD ACOTT ENTITLED MESOSPHERIC MOMENTUM FLUX STUDIES OVER FORT COLLINS CO (41N, 105W) BE ACCEPTED AS FULFILLING IN PART REQUIREMENTS FOR THE DEGREE OF DOCTOR OF PHILOSOPHY.

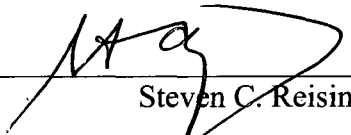
Committee on Graduate Work



David C. Fritts



John L. Harton

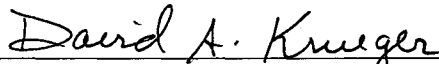


Steven C. Reising



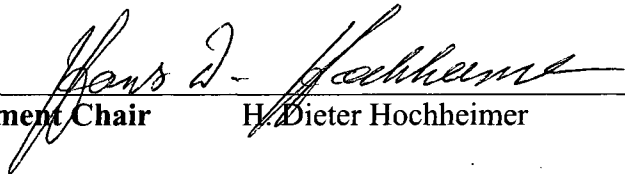
Adviser

Chiao Yao She



Co-Adviser

David A. Krueger



Department Chair

H. Dieter Hochheimer

ABSTRACT OF DISSERTATION

MESOSPHERIC MOMENTUM FLUX STUDIES OVER FORT COLLINS CO (41N, 105W)

System upgrades to the Colorado State University Sodium Lidar have enabled over 300 hours of night-time gravity wave momentum flux measurements with concurrent 24-hour measurements of the mean and tidal wind and temperature fields of the mesosphere and lower thermosphere (MLT) region of the atmosphere above Fort Collins, CO. Results include the vertical profile of nighttime zonal momentum flux divided by density (MF/ρ), as well as nighttime wind and temperature variances; the results also provide some insight into the accompanying gravity wave-tidal interactions.

Statistics of MF/ρ and wind and temperature variability compare well with another reported long term sodium lidar study, Gardner and Liu (2007). MF/ρ is averaged over the breadth of the study from September 2006 to June 2007 and over altitudes from 85 km to 95 km yielding an average value of $-1.1 \pm 0.2 \text{ m}^2\text{s}^{-2}$. A comparison is made of nightly averaged MF/ρ values in the winter months and the months nearest the equinox. This is reported as a monthly mean of $-2.4 \text{ m}^2\text{s}^{-2}$ for the winter months and $+0.5 \text{ m}^2\text{s}^{-2}$ for the months nearest to the two equinoxes.

MF/ρ and tidal interaction is examined. There is anti-correlation between the reconstructed tide and smoothed MF/ρ at the middle altitudes in the observation. This anti-correlation develops with a change in altitude from no noticeable anti-correlation at lower altitudes to anti-correlation at higher altitudes, suggesting interaction between the tides and the high phase speed GWs that are generating the MF/ρ . At highest altitudes in this study the anti-correlation relationship evolves to near quadrature, suggesting that the GWs are no longer being filtered by the tides.

Convergence of the MF/ ρ appears to be anti-correlated and correlated with the tidal amplitudes depending upon the altitude and the day of the measurement. Where clear anti-correlation between the convergence of flux and diurnal tidal amplitude is observed (e.g. day 343, 2006) the growth of diurnal tidal amplitude is damped, suggesting transference of energy from the tides into the short period GWs. Further work in the characterization of the tidal amplitude and phase relationship with the MF/ ρ modulation, with aid from the continuing long-term tidal study, is anticipated.

Phillip Edward Acott
Physics Department
Colorado State University
Fort Collins, CO 80523
Spring, 2009

Table of Contents

Chapter 1: Introduction	1
1.1 Introduction to the Atmosphere	2
1.1.1 Temperature vertical structure	3
1.1.2 Introduction to the Mesosphere	5
1.1.3 Mesopause behavior.....	5
1.1.4 Motivation for GW-Tidal interaction momentum flux measurements	8
1.2 Lasers used for atmospheric remote sensing	9
1.2.1 History.....	10
1.2.2 Lidar systems	10
1.2.3 Colorado State University Lidar	12
1.3 Structure of Dissertation	13
Chapter 2: Sodium Lidar Measurement Methodology	19
2.1 Sodium Theory and Sodium Lidar.....	19
2.1.1 Na spectrum	21
2.1.2 Laser Induced Fluorescence.....	22
2.1.3 Doppler broadening and Doppler shift	24
2.1.4 Sodium lidar equation.....	31
2.1.5 Temperature and winds determined by R_T and R_V ratios	36
2.2 CSU sodium lidar system.....	39
2.2.1 Transmitter.....	42
2.2.2 Receiver	54
2.2.3 Electronics.....	60
Chapter 3: Basic Theory of the Mesosphere.....	68
3.1 Gravity waves	68
3.1.1 Simple Linear Theory of Gravity Waves.....	70
3.1.2 The Dispersion Relation	73
3.2 Introduction to momentum flux.....	77
3.2.1 Momentum Flux Measurements Using the Vincent-Reid Method.....	81
3.3 Tidal effects in atmosphere.....	83
3.3.1 Tidal-GW Interaction.....	84
Chapter 4: Filtering and Analysis Techniques.....	89
4.1 Momentum Flux Analysis	90
4.1.1 Analysis Window and Linear Fit	91
4.1.2 Filtering Effects on Variance	93
4.1.3 Filtering Effects in Wind Measurements	97
4.2 Errors in measurements.....	102
4.2.1 Analysis considerations-error subtraction from variance	102
4.2.2 Monte Carlo Estimate of MF/ ρ Error.....	105
4.2.3 Measurement considerations-angle θ	108
Chapter 5: Measurement Results	111
5.1 Case Study of Day 6343	112
5.1.1 Chirp Calculation	115
5.1.2 Mean Flux, Mean Wind, and Tidal Wind Definitions.....	117
5.1.3 Momentum Flux and Mean Winds	120

5.1.4 Stability	127
5.1.5 Nightly Averages of MF/ ρ and comparison with mean and tidal winds	131
5.2 Measurement Statistics	135
5.3 An initial study of observed gravity wave-tide interactions	144
5.3.1 Data used for GW/tidal interaction studies	145
5.3.2 Observed correlations between momentum flux and tides	149
Chapter 6: Conclusions and Further Work	163
6.1 Conclusions.....	163
6.1.1 Chirp	164
6.1.2 Momentum Flux and Mean Winds	164
6.1.3 Stability	165
6.1.4 Statistics	166
6.1.5 MF/ ρ - Tidal Interaction.....	167
6.2 Further Work.....	167
Appendix I. Correlation and Wavelet Analysis.....	171
I.1 Correlation of Radial Measurements	177
Appendix II. Electronics.....	183
II.1 System Timing	184
II.2 Counting Cards.....	187

LIST OF FIGURES

FIGURE 1-1. TYPICAL VERTICAL ALTITUDE (KM) VS. TEMPERATURE (C) STRUCTURE (RED LINE) WITH NAMED REGIONS IN THE ATMOSPHERE AND EXPECTED AVERAGE AIR PRESSURE ANNOTATED ON THE RIGHT Y-AXIS.....	3
FIGURE 1-2. BALANCE OF FORCES SHOWING THE EFFECT OF WAVE DRAG ON THE MEAN FLOW; WHERE, v IS THE TRUE WIND, F_p IS THE PRESSURE GRADIENT FORCE, F_{Co} IS THE CORIOLIS 'FORCE' AND F_{GW} IS THE BODY FORCE DUE TO GRAVITY WAVE DISSIPATION CAUSING MOMENTUM FLUX DIVERGENCE.	7
FIGURE 2-1. THE ENERGY DIAGRAM OF SODIUM D TRANSITION. ON THE LEFT, THE BASIC MODEL SHOWS A TWO LEVEL SYSTEM; THE OUTER ELECTRON TRANSITION FROM 3S GROUND STATE TO THE 3P STATE. THE INTERMEDIATE MODEL INCLUDES SPIN-ORBIT COUPLING SPLITTING THE D TRANSITION INTO D_1 AND D_2 FINE STRUCTURE. THE FINAL MODEL INCLUDES 3/2 NUCLEAR SPIN-SPIN INTERACTION. THE NUMBERS GIVEN IN A TRANSITION ARROW OF EACH MODEL ARE THE TRANSITION LINE STRENGTH S (NOT BRACKETED) AND THE EINSTEIN COEFFICIENT A (IN THE BRACKET) OF THAT TRANSITION IN UNITS OF THE TRANSITION LINE STRENGTH S_0 AND THE SPONTANEOUS EMISSION RATE A_0 OF THE BASIC MODEL. THE F NUMBER REVEALS THE DEGENERACY ($2F+1$) (SHE AND YU, 1995).....	21
FIGURE 2-2. PDA LINESHAPE NORMALIZED TO A MAXIMUM INTENSITY OF 1. THIS NEAR GAUSSIAN LINESHAPE IS CORRELATED WITH THE NORMALIZED SODIUM LINESHAPE.	27
FIGURE 2-3. FLUORESCENCE IS THE VERTICAL AXIS AND FREQUENCY IS THE HORIZONTAL AXIS. (WHITE, 1999).....	28
FIGURE 2-4. THE 2D CALIBRATION CURVE CONSTRUCTED BY APPLICATION OF THE LINESHAPE FUNCTION FOR THE TEMPERATURE AND WIND AND CORRESPONDING R_T AND R_V RATIOS. THIS IS COMPUTED FROM THE THEORETICAL LASER INDUCED SODIUM FLUORESCENCE SPECTRUM. SOLID LINES ARE CALCULATED FROM THE VOIGT FUNCTION, AND THE DASHED LINES ARE CALCULATED FROM AN APPROXIMATING GAUSSIAN FUNCTION DISREGARDING NATURAL LINESHAPE INFLUENCE. THE CALIBRATION CURVES ARE USED TO RETRIEVE TEMPERATURE AND RADIAL WIND VELOCITY BY USING EXPERIMENTALLY OBTAINED TEMPERATURE AND WIND RATIOS. (WHITE, 1999).....	30
FIGURE 2-5. THE 2D CALIBRATION CURVE CONSTRUCTED BY APPLICATION OF THE LINESHAPE FUNCTION FOR THE TEMPERATURE AND WIND AND CORRESPONDING R_T AND R_V RATIOS. $R_V = 0.1$ AND $R_T = 0.4$ LINES ARE DRAWN IN BLACK. WHERE THEY INTERSECT IS CIRCLED AND TRANSLATES INTO ~ 11 M/S AND ~ 200 K.	38
FIGURE 2-6. ABOVE IS A SIMPLIFIED SYSTEM SCHEMATIC OF THE LIDAR SYSTEM WITH THE TRANSMITTER SUB-SYSTEM ON THE LEFT AND THE RECEIVER SUB-SYSTEM ON THE RIGHT. IN THE CENTER IS THE SYNCHRONIZING AND DATA STORING ELECTRONICS. THIS SCHEMATIC DEPICTS DAYTIME OPERATION (LI, 2005).	42
FIGURE 2-7. (A) DOPPLER FREE FLUORESCENCE SPECTROSCOPY APPARATUS. COUNTER-PROPAGATING BEAMS INDUCED FLUORESCENCE IS FOCUSED ONTO A PMT. THE SYMBOLS ND AND PH DENOTE NEUTRAL DENSITY FILTERS AND PIN HOLES RESPECTIVELY (B) FLUORESCENCE SPECTRUM DEPICTING THE DOPPLER FREE FEATURES OF THE D_{2A} LAMB DIP (ν_A), CROSSOVER (ν_C), AND THE D_{2B} LAMB DIP (ν_B). ALSO DEPICTING WHERE THE SHIFTED FREQUENCIES OCCUR IN THE SPECTRUM ν_- AND ν_+ FOR THE (-) AND (+) SHIFTED LIGHT (SHERMAN, 2002).	45
FIGURE 2-8. RING LASER LOCKING CIRCUIT ADDED TO THE RING LASER TO INSERT A DITHER IN THE REFERENCE FEEDBACK TO THE CONTROL CIRCUITRY.....	46
FIGURE 2-9. A DIAGRAM OF ACOUSTIC-OPTIC MODULATOR (AO) BEAM PATH FOR THE THREE DIFFERENT FREQUENCIES OF LIGHT. NOTE THE PHYSICAL SHIFTING OF LIGHT POSITION WITH THE FREQUENCY SHIFTING OF THE LIGHT. THE CHOPPER BLADE SELECTS THE PATH OF THE TRANSMITTED LIGHT. [FROM VANCE 2004].....	50
FIGURE 2-10. A SCHEMATIC OF LIGHT PATH INSIDE THE PULSE DYE AMPLIFIER (PDA). THE SEED BEAM COMES FROM THE TOP LEFT OF THE SCHEMATIC AND THE PUMP BEAM COMES FROM THE LEFT SIDE OF THE SCHEMATIC (SHERMAN 2002).....	52
FIGURE 2-11. CHIRP FREQUENCY SHIFT IS DETERMINED BY MEASURING NORMALIZED TRANSMISSION THROUGH AN IODINE VAPOR CELL FOR EACH OF THE THREE FREQUENCIES TRANSMITTED. IN THE FIGURE, 1=IODINE CHANNEL AND 2= POWER-NORMALIZATION CHANNEL, L= LENS, D= DIFFUSER, M= MIRROR, POL =POLARIZER, AND BS= BEAMSPLITTER (FROM SHERMAN 2002).	53
FIGURE 2-12. THE DESCRIPTION OF THE NEW TRANSMISSION OPTICAL PATH BEGINS WITH THE PULSED BEAM FROM THE PDA ENTERING FROM THE TOP. IT IS SPLIT BY A 40% REFLECTANCE 60% TRANSMITTANCE BEAM SPLITTER. FOR NIGHTTIME OPERATIONS THE 67% REFLECTANCE 33% TRANSMITTANCE	

BEAMSPLITTER IS IN DIVIDING THE TOTAL BEAM POWER THREE WAYS. DURING DAY TIME OPERATION THE FLIP MIRROR IS DOWN AND 60% OF TOTAL POWER IS TRANSMITTER IN THE NORTH 30° CHANNEL. ALL SHORT DIAGONAL LINES WITHOUT ARROWS ARE MIRRORS UNLESS NOTED AS A BEAMSPLITTER (BS).....	54
FIGURE 2-13. RAY TRACING DIAGRAM SHOWING THE LIGHT PATH FROM THE 75 CM THROUGH THE MATCH ACHROMATIC DOUBLET ONTO A 1.5 MM, 0.37 NA FIBER. DIFFERENT RAYS (GREEN AND BLUE) REPRESENT A SMALL MISALIGNMENT IN THE TELESCOPE OPTICS TO DESIGN FOR MAXIMUM FLEXIBILITY AND RELIABILITY.....	56
FIGURE 2-14. ON THE TOP LEFT IS THE BASE PLATE OF FIBER-TELESCOPE COUPLER. BOTTOM LEFT IS A STANDARD FIBER OPTIC POSITIONER X-Y-Z TRANSLATION STAGE THAT IS MOUNTED TO THE BASE PLATE. ON THE RIGHT IS AN ALUMINUM TUBE THAT FITS INTO THE TELESCOPE EYE-PIECE. MATCHED PAIR OF ACHROMATIC LENSES IS SLID INTO AN INNER SLEEVE THAT IS ATTACHED TO THE BASE PLATE.	56
FIGURE 2-15. CALCULATED LIGHT PATH FROM .9 MM .11 NA OPTICAL FIBER ONTO PMT ACTIVE AREA WITH A CHOPPER WHEEL ROTATING FACE ~2 MM FROM THE FIBER AND A F=25.4 MM COATED ACHROMATE ~ 25 MM FROM THE FIBER FACE FOCUSING THE LIGHT ON A 5 MM ACTIVE AREA.....	58
FIGURE 2-16. PHOTON BACKGROUND IS USED TO SET THE ALTITUDE OF CHOPPING THE LIGHT. THE LEFT PLOT SHOWS THE CHOPPER TEST FOR PHOTONS GENERATED BY A LIGHT BULB. THE COUNTS ARE AVERAGED FOR THE THREE CHANNELS AND THEN SMOOTHED OVER 2 KM. THE DIFFERENCE OF NEIGHBORING COUNTS IS DIVIDED BY THE DIFFERENCE OF NEIGHBORING ALTITUDES, RIGHT PLOT. THE RIGHT PLOT IS FIT TO A GAUSSIAN. THE FULLY CLOSED TO FULLY OPEN VALUE IS REPORTED AS DIFFERENCE IN 3σ VALUES, ~17 KM. NOTE: THE CHOPPER TEST HEIGHT IS SET TO OPEN ~70 KM ENSURING OPENING IN THE MIDDLE OF THE OBSERVED ALTITUDE RANGE OF 0-150 KM. FOR DATA TAKING THE CHOPPER ALTITUDE IS SET TO BE FULLY OPEN AT 20 KM.	59
FIGURE 2-17. A BLOCK DIAGRAM OF THE TIMING ELECTRONICS. IN THE TOP LEFT THE 100 HZ RECEIVING CHOPPER TTL SIGNAL THAT DICTATES THE TIMING OF THE LIDAR ELECTRONICS. WITH EVERY TWO PULSES FROM THE RECEIVER CHOPPER A DIGITAL CLOCK ADVANCES, CONTINUALLY COUNTING 0, 1, AND 2. WITH EVERY CLOCK TICK LAMPS CAUSE THE YAG TO PULSE. BIT 1 AND BIT 2 CONTROL THE AO CRYSTALS AND THUS THE SHIFTED AOM LIGHT. LOWHOLD ENSURES THE FIRST PHOTONS COUNTED EACH FILE ARE WHEN THE TRANSMITTER IS NOT SHIFTED LIGHT. Q-SWITCH COMES FROM THE YAG WHEN A PULSE OF LIGHT IS SENT INTO THE SKY. THE TIMING OF Q-SWITCH DETERMINES THE BINNING OF RETURNED PHOTONS. CHIRP REQUIRES A PULSE BETWEEN CHIRP SAMPLES FOR BACKGROUND.....	62
FIGURE 2-18. COMTEC CARD WITH ACCESS PORTS. TIMING OF WHEN THE LASER IS FIRED Q-SWITCH IS INPUT INTO TRG (START) AND RETURNED PHOTONS (PMT PULSES) ARE COUNTED WITH COUNT (STOP) 1 AND 2 IN. DIG_IO 0 AND 1 ARE USED FOR DIGITAL TAGGING OF AOM.	64
FIGURE 3-1. A PLOT OF MAXIMUM INTRINSIC PHASE SPEED AT THE M=0 THE TURNING LEVEL. THIS LEADS TO INSIGHT INTO PROBABLE HORIZONTAL WAVELENGTHS IN THE MESOPAUSE.	77
FIGURE 3-2. A) A REPRESENTATION OF CO-PLANAR BEAM MEASUREMENT GEOMETRY WHERE V IS THE LINE-OF-SIGHT WIND OBSERVED AT RADIAL DISTANCE R AND TIME T. B) A REPRESENTATION OF A MONOCHROMATIC GRAVITY WAVE WITH SLANTED PHASE FRONT PROPAGATING TOWARD THE EAST. THE MEASURED DOPPLER SHIFTED WIND PERTURBATION IN THE WEST BEAM WILL BE LESS THAN THE EAST BECAUSE OF THE ANGLE OF THE PHASE FRONT RELATIVE TO THE MEASURING BEAM. THE DIRECTION OF GRAVITY WAVE PROPAGATION CAN BE DETERMINED FROM A COMPARISON OF SIGNAL VARIANCES (BOTH AFTER VINCENT AND REID 1983).....	81
FIGURE 4-1. THIS IS A PLOT OF CALCULATED VARIANCE WITH NO FILTERING (GREEN), A WINDOW FILTER OF 2 HOURS WITH NO LINEAR FIT SUBTRACTION (BLUE), AND WITH A LINEAR FIT SUBTRACTION (RED). THE BLUE AND RED LINES REPRESENT THE MEAN VARIANCES OBTAINED FROM THE WINDOWED FILTERING. THE ERROR BARS ARE SET ONE STANDARD DEVIATION FROM THE MEAN. THE LEFT PLOT HAS MONOCHROMATIC WAVE GENERATION WITH THE PERIOD OF THE WAVE ANNOTATED ON THE X-AXIS. THE RIGHT PLOT HAS THE SAME MONOCHROMATIC WAVE SPECTRUM WITH A 12 HOUR WAVE ADDED. THE NON-WINDOWED VARIANCE (GREEN) IS OFF SCALE HIGH FOR MOST OF THE PLOT.	95
FIGURE 4-2. THE LEFT PLOT IS THE EAST LINE OF SIGHT WIND AT ALTITUDES MARKED ON THE RIGHT OF THE PLOT. ON THE RIGHT, THE VARIANCE VALUES CALCULATED FROM THE LOS EAST AND WEST MEASUREMENTS. EAST VARIANCE IS REPRESENTED BY THE SOLID BLUE LINE AND WEST VARIANCE IS THE DASHED RED LINE. THE MEASUREMENTS ARE OBTAINED AT THE ALTITUDES MARKED ON THE	

RIGHT Y-AXIS AND ARE MARKED WITH A DASHED BLACK LINE. THE ANALYSIS WINDOW SPANS 12 HOURS AND THE SCALE IS 10 M/S/KM AND 10 M ² S ⁻² /KM LEFT AND RIGHT PLOTS RESPECTIVELY.	97
FIGURE 4-3. MOMENTUM FLUX GENERATED WITH A 12 HOUR ANALYSIS WINDOW THAT MAY BE CONTAMINATED WITH PERTURBATIONS FROM LONG PERIOD WAVES, SUCH AS TIDES.	98
FIGURE 4-4. THE TWO LEFT PLOTS ARE THE LOS WIND MEASUREMENTS WITH A SIX HOUR ANALYSIS WINDOW (TOP) AND A TWO HOUR ANALYSIS WINDOW (BOTTOM). THE RIGHT TWO PLOTS ARE MOMENTUM FLUX VALUES CALCULATED FROM THE ASSOCIATED WINDS AND THE RESPECTIVE ANALYSIS WINDOW LENGTH, WITH THE SUBTRACTED LINEAR FIT.	99
FIGURE 4-5. THE CALCULATED ERROR DUE TO PHOTON NOISE IN THE LINE OF SITE WIND MEASUREMENT FOR DAY 6343 SHOWS THE THE ERROR BETWEEN 80 KM TO 100 KM IS USUALLY UNDER 1.6 M/S. THE WHITE REGIONS AT THE TOP AND BOTTOM REPRESENT 10 M/S OR GREATER ERROR.	103
FIGURE 4-6. AN ESTIMATE OF ERROR IN THE MOMENTUM FLUX MEASUREMENT SOLELY DUE TO PHOTON NOISE IS GENERATED BY MONTE CARLO SIMULATION USING THE VARIANCE OF THE MOMENTUM FLUX BETWEEN MANY THREE MINUTE MEASUREMENTS. NOTE THAT THE AVERAGE MOMENTUM FLUX (PINK +) IS NOT CENTERED ABOUT ZERO. THIS IMPLIES A BIAS IN THE MOMENTUM FLUX MEASUREMENT THAT IS PHOTON NOISE DEPENDENT.	108
FIGURE 5-1. THE EAST-BEAM LINE-OF-SIGHT WIND FOR DAYS 342 TO 344. THE DATA SET IS MADE UP OF 58 HOURS OF NEARLY CONTINUOUS DATA WITH BRIEF BREAKS FOR SYSTEM MAINTENANCE. THE NIGHTTIME DATA FOR DAY 343 IS SHOWN BETWEEN THE GREEN LINES.	113
FIGURE 5-2. LINE OF SIGHT VELOCITIES ARE MEASURED WITH TWO TELESCOPES POINTING AT 20° FROM ZENITH IN THE A) EAST AND B) WEST CARDINAL DIRECTIONS. NOTE THAT THE WINDS IN EACH CHANNEL ARE APPROXIMATELY OF THE SAME MAGNITUDE AND OF OPPOSITE SIGN; THIS IS DUE TO OBSERVATIONS AT OPPOSITE ANGLES FROM ZENITH.	115
FIGURE 5-3. THE EAST AND WEST LOS WIND VARIANCES AND MF/ρ FOR DAY 343 WITH TWO-HOUR ANALYSIS WINDOW, RESPECTIVELY (TOP), (MIDDLE), AND (BOTTOM). THE ZERO VALUE FOR MF/ρ CONTOUR IS DELINEATED BY A BLACK LINE.	122
FIGURE 5-4. THE FILTER FUNCTION FOR THE .25 TO 1 HOUR FILTER (SOLID) AND 1 HOUR TO 2 HOUR FILTER (DOTS).	124
FIGURE 5-5. THE EAST AND WEST LOS WINDS ARE DISPLAYED IN A TIME SERIES (Y-AXIS) AT DIFFERENT ALTITUDES NOTED ON THE RIGHT. TO HIGHLIGHT THE DIFFERING WAVE PERIODS AND AMPLITUDES OBSERVED IN EACH CHANNEL WE PLOT THE LOS WIND AFTER APPLYING A BAND PASS FILTER, PASSING MOTIONS 1/4 HOUR TO 1 HOUR FOR THE LEFT PLOT AND 1 HOUR TO 2 HOUR MOTIONS FOR THE RIGHT PLOT. EAST LOS WIND IS BLUE AND WEST LOS WIND IS RED.	125
FIGURE 5-6. PROFILES OF MF/ρ (BLUE, +) IS PLOTTED EVERY 2 HOURS WITH 2 HOUR AVERAGE ZONAL WINDS <U> _{2HR} (RED, x). TO THE RIGHT IS THE <MF/ρ> _N AND ZONAL WIND <U> _N NIGHTLY MEANS. THE SCALE FOR THE HODOGRAPH TO THE LEFT IS, MF/ρ: 10 M ² /S ² =1 HOUR, ZONAL WIND 2-HOUR MEAN: 29 M/S = 1 HOUR. THE SCALES FOR THE NIGHTLY MEANS ARE ANNOTATED, ON THE BOTTOM FOR MF/ρ, AND ON THE TOP FOR ZONAL WIND.	126
FIGURE 5-7. BV FREQUENCY (LINES,+) AND THE RICHARDSON'S (DOTS,x) NUMBER ARE PLOTTED BY USE OF EQUATIONS 5.5 AND 5.6 RESPECTIVELY. BOTH VALUES ARE A MEASURE OF STABILITY IN THE ATMOSPHERE. A NEGATIVE N ² (YELLOW + AND CIRCLED IN YELLOW) SUGGESTS A CONVECTIVELY UNSTABLE REGION, WHILE A RI LESS THAN 1/4 (RED x AND CIRCLED IN RED) IS REGARDED BY SOME AS DYNAMICALLY UNSTABLE. NO RICHARDSON NUMBER AFTER 10 UT IS REPORTED DUE THE LARGE MEASUREMENT ERROR REPORTED IN THE NORTH CHANNEL (FIGURE 5-8).	129
FIGURE 5-8. A PLOT OF THE CALCULATED ERROR IN THE LINE OF SITE WIND SIGNAL FOR THE NORTH BEAM SHOWS THE ERROR NEAR 102 KM TO BE CHANGING RAPIDLY AND NEARING 10 M/S. SUCH A LARGE ERROR WOULD NOT ALLOW AN ACCURATE R/ MEASUREMENT AND IS NOT CONSIDERED VALID.	130
FIGURE 5-9. <MF/ρ> _N (BLUE SOLID) IS COMPARED WITH (MF/ρ) _N (LT. BLUE DOTS), AND THEIR DIFFERENCE (DOTS – SOLID = VIOLET DASH), (U) _N (RED DASH DOT), MEAN WIND (A) _N (ORANGE DASH DOT DOT), AND THE TIDAL AMPLITUDES ((A ₂₄) _N , (A ₁₂) _N , PEACH LONG DASH AND LT GREEN DOTS, RESPECTIVELY). (A ₂₄) _N AND (A ₁₂) _N , FOR DAY 343, ARE BASED ON THIRTEEN SLIDING TIDAL FIT AMPLITUDES FOR THE 24 HR, 12 HR, TIDES. NOTE: <MF/ρ> _N USES THE BOTTOM SCALE (-10 TO 20 M ² S ⁻²); ALL OTHERS USE THE TOP SCALE (-50 TO 100 M ² S ⁻² FOR MF AND MS ⁻¹ FOR ALL OTHERS).	133
FIGURE 5-10. THIS IS A PLOT SHOWING THE LOS WIND FILTERED TO PASS MOTIONS WITH PERIODS GEATER THAN 2 HOURS BUT LESS THAN 6 HOURS ON THE LEFT AND 6 TO 8 HOURS ON THE RIGHT. AT THE 88 KM	

AND 92 KM ALTITUDES A COMPARISON IS MADE BETWEEN THE EAST (BLUE, *) AND WEST (RED, ◇) LOS WINDS AND THERE IS A ~4 HOUR WAVE WITH AN AMPLITUDE OF ~ 10 M/S SEEN IN THE WEST CHANNEL THAT IS NOT SEEN IN THE EAST CHANNEL; HOWEVER, THE RIGHT PLOT SHOWS A LARGER AMPLITUDE IN THE EAST CHANNEL FROM THE LONGER PERIOD WAVE SEEN IN BOTH CHANNELS. 134

FIGURE 5-11. A PLOT BREAKING DOWN VARIANCE MEASUREMENTS BY G&L (DASH, □) AND CSU LIDAR (SOLID, ×) SHOWS THE GENERALLY SAME SHAPE OF HIGHER WAVE ACTIVITY IN THE WINTER MONTHS AND A LOWERING OF WAVE ACTIVITY NEAR THE EQUINOX. SUMMER DATA IS NOT USED DUE TO LOWER SODIUM DENSITY CAUSING LOWER SIGNAL TO NOISE..... 139

FIGURE 5-12. THE EAST LOS WINDS FOR DAYS 7015 TO 7020. THE DATA SET CONSISTS OF ~100 HOURS OF NEARLY CONTINUOUS DATA WITH BRIEF BREAKS FOR SYSTEM MAINTENANCE. THE NIGHTTIME DATA ARE BOXED BETWEEN THE GREEN LINES. 146

FIGURE 5-13. THE HOURLY MEAN TEMPERATURE AND EAST LOS WIND PROFILES DURING THE NIGHTS OF 6342 TO 6344. 147

FIGURE 5-14. THE HOURLY MEAN TEMPERATURE AND EAST LOS WIND PROFILES DURING THE NIGHTS OF 7016 TO 7019. 148

FIGURE 5-15. THE DARK BLUE SOLID LINE IS THE CONVERGENCE OF (MF/ρ) AND THE VIOLET DOTTED LINE IS THE CONVERGENCE OF $(MF)/\rho$ 150

FIGURE 5-16. THE LEFT PLOT IS THE SMOOTHED MF/ρ (SOLID, BLUE, SCALE = $5 \text{ m}^2\text{s}^{-2}$ PER KM) AND THE ZONAL DAILY RUNNING TIDE ($U[RS]$) (DOTS, VIOLET, SCALE = 50 ms^{-1} PER KM) OF DAY 343, 2006. THE RIGHT PLOT IS THE CONVERGENCE OF THE SMOOTHED MF/ρ $(\partial(-MF/\rho)/\partial z)$, SOLID, BLUE, SCALE = $5 \text{ m}^2\text{s}^{-2} \text{ km}^{-1}$ PER KM) WITH $U[RS]$ DIURNAL (DOTS, VIOLET, SCALE = 5 ms^{-1} PER KM) AND SEMIDIURNAL AMPLITUDES (DASH, RED, SCALE = 5 ms^{-1} PER KM) . THE ALTITUDES ARE NOTED TO THE RIGHT. THE AVERAGED TIDAL AMPLITUDE FOR THE GIVEN ALTITUDE IS PLOTTED ON THE LEFT, WITH DIURNAL ABOVE AND SEMIDIURNAL BELOW THE STRAIGHT BLACK DASHES THAT REPRESENTS THE ALTITUDE AND THE MEAN AMPLITUDES. 152

FIGURE 5-17. THE LEFT PLOT IS THE SMOOTHED MF/ρ (SOLID, BLUE, SCALE = $5 \text{ m}^2\text{s}^{-2}$ PER KM) AND THE ZONAL DAILY RUNNING TIDE ($U[RS]$) (DOTS, VIOLET, SCALE = 50 ms^{-1} PER KM) OF DAY 16, 2007. THE LEFT PLOT IS THE CONVERGENCE OF THE SMOOTHED MF/ρ $(\partial(-MF/\rho)/\partial z)$, SOLID, BLUE, SCALE = $5 \text{ m}^2\text{s}^{-2} \text{ km}^{-1}$ PER KM) WITH $U[RS]$ DIURNAL (DOTS, VIOLET, SCALE = 5 ms^{-1} PER KM) AND SEMIDIURNAL AMPLITUDES (DASH, RED, SCALE = 5 ms^{-1} PER KM) . THE ALTITUDES ARE NOTED TO THE RIGHT. THE AVERAGED TIDAL AMPLITUDE FOR THE GIVEN ALTITUDE IS PLOTTED ON THE LEFT, WITH DIURNAL ABOVE AND SEMIDIURNAL BELOW THE STRAIGHT BLACK DASHES THAT REPRESENTS THE ALTITUDE AND THE MEAN AMPLITUDES. 154

FIGURE 5-18. THE LEFT PLOT IS THE SMOOTHED MF/ρ (SOLID, BLUE, SCALE = $5 \text{ m}^2\text{s}^{-2}$ PER KM) AND THE ZONAL DAILY RUNNING TIDE ($U[RS]$) (DOTS, VIOLET, SCALE = 50 ms^{-1} PER KM) OF DAY 17, 2007. THE LEFT PLOT IS THE CONVERGENCE OF THE SMOOTHED MF/ρ $(\partial(-MF/\rho)/\partial z)$, SOLID, BLUE, SCALE = $5 \text{ m}^2\text{s}^{-2} \text{ km}^{-1}$ PER KM) WITH $U[RS]$ DIURNAL (DOTS, VIOLET, SCALE = 5 ms^{-1} PER KM) AND SEMIDIURNAL AMPLITUDES (DASH, RED, SCALE = 5 ms^{-1} PER KM) . THE ALTITUDES ARE NOTED TO THE RIGHT. THE AVERAGED TIDAL AMPLITUDE FOR THE GIVEN ALTITUDE IS PLOTTED ON THE LEFT, WITH DIURNAL ABOVE AND SEMIDIURNAL BELOW THE STRAIGHT BLACK DASHES THAT REPRESENTS THE ALTITUDE AND THE MEAN AMPLITUDES. 157

FIGURE 5-19. THE LEFT PLOT IS THE SMOOTHED MF/ρ (SOLID, BLUE, SCALE = $5 \text{ m}^2\text{s}^{-2}$ PER KM) AND THE ZONAL DAILY RUNNING TIDE ($U[RS]$) (DOTS, VIOLET, SCALE = 50 ms^{-1} PER KM) OF DAY 18, 2007. THE LEFT PLOT IS THE CONVERGENCE OF THE SMOOTHED MF/ρ $(\partial(-MF/\rho)/\partial z)$, SOLID, BLUE, SCALE = $5 \text{ m}^2\text{s}^{-2} \text{ km}^{-1}$ PER KM) WITH $U[RS]$ DIURNAL (DOTS, VIOLET, SCALE = 5 ms^{-1} PER KM) AND SEMIDIURNAL AMPLITUDES (DASH, RED, SCALE = 5 ms^{-1} PER KM) . THE ALTITUDES ARE NOTED TO THE RIGHT. THE AVERAGED TIDAL AMPLITUDE FOR THE GIVEN ALTITUDE IS PLOTTED ON THE LEFT, WITH DIURNAL ABOVE AND SEMIDIURNAL BELOW THE STRAIGHT BLACK DASHES THAT REPRESENTS THE ALTITUDE AND THE MEAN AMPLITUDES. 158

FIGURE 5-20. THE LEFT PLOT IS THE SMOOTHED MF/ρ (SOLID, BLUE, SCALE = $5 \text{ m}^2\text{s}^{-2}$ PER KM) AND THE ZONAL DAILY RUNNING TIDE ($U[RS]$) (DOTS, VIOLET, SCALE = 50 ms^{-1} PER KM) OF DAY 19, 2007. THE LEFT PLOT IS THE CONVERGENCE OF THE SMOOTHED MF/ρ $(\partial(-MF/\rho)/\partial z)$, SOLID, BLUE, SCALE = $5 \text{ m}^2\text{s}^{-2} \text{ km}^{-1}$ PER KM) WITH $U[RS]$ DIURNAL (DOTS, VIOLET, SCALE = 5 ms^{-1} PER KM) AND SEMIDIURNAL AMPLITUDES (DASH, RED, SCALE = 5 ms^{-1} PER KM) . THE ALTITUDES ARE NOTED TO THE RIGHT. THE AVERAGED TIDAL AMPLITUDE FOR THE GIVEN ALTITUDE IS PLOTTED ON THE LEFT, WITH DIURNAL

ABOVE AND SEMIDIURNAL BELOW THE STRAIGHT BLACK DASHES THAT REPRESENTS THE ALTITUDE AND THE MEAN AMPLITUDES.	159
FIGURE I-1. A GRAVITY WAVE SPECTRUM SIMULATED WITH SIX WAVES OF DIFFERING PERIODS (SEE MAIN BODY FOR WAVE DESCRIPTION) AND PLOTTED WITH TIME ALONG THE X-AXIS AND ALTITUDE ALONG THE Y-AXIS. THE DATA IS THEN ANALYZED USING A MORLET-AMPLITUDE WAVELET (BOTTOM).	172
FIGURE I-2. WAVELET ANALYSIS IS PERFORMED AT 97 KM WITH DIFFERING CUTOFF PERIODS. THE TOP PLOTS SHOW THE WEST (LEFT) AND EAST (RIGHT) HIGH-PASS BOXCAR FILTERED LOS WINDS WITH A 2 HOUR CUTOFF PERIOD. THE FILTER DIMINISHES THE AMPLITUDES OF WAVEFORMS PERIODS LONGER THAN 2 HOURS BUT DOES NOT COMPLETELY REMOVE OBSERVED WAVES. THE MIDDLE PLOTS EMPLOY THE SAME FILTER WITH A 1 HOUR CUTOFF PERIOD TO SUPPRESS LONGER PERIOD WAVES AND ALLOW BETTER OBSERVATION OF WAVE WITH A PERIOD LESS THAN 2 HOURS. THE BOTTOM PLOT SHOWS THE PHASE RELATIONS BETWEEN THE TWO CHANNELS, SHOWING THE WAVE FORMS IN BOTH BEAMS MOSTLY ANTI-CORRELATED.	175
FIGURE I-3. WAVELET ANALYSIS PERFORMED AT 97KM WITH A 0.25 HOUR CUTOFF PERIOD. GW BURSTS OF 1 TO 2 HOURS IN DURATION PREVAIL FOR THE SHORTER PERIOD GWS.	176
FIGURE I-4. CROSS CORRELATION OF LINEAR FILTERED AND NON-FILTERED LOS TEMPERATURES. LINEAR FIT FILTERED CORRELATIONS ARE PERFORMED WITH ALL DATA POINTS ASSOCIATED WITH A 2 HOUR DATA ANALYSIS WINDOW. THE CROSS-CORRELATION VERSES ALTITUDE (LEFT) AT A TIME LAG OF 0 MINUTES. TO THE RIGHT IS THE CROSS CORRELATION OF THE TWO LOS TEMPERATURES (Y-AXIS) AT THREE DIFFERENT ALTITUDES VS. DIFFERENT LAG VALUES (X-AXIS) WHERE THE LAG IS 3 MINUTES PER INCREMENT ON PLOT. THE TOP THREE SMOOTHER LINES ARE THE NON-FILTERED VALUES.	179
FIGURE I-5. A SERIES OF WAVELET PLOTS FROM 85-99KM EVERY 2KM. ALL PLOTS USE THE SAME SCALE TO ALLOW THE READER SEE THE INCREASE IN AMPLITUDE OF THE WAVES AS THEY TRAVEL +Z IN ALTITUDE. ALTITUDES ARE NOTED IN THE TITLE LINE STARTING AT 85KM IN THE BOTTOM RIGHT AND INCREASING EVERY 2KM UNTIL 99KM IN THE TOP LEFT.	181
FIGURE II-1. A SCHEMATIC OF THE TIMING ELECTRONICS STARTING IN THE TOP LEFT WITH CHOPPER 100, WHICH IS A 100HZ TTL SIGNAL THAT DICTATES THE TIMING OF THE CIRCUIT. THIS SIGNAL IS DIVIDED BY A CLOCK TO SHIFT THE FREQUENCY OF THE TRANSMITTED PULSES, TIME THE TRANSMITTED PULSES, AND ALLOW FOR PROPER BINNING OF THE SEQUENCE OF THE RETURNING PHOTON PULSES. Q_SWITCH, AT THE BOTTOM LEFT, IS A SIGNAL FROM THE YAG LASER INDICATING WHEN THE LASER HAS FIRED. THIS PROVIDES AN ACCURATE TIME OF FLIGHT MEASUREMENT FOR COUNTED PHOTONS.	184
FIGURE II-2. THIS IS A PICTURE OF THE COMTEC CARD WITH THE ACCESS PORTS ANNOTATED AND THE 15-PIN CONNECTOR TO THE RIGHT. TIMING OF WHEN THE LASER IS FIRED (COUNT_THROUGH) IS INPUT INTO TRG (START) AND RETURNED PHOTONS (PMT PULSES) ARE COUNTED WITH COUNT (STOP) 1 AND 2 IN. DIG_IO 0 AND 1 ARE USED FOR SPECTRAL TAGGING.	188
TABLE 1 TYPES OF SCATTERING MEASURED BY LIDAR SYSTEMS.	11
TABLE 2 FREQUENCIES OF D ₂ TRANSITONS RELATIVE TO THE WEIGHTED GROUP CENTER OF THE RESPECTIVE TRANSITIONS WITH LINE WEIGHTING INCLUDING ALL DEGENERACIES WITH AND WITHOUT HANLE EFFECT FROM EARTH'S GEOMAGNETIC POTENTIAL.(SHE AND YU 1995)	24
TABLE 3 A COMPARISON OF RESULTS FROM GARDNER AND LIU (2007), GARDNER AND YANG (1998) AND CSU LIDAR EXTENDED STUDY OF MLT VARIANCE.	141
TABLE 4. A TABLE OF ALL MOMENTUM FLUX MEASUREMENTS, INCLUDING DATE, NUMBER OF HOURS OF MEASUREMENT, AND RECORDED VARIANCES IN WINDS AND TEMPERATURES.	143

Chapter 1: **Introduction**

The atmosphere plays a significant role in everyone's life. Global environmental change has been hotly debated among scientists and in the halls of governments. Now, with the publishing of the IPCC 4th assessment, there is a general consensus among scientists on the issue of global warming. The vast majority of natural scientists agree that the earth is warming and that there is strong evidence to suggest that humans are the cause. Despite this, there are still a few very vocal scientists that do not believe the science used in the IPCC 4th assessment; politicians still debate the actions to be taken and which scientists to believe. With these uncertainties, one thing is certain: we will never understand global environmental change unless we study the atmosphere.

This dissertation is not a study of global warming. Rather, like the study of global warming, in an attempt to understand the atmosphere as a whole, it is often the individual questions of the greater system that are studied. The individual question that this dissertation addresses is how momentum is transferred in the mesosphere lower thermosphere (MLT), specifically the deposition of momentum carried by gravity waves and their interactions with the atmospheric tides.

By modifying the Colorado State University (CSU) lidar system to coplanar beams in the east west plane, zonal momentum flux can now be measured. It is expected that with this new beam alignment, over a period of time, a greater understanding of gravity wave tidal interaction can be realized. In addition, existing momentum flux measurement techniques have been modified to conform to established sodium lidar

measurement priorities such as an ongoing tidal study. Furthermore, a testing framework has been established in order to validate the measurements and the analysis technique to gauge the error in the measurements.

This chapter introduces the parameters used to describe the state of the atmosphere, specifically the mean temperature vertical profile, which is used in combination with pressure to delineate the four separate regions of the atmosphere. This is followed by a brief introduction to the methods of measuring the atmosphere with laser light and a history of the development of lidar systems that make these measurements. The third section introduces Colorado State University lidar history, and the chapter ends with the motivation for and the structure of this dissertation.

1.1 Introduction to the Atmosphere

The state of the earth's atmosphere may be described by two of three physical quantities (pressure, density, temperature) and the three components of the velocity (x , y , z) as functions of space and time. Motions in the atmosphere are governed by the conservation of mass, energy, and momentum. Two frames of reference are useful: the frame that moves with the air parcel, and the frame that is fixed relative to the earth. In the former frame, *Lagrangian* coordinates, the air parcel moves with the surrounding fluid of the atmosphere; therefore the shape of the air parcel will deform as it is subjected to changing forces from the surrounding fluid. All of the variables describing the state of the air parcel (e.g. temperature, density, momentum), can change except the individual particles that make up the parcel itself (mass of the air parcel). In the latter frame, *Eulerian* coordinates, the atmosphere in an infinitesimal volume with sides δx , δy , δz , at a stationary point $\bar{x}(x', y', z')$, is characterized by time-dependent atmospheric

parameters, such as pressure $p(\bar{x}, t)$, density $\rho(\bar{x}, t)$, temperature $T(\bar{x}, t)$, and wind velocity $\bar{u}(\bar{x}, t)$.

1.1.1 Temperature vertical structure

The atmosphere is divided into four different regions defined by the vertical gradient in the temperature profile, $\partial T/\partial z$ (Holton, 1992). Most of the mechanisms that cause the averaged temperature profile of the atmosphere can be explained in general terms of simple physical processes with few exceptions. As always with science, these exceptions draw the most attention. Figure 1-1 depicts the mean temperature vertical profile (red line) and shows the range of altitudes for different named regions in the atmosphere; the far right axis displays the typical pressure at the respective altitudes located on the left y-axis.

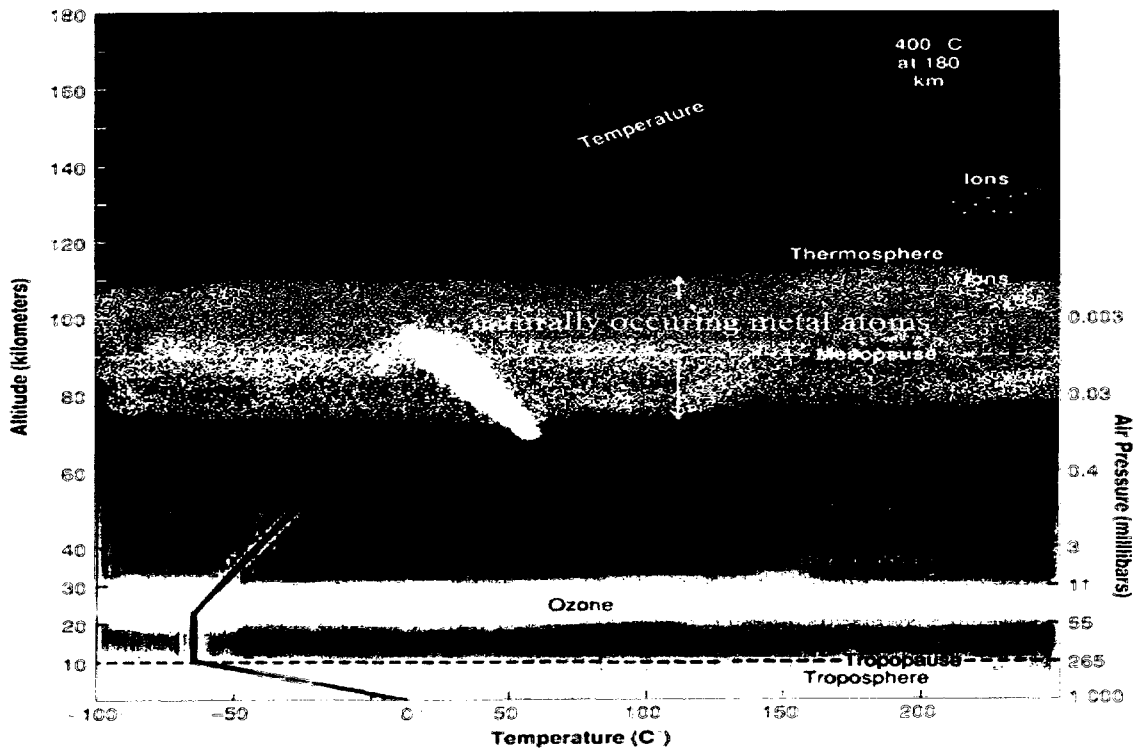


Figure 1-1. Typical vertical altitude (km) vs. temperature (C) structure (red line) with named regions in the atmosphere and expected average air pressure annotated on the right y-axis.

Troposphere - Solar radiation heats the earth's surface which radiates heat into the atmosphere. Temperature decreases as altitude increases. Infrared emission from water vapor and clouds radiates in a 4π steradian solid angle, which causes some energy to be re-radiated into space. There is convective overturning in the troposphere in the afternoon, causing the slope of $\partial T/\partial z$ to be near the saturated adiabatic lapse rate (~ 6.5 K/km). This overturning gives the troposphere its name, from the Greek word *tropē*, meaning to turn or change. Because humans live in the troposphere and weather systems have their primary responses to it, it is the most studied region in the atmosphere.

Stratosphere – The warming of the stratosphere is due to a photochemical process that takes place with molecular oxygen (O_2) and ozone (O_3). The bulk of the O_3 in the atmosphere occurs in the stratosphere. The stratosphere contains the now-famous ozone hole in its polar region. The ozone hole forms and dissipates by a complex interaction in polar region chemistry. A polar vortex forms at the winter pole, effectively separating the polar stratospheric atmosphere from the atmosphere of lower latitudes with steep gradients of potential vorticity. Polar stratospheric clouds form as a result of adiabatic cooling. Chemical interactions that take place on the surface of the ice crystals of these clouds increase the rate of ozone depletion. Because the polar region atmosphere is isolated by the vortex, ozone in this region is depleted; and the ozone hole forms. Rossby waves or planetary waves along the edge of the polar vortex propagate upward, grow in amplitude, and cause instabilities that temporarily destroy the vortex. After this breakdown of the vortex, the polar atmosphere mixes with lower latitude atmosphere, the ozone in the region is replenished, and the ozone hole goes away. The vortex then reforms and the process repeats several times during the winter (Andrews, 2000).

Thermosphere – The thermosphere is so named because it registers the highest temperatures in the earth's atmosphere. The thermosphere ranges from about 90 to 500 km above the surface of the earth. It occurs directly above the mesopause, the coldest region in the atmosphere (~80 to 110 km), and is noted for its large temperature gradient. The thermosphere contains the ionosphere which is important for radio wave propagation to distant places on the earth.

1.1.2 Introduction to the Mesosphere

The mesosphere ranges from about 50 to 100 km above the surface of the earth, and it largely remains the most under-sampled region in the atmosphere. This scientific neglect is mostly due to other regions in the atmosphere being more accessible.

It seemed as if the mesosphere had nothing exciting to offer. All weather systems affecting the surface of the earth take place in the troposphere. The ozone hole occurs in the stratosphere. The thermosphere contains the ionosphere enabling radio and television broadcast. Moreover, the altitude of the mesosphere makes it difficult to measure its characteristics from the surface of the earth. In situ measurements made with falling spheres from rockets and the rockets themselves are an effective way to measure properties of the mesosphere. Yet rockets are expensive and require months if not years of preparations for one launch. An entire laser remote sensing program can be built and funded for years for the cost of one rocket campaign. Each measurement technique offers advantages and has disadvantages in the study of the atmosphere.

1.1.3 Mesopause behavior

The mesopause (the altitude of coldest temperature on earth's atmosphere) separates the mesosphere from the thermosphere and is usually located at about 80 to 90

km in the summer and 95 to 105 km in the winter. The mesosphere has substantially less ozone than the stratosphere, shifting the radiative heat balance toward radiative cooling; this results in the negative $\partial T/\partial z$ slope as heat is radiated away (Figure 1-1). However, it is well known that the observed thermal structure near the mesopause at the solstice is not in radiative equilibrium. And, the mean meridional circulation from the summer to winter hemisphere, with adiabatic heating/cooling of the falling/rising air over the winter/summer pole causes this departure from radiative equilibrium.

Wave dissipation in the atmosphere provides the needed force to cause the meridional circulation, but which waves are responsible for this circulation? Dissipating planetary waves provide some of the balancing force in the winter mesosphere, but they are absent from the summer hemisphere; therefore, they do not contribute to the summer mesospheric momentum budget (Houghton, 1978). The main propagating diurnal mode of the atmospheric tide may be a primary contributor at tropical latitudes, but at mid- and high-latitudes it seems unlikely that they are important on observational and theoretical grounds (Lindzen, 1981; Miyahara, 1980). Only gravity waves are present in both hemispheres (winter/summer) and expected to provide sufficient wave drag at mid- and high-latitudes, to provide the needed balancing force to induce the observed mean wind profiles (Lindzen, 1981; Holton, 1982; Matsuno, 1982).

Qualitatively, the reasons for the mean meridional circulation can be understood as a direct result of the three-way balance among the pressure gradient force, the Coriolis 'force' and turbulent drag due to gravity wave divergence/dissipation. This balance is illustrated in Figure 1-2 by depicting the force balance in the northern hemisphere during winter conditions. In Figure 1-2 North is upward. The zonal wind flows from East to

West in the summer; for the southern hemisphere the zonal wind is in the opposite direction of the northern hemisphere for the respective seasons. Consider if there were no gravity wave propagation and subsequent divergence. Then the pressure gradient force and the Coriolis force would be in equilibrium and the wind (\mathbf{v}) would flow along lines of constant pressure (Figure 1-2, left). If the pressure gradient force and Coriolis were not in equilibrium the wind would be accelerated by the pressure gradient force, increasing the contribution from the Coriolis Effect and equilibrium is soon reached. In fact, oscillations about this equilibrium are called Rosby waves. Due to filtering by the wind at lower altitudes, GWs in the mesosphere have momentum in the opposite direction with the mean wind (Lindzen, 1981). These GWs grow in amplitude and break in the mesosphere, imparting a body force on the wind.

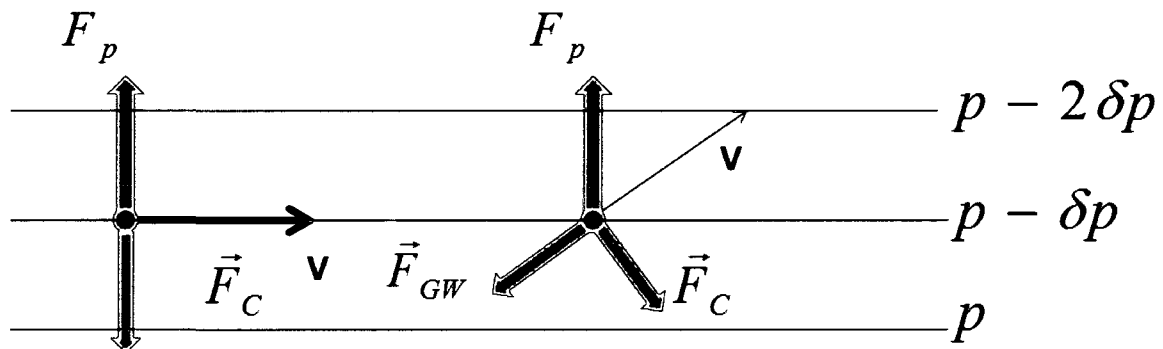


Figure 1-2. Balance of forces showing the effect of wave drag on the mean flow; where, \mathbf{v} is the true wind, F_p is the pressure gradient force, F_C is the Coriolis 'force' and F_{GW} is the body force due to gravity wave dissipation causing momentum flux divergence.

The addition of turbulent drag from dissipating gravity waves (due to gravity wave breaking in the mesosphere) acts as a retarding force on the mean wind. Since the Coriolis force is always normal to wind velocity and the turbulent drag is a retarding force on the wind; their sum can exactly balance the pressure gradient force if the wind is directed toward lower pressure (Figure 1-2, right), giving rise to the pole- to-pole

meridional circulation. Therefore the mean circulation is considered as being wave driven (Plumb, 1982; Holton, 1992).

1.1.4 Motivation for GW-Tidal interaction momentum flux measurements

MLT momentum flux measurements include observations by lidar (Gardner and Yang, 1998; Vance, 2004) and radar (Vincent and Reid, 1983; Fritts and Vincent, 1987; Reid et al., 1988; Tsuda et al., 1990; Wang and Fritts, 1990, 1991; Fritts et al., 1992). In view of the considerable variability and complexity in propagation, filtering and nonlinear interactions with gravity waves, significantly more measurements are needed to guide and/or constrain model development in GW and GW fluxes. Radar measurements in the late 1980s (Fritts and Vincent, 1987; Wang and Fritts, 1991) revealed strong modulation of GW momentum flux by the diurnal tide and are the only observational momentum flux studies dealing with GW-tidal interactions. There are theoretical studies specifically addressing the influences on tidal structure of GW-critical level interactions (Walterscheid, 1981), the excitation or damping of Planetary waves (PWs) by GWs arising from variable source strengths (Holton, 1984), and the modulation of GW filtering by PWs (Miyahara, 1985; Miyahara et al., 1986). These studies hint at possibly important interactions and feedbacks but offer no quantitative guidance. Significant disagreements and controversy remain over the impacts of GW-tidal (and GW-PW) interactions on tidal (and PW) amplitudes, annual variations, and mean momentum deposition (Fritts and Alexander, 2003). A number of studies suggest that such interactions dampen tidal amplitudes (Forbes et al., 1991; Lu and Fritts, 1993; Meyer, 1999; Ortland, 2005); another suggests amplification during the equinox (Mayr et al., 1998a, 1998b) while still others suggest little or no impact on amplitudes (McLandress, 2002) or a potential for

altered mean momentum deposition throughout the dominant tidal periods (Lu and Fritts, 1993; McLandress and Ward, 1994). These conflicting studies reveal that the quantitative descriptions of current GW parameterizations of interactions with either mean or large-scale wave motions should be improved. More momentum flux measurements are required in order to quantitatively define GW-tidal and GW-PW interactions throughout diurnal cycles.

There is a clear need to define the modulation of GW momentum fluxes by tidal structures, the residual mean forcing in the presence of tidal modulation, and the influences of such modulations on the tidal amplitudes in the MLT. Observationally, we must obtain a sufficiently continuous direct measurement of GW momentum fluxes while making simultaneous full diurnal cycle observations to deduce tidal amplitudes and phases of the zonal wind.

1.2 Lasers used for atmospheric remote sensing

Since the advent of the laser, scientists have been pointing this high intensity, highly collimated light source at nearly any object and observing the scattered light to determine the physical property of matter. A use of laser light that naturally springs from radar (**radio detection and ranging**), is lidar (**light detection and ranging**). Most atmospheric lidar systems send a pulsed laser beam into the sky. The backscattered photons are collected by a telescope, filtered, and then counted. The counts are binned with respect to time of flight. Because the time when a pulse of light is sent into the sky and the speed of light are known, the distance that the measured light has traveled is also known.

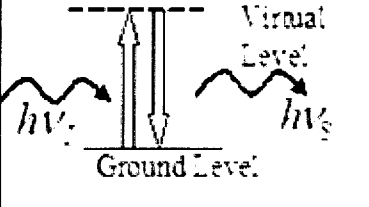
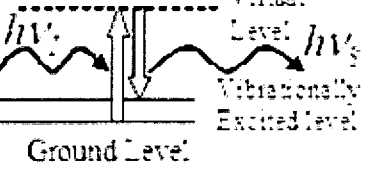
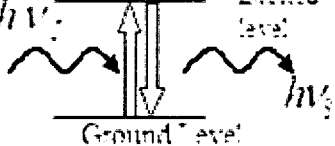
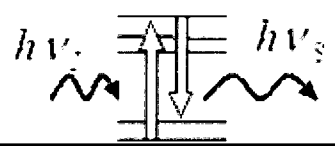
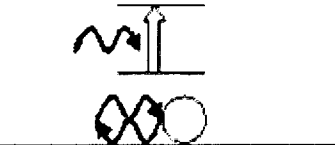
1.2.1 History

Since 1963 when Fiocco and Smullin (1963) detailed the use of optical radar (lidar) for atmospheric studies, scientists have been pointing lasers in to the sky to probe the atmosphere for its secrets. In 1972, when Gibson and Sandford fluoresced atomic sodium near the mesopause sodium fluorescence lidar was born. The development of narrow bandwidth lasers made it possible to probe and resolve fine structure of the sodium in the mesopause to obtain temperatures. In 1979 Gibson et al. made a temperature measurement in the mesopause at the peak density of the sodium layer with a sodium fluorescence lidar.

1.2.2 Lidar systems

Atmospheric lidar systems are characterized by their scattering processes including Rayleigh, Mie, Raman, resonance scattering, fluorescence, and differential absorption (Measures, 1984). Many lidars take advantage of more than one process, e.g. the Rayleigh, Mie, Raman lidar which goes by the moniker RMR lidar (von Zahn et al., 2000). Resonance scattering or fluorescence lidars are usually named after the atom or molecule they probe, atomic, sodium, potassium, iron, and calcium. **Differential Absorption Lidars** are called DIAL systems and have been used to measure ozone and water vapor.

Table 1 Types of scattering measured by lidar systems¹

<p>Rayleigh Scattering – A molecule or atom acts as an electric dipole. Non-resonant light interacts with the electron cloud and starts sympathetic vibrations. The absorbed photon does not have enough energy to raise the atom or molecule to an excited state, but to an intermediate virtual state, this absorption is then reemitted instantaneously in 4π solid angle. Elastic scattering, no change in the frequency of the light.</p>	
<p>Mie Scattering – A particle composed of many molecules and scatters light like Rayleigh scattering but the particle is large enough to get constructive interference from many scatterers interacting with the interior of an individual particle. If the particle is large enough the molecules at the extremities no longer radiate in phase with the inner molecules and therefore destructive interference occurs for shorter wavelengths. Elastic scattering, no change in the wavelength of the light. This lidar is usually used to measure aerosols.</p>	
<p>Raman Scattering – A molecule absorbs a photon, like Rayleigh scattering, but reemitted light has changed frequency. The energy change is imparted to the molecule changing the rotational or vibrational state of the molecule. Inelastic scattering, the frequency of the light changes. This type of lidar is usually used to observe water vapor.</p>	
<p>Resonance Scattering – Light scatters with an atom's large cross-section at the resonant frequency of an atomic transition and raises the electron to higher excited state. The atom emits a photon and the electron returns to the ground state. No change in the frequency of the light.</p>	
<p>Fluorescence – Light undergoes absorption with an atom or molecule's large resonant cross-section at an electronic transition. The light is rapidly (~10⁻⁸ s) reemitted at a different frequency. This is performed with Na, Ca, Fe, and K.</p>	
<p>Differential Absorption – Two frequencies of light are used. One on resonance, one off resonance. The return counts are compared to determine population of constituents. This lidar usually measures Ozone (O₃).</p>	

¹ This disregards a spectral structure that exists in Rayleigh scattered light of a Doppler broadened central peak, called the Cabannes line and side bands that are due to (pure) rotational Raman scattering [She, 2001]. These spectral features are difficult to resolve and generally only become important in very narrow band systems.

1.2.3 Colorado State University Lidar

Colorado State University (CSU) Sodium lidar at Fort Collins, Colorado was first deployed in August 1989 (She et al., 1990) and has been used to perform regular observations of mesopause region temperature since May 29, 1991. For over 15 years the CSU lidar program has collected nocturnal temperatures for continued long term studies of the influence of the solar cycle and temperature trend (She and Krueger, 2004).

In May 2002, the addition of a telescope allowed simultaneous measurements of mesopause region temperature and zonal and meridional winds over full diurnal cycles. This was achieved by pointing laser beams and associated 35cm telescopes east and north, 30° from zenith. These observations provided data which allowed the expansion of science objectives to include dynamics studies of atmospheric waves, which had not previously been possible. Now, with over four years of tidal measurements, CSU has sufficient tidal data to pursue study of the climatology of tides above Fort Collins (Yuan, et al., 2006).

In October 2006 two 75 cm telescopes were deployed with an increase in the return signal by roughly a factor of five. While continuing ongoing studies, this greater signal has allowed the pursuit of additional science: momentum flux measurements in winter night when the Na signal is particularly strong. Since the system upgrade, the two 75 cm telescopes have been pointing at angles 20° east and west from zenith for dual coplanar beam, zonal momentum flux (Vincent and Reid, 1983) and zonal wind measurements. An existing Celestron is pointed to the north 30° from zenith for meridional wind measurements. Instead of the former 50-50 split of transmitter power, night time power is now split 3-ways: 40 percent for each of the two 30” telescopes, and

20 percent for the Celestron. For daytime operation a beam splitter on a flip mount is moved out of the beam path, and the transmitted power is split 2-ways: 40 percent for one of the 75 cm telescopes, and 60 percent for the smaller Celestron. This distribution of power maximizes daytime transmission power for the smaller telescope channel, therefore maximizing its return signal. In this manner simultaneous measurement of nighttime zonal momentum flux and continued 24-hour continuous observation of mesopause region temperature and zonal and meridional winds for full diurnal cycles are performed. The ongoing data set of nighttime zonal momentum flux measurements has the potential to address the not fully understood gravity wave (GW)-tidal interaction. Since the October upgrades there have been over 160 hours of nighttime three-beam observations; of those measurements, seven full diurnal cycles were measured. The temperature and horizontal wind that can be deduced from the same data set allows the continued study of tides, planetary waves (PW), longer period GWs, and long-term and global change based on nocturnal temperatures.

1.3 Structure of Dissertation

Chapter 2 introduces sodium spectroscopy theory and how it is used to determine temperatures and winds in the mesopause with the fluorescence of naturally occurring atomic sodium in the mesopause. This is followed by a description of the CSU high spectral resolution frequency agile lidar, a breakdown of the transmitter, receiver, and the electronics that couple those subsystems together.

Chapter 3 introduces basic theory of the mesosphere and simple gravity wave theory. This is followed with an introduction to momentum flux and the Vincent and

Reid method of measurement with co-planar beams. The chapter concludes with a brief discussion of tidal effects in the atmosphere and tidal gravity wave interaction.

Chapter 4 presents filtering and analysis techniques employed in the momentum flux analysis. This is followed by a discussion of errors in the measurement and an estimate of error based on Monte Carlo simulation.

Chapter 5 presents the data obtained in the study. A case study of a specific night of observations highlights the analysis techniques, allows discussion about wind and momentum flux characteristics, and enables exploration of atmospheric stability. This is followed with a statistical study of all the data and a comparison to another long term MLT momentum flux performed with lidar. Chapter 5 concludes with a discussion about GW-tidal interaction.

Chapter 6 presents conclusions and provides a short discussion about suggested further work.

References

- Andrews, David G., *An Introduction to Atmospheric Physics*, Cambridge University Press, 2000.
- Fiedler, J., G. von Cossart, F. Hübner, H. Mehrstens, U. von Zahn, K.-H. Fricke, G. Nelke, A. Hauchecorne, F. Fierli, and D. Rees, Status of the ALOMAR Rayleigh/Mie/Raman lidar, in *Proc. 13th ESA Symp. On European Rocket and Balloon Programmes and Related Research*, edited by B. Kaldeich-Schürmann, ESA SP-397, 105-110, 1997.
- Fiocco, G. and L. D. Smullin, Detection of Scattering Layers in the Upper Atmosphere (60-140km) by Optical Radar, *Nature*, **199**, 1275-1276, 1963.
- Forbes, J. M., J. Gu, and S. Miyahara, On the interactions between gravity waves and the diurnal propagating tide, *Planet. Space Sci.*, **39**, 1249-1257, 1991.
- Fritts, D. C., and M. J. Alexander, Gravity dynamics and effects in the middle atmosphere, *Rev. Geophys.*, **41**, doi:10.1029/2001RG000106, 2003.
- Fritts, D. C., and R. A. Vincent, Mesospheric momentum flux studies at Adelaide, Australia: Observations and a gravity wave/tidal interaction model, *J. Atmos. Sci.*, **44**, 605-619, 1987.
- Fritts, D. C., and L. Yuan: Measurement of momentum fluxes near the summer mesopause at Poker Flat, Alaska, *J. Atmos. Sci.*, **46**, 2569-2579, 1989.
- Fritts, D. C., L. Yuan, M. H. Hitchman, L. Coy, E. Kudeki, and R. F. Woodman, Dynamics of the equatorial mesosphere observed using the Jicamarca MST radar during June and August 1987, *J. Atmos. Sci.*, **49**, 2353-2371, 1992.
- Gardner, C. S., and W. Yang, Measurement of the dynamical cooling rate associated with the vertical transport of heat by dissipating gravity waves in the mesopause region at the Starfire Optical Range, *J. Geophys. Res.*, **103**, 16,909-16,927, 1998.
- Gibson, A.L., and M. C. W. Sandford, Daytime Lidar Measurements of the Mesospheric Sodium Layer, *Nature*, **33**, 509-511, 1972.
- Gibson, A., L. Thomas, and S. Bhattacharyya, Lidar observations of the ground-state hyperfine structure of sodium and of temperature in the upper atmosphere, *Nature*, **281**, 131-132, 1979.
- Holton, James R., *An Introduction to Dynamic Meteorology*, Elsevier Science (USA), Academic Press, 1992.
- Holton, J. R., The generation of mesospheric planetary waves by zonally asymmetric gravity wave breaking, *J. Atmo. Sci.*, **41**, 3427-3430, 1984.

- Holton, James R., The Role of Gravity Wave Induced Drag and Diffusion in the Momentum Budget of the Mesosphere, *J. Atmos. Sci.* **39**, 791-799, 1982.
- Houghton, J. T., The stratosphere and mesosphere. *Quart. J. Roy. Meteor. Soc.*, **104**, 1-29, 1978.
- Lindzen, R.S., Turbulence and Stress Owing to Gravity Wave and Tidal Breakdown, *J. Geophys. Res.*, **86**, NO. C10, 9707-9714, 1981
- Lu, W., and Fritts, D. C., Spectral estimates of gravity wave energy and momentum fluxes III, Gravity-tide interactions, *J. Atmos. Sci.*, **50**, 3714-3727, 1993.
- Matsuno, T., A quasi-one-dimensional model of the middle atmosphere circulation interacting with internal gravity waves. *J. Meteor. Soc. Japan.*, **60**, 215-226, 1982.
- Mayr, H. G., J. G. Mengel, K. L. Chan, and H. S. Porter, Seasonal variations of the diurnal tide induced by gravity wave filtering, *J. Geophys. Res.*, **25**, 943-946, 1998a.
- Mayr, H. G., J. G. Mengel, C. A. Reddy, K. L. Chan, and H. S. Porter, Variability of the equatorial oscillations induced by gravity wave filtering, *J. Geophys. Res.*, **25**, 2629-2632, 1998b.
- McLandress, C., and W. E. Ward, Tidal/gravity wave interactions and their influence on the large-scale dynamics of the middle atmosphere: Model results, *J. Geophys. Res.*, **99**, 8139-8155, 1994.
- McLandress C., Interannual variations of the diurnal tide in the mesosphere induced by a zonal-mean wind oscillation in the tropics, *J. Geophys. Res.*, **29**, doi:10.1029/2001GL014551, 2002.
- Measures, Raymond M., *Laser Remote Sensing: fundamentals and applications*, New York, Wiley, 1984.
- Meyer, C. K., Gravity wave interactions with the diurnal propagating tide, *J. Geophys. Res.*, **104**, 4223-4240; Erratum: *J. Geophys. Res.*, **104**, 4223-4239, 1999.
- Miyahara, S., Solar diurnal tides and the induced zonal mean flows. *J. Meteor. Soc. Japan.*, **58**, 302-306, 1980.
- Miyahara, S., Suppression of stationary planetary waves by internal gravity waves in the mesosphere, *J. Atmos. Sci.*, **42**, 100-107, 1985.
- Miyahara, S. Y. Hayashi, and J. D. Mahlman, Interactions of gravity waves and planetary-scale flow simulated by the GFDL "SKYHI" general circulation model, *J. Atmos. Sci.*, **43**, 1844-1861, 1986.
- Ortland DA, Generalized hough modes: The structure of damped global-scale waves propagating on a mean flow with horizontal and vertical shear, *J. Atmo. Sci.*, **62**, 2674-2683, 2005.

- Plumb, R. A., The circulation of the middle atmosphere. *Aust. Meteor. Mag.*, **30**, 107-121, 1982.
- Reid, I. M., R. Rüster, P. Czechowsky, G. Schmidt, VHF radar measurements of momentum flux in the summer polar mesosphere over Andenes (69°N, 16°E), Norway, *Geophys. Res. Lett.*, **15**(11), 1263-1266, 10.1029/88GL03439, 1988.
- She, C. Y., and D. A. Krueger, Impact of natural variability in the 11-year mesopause region temperature observation over Fort Collins, CO (41N, 105W) *Adv. Space Phys.* **34**, 330-336, 2004.
- She, C. Y., Jim Sherman, Joe Vance, Titus Yuan, Zhilin Hu, B. P. Williams, Kam Arnold, Phil Acott, and David A. Krueger, Evidence of solar cycle effect in the mesopause region: Observed temperatures in 1999 and 2000 at 98.5 km over Fort Collins, CO (41N, 105W) *J. Atmos. Solar-Terr. Phys.* **64**, 1651-1657, 2002.
- She, C. Y., Spectral structure of laser light scattering revisited: bandwidths of non-resonant scattering lidars, *Applied Optics*, **40**, No. 27, 4875-4884, 2001.
- Thomas, G. E. Is the Polar Mesosphere the Miner's Canary of Global Change? *Adv. Space Res.* **18** No. 3, 149-158, 1996.
- Tsuda, T., Y. Murayama, M. Yamamoto, S. Kato, and S. Fukao, Seasonal variation of momentum flux in the mesosphere observed with the MU radar, *Geophys. Res. Lett.*, **17**, 725-728, 1990.
- Vance, J. P., *The Sum Frequency Generator seeded, ALOMAR Weber Sodium LIDAR and Initial Measurements of Temperature and Wind in the Norwegian Arctic Mesopause Region*, PhD Dissertation, Colorado State University, 2004
- Vincent, R. A. and I. M. Reid, HF Doppler measurements of mesospheric gravity wave momentum fluxes, *J. Atmos. Sci.*, **40**, 1321-1333, 1983.
- von Zahn, U., G. von Cossart, J. Fiedler, K.H. Fricke, G. Nelke, G. Baumgarten, D. Rees, A. Hauchecorne, und K. Adolfsen, The ALOMAR Rayleigh/Mie/Raman lidar: Objectives, configuration, and performance, *Annales Geophysicae*, **18**, 815 - 833, 2000.
- Walterscheid, R. L., Dynamical cooling induced by dissipating internal gravity waves, *Geophys. Res. Lett.*, **8**, 1235-1238, 1981.
- Wang, D.-Y., and D. C. Fritts, Mesospheric momentum fluxes observed by the MST radar at Poker Flat, Alaska, *J. Atmos. Sci.*, **47**, 1511-1521, 1990.
- Wang, D.-Y., and D. C. Fritts, Evidence of Gravity Wave-Tidal Interaction Observed near the Summer Mesopause at Poker Flat, Alaska, *J. Atmos. Sci.*, **48**, 572-583, 1991.

Williams, B. P., J. Sherman, C. Y. She, and F. T. Berkey, Coincident extremely large sporadic sodium and sporadic E layers observed in the lower thermosphere over Colorado and Utah, *Annales Geophysicae*, accepted, 2007.

Yuan, T., *Monthly Climatology in Mean Value Tides in the Mesopause Region*, CEDAR Postdoc Lecture, CEDAR conference, Santa Fe, New Mexico, 2006.

Zhou Q., Y. T. Morton, A case study of mesospheric gravity wave momentum flux and dynamical instability using the Arecibo dual beam incoherent scatter radar, *Geophys. Res. Lett.*, **33**, L10802, doi:10.1029/2005GL025608, 2006

Chapter 2: Sodium Lidar Measurement Methodology

In order to study MLT dynamics, measurements of the regions temperatures and winds are required. Nature has provided a convenient way to allow temperature and wind measurements in the MLT region by providing naturally occurring atomic sodium from roughly 80 km to 110 km. Sodium, fortunately, is one of the few atoms that quantum theory can model accurately and therefore predict fluorescence behavior. This atomic sodium in the MLT region can be fluoresced remotely by narrow linewidth laser light pulses to determine temperatures and winds.

This chapter first discusses sodium fluorescence theory with special attention on the D_2 transition spectral lineshape and how, when it is combined with a pulsed narrow band laser, enables sodium lidar. This is followed by the physical setup needed to enable temperature, wind, and sodium density measurements based on this theory is described.

2.1 Sodium Theory and Sodium Lidar

In the MLT region of the atmosphere, there are naturally occurring metal atoms: sodium, iron, potassium, calcium, and others. These metals are continuously depleted by chemical processes and diffusion and are replenished by meteor ablation (Kirchhoff, 1986). The sodium layer is usually about 20 km thick, occurring at altitudes between 70 and 100 km with mean sodium densities of $\sim 10^9 - 10^{10} \text{ atoms} \cdot \text{m}^{-3}$. Changes in the thickness, altitude and density of the sodium layer occur on time scales that range from years to minutes. Sodium lidar takes advantage of the naturally occurring atomic sodium

by inducing fluorescence with a laser light and observing the light returning from that fluorescence.

Atomic sodium's differential cross-section at sodium resonance is fifteen orders of magnitude greater than the non-resonance interactions at the same wavelength (She, 1990). This greater cross-section allows the fluorescing of sodium atoms with modest output power (<1W) of the probing lidar system; this still allows a relatively large return signal in the sodium layer from which temperature, wind and sodium density is calculated. Sodium lidar systems typically report the lowest measurement error for temperature and winds measurements in the MLT of the devices that make measurements in the region.

There are drawbacks associated with sodium lidar systems. They tend to be much more complex than most other lidar systems because they need to achieve sodium resonance frequency. Also, all lidar systems require clear sky for meaningful measurements. Finally, there are inherent dangers in operating most laser systems; for example, they are not eye-safe until the laser beam has traveled a long distance and exotic, potentially dangerous, dyes are often needed to achieve required frequencies.

2.1.1 Na spectrum

To create a high spectral resolution sodium fluorescence lidar the sodium spectrum must be first understood. The sodium D spectrum has been studied and understood for many years. Three models of the expected transitions in the D spectrum are detailed in Figure 2-1.

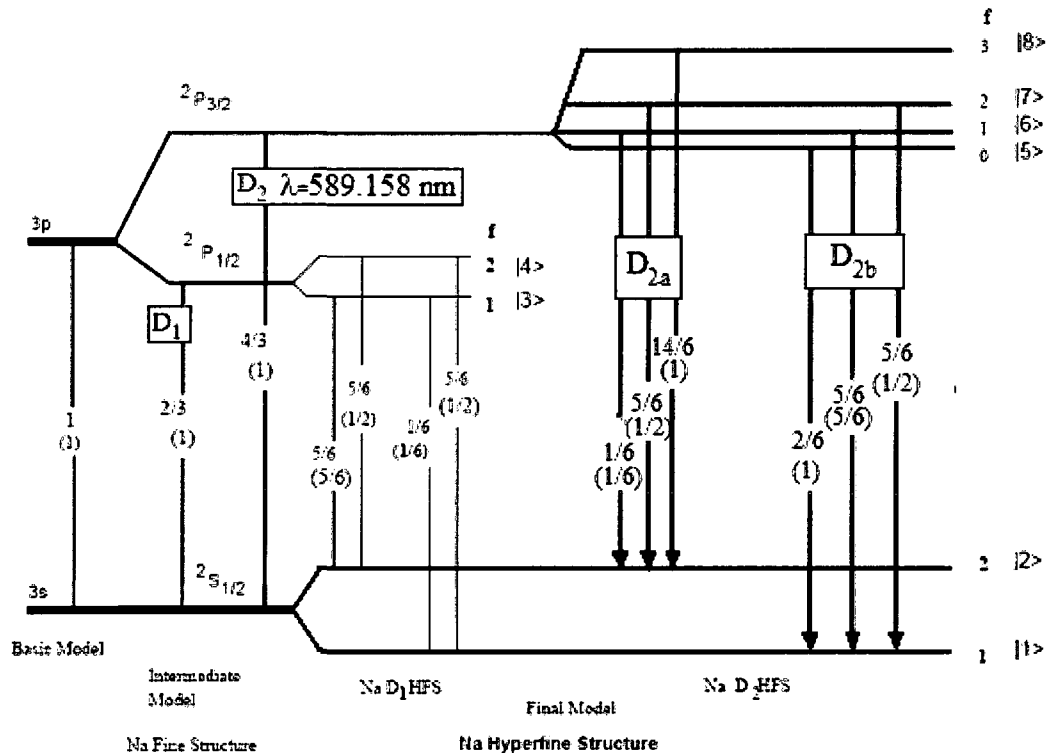


Figure 2-1. The energy diagram of sodium D transition. On the left, the basic model shows a two level system; the outer electron transition from $3s$ ground state to the $3p$ state. The intermediate model includes spin-orbit coupling splitting the D transition into D_1 and D_2 fine structure. The final model includes $3/2$ nuclear spin-spin interaction. The numbers given in a transition arrow of each model are the transition line strength S (not bracketed) and the Einstein coefficient A (in the bracket) of that transition in units of the transition line strength S_0 and the spontaneous emission rate A_0 of the basic model. The f number reveals the degeneracy $(2f+1)$ (She and Yu, 1995).

Because only the Na D transitions will interact with the probing lidar beam, the excited states above the $3p$ orbital are ignored in the model. On the left is the basic model of the Na atom as a two-state system labeled by orbital angular momentum L , i.e., $3s$ and $3p$ with degeneracy's of 1 and 3 respectively. A transition line from the excited state to

the ground state is drawn with the associated line strength (S_0) given above the spontaneous emission rate (A_0), otherwise known as the Einstein A coefficient, in the parenthesis. All other line strengths (S) and spontaneous emission rates (A) given in the model are normalized to these values in the basic model. The electron spin (and therefore spin-orbit coupling) is included in the intermediate model (center). The degeneracies are now doubled, and the excited 3p state splits into a doublet and a quartet, $^2P_{1/2}$ and $^2P_{3/2}$. This splitting engenders the D_1 and D_2 emission lines at 5896 Å and 5890 Å respectively, when transitioning from an excited to ground state ($^2S_{1/2}$). As a final model, nuclear spin of 3/2 and the associated hyperfine interaction that leads to the energy-level structure of hyperfine splitting are included. This causes degeneracy to be increased an additional factor of 4. The states $^2S_{1/2}$, $^2P_{1/2}$, and $^2P_{3/2}$, labeled by total electronic angular momentum (J), split into 2, 2, and 4 states, respectively. The different energies of each state are labeled by the total angular momentum of the atom, f (She and Yu, 1995).

The line strength of the Na atom has been measured to be $S_0 = 38.1(ea_0/\sqrt{2})^2$, as given by the NBS table (Wiese, Smith and Miles, 1969), where e and a_0 are the electronic charge and the Bohr radius, respectively. The associated Einstein coefficient for the D_2 transition line is (She et al., 1992),

$$A_0 = \left(\omega_0^3 / 3\pi\epsilon_0 c^3 \hbar \right) (S_0 / 3) = 61.542 \times 10^6 \text{ s}^{-1}. \quad 2.1$$

2.1.2 Laser Induced Fluorescence

The basic experiment for CSU lidar is laser induced fluorescence (LIF) of sodium in the atmosphere. Whether the sodium is in a lab or at 100 km, the principle is the same. In the fluorescence spectrum there are several broadening mechanisms that give rise to an observed line shape. Broadening mechanisms include natural broadening, pressure

broadening, and thermal or Doppler broadening. To explain these broadening mechanisms, consider a low pressure volume of sodium atoms assumed to be stationary. A monochromatic laser light probes a volume of sodium atoms. Laser frequency is tuned slowly as a photomultiplier tube counts fluoresced photons orthogonal to the laser beam. The lineshape traced out by the number of photon counts (y-axis) versus frequency (x-axis) is due to the superposition of six Lorentzian line shapes centered about the frequency of each transition resonance (Table 2-1). These Lorentzian line shapes are due to what is called natural broadening and is explained by a variation of the Heisenberg uncertainty principle,

$$\Delta E \Delta t \geq \frac{\hbar}{2} \quad 2.2$$

where

ΔE : energy of the transition

Δt : is the lifetime of the excited state

\hbar is Planck's constant divided by 2π

In terms of frequency $\Delta\nu$ we get,

$$h\Delta\nu \geq \frac{h}{4\pi\Delta t} \Rightarrow \Delta\nu \geq (4\pi\Delta t)^{-1}. \quad 2.3$$

The lifetime of the excited state for sodium D₂ transition is 16.237 (35) ns (Oates et al., 1995), (Volz et al., 1996). Using equation 2.3, the natural broadened half-width at half-maximum (HWHM) linewidth for the sodium D₂ transition is 4.9 MHz.

Pressure broadening occurs when the presence of nearby particles will affect the radiation emitted by an individual particle by changing the lifetimes. The atmospheric

pressure in the mesopause region is very low (~ 0.01 mB); therefore the particles are very far apart, and this makes pressure broadening negligible (Yu, 1994).

Table 2 Frequencies of D_2 transitions relative to the weighted group center of the respective transitions with line weighting including all degeneracies with and without Hanle effect from Earth's geomagnetic potential. (She and Yu 1995)

Transition	$^2S_{1/2}$	$^2P_{3/2}$	S_n (no Hanle effect)	S_n (w/Hanle effect)	COM (GHz)	Offset(GHz)
D_{2b}	f = 1	f = 0	2/32	2/34.16	1.0683	1.0408
		f = 1	5/32	5.5/34.16		1.0566
		f = 2	5/32	5/34.16		1.0911
D_{2a}	f = 2	f = 1	1/32	0.98/34.16	-0.6410	-0.7150
		f = 2	5/32	5/34.16		-0.6806
		f = 3	14/32	15.68/34.16		-0.6216

The frequencies of D_1 and D_2 transitions relative to the weighted center of the respective groups of four and six transitions are well known (Wiese, Smith and Miles, 1969). Table 1 lists the combined energy-level structure of the models shown in Figure 2-1. Also shown are the line strengths S and the associated Einstein coefficients A for all allowed transitions in terms of those of the basic model, S_0 and A_0 , respectively.

The Hanle effect is related to the generation of coherent superposition of degenerate Zeeman sublevels of an atom by a light beam. It describes how weak magnetic fields, like the earth's magnetic field, modify the atomic polarization of multilevel atomic systems. The Hanle effect shows how the backscattering line strengths are modified due to the relationship of the orientation of laser beam polarization with respect to the earth's magnetic field (Chen 1997).

2.1.3 Doppler broadening and Doppler shift

Consider a single sodium atom resonantly probed by a laser beam with the laser light propagating along the $+z$ direction at single frequency ν_0 . If the atom is moving

along the laser beam toward the laser source at speed V_z , the atoms observed laser frequency (ν) is Doppler shifted (French, 1968) by,

$$\nu = \nu_0 + V_z \frac{\nu_0}{c} . \quad 2.4$$

Now consider a low pressure volume containing a population of sodium atoms that are in thermal equilibrium, probed by the same laser beam at single frequency ν_0 . Maxwell-Boltzmann statistics give a distribution of velocities projected along one dimension, the z-axis, with a velocity probability density ($f(V_z)$) given by

$$f(V_z) = \left(\sqrt{\frac{m}{2\pi k_B T}} \right) e^{-\frac{mV_z^2}{2k_B T}} \quad 2.5$$

Where:

m is the mass of the Na atom

T is the temperature

V_z is the velocity of the Na atom in the z direction

k_B is the Boltzmann constant.

As T increases, the Gaussian shape that equation 2.5 traces out becomes shorter and wider. This is often called thermal broadening because the shape of this distribution for a certain molecular or atomic species is only affected by temperature. Now the population of sodium atoms has a related distribution of the observed laser frequencies (ν) that is due to temperature. This thermal broadening lends to a thermal broadened lineshape that is observed as the probe laser scans in frequency. It is this property which allows the temperature to be measured in the mesopause.

Now consider that the Maxwell-Boltzmann distribution is not centered about a zero velocity; instead there is a shift in the collective velocity of the gas in the z direction, and thus a shift in all the velocities giving

$$V_z = V_{w(z)} + V_{T(z)}, \quad 2.6$$

Where:

$V_{w(z)}$ is the velocity of the collective motion in gas, in the +z direction

$V_{T(z)}$ is the velocity of the random thermal motion of the gas at temperature T .

Next, observe the experiment of the laser beam resonantly probing these atoms.

The entire population of atoms moving at velocities described by the Maxwell-Boltzmann distribution will experience different frequencies of light interacting with them due to Doppler shifting of the frequency of the probe beam, ν_0 ,

$$\nu = \nu_0 - V_{w(z)} \frac{\nu_0}{c}. \quad 2.7$$

This distribution of velocities gives rise to a thermally-broadened fluorescence lineshape for each of the six sodium lines. Each of the six lineshape functions is multiplied by its respective line strength S_n (Figure 2.1) and then summed to build the normalized sodium D₂ lineshape function (She et al. 1992, She et al. 1995).

$$g_{Na}(\nu, T, V_z) = \left(\frac{D}{\pi T} \right)^{1/2} \sum_{n=1}^6 S_n \exp \left(- \frac{D \left(\nu_0 - V_{w(z)} \frac{\nu_0}{c} - \nu_n \right)^2}{T} \right) \quad 2.8$$

Where:

$$D = m\lambda_0/2k_b = 497.6165 \text{ K(ns)}^2$$

T is temperature

ν_n is frequency of the n^{th} D_2 transition

λ_0 is the wavelength of the weighted center of the six transitions

589.158 326 4(15) nm (Juncar, 1981).

ν_0 is the frequency of the probe beam.

Until this point the laser light source considered has been monochromatic; but all lasers have a linewidth, and that linewidth must be included in the calculation of the lineshape function. The ring laser that provides the seed beam for overall frequency control has a reported linewidth of <500 KHz, by the Coherent laser manual. The pulsed Spectra-Physics Nd:YAG Laser that provides the population inversion in the pulsed dye amplifier, has a FWHM of ~120MHz. These lasers combine in the pulsed dye amplifier (PDA) to produce the transmitted laser light. The laser line shape after the PDA has been measured and is reproduced in Figure 2-2 (Sherman, 2002).

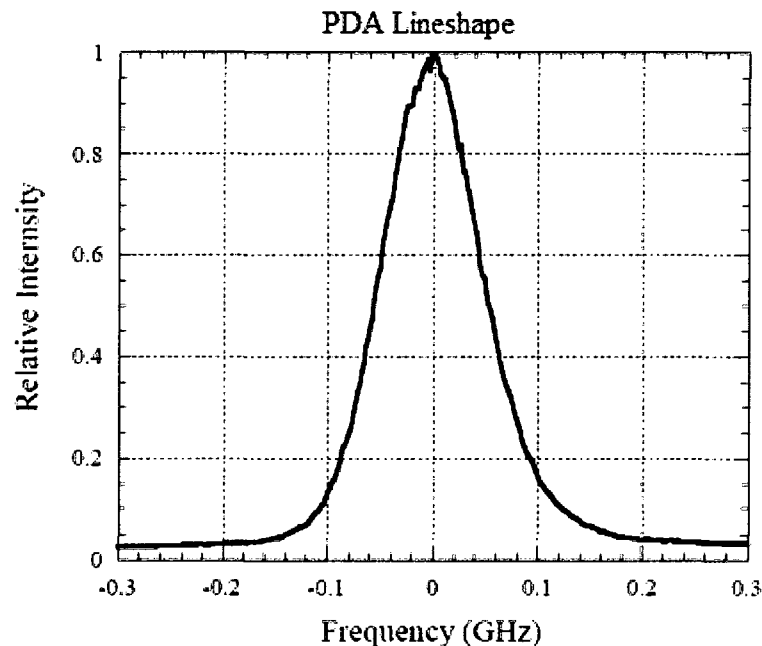


Figure 2-2. PDA lineshape normalized to a maximum intensity of 1. This near Gaussian lineshape is correlated with the normalized sodium lineshape.

The observed spectral lineshape comes from the correlation of the expected normalized sodium lineshape, $g_{Na}(v,T,V)$ and the normalized laser lineshape $L(v-v_L)$ (Figure 2-2),

$$g(v,T,V) = \int_{-\infty}^{\infty} L(v') g_{Na}(v+v',T,V) dv'. \quad 2.9$$

With equation 2.9 the effect of different temperatures and velocities is quantified and combined with the known laser lineshape function allowing a model of the correlated lineshape function to be generated. By allowing only the temperature (wind) to change and holding the wind (temperature) constant the changing temperature's (wind's) effect on the D_2 lineshape is highlighted (Figure 2-3 left (right)).

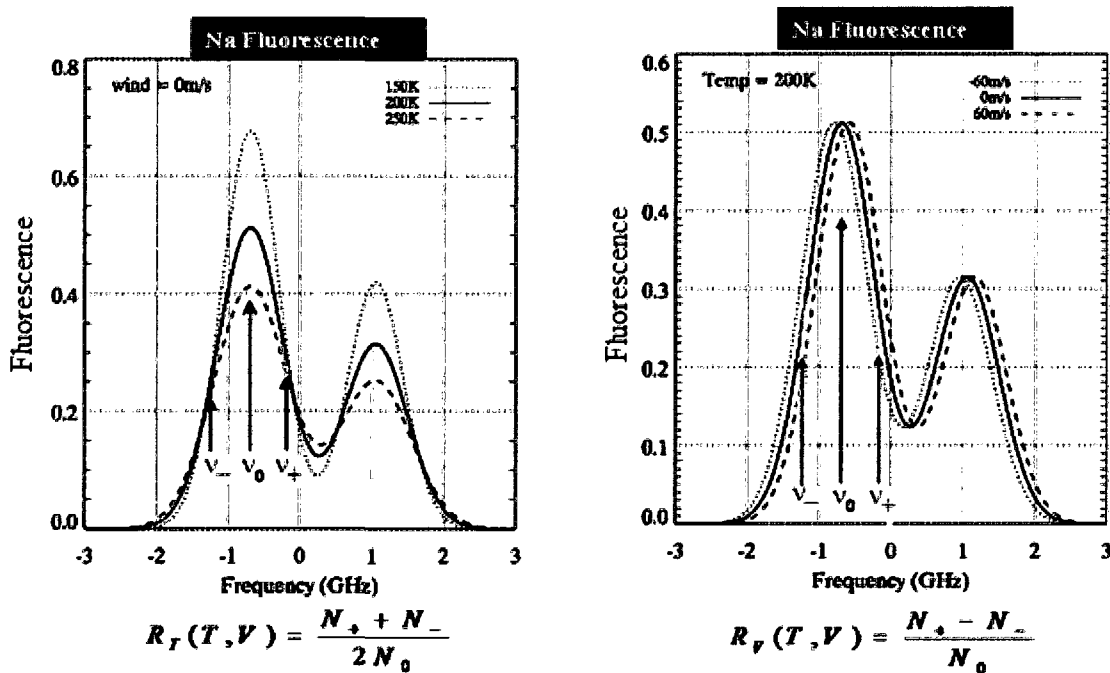


Figure 2-3. Fluorescence is the vertical axis and frequency is the horizontal axis. (White, 1999)

The two peaks in both plots of Figure 2-2 represent the fluorescence from the D_{2a} (left) and D_{2b} (right) spectral lines of sodium. Each graph has three lines: v_- , v_0 , v_+ , which

corresponds to the three frequencies of light transmitted. The y-axis is frequency in GHz set to zero GHz at the center of mass of the D2 line shape. The x-axis is arbitrary units of fluorescence. The left plot depicts the expected fluorescence lineshape for different temperatures with wind speed set to zero; the dotted line represents the spectral line shape at 150 K; the solid line is 200 K; and the dashed is 250 K. The right plot depicts the Doppler shifting of the lineshape function by changes in the line of sight winds with temperature held constant at 200 K; the dotted line represents the expected spectral line shape with the wind traveling at -60 m/s with respect to the laser; the solid line the wind is 0 m/s; and the dashed line the wind is traveling at +60 m/s. A negative value for the velocity represents traveling away from the laser. Ratios of the expected observed fluorescence values R_T and R_V , depicted at the bottom of Figure 2-3, are determined for combinations of temperatures and winds from 100K to 300K and ± 150 m/s respectively.

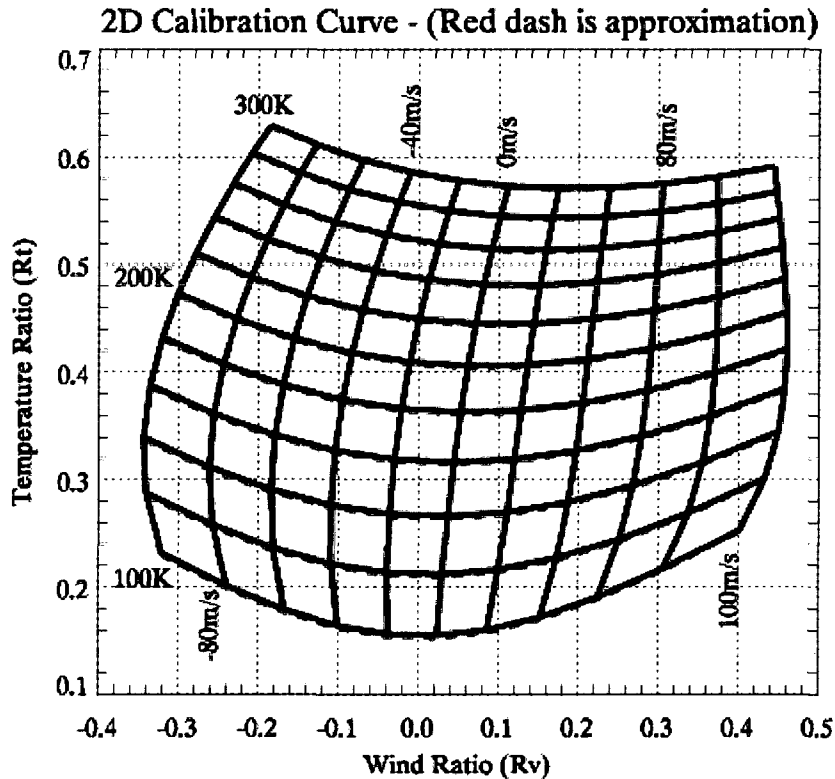


Figure 2-4. The 2D calibration curve constructed by application of the lineshape function for the temperature and wind and corresponding R_t and R_v ratios. This is computed from the theoretical laser induced sodium fluorescence spectrum. Solid lines are calculated from the Voigt function, and the dashed lines are calculated from an approximating Gaussian function disregarding natural lineshape influence. The calibration curves are used to retrieve temperature and radial wind velocity by using experimentally obtained temperature and wind ratios. (White, 1999)

CSU's lidar system is a three-frequency lidar, which utilizes the scattered fluorescence intensity at three transmitted frequencies to form two ratios, one most sensitive to temperature (R_T) and the other most sensitive to velocity (R_V). The pulsed transmitter centerline frequencies are the D_{2a} peak and ± 630 MHz relative to it; these frequencies noted in Figure 2-3 as ν_0 , ν_+ , and ν_- .

For the determination of temperatures and winds it is instructive to look forward to the lidar equation (Equation 2.13) and note that the term $\sigma_{\pi}^{Na}(\nu_L, T, V)$ contains the all of temperature and winds information of the sodium layer. The total cross-section for isotropic scattering is given by

$$\sigma_{\pi}^{Na}(\nu, T, V) = \left(\frac{g_2}{g_1} \right) \left(\frac{\lambda_0^2}{8\pi} \right) A_{21} g(\nu - \nu_L, T, V). \quad 2.10$$

Where:

$\frac{g_2}{g_1}$ is the degeneracy ratio

λ_0 is the wavelength of the weighted center of the six transitions

589.158 326 4(15) nm (Juncar, 1981)

A_{21} : Einstein A coefficient for the sodium D_2 transition ($61.542(71) \times 10^6$ Hz).

$g(\nu - \nu_L, T, V)$: is given by equation 2.9

The R_T and R_V ratios can be expressed as ratios of equation 2.10,

$$R_T(z, t) = \frac{\sigma_{\pi}^{Na}(\nu_+, T, V) + \sigma_{\pi}^{Na}(\nu_-, T, V)}{2 \cdot \sigma_{\pi}^{Na}(\nu_0, T, V)} = \frac{g(\nu - \nu_+, T, V) + g(\nu - \nu_-, T, V)}{2 \cdot g(\nu - \nu_0, T, V)} \quad 2.11$$

$$R_V(z, t) = \frac{\sigma(\nu_+, T, V) - \sigma(\nu_-, T, V)}{\sigma(\nu_0, T, V)} = \frac{g(\nu - \nu_+, T, V) - g(\nu - \nu_-, T, V)}{g(\nu - \nu_0, T, V)} \quad 2.12$$

The right most terms in equations 2.11 and 2.12 illuminate that ratios have the distinct advantage of canceling like, yet possibly unknown, terms in equation 2.10. Ratios of the sodium lidar equation (equation 2.13) will be used to determine the center terms in equations 2.11 and 2.12.

2.1.4 Sodium lidar equation

This section is prefaced by the caveat that a simple form of the sodium lidar equation is addressed first and complications are added later. Complications include such salient aspects as the transmitted laser line shape (Sherman, 2002) and that the transmitted photon frequencies are not the only frequencies of the returning photons after undergoing fluorescence. Because there are different frequencies of photons returning

than those transmitted the attenuation of the returning photons in the sodium layer is different than that of the transmitted photons (White, 1999).

The sodium lidar equation can be explained in simple terms: a number of photons are emitted from a laser, there are photon losses through the atmosphere, the photons interact with sodium, and some photons return to be counted. While the sodium lidar equation described in these terms is indeed simple, there are substantial subtleties involving the quantum mechanics employed in the determination of the cross-section and transmission terms (David Krueger, via direct communication).

$$N(z, \nu_L, T, V) = \overbrace{N_L(\nu_L)}^{\text{transmitted photons}} \overbrace{(\eta T^2(\nu_L, \rho, z)) T_{\uparrow} T_{\downarrow}}^{\text{photon losses}} \overbrace{\rho_{Na} \Delta z_{Na} \sigma_{\pi}^{Na}}^{\text{returning photons}} (\nu_L, T, V) \overbrace{\left(\frac{A}{z^2}\right)}^{\text{collected photons}} + N_B \quad 2.13$$

Where:

N : number of the returning photons from a distance z

ν_L , frequency of transmitted light

T , temperature

V is the radial speed of the sodium atoms

$N_L(\nu_L)$ is the number of photons transmitted in a pulse at frequency ν_L

$(\eta T^2(\nu, \rho, z)) T_{\uparrow} T_{\downarrow}$

η : system efficiency : fiber coupling, photomultiplier tube (PMT)

$T^2(\nu_L, \rho, z)$: attenuation of photons below the sodium layer (2.1.3.1)

$\rho(z)$: number density of the scatterers in the atmosphere.

T_{\uparrow} and T_{\downarrow} is the attenuation of signal through the sodium layer (2.1.4.1.)

$$\rho_{Na}(z, t, T) \Delta z_{Na} \sigma_{\pi}^{Na}(v_L, T, V) -$$

$\rho_{Na}(z, t, T)$ is the number density of sodium atoms at a distance z ,

Δz_{Na} is a slice in altitude that relates to binning time of the counting card

$\sigma_{\pi}^{Na}(v, T, V)$ is the differential backscatter cross-section

$\left(\frac{A}{z^2}\right)$: solid angle subtended by the receiver telescope with an area A

N_B : noise due to sky background and dark counts from the PMT.

2.1.4.1 Attenuation in the Sodium Layer

Figure 2-1 shows the ten path ways for laser induced fluorescence (LIF) to occur. The sodium valence electron can exist in either one of the two $^2S_{1/2}$ ground states and can be excited to one of four $^2P_{3/2}$ excited states. Due to selection rules, there are six allowed transitions between the excited state, $^2P_{3/2}$, and the ground state, $^2S_{1/2}$. Starting from one of the ground states, an electron may absorb a photon of resonant frequency and be excited to one of the three allowed excited state via three allowed transitions as shown in figure 2.1. A while later ($\sim 10^{-8}$ s), the electron in one of the allowed excited states will fluoresce a photon and return to the same ground state. If the excited electron is in the $^2P_{3/2} f = 1$ or 2 state, it is permitted to return to either ground state leading to a total of five path ways for LIF (figure 2.1). At the temperatures existing in the mesopause both ground states are occupied, giving ten paths for sodium D₂ fluorescence for a single frequency incident. To account for the possible difference in attenuation between a transmitted photon and a returning photon the transmission functions in the sodium layer must be modified. The transmission function of a photon traveling up in the atmosphere can be expressed as,

$$T_{\uparrow}(z + \Delta z, T(z + \Delta z), V(z + \Delta z)) = T_{\uparrow}(z, T(z), V(z)) \exp(-\rho_{Na}(z) \sigma_A(\nu, T, V) \Delta z) \quad 2.14$$

$\rho_{Na}(z)$ is the density of sodium at an altitude z , and $\sigma_A(\nu, T, V)$ is the total absorption cross-section at the laser frequency ν . However, the transmission after fluorescence, going down through the layer, must be modified due to the ten possible energy transition paths. The weighted sum of all the absorptions is used to determine the total transmission down through the sodium layer.

$$T_{\downarrow}(z + \Delta z, T, V) = \sum_{k=0}^9 \frac{\sigma_{SB}(\nu_k, T, V)}{\sigma_{SB}(\nu, T, V)} T_{\downarrow}^k \exp(-\rho_{Na}(z) \sigma_A(\nu_k, T, V)) \quad 2.15$$

Where T_{\downarrow}^k is the k^{th} transmission coefficient of the k^{th} channel and $\sum_{k=0}^9 \frac{\sigma_{SB}(\nu_k, T, V)}{\sigma_{SB}(\nu, T, V)}$ is

the branching ratio of the fractional probability of a resonantly backscattered photon emitted through the k^{th} channel (White, 1999).

Daytime measurements require ultra-narrow band pass faraday filters inserted in the receiver channel to remove the daylight background. In the process of removing daylight background, faraday filters further attenuate the returning signal with frequency dependence (Yuan, 2004). To correct for the faraday filter attenuation, the transmission coefficient must be corrected with the transmission function through the faraday filter at the prescribed returning frequencies by,

$$T_{\downarrow}(z + \Delta z, T, V) = \sum_{k=0}^9 \frac{\sigma_{SB}(\nu_k, T, V)}{\sigma_{SB}(\nu, T, V)} T_{\downarrow}^k T_{filter}^k \exp(-\rho_{Na}(z) \sigma_A(\nu_k, T, V)). \quad 2.16$$

This transmission function is measured directly by transmitting laser light through the faraday filter. The laser is scanned in frequency and a plot of the transmission

function is generated. From the generated transmission function the faraday filter corrected attenuation for the prescribed returning frequencies is determined (Chen, 1997).

The theoretical foundation is now set, and now only a few points must be addressed to analyze the data. Analyzing the data is an iterative process. The data is collected in 150 m bins. Before the winds and temperatures can be analyzed for a specific bin, the transmission of the signal due to sodium in the bins below it must be known. This is illustrated by use of the Rayleigh lidar equation

$$N_R(z_{ref}, \nu_L, t) = \left(\frac{E_L}{E_p} \right) \left(\eta T_A^2 \rho_{air}(z_{ref}, t) \sigma_\pi^R(\nu_L) \Delta z \right) \left(\frac{A}{z_{ref}^2} \right) + N_B, \quad 2.17$$

Where

T_A^2 is the attenuation in the atmosphere below the measurement

σ_π^R : Rayleigh differential backscatter cross-section for the frequency of the laser,

ρ_{air} : density of the air at reference altitude z .

The reference altitude is selected as an altitude that cannot be contaminated by sodium or particulate (Mie scattering) so that the only scattering process is Rayleigh scattering. The altitude needs to be low enough to acquire enough Rayleigh signal to allow for a 10km fit (equation 2.22) centered at the reference altitude. For Fort Collins the reference altitude is chosen to be 30 km. Substitution of equation 2.17 into equation 2.13 yields,

$$\frac{N(z, \nu_L, T, V) - N_B}{(N_R(z_{ref}, \nu_L) - N_B) T \uparrow T \downarrow} = \left(\frac{z_{ref}^2 \rho_{Na}(z, t)}{z^2 \rho_{air}(z_{ref}, t) \sigma_\pi^R(\nu_L)} \right) \sigma_\pi^{Na}(\nu_L, T, V). \quad 2.18$$

The bracketed term on the right side has frequency dependence in the σ_π^R term, but the sensitivity to frequency is negligible and indistinguishable in the 1260MHz range

of the three frequencies at which the lidar operates. Note that N_B can be different for different frequencies.

2.1.5 Temperature and winds determined by R_T and R_V ratios

The temperature and wind ratios are now calculated with all terms on the right side of equation 2.18 canceling except $\sigma_\pi^{Na}(v_L, T, V)$ resulting in

$$R_T = \frac{\sigma_\pi^{Na}(v_+) + \sigma_\pi^{Na}(v_-)}{2 \cdot \sigma_\pi^{Na}(v_0)} = \frac{\frac{N_+ - N_{B+}}{(N_R - N_B)(\tau \uparrow \tau \downarrow)_+} + \frac{N_- - N_{B-}}{(N_R - N_B)(\tau \uparrow \tau \downarrow)_-}}{2 \cdot \frac{N_0 - N_{B0}}{(N_R - N_B)(\tau \uparrow \tau \downarrow)_0}} \quad 2.19$$

$$R_T = \frac{\sigma_\pi^{Na}(v_+) - \sigma_\pi^{Na}(v_-)}{\sigma_\pi^{Na}(v_0)} = \frac{\frac{N_+ - N_{B+}}{(N_R - N_B)(\tau \uparrow \tau \downarrow)_+} - \frac{N_- - N_{B-}}{(N_R - N_B)(\tau \uparrow \tau \downarrow)_-}}{\frac{N_0 - N_{B0}}{(N_R - N_B)(\tau \uparrow \tau \downarrow)_0}} \quad 2.20$$

Looking at the middle term in equations 2.19 and 2.20 we can see that the middle terms in equations 2.11 and 2.12 have been retrieved. In order to determine the center ratios, the right hand side of equations 2.19 and 2.20 must be solved. Observations provide N_R, N_+, N_0, N_-, N_B . To calculate the transmission of signal through an altitude bin (equations 2.14 and 2.15) the sodium density for that altitude bin must be determined. To determine the sodium density equation 2.18 is rearranged to solve for the sodium density yielding

$$\rho_{Na}(z, t) = \frac{N(z, v_L) \rho_{air}(z_{ref}, t) \sigma_\pi^R(v_L) z^2}{N_R(z_{ref}, v_L) \sigma_\pi^{Na}(v_L, T, V) \tau \uparrow \tau \downarrow z_{ref}^2} \quad 2.21$$

All the terms in the equation 2.21 are known or can be approximated; N 's are measured, $\sigma_\pi^R = 6.11 \cdot 10^{-32} \text{m}^2 \cdot \text{sr}^{-1}$, $\tau \uparrow \tau \downarrow$ is calculated from the sodium densities

below the current bin where we take $T \uparrow(z=70km) = T \downarrow(z=70km) = 1$, altitude (z) is known from time of flight, $z_{ref}=30km$, $\rho_{air}(30km) \cong 3.249 \cdot 10^{23} \text{ m}^{-3}$ (MSIS-E-90 atmospheric model), and σ_{π}^{Na} is calculated from the temperature and winds analysis at the current bin altitude.

The iterative process starts at 70 km to ensure there is no sodium below the first calculation. Rayleigh scattering from 25-35 km is fit using the technique of least squares to the curve

$$N_R(z, v_L, t) = \frac{\beta_L}{z^2} e^{-\frac{z}{H_L}}. \quad 2.22$$

Where β_L and H_L are coefficients fit for a specific laser frequency, then, using the coefficients, we evaluate the return counts at the reference altitude ($z_{ref} = 30km$).

For each binning altitude equations 2.19 and 2.20 are applied, yielding R_T and R_V ratios. The relationship shown in Figure 2-4 is now used to determine the resulting temperature, wind and errors in the measurement. For instance, an experiment is performed with the results of $R_T=0.4$ and $R_V=0.1$. These values of R_T and R_V are projected out from the x and y axis until they intersect. Where they intersect, the values of the associated temperature and wind are determined. In the case of our example the resulting wind and temperature are near 11 m/s and 200 K. The exact values do not fall on a line but in a region that is bound by a box from 0-20 m/s and 200-180 K. A more precise determination of temperatures and winds is accomplished via bilinear expansion of the bound region. In practice the temperatures and winds are divided into a much finer fine grid resolution than displayed in Figure 2-5.

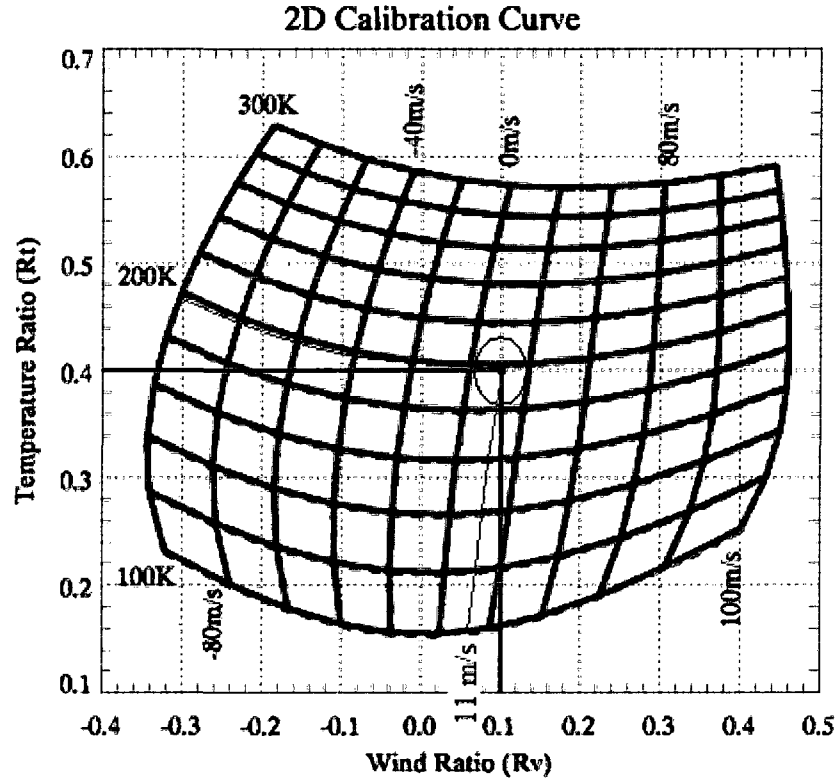


Figure 2-5. The 2D calibration curve constructed by application of the lineshape function for the temperature and wind and corresponding R_T and R_V ratios. $R_V = 0.1$ and $R_T = 0.4$ lines are drawn in black. Where they intersect is circled and translates into ~ 11 m/s and ~ 200 K.

The estimates of error in the temperature and wind measurements are based on photon counting statistics and estimates of system transmitter frequency error. The error in the temperature and wind due to photon counting is calculated using error propagation and Poisson statistics. Because T and V are functions of R_T and R_V the estimated error in T and V can be expanded and written as,

$$\delta T = \delta R_T \frac{\partial T}{\partial R_T} + \delta R_V \frac{\partial T}{\partial R_V}, \delta V = \delta R_T \frac{\partial V}{\partial R_T} + \delta R_V \frac{\partial V}{\partial R_V}. \quad 2.23$$

Now recall that equations 2.19 and 2.20 with neither the transmission term nor Rayleigh normalization are,

$$R_T = \frac{N_+ + N_-}{2N_0}, R_V = \frac{N_+ - N_-}{N_0}. \quad 2.24$$

Therefore the uncertainties in R_T and R_V are given as,

$$\delta R_T = \frac{\delta N_+}{2N_0} + \frac{\delta N_-}{2N_0} - \frac{\delta N_0}{N_0} R_T \quad 2.25$$

$$\delta R_V = \frac{\delta N_+}{N_0} - \frac{\delta N_-}{N_0} - \frac{\delta N_0}{N_0} R_V. \quad 2.26$$

Inserting equations 2.24, 2.25 and 2.26 into equations 2.23 squaring and taking an ensemble average yields the mean squared uncertainties (Vance 2004).

$$\langle \delta T^2 \rangle = \frac{1}{N_0^2} \left(\delta N_+^2 \left(\frac{1}{2} \frac{\partial T}{\partial R_T} + \frac{\partial T}{\partial R_V} \right)^2 + \delta N_-^2 \left(\frac{1}{2} \frac{\partial T}{\partial R_T} - \frac{\partial T}{\partial R_V} \right)^2 + \delta N_0^2 \left(R_T \frac{\partial T}{\partial R_T} + R_V \frac{\partial T}{\partial R_V} \right)^2 \right) \quad 2.27$$

$$\langle \delta V^2 \rangle = \frac{1}{N_0^2} \left(\delta N_+^2 \left(\frac{1}{2} \frac{\partial V}{\partial R_T} + \frac{\partial V}{\partial R_V} \right)^2 + \delta N_-^2 \left(\frac{1}{2} \frac{\partial V}{\partial R_T} - \frac{\partial V}{\partial R_V} \right)^2 + \delta N_0^2 \left(R_T \frac{\partial V}{\partial R_T} + R_V \frac{\partial V}{\partial R_V} \right)^2 \right) \quad 2.28$$

The derivatives and ratios in the above equations are taken from the calibration curve directly at the respective temperatures and velocities. By design, velocity is not sensitive to change in R_T , and temperature is not sensitive to change in R_V , therefore

$\frac{\partial V}{\partial R_T}$ and $\frac{\partial T}{\partial R_V}$ contribute negligible uncertainty. Cross terms of counting uncertainty

from differing frequencies are zero because they are uncorrelated signals.

Estimates of system transmitter error are discussed later in section 2.2.

2.2 CSU sodium lidar system

Section 2.2 departs from theory and describes the sodium lidar system located at Fort Collins, Colorado, U.S.A., breaking it down into the transmitter (2.2.1) and receiver (2.2.2) subsystems, and describes how they are integrated with electronics (2.2.3).

Together these sub-systems cause laser-induced fluorescence in the atmosphere and measure and record the returned photons from it. Using the theory described in 2.1 and the system described in 2.2, the winds and temperatures in the MLT region are deduced.

Colorado State University employs a high spectral resolution sodium fluorescence lidar that utilizes naturally occurring atomic sodium in the mesopause region. The system is designed to take advantage of the known properties of the sodium D₂ transition spectral features (see 2.1.2. and 2.1.4.1.). Pulses of light are emitted at a 50 Hz repetition rate cycling through frequencies centered on and about the sodium D_{2a} resonance Lamb dip. The transmitted frequency is cycled sequentially from at the resonance Lamb dip frequency (0), then shifted +630 MHz above (+), and then -630 MHz below (-) the resonance Lamb dip. Each emitted pulse has about 20 mJ of energy, which translates into roughly 5×10^{16} photons. For each pulse of 5×10^{16} photons transmitted usually fewer than 500 photons return from resonant backscattering in the sodium layer to be counted. The returned photons are collected by telescope and directed via optical fiber to be focused onto a photomultiplier tube (PMT).

A photon interacts with the active area of a photomultiplier tube via the photoelectric effect, ejecting an electron. The ejected electron is accelerated toward an array of cathodes where a single electron ejected by one photon is amplified by 10^{12} . Photons are counted with nearly 40% efficiency with our newer PMTs. When a photon is counted, the PMT creates an electronic pulse of ~2 volts in amplitude and 8-20 ns in duration. These electronic pulses are recorded by counting cards that bin them with respect to the time of the laser pulse and hence record the time of flight. This binning method allows the determination of the altitude at which the backscatter process has occurred.

CSU's lidar system is more complicated than most other lidar systems in two ways. First it is difficult to achieve sodium resonant frequency with lasers, often

requiring sophisticated dye lasers or subtle non-linear sum frequency generation technology; this is compounded by the need for a very narrow linewidth to resolve the fine structure. Second, the three frequencies needed for the R_T and R_V ratios are shifted pulse-by-pulse, and as to be detailed below, this requires precise timing between the two chopper wheels, one for the shifting of the light frequency and the other for the firing of pulsed laser.

All lidar systems can be broken down into two sub-systems: transmitter and receiver (Figure 2-6). This section will start with a description of the transmitter (2.2.1) and the beam path and operation of two and three beam measurements. This leads to a discussion of the receiver which is followed by a description of the necessary electronics.

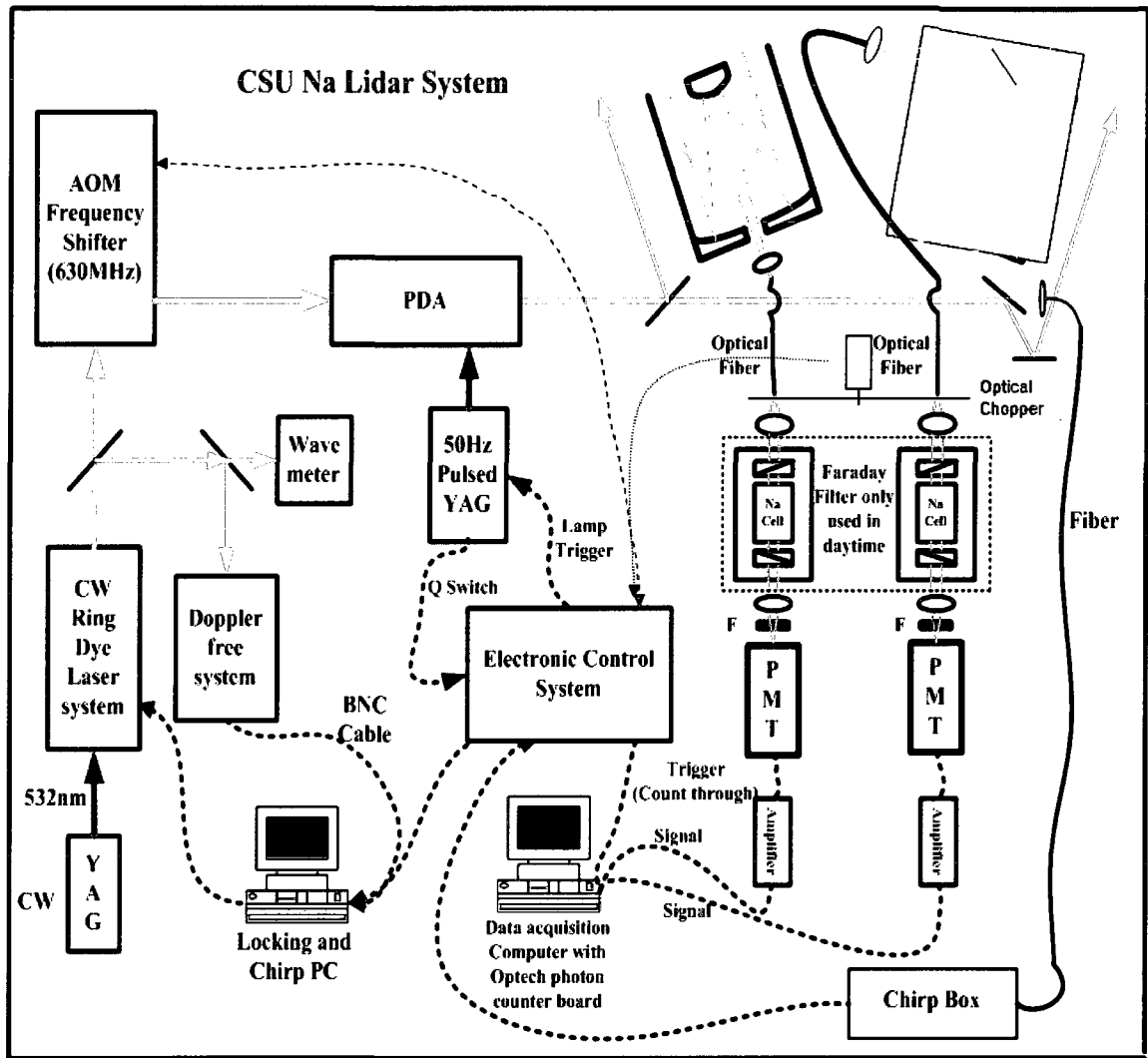


Figure 2-6. Above is a simplified system schematic of the lidar system with the transmitter sub-system on the left and the receiver sub-system on the right. In the center is the synchronizing and data storing electronics. This schematic depicts daytime operation (Li, 2005).

2.2.1 Transmitter

The transmitter subsystem has three lasers in the transmitter. The transmitter can be broken down into three distinct subsystems interconnected with electronics. Section 2.1.1.1 describes the seed beam creation and frequency control subsystem. This subsystem creates 589.159nm cw light and locks it to the sodium D_{2a} Doppler free Lamb dip feature and then shifts the light through the three needed frequencies for determining the R_T and R_V ratios. This light is fed into the next subsystem (2.1.1.2), which is the pulse

amplifying and frequency monitoring subsystem. This subsystem takes the approximately 100mW of cw light and amplifies it to approximately 1.0 W of pulsed light at the shifting frequencies. The transmitted light is pulsed at a 50Hz repetition rate with each pulse about 12 ns at full width half max (FWHM). This subsystem also samples each pulse for frequency chirp determination and correction; chirp is a subtle shift in the center of mass of the transmitted frequency that can result in false measurements. The last subsystem (2.1.1.3) divides the laser light into different channels depending on the requirements of the observations. The night time transmitter power is split into three channels: 40% of total PDA output power for each of the two 76cm telescopes and 20% for the 35cm telescope. For daytime operation a beam splitter on a flip mount is moved out of the beam path, and the transmitted power is split two ways: 40% for one of the 76cm telescopes and 60% for the smaller 35cm telescope. This distribution of power increases daytime output power for the smaller telescope channel, thereby increasing its return signal. In this manner we can measure nighttime zonal momentum flux while simultaneously continuing the long term observations of mesopause region temperature and zonal and meridional winds over full diurnal cycles.

2.2.1.1 Seed beam creation and precision frequency control

The entire transmitter subsystem starts with a Millennia Pro continuous wavelength (cw) diode pumped laser that produces light at 532nm. The 5 W laser is typically operated at an output power of 3.5 W, to pump a Coherent 899-21 ring-dye laser that produces light around 589.159nm. The Coherent 899-21 is an actively stabilized, scanning single-frequency ring-dye laser, with a single external reference cavity that provides frequency stabilization for operation at a linewidth of less than 500 kHz. The

output power of this tunable single-mode ring-dye-laser is ~ 250 mW. A small fraction of the light ($<200\mu\text{W}$) is sent into a sodium cell for active locking of the laser to the deepest feature of the Na Doppler free saturation fluorescence spectroscopy as discussed below

2.2.1.1.1 Ring laser locking and Doppler free spectroscopy

The derivation of temperature and wind from returned fluoresced photons is highly dependent on the absolute frequency of the probe laser. An unknown shift in laser frequency will cause erroneous temperatures and winds to be calculated. In order to actively control the output frequency of the ring dye laser to $\pm 1.5\text{MHz}$ (Sherman, 2002), Doppler-free saturation fluorescence spectroscopy (She and Yu, 1995) is used to determine laser frequency. A 1.5MHz uncertainty translates into an RMS locking of 1.25 m/s (radial velocity) for a given 2 minute file. When hourly averaging of the velocity profiles (~ 28 per hour for 2 minute files) is applied, an hourly-averaged RMS locking uncertainty of ~ 0.24 m/s is obtained. Active locking to a Doppler free fluorescence spectral feature is maintained by feedback to the ring laser from the output of a monitoring PMT and a laser locking computer (Figure 2-7).

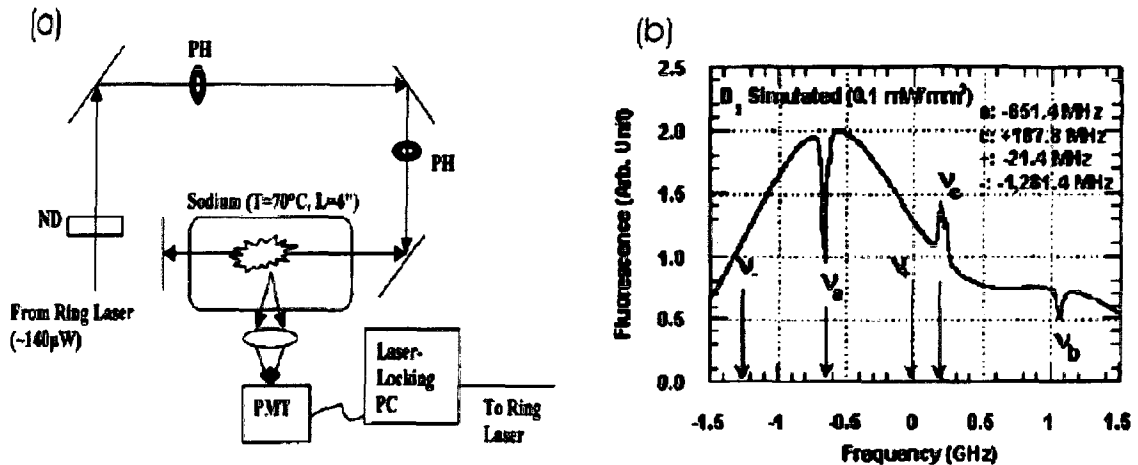


Figure 2-7. (a) Doppler free fluorescence spectroscopy apparatus. Counter-propagating beams induced fluorescence is focused onto a PMT. The symbols ND and PH denote neutral density filters and pin holes respectively (b) Fluorescence spectrum depicting the Doppler free features of the D_{2a} Lamb dip (ν_a), crossover (ν_c), and the D_{2b} Lamb dip (ν_b). Also depicting where the shifted frequencies occur in the spectrum ν_- , and ν_+ for the (-) and (+) shifted light (Sherman, 2002).

Due to the narrow linewidth of the ring dye laser (<500 kHz) the sodium Doppler-free fluorescence spectrum, when probed in a sodium cell, reveals Doppler-free features near the D_{2a} and D_{2b} peaks and an enhancement called the crossover between these two peaks. The ring laser is actively locked to the deepest feature in the D_{2a} Doppler-free spectrum. This lock is accomplished using standard signal locking techniques with an external dither (200 Hz is typically used) and monitoring the Doppler-free output signal. A 50 mV peak-to-peak 200Hz sine wave dither is inserted into the ring laser dither circuit (Figure 2-8), which buffers this signal and sums it with the external etalon reference signal. This changing voltage causes a dithering mismatch in the ring laser single frequency lock circuit resulting in the laser frequency being modulated ~ 3.0 MHz in frequency (Sherman, 2002) at the same 200 Hz rate.

An estimate of the laser frequency mismatch can be made by observing the modulation of PMT voltage while the ring laser remains unlocked but tuned to a side wall in the D_{2a} Doppler free feature. The side walls of the D_{2a} Doppler free feature have steep

beam two populations of atoms, traveling at the same speed but in opposite directions, experience a Doppler shifted light frequency. The population of Na atoms that can resonantly interact with the laser light is roughly double that of a beam that does not pass through the cell twice. This larger population of atoms at resonance causes an enhancement in the observing PMT's signal. Now suppose the laser was tuned to a frequency where only stationary Na atoms will experience resonance transition frequency. The stationary atoms would interact with the incident and the reflected beam. Therefore, the population of atoms available for induced fluorescence is reduced compared to the Doppler shifted population; the enhancement is much reduced, causing a dip in the PMT output, resulting in a Lamb-dip spectral feature.

Because the energy levels of sodium are more complex than one resonance line from a two-level atom, there are several dips in the spectral features along with various associated crossover features. For example, within the D_{2a} Doppler-free spectral features, marked by ν_a in Figure 2-7(b), there are three saturation dips, resulting from three allowed transitions. Since there exists a crossover line between a pair of allowed transitions (to be explained briefly), a total of six dips with different depths are present in the D_{2a} Doppler-free spectrum. Since the natural linewidth (~ 10 MHz) of each dip is broad compared to the frequency difference between these features, these dips are not resolved, giving rise to a smeared spectrum with three discernable minima, the deepest of which ($\nu_a = -0.6514$ GHz) is used to lock the ring-dye-laser frequency.

To appreciate the existence of the crossover lines, we briefly consider the main crossover spectral feature, marked ν_c in Figure 2-7(b). While the D_{2a} and D_{2b} fluorescence features, marked ν_a and ν_b , respectively in Figure 2-7(b), are resulting

mainly from population of atoms in the $^2S_{1/2}(f=2)$ and $^2S_{1/2}(f=1)$ ground state, respectively, atoms in both ground states, which travel at a speed corresponding to a Doppler shift of $(v_b - v_a)/2$, can take part in the main crossover spectral feature. Since the populations in the two ground states are to the first-order independent, instead of saturation, one sees enhancement in this spectrum. Since both ground states are invoked, there are twelve non-resolving lines, six allowed transitions and six crossover transitions, leading to a complicated, smeared main crossover spectrum with three barely discernable maxima. Again, because the sodium atom has six different D_2 transitions, the crossovers in the Sodium D_2 spectrum are more subtle than the simple case described here (She and Yu 1995).

2.2.1.1.2 Acoustical Optical Modulation (AO)

The ring laser is locked to a feature in the D_{2a} Doppler free spectrum producing a very narrow band light centered about a single frequency. The two shifted frequencies are created from the double-pass 630MHz acousto-optic modulator frequency shifter (Figure 2-9), referred to as the AO. The AO permits rapid cycling between the three lidar operating frequencies (White, 1999). The AO crystals operate similar to the principle of Bragg scattering. A piezo-electric transducer on one side of AO crystal creates sinusoidal traveling waves by stressing the crystal. These traveling waves create wave fronts of traveling changes in the index of refraction in the crystal, by which the light is partially diffracted. Constructive interference is observed when the angle of the beam's travel with respect to the variation in the index of refraction phase front is set to an angle θ

$$\sin \theta = m \frac{\lambda}{2\Lambda}. \quad 2.29$$

Where λ is the laser light wavelength, Λ is the wavelength of the index variation (acoustic wave), and m ($m = 1$ in this case) is an integer where constructive interference will occur. At these angles the incremental reflections separated by the variation's wavelength have a phase shift of 2π so that they interfere constructively (White, 1999). Due to the incident beam size and the crystal length it traverses (~ 100 mm compared to 1 mm), the incident and diffracted beam can overlap and interact for a substantial length only when θ is small. Because θ should be small, the greatest intensity of shifted light is produced when $m = 1$, so the angle of the crystal is set to $\theta = 1.22^\circ$, maximizing shifted transmitted power. The light beam frequency is shifted by +315MHz or -315MHz, depending on the direction of the acoustic wave relative to the light beam. The beam passes through each crystal twice retracing its original path (Figure 2-9). The angle θ is the same angle in both directions, adding an additional frequency shift of +315MHz or -315MHz, for a total frequency shift of +630MHz or -630MHz. The theoretical efficiency of which the input light is converted to frequency shifted light is $\sim 80\%$ for single pass, and as such is $\sim 64\%$ for double pass. Observed shifted light intensities are slightly lower ($\sim 55\%$ - 60%) due to alignment issues, cleanliness of the optics, and the age of the crystals.

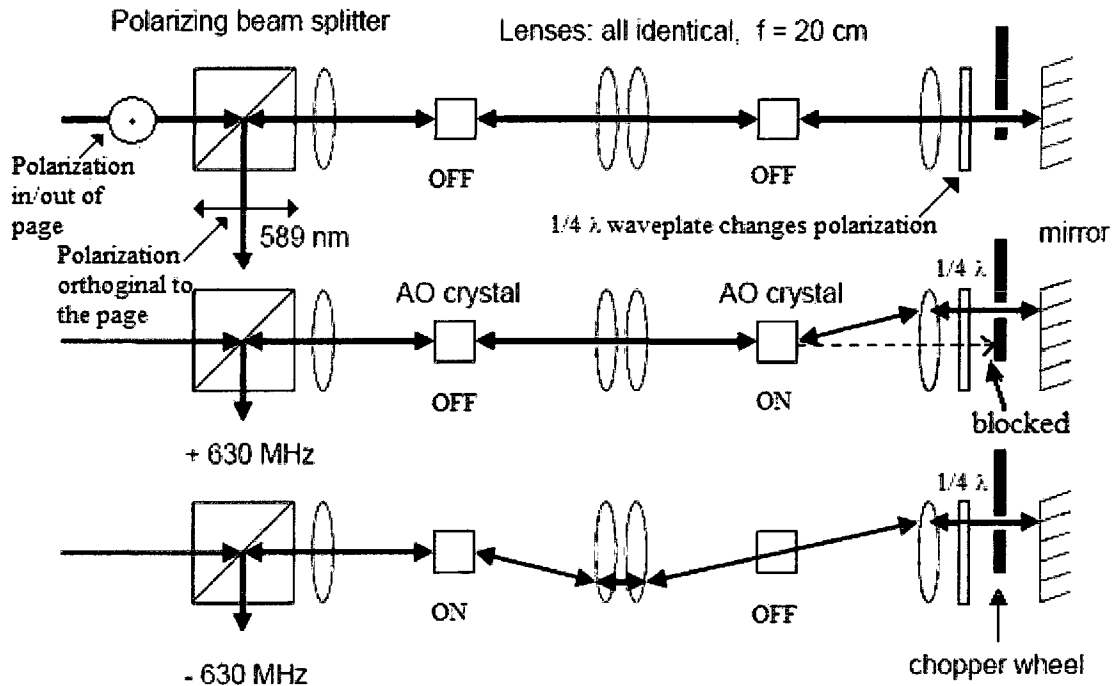


Figure 2-9. A diagram of Acoustic-Optic Modulator (AO) beam path for the three different frequencies of light. Note the physical shifting of light position with the frequency shifting of the light. The chopper blade selects the path of the transmitted light. [from Vance 2004]

Because the conversion of the light will never be 100%, an optical chopper blocks the unconverted light from contaminating the shifted beam when either crystal transducer is powered (Figure 2-9). The timing of the chopper wheel phase in relation to the shifting of the beams is crucial to the entire operation of the lidar system. Due to the need to protect the PMT from low altitude lidar return signal, a receiver chopper is used to trigger the timing system of the lidar system (see 2.23). The timing of the chopper wheel phase is maintained by a commercial 300 Synch Chopper Synchronizer made by Boston Electronics, that is synchronized with a 16.66 Hz square waveform, termed reset, generated from the system timing electronics (Figure II-1) to allow locking of the AO chopper in phase with the AO crystal's shifting of the beam.

The light entering the AO before the beam splitting cube is horizontally polarized so that ~96% of the light is passed straight through by the cube. The ~ 4% of light that reflects off of the 45° surface and splits from the AO beam path is again split in two: one beam provides light for a wavemeter and one for the Doppler free frequency control (section 2.2.1.1). The light passing straight through the cube has its path directed with four identical 20cm lenses. The lenses are arranged to direct the retro-reflected beams along the same path, making the light leaving the AO independent of the final frequency.

On the right side of the AO (Figure 2-9) the light transmits through a quarter-waveplate (annotated as $\frac{1}{4} \lambda$), converting the linear polarized AO light to right hand circular polarization. The light then reflects off a mirror and passes through the $\frac{1}{4} \lambda$ again, converting the right hand circular light back to linear polarized light. Passing through a $\frac{1}{4} \lambda$ twice effectively acts as a half-waveplate that is set to rotate the linear polarization of the AOM light by 90°. When the returning light enters the polarizing beam cube again, it is reflected by the angled splitting surface and is sent out of the AO (in a direction perpendicular to the incident beam) to collimating optics and later onto the pulsed dye amplifier (PDA).

2.2.1.2 PDA and Pulsed YAG

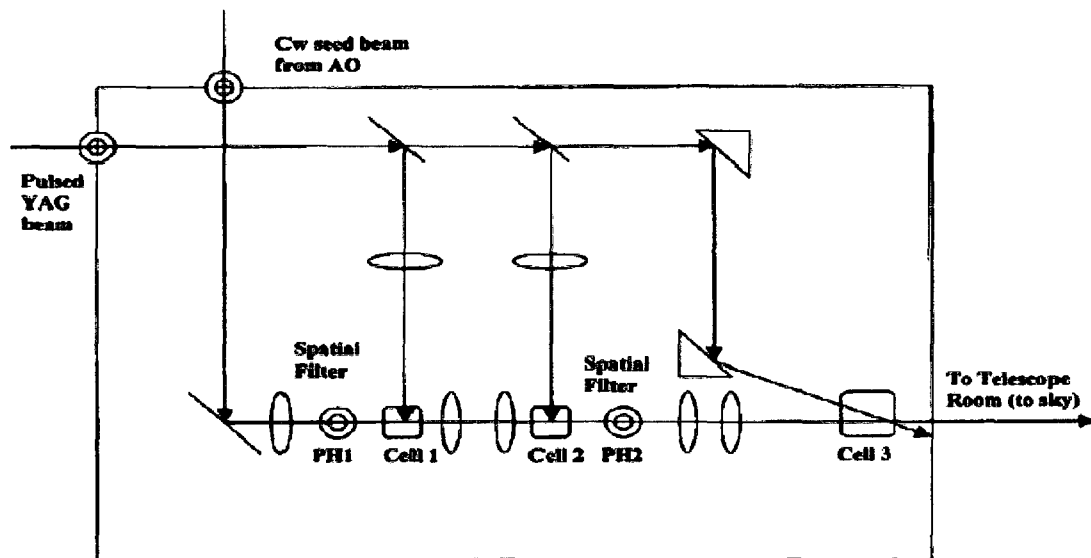


Figure 2-10. A schematic of light path inside the pulse dye amplifier (PDA). The seed beam comes from the top left of the schematic and the pump beam comes from the left side of the schematic (Sherman 2002)

The PDA (Figure 2-10) takes $\sim 100\text{mW}$ of $\sim 589.160\text{ nm}$ seed beam and $\sim 15\text{W}$ 50 Hz pulsed 532nm pump beam and combines them in a gain medium of dye/methanol to yield $\sim 1.2\text{W}$ pulsed output beam with a center line frequency of the seed beam. Spatial mode matching of the three seed input beams at different frequencies is crucial for conversion efficiency in the PDA. Optics inside the PDA are aligned to minimize amplified spontaneous emission (ASE) in the output beam by twisting two of the focusing lenses and thereby minimizing back reflections. Due to the difference in seed power at different frequencies, typical output powers for the PDA are 1.2W, 1W, 1W for the three frequencies ν_0 , ν_+ , ν_- with $<15\text{mW}$ ASE .

Asymmetries in the pulse line shape due to non-linear interactions between the seed beam and the pump beam in the PDA induce a frequency chirp (Siegman, 1986) in the transmitted pulse that induces an offset in the measured radial wind. This chirp is

corrected by sampling the transmitted pulse and comparing transmission of the three pulsed frequencies through an Iodine (I_2) vapor filter (Figure 2-11). The lineshape of the absorption of I_2 is characterized for the normalized intensities of three transmitted frequencies. A ratio is constructed of these pulsed intensities and fit to a calibration curve to determine the frequency chirp and the subsequent shift in winds. The chirp system has been periodically verified to work by vertical wind tests. Vertical winds in the MLT region average only a few cm/s (Holton, 1992) when integrated over one hour. A vertical wind test is accomplished by measuring the vertical winds for a few hours and ensuring that the average vertical wind is corrected to ~ 0 m/s.

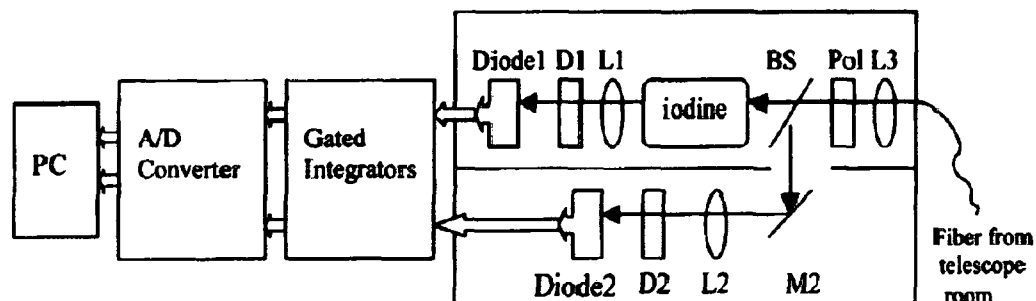


Figure 2-11. Chirp frequency shift is determined by measuring normalized transmission through an Iodine vapor cell for each of the three frequencies transmitted. In the figure, 1=iodine channel and 2=power-normalization channel, L= lens, D= diffuser, M= mirror, Pol =polarizer, and BS= beamsplitter (from Sherman 2002).

2.2.1.3 Transmitter Optics

Daytime momentum flux measurements are beyond the lidar system's current capabilities. Therefore, only one zonal and one meridional channel are needed during daytime operation to resolve tides. A new design (Figure 2-12) maximizes the signal for daytime measurements without compromising pointing accuracy and co-planar alignment of nighttime measurements. The telescopes are fixed during the observations, maintaining transmitter pointing accuracy. The optics allow for the transmission of three beams

during nighttime operation and the transmission of two beams during daytime operation. A flip mirror changes the distribution of laser power between daytime and nighttime observations. During nighttime operation, transmitted power is distributed 40/40/20 percent for the East/West/North channels and for daytime operation 40/60 percent for East/North channels.

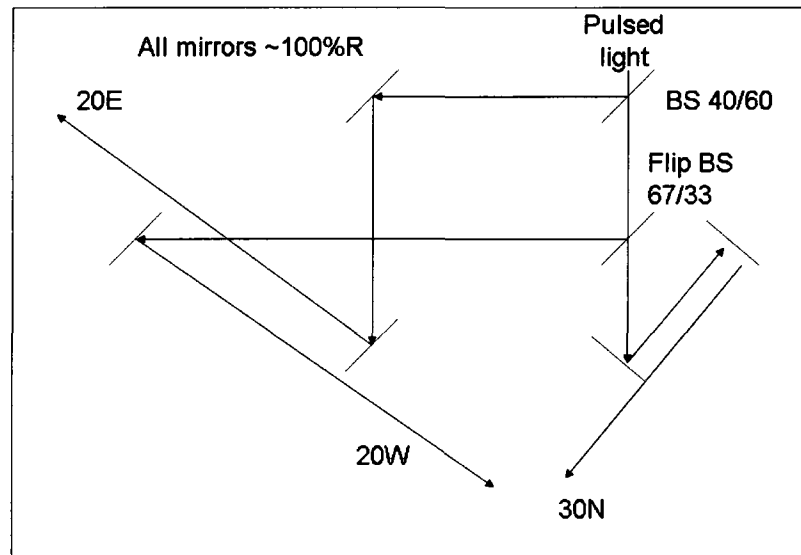


Figure 2-12. The description of the new transmission optical path begins with the pulsed beam from the PDA entering from the top. It is split by a 40% reflectance 60% transmittance beam splitter. For nighttime operations the 67% reflectance 33% transmittance beamsplitter is in dividing the total beam power three ways. During day time operation the flip mirror is down and 60% of total power is transmitter in the North 30° channel. All short diagonal lines without arrows are mirrors unless noted as a beamsplitter (BS).

2.2.2 Receiver

In September 2006 two 76 cm f/4.0 Newtonian Starsplitter II telescopes were installed, giving an increase in the returned signal of roughly a factor of five. While continuing the ongoing studies, this greater signal has allowed the pursuit of an additional science objective, gravity wave (GW) zonal momentum flux measurements in winter night when the Na signal is particularly strong. Since the system upgrade, the two 76 cm telescopes have been pointing at angles 20° east and west from zenith for dual co-planar

beam, zonal momentum flux (Vincent and Reid, 1983), and zonal wind and temperature measurements. An existing 35 cm f/11.0 Schmitt Cassegrain Celestron C-14 telescope is pointed to the north 30° from zenith for meridional wind and temperature measurements. The current data set of nighttime zonal momentum flux measurements has the potential to begin to address the important, and not fully understood, problem of GW-tidal interactions, and is a primary goal of this thesis.

2.2.2.1 Receiver Optics

The returning fluoresced photons are collected by the telescopes, and the light is focused into an optical fiber. There are two types of optical fibers used for the two different telescopes. The fiber for the 35cm telescope is a 0.9mm in diameter and has a 0.116 numerical aperture (NA), while the 76cm telescope fibers are 1.5mm, 0.37 NA fibers. The reason for the differences is to pass the maximum amount of accepted telescope light into the optical fiber using conservation of etendue (Li 2004). Etendue is defined as $NA \cdot \text{Diameter}$, and is used to describe how spread out light is on optical surfaces. The fiber is coupled to the telescope via a matched pair of achromatic lenses designed to match the telescope (NA) and light spot size with that of the accepting fiber (Figure 2-14). The doublet pair is housed in an aluminum tube (Figure 2-14) which is inserted into the eyepiece of the 75cm telescope. The optical fibers guide the collected light from the observatory to the receiver optical table. The light from the fiber is filtered with a ~ 1 nm band pass interference filter and focused onto the active area of a photomultiplier tube. During daytime operations an extreme narrow band Faraday filter is added before the photomultiplier tube to filter out the increased sky background.

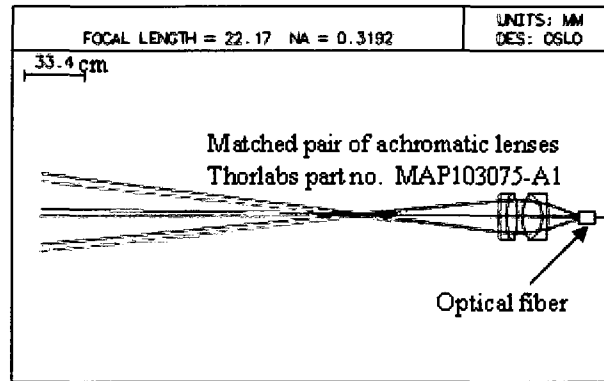


Figure 2-13. Ray tracing diagram showing the light path from the 75 cm through the match achromatic doublet onto a 1.5 mm, 0.37 NA fiber. Different rays (green and blue) represent a small misalignment in the telescope optics to design for maximum flexibility and reliability.

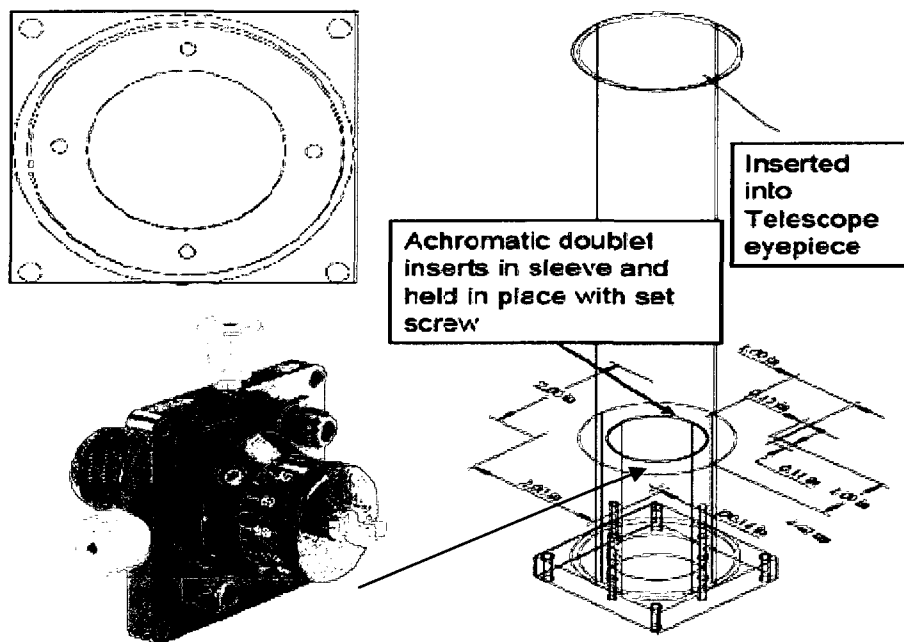


Figure 2-14. On the top left is the base plate of fiber-telescope coupler. Bottom left is a standard fiber optic positioner x-y-z translation stage that is mounted to the base plate. On the right is an aluminum tube that fits into the telescope eye-piece. Matched pair of achromatic lenses is slid into an inner sleeve that is attached to the base plate.

Receiver chopper - The returning light for the north signal is chopped by a Boston Electronics 300C optical chopper, with two open slots. The chopper has a sensor on the base that creates a digital output of high when the open slot passes over and low when opening is not present. With a two slot wheel rotating at 50 Hz the digital output

signal is 100 Hz, which will hereafter be called Chopper_100. A 0.9 mm diameter, 0.11 NA optical fiber located 2.7 mm from the face of the chopper wheel will make a spot size at the plane of the chopper blade:

$$0.9 \text{ mm} + 2 \cdot 2.7 \text{ mm} \cdot \sin(0.11) \approx 1.5 \text{ mm} \quad 2.30$$

The fiber is positioned ~58 mm from the center of the rotating axis of the chopper wheel (Figure 2-15). With the chopper wheel spinning at 50 Hz, the altitude range of the chopper wheel from fully closed to fully open is calculated as:

$$\begin{aligned} 50 \text{ s}^{-1} (58 \text{ mm}) 2\pi &\cong 16000 \text{ mm/s} \\ \frac{1.5 \text{ mm}}{16000 \text{ mm} \cdot \text{s}^{-1}} &\approx 94 \mu\text{s} \end{aligned} \quad 2.31$$

Light travels about 28 km in 94 us. For the light to travel into the sky, scatter, and then return, the best the chopper can effectively chop the beam from closed to full open is 28 km/2=14 km. The smaller telescope uses a 0.9 mm fiber, and the larger telescopes use a fiber with 1.5 mm and .37 NA; therefore, using equations 2.30 and 2.31 the fiber for the larger telescopes should be set 0.1 mm from the chopper wheel face to have the same full closed to full open values.

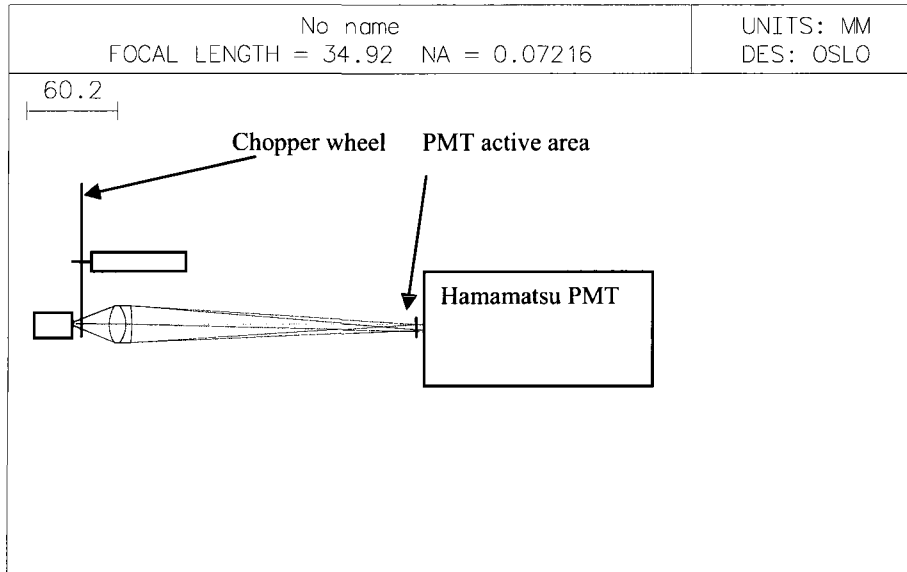


Figure 2-15. Calculated light path from .9 mm .11 NA optical fiber onto PMT active area with a chopper wheel rotating face ~2 mm from the fiber and a $f=25.4$ mm coated achromate ~25 mm from the fiber face focusing the light on a 5 mm active area.

A test of the chopping ability was performed with the small telescope optical path (Figure 2-16). Photon background generated by a light bulb in the observatory is used to set the altitude of chopping the light and to determine chopping levels. The chopper test height is set to open in the middle of the observed altitude range, ~70 km. Photon counts for the three counted channels (Figure 2-16(a)), where each would represent a different transmitter frequency, are averaged. The average of the three channels is then smoothed over 2 km in altitude. A derivative of counts with respect to altitude is least squares fit to a Gaussian curve. A Gaussian curve is a good approximation of the expected light intensity profile. The data set is truncated when negative values begin to appear due to photon noise. The fully closed to fully open value reported is the difference in 3σ values, ~17 km. Note: For data taking the chopper altitude is set to be fully open at 20 km.

Tests of the chopping of the light at the fiber face (Figure 2-16) show that the value for fully open to fully closed is closer to ~17 km. This value is compared to the expected value of ~14 km for the smaller fiber.

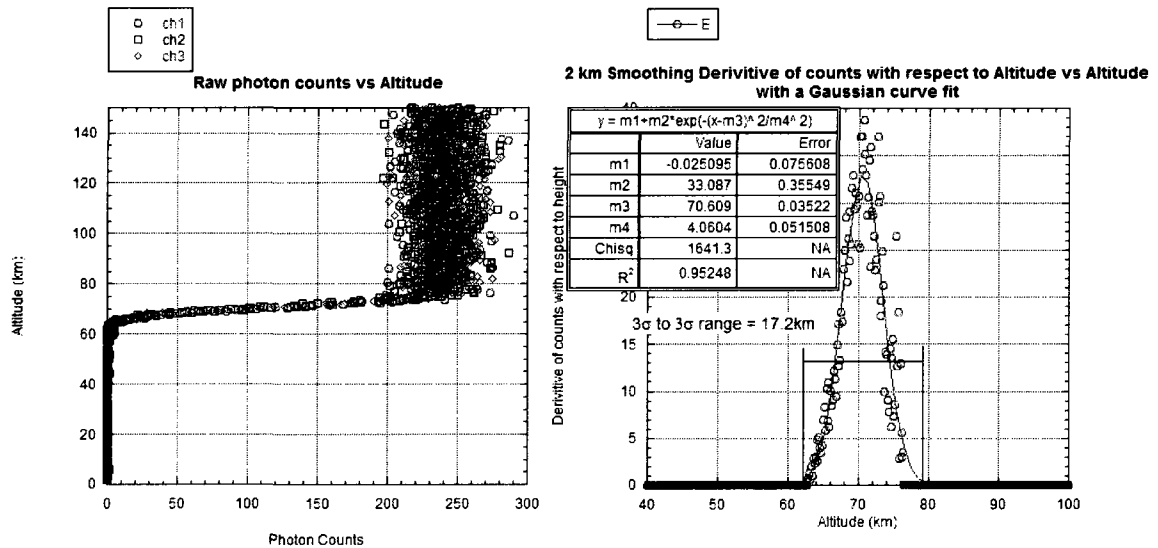


Figure 2-16. Photon background is used to set the altitude of chopping the light. The left plot shows the chopper test for photons generated by a light bulb. The counts are averaged for the three channels and then smoothed over 2 km. The difference of neighboring counts is divided by the difference of neighboring altitudes, right plot. The right plot is fit to a Gaussian. The fully closed to fully open value is reported as difference in 3σ values, ~17 km. Note: the chopper test height is set to open ~70 km ensuring opening in the middle of the observed altitude range of 0-150 km. For data taking the chopper altitude is set to be fully open at 20 km.

The opening time for the chopper wheel becomes important in data analysis because of the curve that is fit to the returning Rayleigh photons in calculating the transmitted power and the attenuation of transmitted and returning signal below 75 km (equation 2.21). If the chopper wheel opens too slowly, the curve fit to analyze the Rayleigh return would be incorrect and this could cause the data to be incorrectly analyzed.

2.2.2.1.1 PMTs

In September 2006 two new 40 percent quantum efficiency (QE) Hamamatsu PMTs were installed for lidar measurements. Currently the new PMTs are used as the nighttime 20° East and West channel PMTs. The PMTs are optically chopped because

they do not have the electronic blanking capabilities that are provided by the older PMT. The blanking of a PMT is when the bias on the first two cathodes is reversed by on board circuitry due to an external signal. There are several differences between the new PMT (Hamamatsu H7421-40) and the older PMT's (Hamamatsu R934-02) that should be highlighted. The older PMT has a 15-17 percent QE at 589nm compared to 40 percent for the new PMT, allowing greater than a factor of two gain in the signal. The old PMT has a pulse width of 8 ns while the new PMT has a pulse width of 20 ns; the longer pulse width limits the count rate of the newer PMTs to 5 million counts per second.

The old PMT is connected to a preamp and then a discriminator, which has a negative output pulse (-0.6 V). The new PMT has an on board preamp and discriminator and provides a positive voltage (+2.5 V) for the output pulse. The card that counts the older PMT pulses requires adjustment of the threshold amplitude to be adjusted by a potentiometer located on the mother board of the card. Fortunately a new counting card (COMTEC) was also acquired for the system upgrade, which allows adjustment of the threshold via a software interface.

2.2.3 Electronics

A laser pulses light into the atmosphere with a 50 Hz repetition rate; some of the light is backscattered by the atmosphere to be collected by telescopes. Returning photons are counted by photomultiplier tubes in 1 μ s bins from ~20-250 km. The time of flight is calculated with the knowledge of when the laser pulses and the speed of light. With the time of flight known, the distance where the backscattering interaction takes place is known within ~150 m. Data is integrated for two minutes before December 5th 2006 and

for one minute thereafter, to yield a statistically significant temperature, wind and Na density.

The CSU lidar electronics subsystem is more complicated than most other lidar system due to the shifting between the three frequencies required for obtaining the R_T and R_V ratios (section 2.1.4.1). First, the transmitter seed light is shifted via the AO (section 2.2.1.2) which requires that the AO crystals be turned on and off synchronously with the AO chopper wheel, which allows through the shifted light and blocks the non-shifted light. Secondly, the receiver chopper wheel is timed precisely with the firing of the pulsed YAG laser, ensuring a consistent chopping height of returned photons; this is to produce reliable data and prevent damage to the PMTs. Thirdly, the new electronics subsystem allows for two data acquisition cards to count and record returning photons for four separate channels (currently only three channels are used). Finally, the signals to the YAG and the counting cards are conditioned for impedance matching and pulse width to meet required specifications. The timing of the electronics sub-system is maintained with a digital clock, one-shots, simple digital logic, and current supplies (see Appendix II for more details).

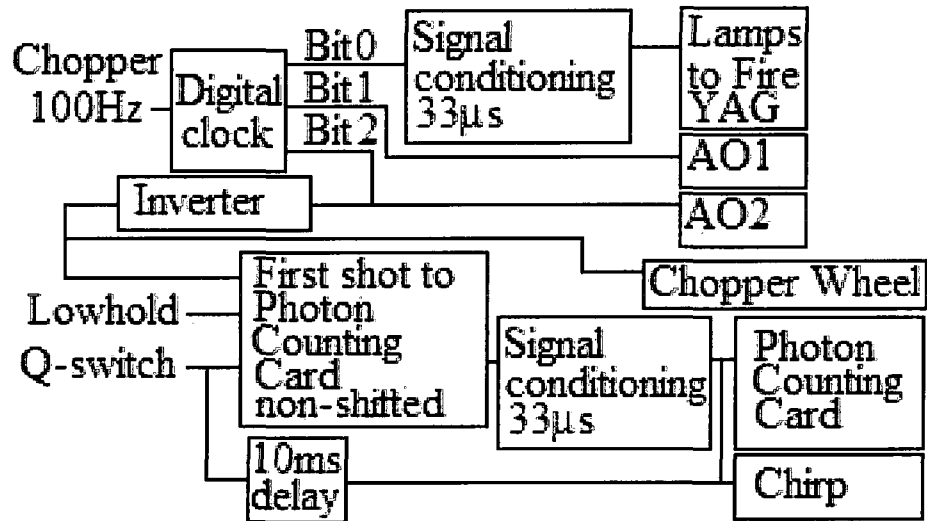


Figure 2-17. A block diagram of the timing electronics. In the top left the 100 Hz receiving chopper TTL signal that dictates the timing of the lidar electronics. With every two pulses from the receiver chopper a digital clock advances, continually counting 0, 1, and 2. With every clock tick Lamps cause the YAG to pulse. Bit 1 and Bit 2 control the AO crystals and thus the shifted AOM light. Lowhold ensures the first photons counted each file are when the transmitter is not shifted light. Q-switch comes from the YAG when a pulse of light is sent into the sky. The timing of Q-switch determines the binning of returned photons. Chirp requires a pulse between chirp samples for background.

Figure 2-17 is a block diagram of the timing electronics. In the top left corner the 100 Hz receiving chopper TTL signal dictates the timing of the rest of the sub-system. Because the YAG is fired at 50 Hz and the chopper wheel is supplying a 100 Hz signal, for every two pulses from the receiver chopper a digital clock advances once. The digital clock continually counts through three, for the three frequencies transmitted into the atmosphere. With every clock tick a 5 V, 33 μ s pulse is sent to the laser Lamps/Input channel on the pulsed YAG causing the Q-switch to allow the laser to fire. The Q-switched firing of the YAG occurs about 200 μ s after the initial Lamps/Input signal.

Bits 1 and 2 of the digital clock control the AO crystals 1 and 2, respectively. When a bit goes high the crystal transducer control powers an AO crystal transducer, shifting the light. The AO chopper is synchronized with the shifting of the light by the

AO crystals, by the providing the inverted signal from Bit 2 to the chopper synchronizer (section 2.2.1.1.b).

Lowhold suppress the Q-switch signal from reaching the counting card while saving files and during the scan and re-locking of the ring laser. This combines with the signal from Bit 2 to ensure the first photons counted each new file are from a non-AOM-shifted laser shot. This is due to a limitation of the somewhat antiquated Optech counting card, that, this aside, has amazingly been providing excellent photon counting for over ten years of service.

The Q-switch signal comes from the YAG when the Q-switch permits a pulse of light to be sent into the sky. It is the timing of Q-switch signal that provides time of flight information and thus determines the binning of returned photons in the counting cards. The signal must be conditioned differently for the two different counting cards to prevent double triggering and erroneous counting or miss binning of data.

The chirp sampling requires background samples between each sample of the transmitted beam; therefore a 10ms delay of Q-switch is used to sample background. This delay can be adjusted up to the time that Q-switch fires again, 20 ms. It recently has been suggested that this delay be increased to sample the background 1ms before the Q-switch signal to reduce the effect of ringing between the chirp fast diodes and the box-car integrators. This has not been implemented at the time of this writing.

2.2.3.1 Counting cards

There are two types of counting cards use in the CSU lidar--the Optech fdc700m card and the Comtec P7882 card. The Optech card has been used for over 10 years in the CSU lidar system, and its operation has been described in previous dissertations (White,

1999; Li, 2005). Due to the age of the Optec card it is desirable to have a verifiable substitute that can be integrated into the current system with minor modifications. In addition, the Optec card can only sample two channels and the current experiment required three beam operations. The recently installed Comtec card (Figure 2-18) allows two channel inputs with software adjustable bin width down to 200ns in dual input mode with counting rates in excess of 350 MHz.

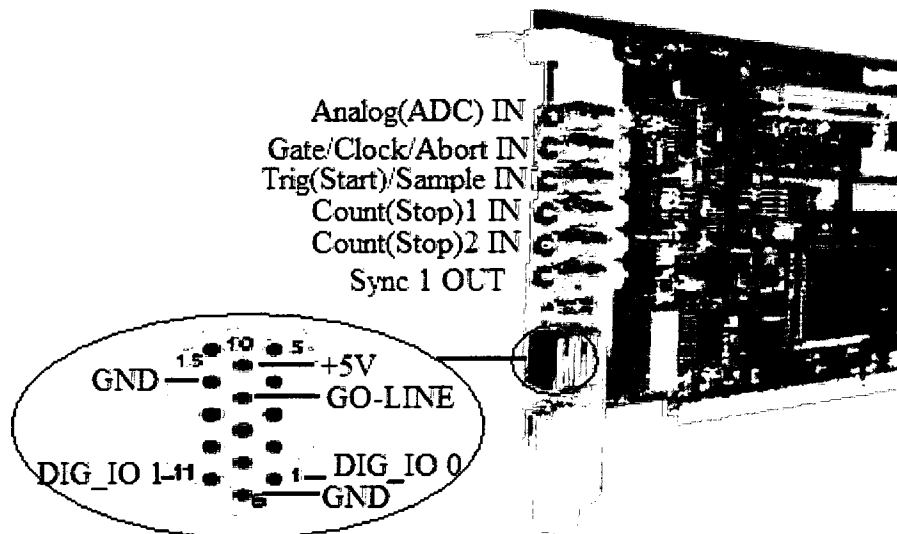


Figure 2-18. Comtec card with access ports. Timing of when the laser is fired Q-switch is input into TRG (START) and returned photons (PMT pulses) are counted with COUNT (STOP) 1 and 2 IN. DIG_IO 0 and 1 are used for digital tagging of AOM.

The buffered Q-switch signal is connected to TRG(START)/SAMPLE IN (Figure 2-18). PMT signals are sampled as COUNT(STOP)1 IN and COUNT(STOP)2 IN. A 15 pin connector is used for digital tagging: DIG_IO 0 (pin 1) and DIG_IO 1 (pin 11) for AO1 and AO2 respectively. When the signal is high (>+2.3V) and it turns on the associated transducer for the AOM shifted light, it also turns on the associated Comtec signal channel, thus enabling the digital tagging to sort out the received signal into separate storage channels with respect to transmitted frequency. The ‘GO’-LINE is used

if the Comtec board is used to generate Low Hold. Low Hold is currently generated by the Optech card due to the Comtec card not being used during daytime operations.

Having laid the necessary ground work of how measurements are made in the mesopause, chapter 3 transitions to current atmospheric theory. Discussion in chapter 3 continues with an introduction to gravity waves, what they are, and how they can impact the momentum budget in the mesosphere; this is followed by a brief discussion on atmospheric tides.

References

- Acott, P. E., Krueger, D. A., She, C. Y., Williams, B. P., and Fritts, D. C., *On sodium lidar measurements of gravity-wave momentum fluxes and assessment of gravity-wave/tidal interactions*, Annual CEDAR conference Santa Fe, NM poster, 2006
- Chen, H., *A sodium fluorescence lidar for daytime operation using dispersive faraday vapor filter*, Ph.D. Dissertation, Colorado State University, 1997
- Corney, A., *Atomic and Laser Spectroscopy*, Oxford, **39**, 1977.
- French, A.P., *Special Relativity*, W. W. Norton & Company, Inc., 1968
- Holton, J. R., *An Introduction to Dynamic Meteorology*, International Geophysics Series, Volume **48**, Elsevier Science (USA), Academic Press, 1992.
- Juncar, P., J. Pinard, J. Hamon and A. Chartier, Absolute Determination of the Wavelengths of the Sodium D₁ and D₂ Lines by Using a CW Tunable Dye Laser Stabilized on Iodine, *Metrologia*, **17**, 77-79 , 1981
- Kirchhoff, V. W. I., Theory of the atmospheric sodium layer: a review, *Can. J. Phys.* **64**, 1664-1672, 1986.
- Li, T., *Sodium lidar observed variability in mesopause region temperature and horizontal wind: Planetary wave influence and tidal-gravity wave interactions*, Ph.D. Dissertation, 2005
- Oates, C. W., K. R. Vogel, and J. L. Hall, High Precision Linewidth of Laser-Cooled Atoms: Resolution of the Na 3p²P_{3/2} Lifetime Discrepancy, *Phys. Rev. Lett.* **76**, 2862-2869, 1996.
- She, C. Y., Remote measurement of atmospheric parameters: new applications of physics with lasers, *Contemporary Physics*, **31**(4), 247-260, 1990.
- She, C. Y., and J. R. Yu, Doppler-free saturation fluorescence spectroscopy of Na atoms or atmospheric application, *Appl. Opt.*, **34**(6), 1063-1075, 1995
- She, C. Y., J. R. Yu, H. Latifi, and R. E. Bills, High-Spectral-Resolution Fluorescence Lidar for Mesospheric Sodium Temperature Measurements, *Appl. Opt.* **31**, 2095-2106 1992
- Sherman, J. P., *Mesopause Region Thermal and Dynamical Studies Based on Simultaneous Temperature, Zonal and Meridional Wind Measurements with an Upgraded Sodium Fluorescence Lidar*, Ph.D. Dissertation, Colorado State University, 2002
- Siegman, A.E., *Lasers*, University Science Books, Mill Valley CA. 1986

- Vance, J. P., *The Sum Frequency Generator seeded, ALOMAR Weber Sodium LIDAR and Initial Measurements of Temperature and Wind in the Norwegian Arctic Mesopause Region*, PhD Dissertation, Colorado State University, 2004
- Vincent, R. A. and I. M. Reid, HF Doppler measurements of mesospheric gravity wave momentum fluxes, *J. Atmos. Sci.*, **40**, 1321-1333, 1983
- Voltz, U. M. Majerus, H. Liebel, A. Schmitt, and H. Schmoranzner, Precision Lifetime Measurements on Na I $3p^2P_{1/2}$ and $3p^2P_{3/2}$ by Beam-Gas-Laser Spectroscopy, *Phys. Rev. Lett.*, **76**, 2862-2865, 1996.
- White, M. A., *A Frequency-agile Na Lidar for the Measurement of Temperature and Velocity in the Mesopause Region*, Ph.D. Dissertation, Colorado State University, 1999
- Wiese, W. L., M. W. Smith, and B. M. Miles, "Atomic transition probabilities", *Nat. Stand. Ref. Data Ser. Nat. Bur. Stand.*, **22**, (National Bureau of Standards, Washington, D.C., 1969).
- Yu, J. R., *A sodium wind/temperature lidar and observed mesopause thermal structure over Ft. Collins, CO*, Ph.D. dissertation, Colorado State University, 1994
- Yuan, T., *Seasonal variations of Diurnal and semidiurnal tidal-period perturbations in mesopause region temperature and zonal and meridional winds above Ft. Collins, CO (40°N, 105°W) based on Na-Lidar observation over full diurnal cycles*, Ph.D. dissertation, Colorado State University, 2004

Chapter 3: **Basic Theory of the Mesosphere**

The mesosphere and lower thermosphere (MLT) region of the atmosphere exhibits the counter-intuitive behavior of an average seasonal temperature that is cooler at the summer hemisphere pole and warmer at the winter hemisphere pole, suggesting that these regions are not in radiative heat balance. Experimental evidence shows that the counter-intuitive thermal structure exists at mid-latitudes as well, roughly between 65 and 100 km (She et al., 1995). The existence of a persistent pole-to-pole meridional flow and its associated adiabatic circulation with rising (falling) air cooling (heating) at the summer (winter) pole explains the mean polar temperature's departure from radiative equilibrium. If the wave momentum contribution to the MLT were to stop, there would be no meridional pole-to-pole transport; in effect it is the meridional transport that is GW driven (section 1.1.3.).

This chapter introduces gravity waves, some of their known sources, and the GW dispersion relation that relates the GW temporal characteristics (frequency) to GW spatial characteristics (wave numbers). This is followed by a brief discussion of Momentum Flux (MF), which is central to momentum transport and deposition in the MLT. Next, the experimental setup to retrieve MF measurements is explained. Finally, atmospheric tides are discussed with an emphasis on GW-tidal interaction.

3.1 **Gravity waves**

Gravity Waves (GW), also called buoyancy waves, are waves in the atmosphere reflecting the competing effects of the force of gravity and buoyancy acting on a parcel of

air in a stably stratified background state. The restoring force for gravity wave oscillations is the buoyancy that results from the displacements of these air parcels from equilibrium. The equations that describe the movements in the atmosphere can be simplified considerably by adopting the *Boussinesq approximation*², which assumes that density is a constant (ρ_0) except where coupled with gravity (g). Mathematically this means density is a constant when not multiplied by g .

Consider a stably stratified atmosphere with an air parcel at its equilibrium level. The air parcel is then displaced vertically some small distance $+\delta z$, from its current location, without disturbing the surrounding atmosphere. If the environment is in hydrostatic balance (equation 3.1),

$$\rho_0 g = -\frac{dp_0}{dz} \quad 3.1$$

(where p_0 is the pressure of the surrounding atmosphere), then the air parcel will expand adiabatically to match the surrounding atmospheric pressure. As the parcel adiabatically expands it cools. By the ideal gas law we can see that an air parcel cooler than, but at the same pressure as, the surrounding air has higher density than surrounding air (equation 3.2).

$$\frac{p}{RT} M = \rho \quad 3.2$$

Here p is pressure, T is temperature, M is the molar mass of air, R is the gas constant, and ρ is the mass density of the air. Adiabatic expansion and compression change the density of the air parcel accompanying upward and downward motions about its equilibrium, similar to a mass on a spring.

² The *Boussinesq approximation* is only valid for motions in which the vertical scale of wave perturbation is less than the atmospheric scale height H (≈ 8 km).

The maximum frequency that this air parcel can oscillate is determined by the relationship between the temperature gradient in height and the dry adiabatic lapse rate (g/c_p), about 9.5 K/km at 90 km multiplied by the forcing term of gravity (g) divided by the surrounding temperature (T_0) (equation 3.3). This angular frequency is called the Brunt-Väisälä frequency (N) (Andrews, 2000).

$$N^2 \equiv \frac{g}{T_0} \left(\frac{dT_0}{dz} + \frac{g}{c_p} \right) = g \frac{d \ln \theta_0}{dz} \quad 3.3$$

Here potential temperature (θ) is introduced as $\theta = T(p_s / p)^{R/c_p}$. Simply put, θ is the temperature that a parcel of dry air at pressure p and temperature T would have if it were expanded or compressed adiabatically to standard pressure p_s (1000 mb) (Holton, 1992).

Most GWs originate in the troposphere; they are generated by many sources including weather systems (Fritts and Alexander, 2003), flow over topographical features such as mountains (Nappo, 2002), large convective clouds (Song, Chun and Lane, 2003), and meteors (Hecht et al., 2002).

3.1.1 Simple Linear Theory of Gravity Waves

Here we employ simple linear theory to describe GW structure and behavior, though their real behavior in the MLT is assuredly highly nonlinear. GWs are treated as small perturbations about a stably stratified background state that only varies with altitude. Fundamental fluid equations of conservation of mass, energy and momentum (equations 3.4, 5, 6 respectively) are simplified to neglect viscosity terms and adopt the Boussinesq approximation. The equations expressed in a coordinate system on the rotating earth are given as, (Holton, 1992),

$$\frac{1}{\rho} \frac{D\rho}{Dt} + \bar{\nabla} \cdot \mathbf{U}(u, v, w) = 0 \quad 3.4$$

$$\frac{D\theta}{Dt} = \bar{Q} \quad 3.5$$

$$\frac{D\mathbf{U}}{Dt} = -\frac{1}{\rho} \nabla p - 2\boldsymbol{\Omega} \times \mathbf{U}(u, v, w) + \mathbf{g} + \mathbf{F}_r \quad 3.6$$

Where:

u, v, w are the winds in the zonal, meridional, and vertical directions respectively

ρ is the mass density

\mathbf{U} is the wind velocity vector

\bar{Q} is a heat source and θ is the potential temperature

\mathbf{F}_r forces due to friction, dominated by the diffusive viscous force in the fluid

\mathbf{g} is the acceleration due to gravity.

$\boldsymbol{\Omega}$ is the angular velocity of the earth's rotation

These seemingly linear fluid equations, 3.3 – 3.6 are actually nonlinear because

the advective or total derivative $\frac{D}{Dt}$, which depicts the rate of change with respect to

time following the motion of an air parcel, is related to the rate of changes with respect to

time and space at a fixed point, $\frac{\partial}{\partial t}$, and $\nabla = \frac{\partial}{\partial x} + \frac{\partial}{\partial y} + \frac{\partial}{\partial z}$, nonlinearly as:

$\frac{D}{Dt} = \frac{\partial}{\partial t} + \mathbf{U} \cdot \nabla$. Here, x and y are respectively distances along lines of longitude and

latitude on the earth's surface, and z is altitude from the earth's surface.

These equations are ‘linearized’ by expressing the dependent variables as the sum of a basic (background or mean) state, represented with an overhead bar (e.g. \bar{p}), and a small perturbation about that state, represented with a prime (e.g. p'), and assuming negligible frictional force. Further, the wave equations assume that the background state depends only on altitude (z) and an exponentially decaying atmospheric density, $\rho(z)=\rho_0\exp[-z/H]$. Thereby the perturbation grows exponentially, conserving wave energy.

In terms of a maximum perturbation at the initiation altitude, represented with an overhead tilde (e.g. \tilde{p}), the wave solutions (GWs) take the form of:

$$\left(u', v', w', \frac{\theta'}{\theta}, \frac{p'}{\rho}, \frac{\rho'}{\rho} \right) = (\tilde{u}, \tilde{v}, \tilde{w}, \tilde{\theta}, \tilde{p}, \tilde{\rho}) \cdot \exp[i(kx + ly + mz - \omega t) + z\alpha], \quad 3.7$$

Here $\alpha \equiv 1/2H$ and $H \equiv R\langle T \rangle / Mg$, where H is the vertical scale height ($H \approx 6$ km near the mesopause. $\therefore \alpha \approx 8.3 \times 10^{-5} \cdot \text{m}^{-1}$). And $g \approx 9.53 \text{ m s}^{-2}$ is the magnitude of the acceleration due to gravity near 80 to 100 km, $M = 28.9 \text{ g mol}^{-1}$ is molecular mass of air, $\langle T \rangle = 200\text{K}$ is the assumed mean temperature, and $R = 8.3143 \text{ m}^3 \cdot \text{Pa} \cdot \text{K}^{-1} \cdot \text{mol}^{-1}$ is the gas constant and (k, l, m) is the wavenumber vector, and ω is the angular frequency of the GW.

The detailed derivation of equation 3.7 can be found in several text books (Holton, 1992; Andrews, 2000; Nappo, 2002) and papers (Fritts and Rastogi, 1985; Dunkerton, 1989; Fritts and Alexander, 2003). The resulting equations provide insight into the behavior of gravity waves.

3.1.2 The Dispersion Relation

Linearization of equations 3.4, 5, 6 yields the dispersion relation (equation 3.8) which relates the wave's intrinsic frequency ($\hat{\omega}$) and the wave's spatial dependence (Fritts and Alexander, 2003). The dispersion relation can be expressed with the following notation.

$$\hat{\omega}^2 = \frac{N^2(k^2 + l^2) + f^2(m^2 + \alpha^2)}{k^2 + l^2 + m^2 + \alpha^2} \quad 3.8$$

The Coriolis parameter (equation 3.9) otherwise known as the inertial frequency (f) is given as

$$f = 2\Omega \sin \varphi \quad 3.9$$

where Ω is the Earth's rotation rate and φ is the latitude.

Intrinsic frequency is the wave frequency in the reference frame moving with the horizontal background wind. The wavenumber vector, $\mathbf{k} = (k, l, m)$, defines the propagation of the wave; the average wind vector $\mathbf{U} = (\bar{u}, \bar{v}, \bar{w})$ describes how the reference frame is moving compared to a point stationary to the surface of the earth; and we define $\mathbf{c}_\phi = (c_{\phi x}, c_{\phi y}, 0)$ as the ground-based horizontal phase speed of the wave (which is always parallel to the horizontal component of \mathbf{k}). The average vertical winds are ~ 0 m/s, therefore $\mathbf{U} \cong (\bar{u}, \bar{v}, 0)$. Then relation between the intrinsic frequency and the ground-based observation frequency ($\omega = \mathbf{k} \cdot \mathbf{c}_\phi$) becomes (Eckermann, 1992)

$$\hat{\omega} = \mathbf{k} \cdot (\mathbf{c}_\phi - \mathbf{U}) = \omega - \bar{u}k - \bar{v}l. \quad 3.10$$

A sense of GW behavior can be developed by solving for the wave group velocity and phase speed. The wave group velocity describes energy transport and wave packet propagation and, using equation 3.8, and 3.10, is written as,

$$\mathbf{c}_g = (c_{gx}, c_{gy}, c_{gz}) = \left(\frac{\partial \omega}{\partial k}, \frac{\partial \omega}{\partial l}, \frac{\partial \omega}{\partial m} \right) = (\bar{u}, \bar{v}, 0) + \frac{[k \cdot (N^2 - \hat{\omega}^2), l \cdot (N^2 - \hat{\omega}^2), m \cdot (f^2 - \hat{\omega}^2)]}{\hat{\omega} \cdot (k^2 + l^2 + m^2 + \alpha^2)}. \quad 3.11$$

The intrinsic phase speed describes the rate that the phase of the wave is moving relative to the wind and is given as,

$$\hat{\mathbf{c}}_\phi = (\hat{c}_{\phi x}, \hat{c}_{\phi y}, \hat{c}_{\phi z}) = \left(\frac{\hat{\omega}}{k}, \frac{\hat{\omega}}{l}, \frac{\hat{\omega}}{m} \right) = \left(\frac{\omega - l\bar{v}}{k} - \bar{u}, \frac{\omega - k\bar{u}}{l} - \bar{v}, \frac{\omega - k\bar{u} - l\bar{v}}{m} \right) \quad 3.12$$

It should be noted that $\hat{\mathbf{c}}_\phi$ is not a vector and that the propagation direction of wave's phase is given by the wavenumber vector (k, l, m).

The velocity of the entire wave packet (\mathbf{c}_g) defines the propagation of energy of the wave packet. If the maximum frequency of oscillation is given as N (equation 3.3) and we adopt the sign convention of $\hat{\omega}$ being positive and real, a positive wavenumber k (l) means the GW is propagating in the zonal (meridional) direction (equation 3.10) and the phase is propagating in the same direction.

The magnitude of the Coriolis parameter f (equation 3.9) at mid-latitudes is very small compared to GW intrinsic frequency ($\hat{\omega}$) for all but very low frequency waves. Using equation 3.9 we can see that $f = .0546 \text{ hr}^{-1}$ at Fort Collins, CO (41° N), which corresponds to a period of ~ 18 hrs. If we neglect the contribution due to f in equations 3.11 and 3.12 and compare, we can see the vertical components of intrinsic phase speed and the group velocity are of opposite sign. By convention, m is negative for an upward group velocity and positive for a downward group velocity. Therefore an eastward ($k > 0$) and upward ($m < 0$) propagating wave would have intrinsic phases propagating eastward and downward relative to the wind.

It is helpful to re-write the dispersion relation to lend insight into GW behavior in the vertical direction. We re-write the dispersion relation (equation 3.8) now with $f=0$ to yield an expression for m , the vertical wavenumber, as a function of all other parameters in the dispersion relation,

$$m^2 \cong \frac{(k^2 + l^2)(N^2 - \hat{\omega}^2)}{\hat{\omega}^2} - \alpha^2 \quad 3.13$$

From equation 3.11 we see that the magnitude and sign of m determine the group velocity and direction of wave propagation in the vertical, and we can see the impact variations in N , $\hat{\omega}$, and $(k^2 + l^2)$, will have on m holding all other variables constant. As horizontal wavelengths grow so does the vertical wavelength. Therefore as intrinsic frequency increases the m decreases, increasing vertical wavelengths. The reader is reminded that $\alpha \equiv 1/2H$.

It is of interest to look at limiting cases for the frequency of gravity waves. Gravity wave frequency lends insight into wavelength, turning levels, and the filtering of gravity waves in the stratosphere. For instance, Fritts and Alexander in their 2003 paper break down gravity waves into three categories: high-frequency waves ($\hat{\omega} \gg f$), medium-frequency waves ($N \gg \hat{\omega} \gg f$), and low-frequency waves ($\hat{\omega} \sim f$). Because data analysis in this study filters out GWs with periods greater than 2 hours we confine further discussion to the high and medium-frequency waves where ($\hat{\omega} \gg f$), ($N \gg \hat{\omega} \gg f$) and, for this study, f is neglected.

3.1.2.1 High-frequency and Medium-Frequency Waves

If GW vertical wavelengths are 30 km or greater as they approach the mesopause changes in the background air density over the vertical wavelength become significant

and one of the larger compressibility effects associated with gravity wave motions can occur. As the vertical wave number m approaches 0 the wave can undergo total internal reflection; and, as m passes through 0, the vertical group velocity changes sign (equation 3.11). This is called a turning level.

By setting $m = 0$ in the dispersion relation we get an expression for the intrinsic high-frequency cutoff ($\hat{\omega}_c$) for waves of a given horizontal wave number $\mathbf{k} = (k, l, 0)$ and the range of permitted intrinsic frequencies given by $N \geq \hat{\omega}_c > \hat{\omega} \gg f$ as,

$$\hat{\omega}_c^2 = N^2 \left(1 - \frac{\alpha^2}{k^2 + l^2 + \alpha^2} \right) \quad 3.14$$

This approximation to the fully compressible solution neglects the effects due to sound waves and rotation (f). Solutions found are used as an upper bound of the possible phase speeds using,

$$|\hat{c}_{\varphi-\max}| = \frac{\hat{\omega}_c}{|\mathbf{k}|} = N(k^2 + l^2 + \alpha^2)^{-\frac{1}{2}}. \quad 3.15$$

The plot of the intrinsic phase speed (y-axis) and the vertical wavelength (x-axis), Figure 3-1, suggests that gravity waves with short horizontal wavelengths (<10 km) are likely to exhibit lower phase speeds (<30 m/s).

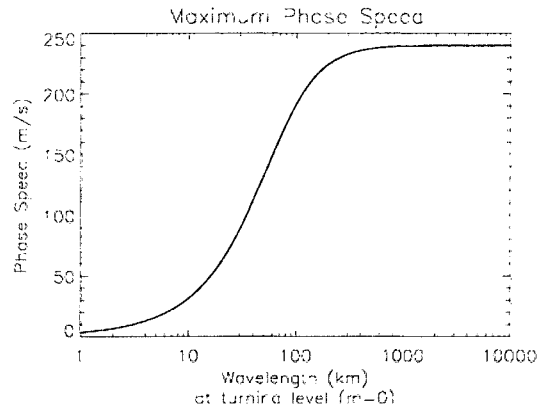


Figure 3-1. A plot of maximum intrinsic phase speed at the $m=0$ the turning level. This lends to insight into probable horizontal wavelengths in the mesopause.

Since lower phase speed waves are likely to be filtered by the mean wind in the stratosphere before they reach the mesopause (Lindzen 1981) an estimate is made of the minimum horizontal wavelength expected in the mesopause of ~ 10 km. Because spectrum of gravity waves is expected to be present in the mesopause, significantly longer wavelength gravity waves are expected.

3.2 Introduction to momentum flux

Momentum Flux (MF or $\rho_0 \overline{u'w'}$, is the vertical flux of horizontal momentum which is also the horizontal flux of vertical momentum. The correct interpretation depends on how this quantity is averaged. When averaged in time at a fixed altitude, as in this dissertation, then $\rho_0 \overline{u'w'}$ is the vertical flux of horizontal momentum.

GWs do not transport mass from the troposphere into higher regions of the atmosphere; however, they do transport momentum and associated total energy. Their oscillating motions act on the background wind applying a force, in effect transporting momentum from lower to higher altitudes. Momentum flux has the same units as stress and it plays the same role as Reynolds' stress in turbulent flow but here it is imposed by waves rather than by correlated velocities in turbulence. The dissipation of gravity waves

is represented by momentum flux divergence with altitude. The force applied to the wind (section 1.1.3) from this divergence has been best described with eddy diffusion (Lindzen, 1981; Holton, 1982). GWs also transport energy with a non-zero divergence of GW's heat flux (associated with change of potential temperature).

When perturbed due to waves and/or turbulence, the atmospheric variables in momentum equation (equation 3.6), and continuity equation (equation 3.4), may be decomposed into the sum of background state and perturbation. Thus, $u = \bar{u} + u'$ and $w = \bar{w} + w'$. Therefore the means of the fluctuating components vanish as well as terms with the product of a mean deviation and a mean. So when multiplied and averaged, $\overline{uw} = \bar{u}\bar{w} + \overline{u'w'}$. In order to clarify the relationship between GW momentum flux divergence and horizontal mean wind, the momentum equation (equation 3.6) is rewritten with aid of the continuity equation (equation 3.4), ignoring molecular viscosity and horizontal momentum flux divergence terms, to express the equations of mean horizontal flow as,

$$\begin{aligned}\frac{\bar{D}\bar{u}}{Dt} &= -\frac{1}{\rho_o} \frac{\partial \bar{p}}{\partial x} + f\bar{v} - \frac{\partial u'w'}{\partial z} \\ \frac{\bar{D}\bar{v}}{Dt} &= -\frac{1}{\rho_o} \frac{\partial \bar{p}}{\partial y} - f\bar{u} - \frac{\partial v'w'}{\partial z}\end{aligned}\tag{3.16}$$

Note that expressing the mean flow this way also brings into focus the discussion from section 1.1.3. The right side of equation 3.16 contains the three-way balance among the pressure gradient force, the Coriolis force and the drag due to momentum flux divergence. Without the forcing due to gravity wave divergence, the pressure gradient force and the Coriolis force are soon in balance (geostrophic balance) and there is no acceleration of the mean zonal wind.

The turbulence associated with gravity wave breaking should generate turbulent diffusion and also a net zonal drag force. That associated turbulence is assumed to account for an enhanced diffusion. Both MF divergence and eddy mixing, or diffusion, accompany turbulence, but they are not the same thing. Assuming that the perturbations in pressure and density are relatively small, and that effect of the perturbations in the meridional plane is negligible, the initial value problem for the zonally symmetric flow can then be reduced to a one-dimensional calculation of the vertical profile of the mean zonal wind. We express the relation of the background wind acceleration to momentum flux divergence and the eddy diffusion accompanying turbulence resulting from GW propagation as thus (Holton, 1982),

$$\frac{\partial \bar{u}}{\partial t} = f \bar{v} - \frac{1}{\rho_0} \frac{\partial \overline{\rho_0 u' w'}}{\partial z} + \frac{\partial}{\partial z} \left(D \frac{\partial \bar{u}}{\partial z} \right). \quad 3.17$$

Where the drag due to eddy diffusion is represented by an eddy diffusion coefficient (D), resulting from correlated wave perturbation or turbulence. In the MLT D depends on the background environment in which the GWs propagate. Past studies show that D can grow to large values, up to 500 m²/s (Forbes, 1982) during gravity wave breaking events (Li et al., 2008). Furthermore, organized structures exist in the small-scale eddies; and, unlike random molecules, this coherence in eddies could make the effective value of D negative (Andrews, 2000).

Neglecting Coriolis and assuming molecular interaction at the observed altitudes is small we rewrite equation 3.17 as

$$\frac{\partial \bar{u}}{\partial t} \approx - \frac{1}{\rho_0} \frac{\partial \overline{\rho_0 u' w'}}{\partial z}. \quad 3.18$$

Therefore the negative of the divergence of the MF, the convergence of the MF, (divided density) provides a body force on the mean wind. This forcing relationship is depicted in Figure 1-2.

Since GWs are intermittent with various sources that can cause different phase speeds, wavelengths, and group velocities, the expected negative correlation between mean state and MF does not necessarily exist throughout the entire night or through all altitudes (Holton, 1992).

From equation 3.7 we see that, if the divergence of momentum flux is zero, GW amplitude grows exponentially with a change in height. When the wave amplitude of the wind grows to $u' = |c - \bar{u}|$, where c is wave's phase velocity and \bar{u} is the background wind, the wave motion becomes convectively unstable. At this point the GW is saturated or breaks and its amplitude is considered clamped and no longer grows exponentially. Thus the GW is able to change in amplitude only when the background wind changes (Lindzen, 1981). In regions of saturation, momentum flux divergence is no longer zero. Using the GW dispersion relations and assuming continuity, the divergence of GW momentum flux can be explicitly expressed in terms of N , \bar{u} and H of the background and GW parameters, k , l and c , as (Lindzen, 1981):

$$-\frac{1}{\rho_o} \frac{\partial}{\partial z} \overline{\rho_o u' w'} \approx \frac{-k}{2HN} \frac{(\bar{u} - c)^3}{(1 + l^2/k^2)^{3/2}} \quad 3.19$$

Thus, divergence of GW induced flux provides a body force to pull the background wind to the phase velocity of the wave (equation 3.18). It is this flux divergence induced acceleration that is responsible for the drag on the zonal wind in the MLT region, and, in turn, induces a mean meridional wind in the MLT from summer to winter pole.

3.2.1 Momentum Flux Measurements Using the Vincent-Reid Method

Up to this point in the chapter, the discussion has centered on a review of existing theory. Now, we consider the observation of momentum flux.

The Vincent and Reid (1983) method of performing co-planar beam momentum flux measurements was initially developed for measurements with radar, but can be applied to the lidar measurements in this dissertation. The experiment requires two co-planar beams pointing at angles $+\theta$ and $-\theta$ from zenith. For zonal momentum flux the beams are aligned in the East-West plane.

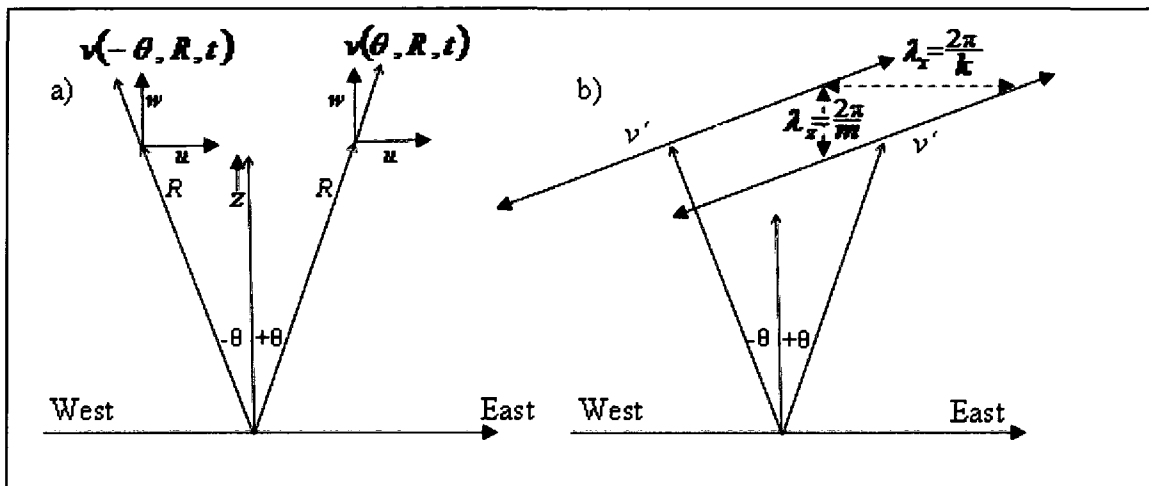


Figure 3-2. a) A representation of co-planar beam measurement geometry where V is the line-of-sight wind observed at radial distance R and time t . **b)** A representation of a monochromatic gravity wave with slanted phase front propagating toward the East. The measured Doppler shifted wind perturbation in the West beam will be less than the East because of the angle of the phase front relative to the measuring beam. The direction of gravity wave propagation can be determined from a comparison of signal variances (both after Vincent and Reid 1983).

Figure 3-2 b is a simplified diagram of a monochromatic wave spectrum with a gravity wave propagating upward to the East. Note that the magnitude of the Doppler shifting due to the GW perturbation observed in each beam would be different due to pointing angle. In this case a positive zonal momentum flux would be measured thus determining the direction of the gravity wave propagation.

The line of sight wind (v) at a radial distance (R) and time (t) for each beam can be expressed in the terms of the measured vertical (w) and zonal wind (u).

$$v(\theta, R, t) = w(\theta, R, t) \cdot \cos(\theta) + u(\theta, R, t) \cdot \sin(\theta) \quad 3.20$$

$$v(-\theta, R, t) = w(-\theta, R, t) \cdot \cos(-\theta) + u(-\theta, R, t) \cdot \sin(-\theta) \quad 3.21$$

Again the atmospheric wind is decomposed into the sum of background state and perturbation. Thus, $v = \bar{v} + v'$, $u = \bar{u} + u'$ and $w = \bar{w} + w'$. Therefore, the mean of fluctuating components vanishes as well as terms with the product of a mean deviation and a mean. So when multiplied and averaged, $\overline{uw} = \bar{u}\bar{w} + \overline{u'w'}$. If we take equations 3.19 and 3.20 and square them and then average them over time, we get,

$$\begin{aligned} & (\overline{v^2 + v'^2})(\theta, R, t) \\ &= (\overline{w^2 + w'^2})(\theta, R, t) \cos(\theta) \end{aligned} \quad 3.22$$

$$\begin{aligned} & + (\overline{u^2 + u'^2})(\theta, R, t) \sin(\theta) + 2(\overline{u'w'}) \sin(\theta) \cos(\theta) \\ & (\overline{v^2 + v'^2})(-\theta, R, t) \\ &= (\overline{w^2 + w'^2})(-\theta, R, t) \cos(-\theta) \\ & + (\overline{u^2 + u'^2})(-\theta, R, t) \sin(-\theta) \\ & + 2(\overline{u'w'}) \sin(-\theta) \cos(-\theta) \end{aligned} \quad 3.23$$

We assume that the statistics of the motions are independent of horizontal position and $z = R \cos(\theta)$ which gives,

$$\begin{aligned} \overline{v^2}(\theta, R) &= \overline{v^2}(-\theta, R) = \overline{v^2}(z) \\ \overline{u^2}(\theta, R) &= \overline{u^2}(-\theta, R) = \overline{u^2}(z) \end{aligned} \quad 3.24$$

$$\begin{aligned} \overline{w^2}(\theta, R) &= \overline{w^2}(-\theta, R) = \overline{w^2}(z) \\ \overline{u'^2}(\theta, R) &= \overline{u'^2}(-\theta, R) = \overline{u'^2}(z) \end{aligned} \quad 3.25$$

$$\overline{w'^2}(\theta, R) = \overline{w'^2}(-\theta, R) = \overline{w'^2}(z)$$

$$\overline{u'w'}(\theta, R) = \overline{u'w'}(-\theta, R) = \overline{u'w'}(z)$$

Because of the differing relative angles each beam makes with the phase lines of the observed gravity wave motions $\overline{v^2}(\theta, R) \neq \overline{v^2}(-\theta, R)$ (Figure 3-2). Subtracting equation 3.21 from 3.22 and re-organizing terms we get

$$\overline{u'w'}(z) = \frac{\overline{v'^2}(\theta, R) - \overline{v'^2}(-\theta, R)}{2 \sin(2\theta)} \quad 3.26$$

The observational system is set with $\theta=20^\circ$ and $-\theta=-20^\circ$ in the east-west plane.

3.3 Tidal effects in atmosphere

Solar tides in the atmosphere are global-scale waves with periods that are harmonics of a solar day; for example, a period of 24-hours for diurnal and 12-hours for semi-diurnal tides. Migrating tides have phases which propagate westward, synchronized with the apparent motion of the sun. The phases of non-migrating tides are not linked to the motion of the sun. Tides can be excited, for example, by the absorption of solar radiation, by large-scale latent heat release associated with deep convective activity in the troposphere, by nonlinear interactions between global-scale waves (Miyahara and Miyoshi, 1997; Hagan and Roble, 2001; McLandress, 2001), and by interaction between gravity waves and tides (McLandress and Ward, 1994).

Migrating solar atmospheric tides are thermally forced by the absorption of solar radiation by tropospheric H₂O (in the near-infrared), by stratospheric and lower mesospheric O₃ (in the ultraviolet), by lower thermospheric O₂ and N₂ (in the Schumann-Runge bands and continuum), and by O in the upper thermosphere (in the extreme ultraviolet). The associated excitation gives rise to both evanescent and propagating

components of the diurnal and semidiurnal tides. The components which propagate upward grow in amplitude as neutral atmospheric density decreases and are the dominant tidal signatures in the MLT region.

Tidal theory proposes that a significant source of non-migrating tides could be latent heat release associated with cloud and/or raindrop formation (Lindzen, 1978 and Hong and Wang, 1980). Using rainfall data in combination with numerical models, Hamilton (1981) examined latent heat release as a possible tidal excitation mechanism and provided strong support for the theory. He concluded that the diurnal variation of the latent heat release from rainfall should be significant. Furthermore, he noted that diurnal surface pressure variations are characterized by large geographic variations which cannot be explained by the migrating tide.

Tides achieve large wind and temperature amplitudes in the MLT, and large vertical scales compared to a scale height over which GW amplitudes may change significantly. It is for these reasons that when combined with the sensitivity of GW structure and propagation to their thermal and wind environment, GW-tidal interactions are expected (and observed) (Fritts and Vincent, 1987, and Wang and Fritts, 1990) to be important to the overall GW forcing of the MLT.

3.3.1 Tidal-GW Interaction

Radar measurements in the late 1980's (Fritts and Vincent, 1987, and Wang and Fritts, 1990) revealed strong modulation of GW MF by the diurnal tide and are the only observational MF studies dealing directly with GW-tidal interactions to date. There are theoretical studies specifically addressing the influences on tidal structure of GW-critical level interactions (Walterscheid, 1981), the excitation or damping of planetary waves

(PWs) by GWs arising from variable source strengths (Holton, 1984), and the modulation of GW filtering (Miyahara, 1985 and Miyahara, Hayashi, and Mahlman, 1986). These studies hint at possibly important interactions and feedback, but offer no quantitative guidance. Significant disagreements and controversy remain over the impacts of GW-tidal (and GW-PW) interactions on tidal (and PW) amplitudes, annual variations, and mean momentum deposition (Fritts and Alexander, 2003). A number of studies suggest that such interactions dampen tidal amplitudes (Forbes et al., 1991, Lu and Fritts, 1993, Ortland, 2005, Meyer, 1999); another suggests amplification (Mayr et al., 1998), while still others suggest little or no impact on amplitudes (McLandress, 2002) or a potential for altered mean momentum deposition (Lu and Fritts, 1993). These conflicting studies reveal that the quantitative descriptions of current GW parameterizations of interactions with either mean or large-scale wave motions should be improved. More quantitative MF measurements are required in order to define GW-tidal and GW-PW interactions throughout diurnal cycles.

Chapter 3 has laid the foundations of gravity waves, tidal waves and momentum flux. We can now proceed to MF observations with sense of what the observations mean. To add validity to the measurements presented in chapter 5, chapter 4 presents the filtering and analysis techniques used to obtain the results as well as the technique used obtaining an estimate of error.

References

- Andrews, D. G., *An Introduction to Atmospheric Physics*, Cambridge University Press, 2000.
- Dunkerton, T., Body Force Circulations in a Compressible Atmosphere: Key Concepts, *PAGEOPH*, **130**(2/3), 243-262, 1989
- Eckermann, S. D., Ray-tracing simulation of the global propagation of inertia gravity waves through the zonally averaged middle atmosphere. *J. Geophys. Res.*, **97**, 15,849-15,866, 1992.
- Forbes, J. M., J. Gu, and S. Miyahara, On the interactions between gravity waves and the diurnal propagating tide, *Planet. Space Sci.*, **39**, 1249-1257, 1991.
- Forbes, J. M., Atmospheric Tides, I, Model Description and Results for the Solar Diurnal Component, *J. Geophys. Res.*, **87**, 5222-5240, 1982.
- Fritts, D. C., and P. K. Rastogi, Convective and dynamical instabilities due to gravity wave motions in the lower and middle atmosphere: Theory and observations, *Radio Science*, **20**(6), 1247-1277, 1985.
- Fritts, D. C., and M. J. Alexander, Gravity dynamics and effects in the middle atmosphere, *Rev. Geophys.*, **41**, doi: 10.1029/2001RG000106, 2003.
- Fritts, D. C., and R. A. Vincent, 1987: Mesospheric momentum flux studies at Adelaide, Australia: Observations and a gravity wave/tidal interaction model, *J. Atmos. Sci.*, **44**, 605-619.
- Gardner, C. S., and W. Yang, Measurement of the dynamical cooling rate associated with the vertical transport of heat by dissipating gravity waves in the mesopause region at the Starfire Optical Range, *J. Geophys. Res.*, **103**, 16,909-16,927, 1998.
- Hagan, M. E., and R. G. Roble, Modeling diurnal tidal variability with the National Center for Atmospheric Research thermosphere–ionosphere–mesosphere–electrodynamics general circulation model, *J. Geophys. Res.*, **106**, 24, 869-882, 2001.
- Hamilton, K., Latent heat release as a possible forcing mechanism for atmospheric tides, *Mon. Weather Rev.*, **109**, 3– 17, 1981.
- Hecht J. H., R. L. Walterscheid, M. P. Hickey, R. J. Rudy, and A. Z. Liu, An observation of a fast external atmospheric acoustic-gravity wave, *J. Geophys. Res.*, **107** (D20), 4444, doi: 10.1029/2001JD001438, 2002.
- Holton, J. R., The Role of Gravity Wave Induced Drag and Diffusion in the Momentum Budget of the Mesosphere, *J. Atmos. Sci.*, **39**, 791-799, 1982.

- Holton, J. R., The generation of mesospheric planetary waves by zonally asymmetric gravity wave breaking, *J. Atmo. Sci.*, **41**, 3427-3430, 1984.
- Holton, J. R., *An Introduction to Dynamic Meteorology*, International Geophysics Series, Volume **48**, Elsevier Science (USA), Academic Press, 1992.
- Hong, S. S., and P. H. Wang, On the thermal excitation of atmospheric tides, *Bull. Geophys. Natl. Cent. Univ. Taiwan*, **19**, 56–83, 1980.
- Li, T., C.-Y. She, H.-L. Liu, and M. T. Montgomery, Evidence of a gravity wave breaking event and the estimation of the wave characteristics from sodium lidar observation over Fort Collins, CO (41°N, 105°W), *Geophys. Res. Lett.*, **34**, L05815, doi:10.1029/2006GL028988, 2007.
- Lindzen, R.S., Effect of daily variations of cumulonimbus activity on the atmospheric semidiurnal tide, *Mon. Weather Rev.*, **106**, 526– 533, 1978.
- Lindzen, R.S., Turbulence and Stress Owing to Gravity Wave and Tidal Breakdown, *J. Geophys. Res.*, **86**, NO. C10, 9707-9714, 1981.
- Lu, W., and Fritts, D. C., Spectral estimates of gravity wave energy and momentum fluxes III, Gravity-tide interactions, *J. Atmos. Sci.*, **50**, 3714-3727, 1993.
- Matsuno, T., A quasi one-dimensional model of the middle atmosphere circulation interacting with internal gravity waves, *J. Meteorol. Soc. Jpn.*, **60**, 215–226, 1982.
- Mayr, H. G., J. G. Mengel, K. L. Chan, and H. S. Porter, Seasonal variations of the diurnal tide induced by gravity wave filtering, *J. Geophys. Res.*, **25**, 2629-2632, 1998.
- McLandress C., and W. E. Ward, Tidal/gravity wave interactions and their influence on the large-scale dynamics of the middle atmosphere: Model results, *J. Geophys. Res.*, **99**, 8139– 8155, 1994.
- McLandress, C., The seasonal variation of the propagating diurnal tide in the mesosphere and lower thermosphere, part I, The role of gravity waves and planetary waves, *J. Atmos. Sci.*, **59**, 893–906, 2001.
- McLandress C., Interannual variations of the diurnal tide in the mesosphere induced by a zonal-mean wind oscillation in the tropics, *J. Geophys. Res.*, **29**, 19-1 to 19-4, 2002.
- Meyer, C. K., Gravity wave interactions with the diurnal propagating tide, *J. Geophys. Res.*, **104**, 4223-4240; Erratum: *J. Geophys. Res.*, **104**, 4223-4239, 1999.
- Miyahara, S., Suppression of stationary planetary waves by internal gravity waves in the mesosphere, *J. Atmos. Sci.*, **42**, 100-107, 1985.

- Miyahara, S., Y. Hayashi, and J. D. Mahlman, Interactions of gravity waves and planetary-scale flow simulated by the GFDL “SKYHI” general circulation model, *J. Atmos. Sci.*, **43**, 1844-1861, 1986.
- Miyahara, S., and Y. Miyoshi, Migrating and nonmigrating atmospheric tides simulated by a middle atmosphere general circulation model, *Adv. Space Res.*, **20**, 1201–1207, 1997.
- Nappo, C. J., *An Introduction to Atmospheric Gravity Waves*, International Geophysics Series, Volume **85**, Elsevier Science (USA), Academic Press, 2002.
- Ortland DA, Generalized Hough modes: The structure of damped global-scale waves propagating on a mean flow with horizontal and vertical shear, *J. Atmo. Sci.*, **62**, 2674-2683, 2005.
- She, C., J. Yu, D. Krueger, R. Roble, P. Keckhut, A. Hauchecorne, and M.-L. Chanin, Vertical Structure of the Midlatitude Temperature from Stratosphere to Mesopause (30 - 105 km), *Geophys. Res. Lett.*, **22**(4), 377-380, 1995.
- She, C.Y., Initial full-diurnal-cycle mesopause region lidar observations: Diurnal-means and tidal perturbations of temperature and winds over Fort Collins, CO (41N, 105W), *J. Atmo. Solar-Terr. Phys.* **66**, 663-674, 2002.
- Song I. S., Chun H. Y., Lane T. P. Generation Mechanisms of Convectively Forced Internal Gravity Waves and Their Propagation to the Stratosphere, *J. Atmos. Sci.*, **60**, No. 16, 1960–1980, 2003.
- Tsuda, T., Y. Murayama, M. Yamamoto, S. Kato, and S. Fukao, Seasonal variation of momentum flux in the mesosphere observed with the MU radar, *Geophys. Res. Lett.*, **17**, 725-728, 1990.
- Vincent, R. A. and I. M. Reid, HF Doppler measurements of mesospheric gravity wave momentum fluxes, *J. Atmos. Sci.*, **40**, 1321-1333, 1983.
- Walterscheid, R. L., Dynamical cooling induced by dissipating internal gravity waves, *Geophys. Res. Lett.*, **8**, 1235-1238, 1981.
- Wang, D.-Y., and D. C. Fritts, Mesospheric momentum fluxes observed by the MST radar at Poker Flat, Alaska, *J. Atmos. Sci.*, **47**, 1511-1521, 1990.
- Wehrbein, W. M., and C. B. Leovy, An accurate radiative heating and cooling algorithm for use in a dynamical model of the middle atmosphere. *J. Atmos. Sci.*, **39**, 1982

Chapter 4: **Filtering and Analysis Techniques**

In August 2006, two 76 cm telescopes were added to the current lidar system increasing the nighttime signal five-fold and facilitating zonal momentum flux measurements in the mesopause region from September 2006 to May 2007. In the first season of three-beam operation, observations were made with a beam geometry of east-west, dual, co-planar beams 20° from zenith and the third beam north 30° from zenith. This geometry allows the determination of nighttime gravity wave zonal momentum flux in conjunction with simultaneous 24-hour measurements of the mean and tidal fields of the mesopause region temperature and zonal and meridional winds. The data not only provide the vertical profile of nighttime zonal momentum flux, but also shed some light on the accompanying gravity wave-tidal interactions. In order to understand the results of the study and bolster confidence in the data set, the reader must first be familiar with the analysis techniques used.

In this chapter, data is presented, as well as the analysis techniques developed to obtain the zonal momentum flux and the tides with the associated error. In Section 4.1, a sliding window is employed in the application of Vincent and Reid's formula in the calculation of momentum flux. Within the sliding analysis window the data are further filtered with a linear fit. The effect the sliding window has on data with and without the linear fit is tested. Section 4.2 follows this discussion by examining errors in momentum flux analysis. Additionally, introduction of Monte Carlo simulation allows comparison of

the known simulation error with actual measurement error enabling an estimate of momentum flux error.

4.1 Momentum Flux Analysis

Because most measurements using the co-planar beam measurement of MF have been performed with radar (for example, Vincent and Reid, 1983; Fritts and Vincent, 1987; Fritts and Yuan, 1989; Janches et al, 2006), techniques used to analyze momentum flux have primarily focused on analysis methods germane to radar observations. MF measurements made with sodium lidar data have been limited in number and have focused on an average MF value for the duration of the data set (Gardner and Liu, 2007; Vance, 2004) and have not shown how MF changes during the observation. By only addressing nightly averages, these studies did not allow investigation of the possible interaction of gravity-waves with atmospheric tides. The analysis presented here employs sliding windows that show the temporal progression of momentum flux in an observation period. Furthermore, in these studies, attempts to remove long period oscillations, such as tides, by subtraction of a linear fit, have been applied to entire data sets (Alan Liu, private communication), some of 12 hours duration. Data sets in the mesopause near 12 hours duration often contain a strong semi-diurnal tidal signature. A simple linear fit of the entire night subtracted from the data is insufficient in removing this semi-diurnal signature. Moreover, analysis shows that even if the night is divided into two linear fits of 6 hours in duration, a strong semi-diurnal tidal signature is still present (see section 4.1.2). A process of removing data that do not fall within 3 standard deviations of the linear fit was used to remove the variations associated with tide from the analysis, but these variations may also be from gravity wave perturbation. The analysis employed in

this dissertation removes tidal variations by subtracting linear fits from segments of the night of shorter duration (2 hours) from the data.

4.1.1 Analysis Window and Linear Fit

To remove oscillations with periods greater than two hours the linear fit is confined to two hour subsets of the entire night time of observations³ that may last up to thirteen hours. To express this in mathematical terms, a measurement of the LOS wind is defined as v , and an entire night of measurements (N measurements) at the k^{th} altitude bin are defined as $\mathbf{V}_k = \{v_1, v_2, \dots, v_N\}_k$ at the associated times $[t_1, t_2, \dots, t_N]$. A subset of the vector \mathbf{V}_k centered at j^{th} data point is defined as $\mathbf{v}_{k,j} = \{v_{j-\frac{n}{2}}, \dots, v_j, \dots, v_{j+\frac{n}{2}}\}_k$. The $n+1$ measurements that compose $\mathbf{v}_{k,j}$ can span any amount of time, but for the analysis presented in this dissertation $\mathbf{v}_{k,j}$ is two hours in length centered on the j^{th} data point at time t_j .

The LOS wind data is fit using the LINFIT function in the IDL language. The LINFIT function fits the paired data $\{t_i, v_i\}$ to the linear model, $v_i = A + Bt_i$, by minimizing the chi-square error statistic. Each set of A, B coefficients is associated with a j^{th} term, where the linear fit is centered. This linear fit is then subtracted point-by-point in the two hour analysis window yielding the linear fit filtered data,

$$\left[x_{i,j} = v_{i+j-\frac{n}{2}} - \left(A_j + B_j t_{i+j-\frac{n}{2}} \right) \right]_k \quad 4.1$$

yielding the data set $x_{k,j} = \{x_{j-\frac{n}{2}}, \dots, x_j, \dots, x_{j+\frac{n}{2}}\}_k$ where i runs from 0 to n and the index k designates the altitude bin.

³ An entire night time of observations is based on the amount of time there is adequate signal to noise for momentum flux calculation, about 10 to 13 hours weather permitting.

As an example, if an entire night of data lasted 12 hours in length and data were integrated over 3 minutes, this would mean that in 60 minutes there would be 20 measurements and in 12 hours there would be a total of 240 measurements. Therefore $N=240$ for an entire night of data and $n=40$ for two hours of measurements. Consider the second hour and the 100th altitude bin, $j = 40$ and $k = 100$. Then the $n + 1$ measurements that compose $\mathbf{v}_{k,j}$ would be expressed as $\mathbf{v}_{100,40} = \{v_{20}, v_{21}, \dots, v_{40}, \dots, v_{60}\}_{100}$ and a line would be fit to this sub-set of data yielding the coefficients $A_{100,40}$ and $B_{100,40}$. This linear fit is then point-by-point subtracted from the data in the window yielding the data set $\mathbf{x}_{100,40} = \{x_{20}, \dots, x_{40}, \dots, x_{60}\}_{100}$ (equation 4.1).

The analysis of the data at the edges is truncated. For example, for the $j=1$ window $n = 20$. This is because there is no recorded data before the first three minute observation of the night. Likewise, the $j=240$ window contains no data after observations were curtailed and therefore $n=20$ for that window also. Windows in between expand as more data is made available until the two hour window limit is met. For example for $j=2$, $n=21$ and for $j=3$, $n=22$ and so on until $n=40$.

Next the variance is calculated for the linear fit subtracted data set centered at the j^{th} data point ($\mathbf{x}_{z,j}$) using the standard formula for variance,

$$\sigma_{k,j}^2 = \frac{\sum_{i=j-\frac{n}{2}}^{j+\frac{n}{2}} (x_{j,i} - \bar{x}_j)_k^2}{n + 1} \quad 4.2$$

Where:

$$\bar{x}_j = \frac{1}{n + 1} \sum_{i=j-\frac{n}{2}}^{j+\frac{n}{2}} x_{j,i} \quad 4.3$$

and $n = 40$. Note that due to the linear fit $\bar{x}_j = 0$ for all j 's. Using equation 4.2 the Vincent and Reid formula is re-written as,

$$\langle u'w' \rangle_{k,j} = \frac{(\sigma_{z,j}^2)_E - (\sigma_{z,j}^2)_W}{2 \sin(2\theta)} \equiv [MF/\rho]_{k,j}. \quad 4.4$$

Equation 4.4 yields MF/ρ at all times (t_j) and for all altitude bins (k) during the entire night of observations, centered in a sliding window of set time duration. By adjusting the window size to two hours, only the data within that window are included in each $[MF/\rho]_{k,j}$ calculation, effectively filtering longer period oscillations from the variance calculation and the resulting MF/ρ calculation.

4.1.2 Filtering Effects on Variance

To better understand how windowing with and without the subtracted linear fit filters the data; consider the effect these filters have on the calculated variance of a simulated signal. A data set of $N=480$ data points is generated to simulate 24 hours of data sampled at three minute intervals. The generated data is first composed of a pure sine wave,

$$v_j = \sin(2\pi t_j/\tau). \quad 4.5$$

Where j is the index that runs from 1 to 480 and τ is the period of the generated wave.

This simulation generates 44 data sets changing τ in half hour intervals from two hours to twenty-four hours and an additional 40 data sets changing τ from 3 minutes to two hours by three minute intervals. There is no random noise added to this simulation. In total there are 84 data sets of monochromatic waves that are analyzed three different ways.

First, the variance is calculated with no window. This is the standard definition of variance and is expressed as

$$\sigma_{\tau}^2 = \frac{\sum_{j=1}^N (v_j - \bar{v})_{\tau}^2}{N}. \quad 4.6$$

The resulting set of 84 calculated variances for different τ 's is then plotted with the variance value on the y-axis and period on the x-axis in the left plot of Figure 4-1 (green line with diamonds).

Second the waveforms are also analyzed with a two hour window ($n = 40$), but no linear fit. This is expressed using the notation of section 4.1.1 as

$$\sigma_{\tau,j}^2 = \frac{\sum_{i=j-\frac{n}{2}}^{j+\frac{n}{2}} (v_i - \bar{v}_j)_{\tau}^2}{n + 1}. \quad 4.7$$

Twenty four hours of data gives 480 variances for each period from which an average variance and standard deviation of the variance is calculated and plotted (left plot Figure 4-1, blue line with squares), with the error bars representing the span of one standard deviation from the mean.

And finally, the waveforms are analyzed with a two hour window ($n = 40$) and linear fit. The linear fit is calculated and applied to the data in the same fashion as expressed in equation 4.1, with the exception that the data sets are not varying in altitude but with the period of the generated waveform. We express this as

$$\left[x_{i,j} = v_{i+j-\frac{n}{2}} - \left(A_j + B_j t_{i+j-\frac{n}{2}} \right) \right]_{\tau}. \quad 4.8$$

Where i runs from 0 to n , j runs from 1 to 480, which is repeated for each of the 84 τ 's. From this data the variances are again calculated for each period and this is expressed as

$$\sigma_{\tau,j}^2 = \frac{\sum_{i=j-\frac{n}{2}}^{j+\frac{n}{2}} (x_{j,i} - \bar{x}_j)^2}{n+1} \quad 4.9$$

This again creates 480 variances for each period from which an average and standard deviation is calculated and plotted in the left plot of Figure 4-1 (red line with circles), with the error bars representing the span of one standard deviation from the mean.

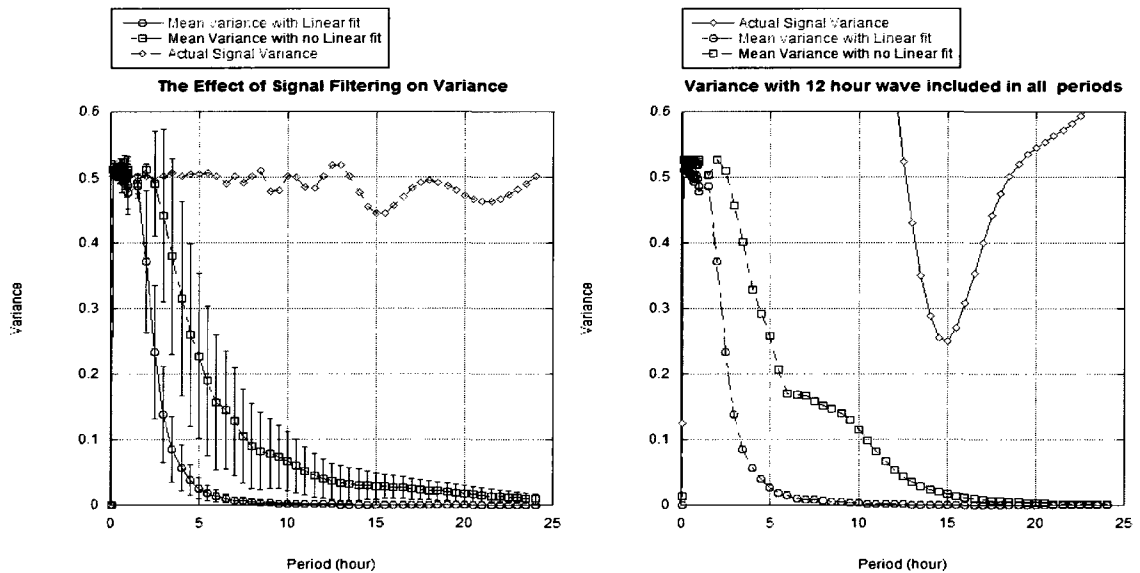


Figure 4-1. This is a plot of calculated variance with no filtering (green), a window filter of 2 hours with no linear fit subtraction (blue), and with a linear fit subtraction (red). The blue and red lines represent the mean variances obtained from the windowed filtering. The error bars are set one standard deviation from the mean. The left plot has monochromatic wave generation with the period of the wave annotated on the x-axis. The right plot has the same monochromatic wave spectrum with a 12 hour wave added. The non-windowed variance (green) is off scale high for most of the plot.

The error bars in Figure 4-1 left highlight the variation in the calculated variance due to the location of the sample window relative to the phase of the monochromatic wave. This error due to phase mismatch is more pronounced when the monochromatic wave period nears the window width. This is also seen in the single value variance calculation for entire night (green) that should be a flat line at 0.5, but is not. Furthermore, the linear fit analysis (red) has consistently a lower error due to phase

mismatch (error bars) than the non-linear fit subtracted data (blue). The plot on the right in Figure 4-1 details the change in the variance when a 12 hour wave is summed with the monochromatic wave of period τ . Now the generated waveform on which subsequent analysis is performed becomes

$$v_i = \sin(2\pi t_i/\tau) + \sin(2\pi t_i/12). \quad 4.10$$

The linear fit subtracted data (red) results in the right and left plots are essentially the same. This suggests that the inclusion of the subtracted linear fit in this analysis filters motions with 12 hour periods or greater from the variance calculation. Furthermore, if the linear fit is not subtracted (blue), the calculated variance does not adequately filter 12 hour motions from the variance calculation as evidenced by the visible change in the variance from 6 to 12 hours in the right plot.

The phase relationship between the waveform phase and window size and location in time does play a role in this simulation, such as where the increase in the blue line occurs and why the green line is not a constant 0.5, but this is not a study to answer all the possible outcomes of the waveform and window size phase relation. This simulation is designed to better understand why the inclusion of the linear fit is necessary, and the inclusion of the linear fit achieves the desired effect; its inclusion effectively suppresses the amplitude of longer period waves, yet allows a measurement of variance, and therefore the MF from the shorter period waves.

4.1.3 Filtering Effects in Wind Measurements

Figure 4-2 contains plots of the east pointing transmitter's line-of-sight wind measurement (left) for December 9th, 2006 (day 6343) at four altitudes, noted on the right of each plot [84, 88, 92, 96] km, and the corresponding calculated variance (right).

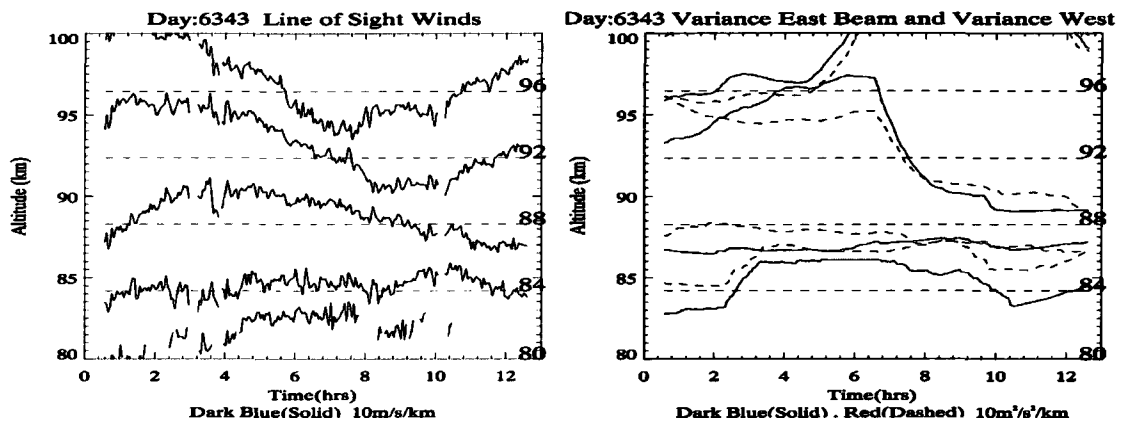


Figure 4-2. The left plot is the east line of sight wind at altitudes marked on the right of the plot. On the right, the variance values calculated from the LOS east and west measurements. East variance is represented by the solid blue line and West variance is the dashed red line. The measurements are obtained at the altitudes marked on the right y-axis and are marked with a dashed black line. The analysis window spans 12 hours and the scale is 10 m/s/km and 10 m²s⁻²/km left and right plots respectively.

When the linear fit over the entire night is subtracted from the data, the resulting variance (Figure 4-2, right) contains a contribution from long period waves; including tides (section 4.1.2).

Values of the wind and momentum flux are multiplied by a scaling factor; therefore, a difference of 1 km in altitude corresponds to 10 ms⁻¹ or 10 m²s⁻² respectively. Positive/negative values are represented with a greater/lower altitude than the corresponding dashed horizontal line at each given altitude.

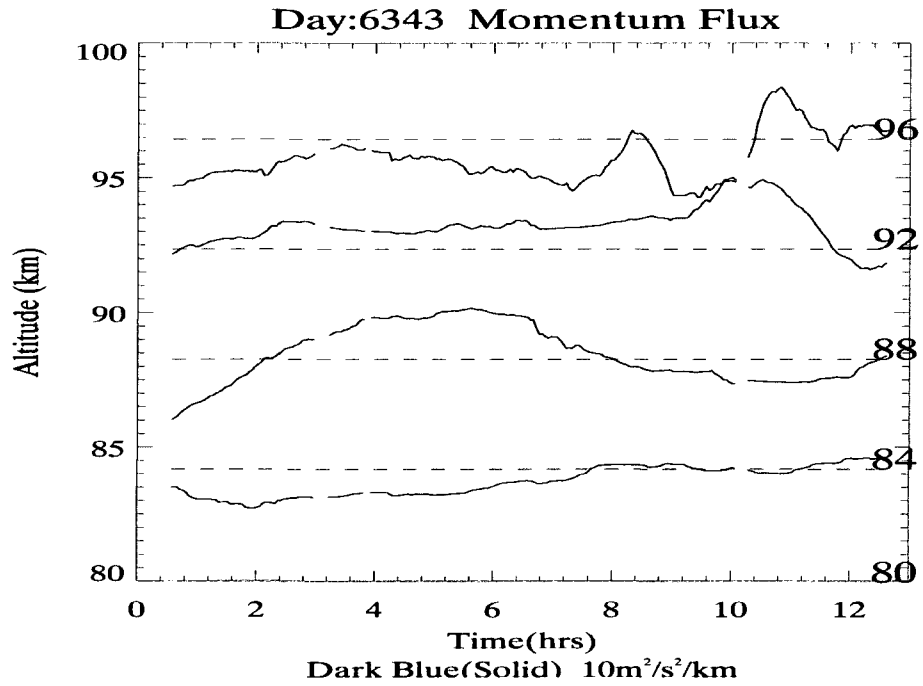


Figure 4-3. Momentum Flux generated with a 12 hour analysis window that may be contaminated with perturbations from long period waves, such as tides.

To ensure that tides do not bias the calculated MF the contribution from the semi-diurnal and diurnal tides to the resulting momentum flux must be filtered. The question then becomes what size of analysis window will remove the tides and pass the shorter period waves?

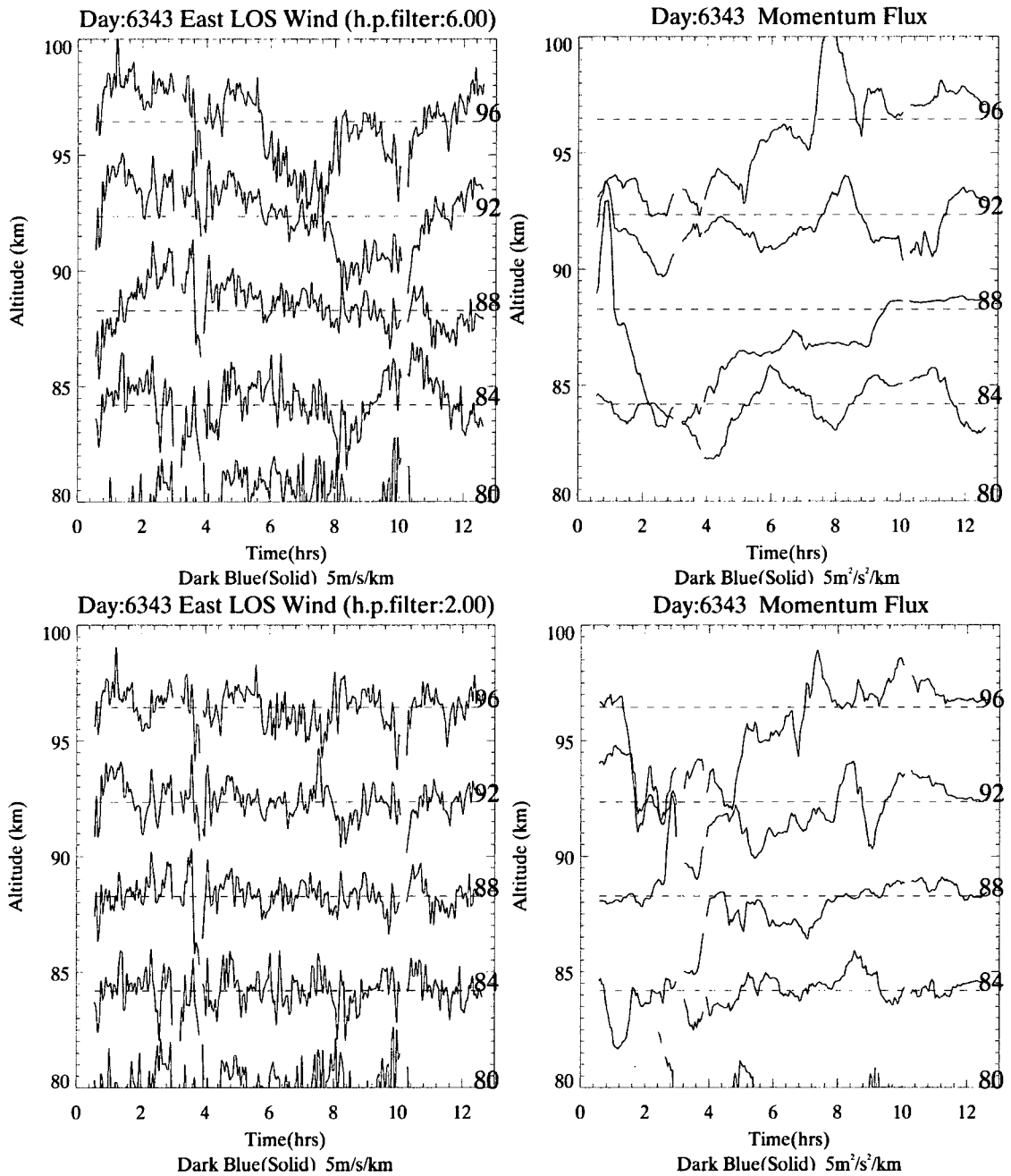


Figure 4-4. The two left plots are the LOS wind measurements with a six hour analysis window (top) and a two hour analysis window (bottom). The right two plots are momentum flux values calculated from the associated winds and the respective analysis window length, with the subtracted linear fit.

Figure 4-4 illustrates the difference between a six hour analysis window (top row) and a two hour analysis window (bottom row) using again day 6343. A six hour high-pass filter is imposed on the LOS wind to simulate a 6-hour window (Figure 4-2, top

left). To better understand this high-pass filter we first express the equation for the boxcar SMOOTH function in IDL as,

$$R_j = \left\{ \begin{array}{l} \frac{1}{n+1} \sum_{i=0}^n v_{i+j-\frac{n}{2}}, \quad j = \frac{n-1}{2}, \dots, N - \frac{n+1}{2} \\ v_j, \text{ otherwise} \end{array} \right\}. \quad 4.11$$

Where n is the window width of data points in six hours ($n=120$), R_j is the resulting smoothed v values. These smoothed values are point by point subtracted from the data leaving only the high frequency waves. This is expressed as,

$$A_j = v_j - R_j. \quad 4.12$$

A high pass filter is employed here because a 6-hour sliding window that has a linear fit subtracted inside the window cannot show the linear fit filtered wind. Each sliding step presents a new set of data points on which to perform the linear fit and subsequent variance calculation. This point is clarified with an aside: an example with a two hour window.

For the 40th value in a nighttime of data at a specific altitude how do we represent the linear fit filtered data? Using the naming conventions detailed in section 4.1.1, do we report the $i=20$ value when the window is centered on $j = 40$ or do we report the $i=19$ value when $j=41$. Both represent a value at the same altitude at the same time, but it is likely that they will have different values due to the changing coefficients in the linear fit. We remind the reader of equation 4.1,

$$\left[x_{i,j} = v_{i+j-\frac{n}{2}} - \left(A_j + B_j t_{i+j-\frac{n}{2}} \right) \right]_k \quad 4.13$$

And then insert the values given in the example of a two hour window, $\frac{n}{2} = 20, j = 40$ or 41 and $i = 20$ or 19 . We yield two equations representing the same filtered data point. We express this as

$$\begin{aligned} [x_{20,40} = v_{20+40-20} - (A_{40} + B_{40}t_{20+40-20})]_z \text{ or } [x_{19,41} \\ = v_{19+41-20} - (A_{41} + B_{41}t_{19+41-20})]_z. \end{aligned} \quad 4.14$$

The six hour analysis window processed data still exhibits evidence of long period waves, presumably tidal structure. Tidal structure is manifest in the data with the large amplitude, approximately twelve hour period, oscillation seen in altitudes 88 km and above in Figure 4-4, top left. The resulting momentum flux could still contain a tidal signature and thereby change MF results. With a two hour analysis window the LOS wind (Figure 4-2, bottom left) exhibits no obvious tidal structure yet maintains considerable variability, evidence of high frequency gravity wave activity. Thus the corresponding momentum flux (Figure 4-4, bottom right) is assumed not to include tidal amplitude effects from the variance calculation, and the only gravity wave tidal correlations are from short period gravity wave tidal interaction.

An analysis window of two hours was chosen for all measurements to compute gravity wave momentum flux, allowing filtering out of tidal structure but passing most higher-frequency gravity wave motions. Although the momentum flux due to low-frequency gravity wave motions will be removed from this analysis, they are expected to be a smaller contributor to the entire momentum flux magnitude (Fritts and Vincent, 1987).

4.2 Errors in measurements

The uncertainties in the reported MF values can be broken down into two distinct types: uncertainties introduced by the analysis technique and error in LOS wind measurement. The uncertainties in the analysis technique are due to the spectrum of GWs present in the atmosphere, the horizontal separation of the radial beams, and the windowing of the data. The error in the LOS wind measurement is due to photon counting statistics and systematic errors of the transmitter.

4.2.1 Analysis considerations-error subtraction from variance

The criteria for ruling out data starts with the measurement of the line of sight wind. For small total photon counts used in determining wind and temperature, the error in those measurements becomes high. Only data with error in the LOS wind measurement due to photon noise less than 10 ms^{-1} are deemed of sufficient accuracy to provide MF measurements. Furthermore, data where the calculated uncertainty in the wind measurement due to photon noise is greater than the observed variance must be eliminated from the MF calculation. This is combined with the requirement that 80% of the data points in the analysis window must be valid and meet the above criteria to report a MF value. Because the signal is generally very good at night during MF measurements, these criteria usually do not affect the reported data in the altitude range above 80 km and under 100 km (Figure 4-5).

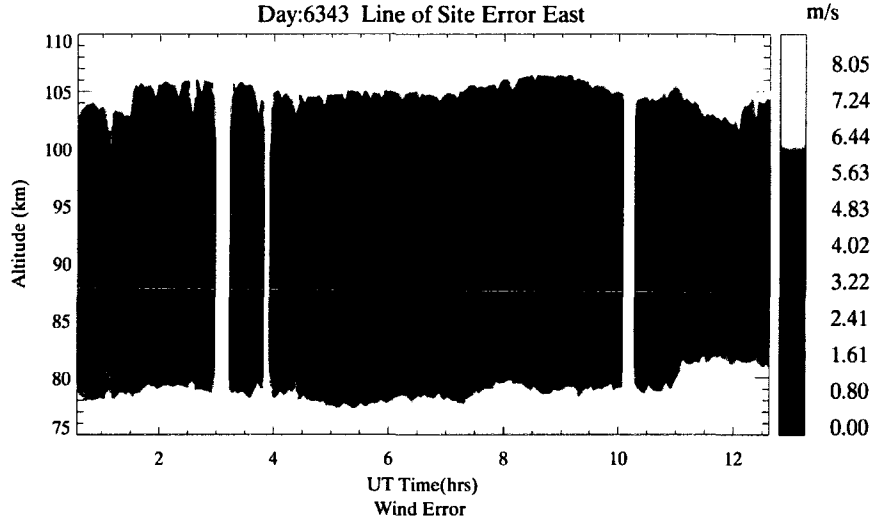


Figure 4-5. The calculated error due to photon noise in the line of site wind measurement for day 6343 shows the the error between 80 km to 100 km is usually under 1.6 m/s. The white regions at the top and bottom represent 10 m/s or greater error.

The data analysis program that calculates LOS winds, temperatures, and sodium densities, also calculates the magnitudes of their errors using photon counting statistics and propagation of error. If the reported value of error at j^{th} point and the k^{th} altitude bin is $\delta v_{k,j}$ then calculated mean squared error associated with the point j is given by

$$\overline{\delta v_{k,j}^2} = \frac{1}{n+1} \left[\sum_{i=j-\frac{n}{2}}^{j+\frac{n}{2}} \delta v_i^2 \right]_k \quad 4.15$$

Consider an atmosphere with no wave activity; a constant wind and constant temperature would be observed in both LOS channels if there were no photon noise. But there is always photon noise and measurements of this benign atmosphere report a variance in LOS winds and temperatures. The variance in the observed signal (equation 4.2) is a combination of variances: the variance due to waves propagating through the LOS beams **and** variance due to photon noise. Assuming that geophysical (natural) variability, $\sigma_{k,j}^2$ and photon noise variation, $\overline{\delta v_{k,j}^2}$ are statistically independent we may express,

$$(\sigma_{k,j}^2)_{waves} = \sigma_{k,j}^2 - \overline{\delta v_{k,j}^2} \quad 4.16$$

and $(\sigma_{k,j}^2)_{waves}$ becomes the calculated wind variance due to gravity waves propagating through the LOS measurements. Rewriting the momentum flux calculation (equation 4.4) to include only variance from the wind (equation 4.16) yields,

$$\langle u'w' \rangle_k = \frac{(\sigma_{k,j}^2)_{E,waves} - (\sigma_{k,j}^2)_{W,waves}}{2 \sin(2\theta)} \quad 4.17$$

Averaging the error in the wind measurement in each window is done because $\sigma_{k,j}^2$ is also based on the variance of an entire window. Because the variance of the LOS winds is obtained through propagation of error of photon noise through data analysis it is possible for $(\sigma_{k,j}^2)_{waves}$ in equation 4.17 to be negative. A negative variance does not make physical sense, therefore a MF/ ρ value calculated from a negative variance does not make physical sense and does not capture the natural variability of the wind; such data points are excluded from the analysis. It is of special note that for the data reported in this dissertation, gravity wave motions were so prevalent and the recorded data was of such a high caliber, that such a small percentage of data is excluded from analysis in the region of reported MF (80 km to 100 km) as to make use of this rule negligible.

If $(\sigma_{k,j}^2)_{waves}$ is a positive value and the photon counts are roughly the same in each channel, then the calculated error in each channel should be roughly the same, and the subtraction of $\overline{\delta v_{k,j}^2}$ from $\sigma_{k,j}^2$ in equation 4.13 can be included or removed for most measurements between 80 km to 100 km, because the $\overline{\delta v_{k,j}^2}$ terms cancel. In this analysis the subtraction of $\overline{\delta v_{k,j}^2}$ terms is included.

4.2.2 Monte Carlo Estimate of MF/ρ Error

The estimated error in a single MF value is calculated by propagation of error in the line of site wind measurements. In the derivation of the error equation it is assumed that the error distribution in the line of site wind error is Gaussian (David Krueger, private communication) and that the error in the two channels is not correlated.

$$\begin{aligned} \langle (\text{MF}/\rho)^2 \rangle = & \frac{2}{(n+1)(2\sin(2\theta))^2} \left(2 \sum_{i=0}^n (x_i^E)^2 \overline{(\delta v_i^E)^2} \right. \\ & + \sum_{i=0}^n \overline{((\delta v_i^E)^2)^2} \\ & \left. + 2 \sum_{i=0}^n (x_i^W)^2 \overline{(\delta v_i^W)^2} + \sum_{i=0}^n \overline{((\delta v_i^W)^2)^2} \right) \end{aligned} \quad 4.18$$

Where for a two hour window and a three minute integration $n = 40$, x_i^E (x_i^W) is the reported eastward (westward) pointing radial wind measurement after the linear has been removed (equation 4.1), and δv_i^E (δv_i^W) is the reported error from the eastward (westward) pointing radial measurement. This analytical approach is compared to an estimate of the error in momentum flux measurement solely due to photon counting made via Monte Carlo simulation.

A simulation of counts in a hypothetical lidar experiment is created using a simulated known Gaussian atomic sodium distribution, similar to observed distributions, and constant winds. The momentum flux is calculated with the only variation in signal due to photon noise based on Poisson statistics. The ratio of photon counts that would yield static temperatures of 200 K and winds of 10 m/s for the East beam and -10 m/s for the West beam are generated to simulate actual data. This is a simulation of data and is not to be confused with the error bar limit of 10 m/s. Random photon noise in the

simulated return signal and a background are introduced in the simulated data and are the only factors creating noise in the signal. A new file of photon counts is generated every two minutes for 720 samples. The limit of 720 photon files is due to an analysis program constraint that the data be limited to 24 hours in duration. The simulated data are analyzed with a five minute temporal resolution and smoothed in the vertical by a 4 km Hanning window. The altitude and temporal smoothing are the same values used in the analysis of real data for the 2006 data sets before day 6338.

The average momentum flux is calculated for a sliding two hour window as described in section 4.1.1., which creates a momentum flux value for every five minute period. The mean and variance of the momentum flux as well as the mean and the variance of the LOS wind is then determined for each day, 288 data points. The data is further averaged by taking the average of 1500 days to smooth the results (Figure 4-6).

This plot shows that the estimate of momentum flux error from Monte Carlo simulation is consistent with the calculated momentum flux error generated by propagation of error. This is also a good way to verify data analysis error estimates of LOS wind, which is also consistent with the Monte Carlo simulation.

Of note is a discrepancy in the mean momentum flux value. The momentum flux measured from a constant 10 m/s zonal wind, averaged over many hours, should be near zero. However the data simulation highlights a $+v$ and $-v$ asymmetry in the LOS wind error calculation that leads to a nonzero bias (Figure 4-6, pink +). That is, while the photon noise in the East beam and West beam are symmetric, an asymmetry in the 2-D manifold used to calculate the winds and temperatures (Figure 2-4) causes photon distributions of the same width to have different widths in the wind distributions after

projected on the 2-D manifold. With all other factors remaining the same the width difference is seen to be dependent on the value of the mean. For instance, in this example the average variance from the 10 m/s wind is smaller than the -10 m/s wind.

While this bias in the momentum flux measurement exists, the values obtained by simulation are very small ($-0.09 \text{ m}^2/\text{s}^2$ averaged 80 km to 100 km); furthermore, because the error formula (equation 4.15) contains values obtained from variability due to atmospheric motions, a more in-depth study should be made employing simulated gravity waves to better understand this bias before it is included in reported results. Note that the results in Figure 4-6 have a larger reported uncertainty at 80 km and 100km than at 90 km. This is due to the choice of atomic sodium layer distribution used in the simulation, which was intended to simulate the actual sodium layer.

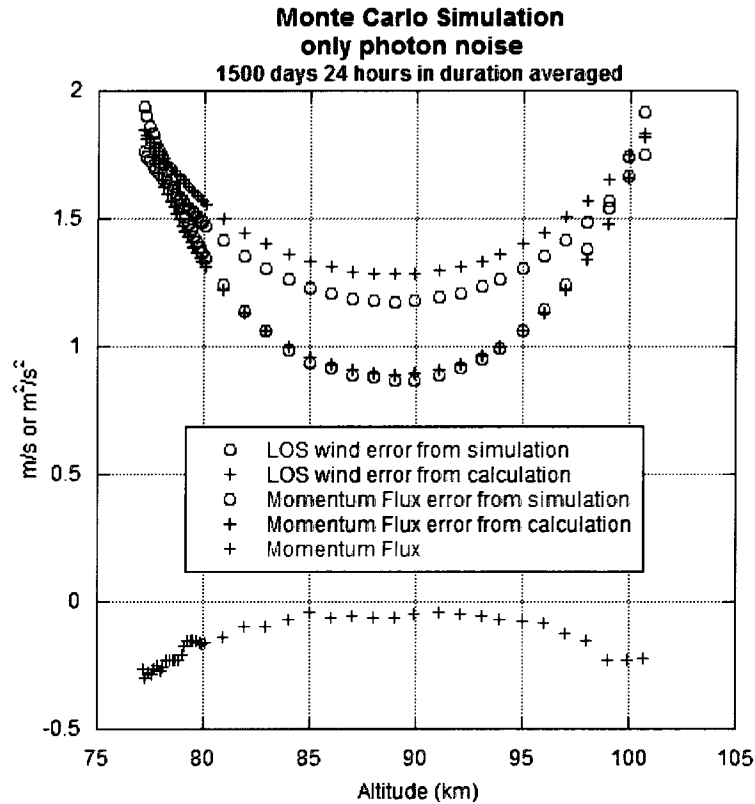


Figure 4-6. An estimate of error in the momentum flux measurement solely due to photon noise is generated by Monte Carlo simulation using the variance of the momentum flux between many three minute measurements. Note that the average momentum flux (pink +) is not centered about zero. This implies a bias in the momentum flux measurement that is photon noise dependent.

4.2.3 Measurement considerations-angle θ

Since the dual beam technique samples two different parts of sky, to maintain the coherence of the MF/ρ measurement, the pointing angle θ should be small. On the other hand, to minimize the propagation of LOS wind error in MF/ρ , as shown in equation 4.17, the pointing angle θ should be 45° . Thorsen et al, [2000] considered a compromise between these two (coherence and wind measurement error) considerations for radar measurements of MF/ρ , and determined that the optimum choice is a bit larger than $\theta = 13^\circ$. The corresponding analysis for lidar measurements of MF/ρ for altitudes 80 km to

100 km has not been made; since it should be between 0° and 45° it is commonly thought that 15° or 20° are reasonable choices. Here, we use $\theta = 20^\circ$ for convenience.

In summary chapter 4 covered the momentum flux measurement and analysis method. Possible sources of error and the equation used to estimate the error in the momentum flux measurement were highlighted. Discussion about the angle at which the beams point and reasons were discussed in support of larger pointing angles due to the monotonically decreasing function of MF error in lidar MF measurements. This can be compared to the spectrum of gravity wave wavelengths as seen by correlations between the two transmitted beams (Appendix I).

Chapter 5 will show momentum flux measurements and introduce sliding tidal analysis in an effort to display gravity-wave tidal interaction by changes in diurnal and semi-diurnal tidal phases and amplitudes correlated with large magnitudes in momentum flux.

References

- Fritts, D. C., and R. A. Vincent, Mesospheric momentum flux studies at Adelaide, Australia: Observations and a gravity wave/tidal interaction model, *J. Atmos. Sci.*, **44**, 605-619, 1987.
- Fritts, D. C., and L. Yuan, Measurement of momentum fluxes near the summer mesopause at Poker Flat, Alaska, *J. Atmos. Sci.*, **46**, 2569-2579, 1989.
- Gardner, C. S., A. Z. Liu, Seasonal variations of the vertical fluxes of heat and horizontal momentum in the mesopause region at Starfire Optical Range, New Mexico, *J. Geophys. Res.*, **112**, D09113, 2007
- Janches, D., D. C. Fritts, D. M. Riggin, M. P. Sulzer, and S. Gonzalez, Gravity waves and momentum fluxes in the mesosphere and lower thermosphere using 430 MHz dual-beam measurements at Arecibo: 1. Measurements, methods, and gravity waves, *J. Geophys. Res.*, **111**, D18107, doi:10.1029/2005JD006882., 2006
- She, C. Y., and J. R. Yu, Doppler-free saturation fluorescence spectroscopy of Na atoms or atmospheric application, *Appl. Opt.*, **34**(6), 1063-1075, 1995.
- Thorsen, D., S. J. Franke, E. Kudeki, Statistics of momentum flux estimation using the dual coplanar beam technique, *Geophys. Res. Lett.*, **27**(19), 3193-3196, 10.1029/1999GL011196, 2000.
- Vance, J. P., *The Sum Frequency Generator seeded, ALOMAR Weber Sodium LIDAR and Initial Measurements of Temperature and Wind in the Norwegian Arctic Mesopause Region*, PhD Dissertation, Colorado State University, 2004
- Vincent, R. A. and I. M. Reid, HF Doppler measurements of mesospheric gravity wave momentum fluxes, *J. Atmos. Sci.*, **40**, 1321-1333, 1983
- White, M. A., *A Frequency-agile Na Lidar for the Measurement of Temperature and Velocity in the Mesopause Region*, Ph.D. Dissertation, Colorado State University, 1999

Chapter 5: Measurement Results

Since the system upgrades over 300 hours of night-time gravity wave zonal momentum flux observations have been recorded. Eleven data sets are greater than 24 hours in duration with simultaneous 24-hour measurements of the mean and tidal fields of the mesopause region temperature and zonal and meridional winds. This data set not only provides the vertical profile of nighttime zonal momentum flux, but also sheds some light on the accompanying gravity wave-tidal interactions.

Chapter 5 is divided into three sections.

Section 5.1 starts with a case study of December 9th 2006, day 343 of 2006 or sometimes referred to as 6343. This case study describes the basic conditions during the observation period including the system setup, weather conditions, and the length of the observation. This is followed by a breakdown of the winds into line of sight (LOS) east wind measurement, line of sight west wind measurement, and an estimate of the horizontal wind. Further, system geometry and knowledge of average atmospheric LOS wind measurements allows a comparison of the wind data to that of the of the chirp correction sub-system. With the associated temperature measurements, the zonal and meridional wind estimates allow an assessment of local atmospheric stability.

The reader is reminded that before day 338 of the first year of MF measurements, data files were acquired and integrated over two minutes and later smoothed over five minutes when analyzed and after day 338 the data was integrated over one minute and

smoothed over three minutes thereafter. Thus data for day 343 were acquired with one minute integration and three minute smoothing.

In Section 5.2, the statistical data of the nightly MF observation between September 2006 and April 2007 is reported, including variances in wind, temperature, and momentum flux nightly means, as well as tabulated estimates of their error. The variances obtained will be compared with an existing long term lidar study in the mesopause region, Gardner and Liu (2007).

Finally, section 5.3 considers gravity wave-tidal interactions by examining the correlations between gravity wave momentum fluxes and the superposition of the mean wind, diurnal and semidiurnal tides. There remain significant disagreements and controversy over the impacts of GW-tidal interactions on tidal amplitudes, and mean momentum deposition into the mesosphere and lower thermosphere (MLT) region; however, as our data will show, there is significant modulation of GW induced MF that is anti-correlated with the tide. Furthermore, when divergence of the MF is largely anti-correlated with the local diurnal tidal amplitude, non-exponential growth in the diurnal tide is observed, suggesting a dampening of the diurnal tidal amplitude by high phase speed short period GWs. Our observations in equinox and winter seasons will provide additional tests for theories of GW-tidal interactions in the MLT.

5.1 Case Study of Day 6343

Focusing on a specific night of observations highlights the analysis techniques, allows discussion of wind and momentum flux characteristics, and enables exploration of atmospheric stability. Day 343 is selected because the continuous data surrounding the night of 343 is of sufficient length that a sliding tide analysis can be performed on the

entire night. Also, of all the data that supports sliding tide analysis, day 343 is closest to the mean calculated wind error for the entire data set from September 2006 until April 2007 listed in Table 4 on page 143.

Data acquisition occurred when the weather forecast predicted very clear weather spanning several days, enabling several days of continuous observation. The data examined here are continuous from 02:32 UT day 342 until 13:37 UT day 344, with the exception of sporadic clouds, periodic system maintenance (dye change, section 2.2.1.2), and required beam re-alignment. The nighttime data of day 343 is nearly centered in the continuous 59 hour data set (Figure 5-1, green lines), with 22 hours of data before the night and 24 hour after.

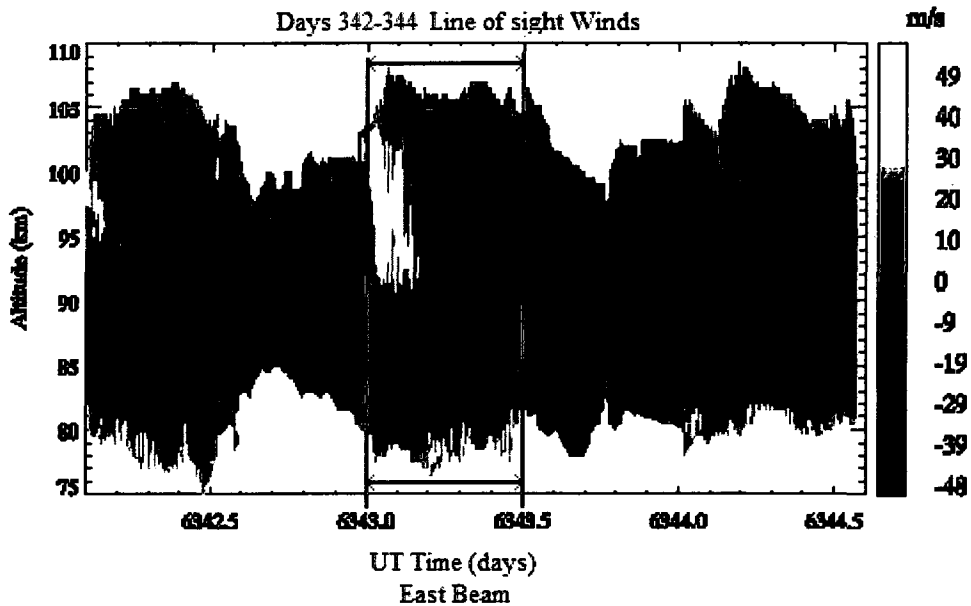


Figure 5-1. The east-beam line-of-sight wind for days 342 to 344. The data set is made up of 58 hours of nearly continuous data with brief breaks for system maintenance. The nighttime data for day 343 is shown between the green lines.

Backscattered signal photons and background photons are collected in 150 m bins and integrated over 1000 laser pulses at a 50 Hz repetition rate. The transmitter cycles pulse-by-pulse through each of the three observation frequencies; therefore, a data file is

completed every 3000 total laser pulses for an integration time of one minute. Smoothing in altitude is performed with a Hamming window and the FWHM value for smoothing is reported in this dissertation. Temporal and spatial averaging during analysis yields winds, temperatures and sodium densities every three minutes and 2 km in altitude for nighttime measurements, and every 15 minutes and 4 km for daytime measurements. For the smaller North telescope, the signal is averaged every 15 minutes and 2 km for nighttime measurements and 15 minutes and 4 km for daytime measurements.

The line of sight winds (LOS) along the East and West beams are shown in Figure 5-2. The gap in the data located at hour three in Figure 5-2 is due to system maintenance, a PDA dye change (section 2.2.1.2). The presence of no gaps in Figure 5-1 is due to data interpolation in multiple day plots. Note: data interpolation is **not** used in MF or variance calculations. Once every 24 hours the system is shut down for about 30 minutes to change pulsed-dye amplifier dye to maintain transmitter output power. The other two gaps in the data located in the fourth hour and in the tenth hour were due to an adjustment of the transmitter alignment by the operator. Thermal effects on the three lasers and one amplifier in the system require the operator to occasionally adjust the lasers to maximize output power and make slight adjustments to the beam alignment to maintain peak system operation. It is common practice to curtail data collection during laser adjustments.

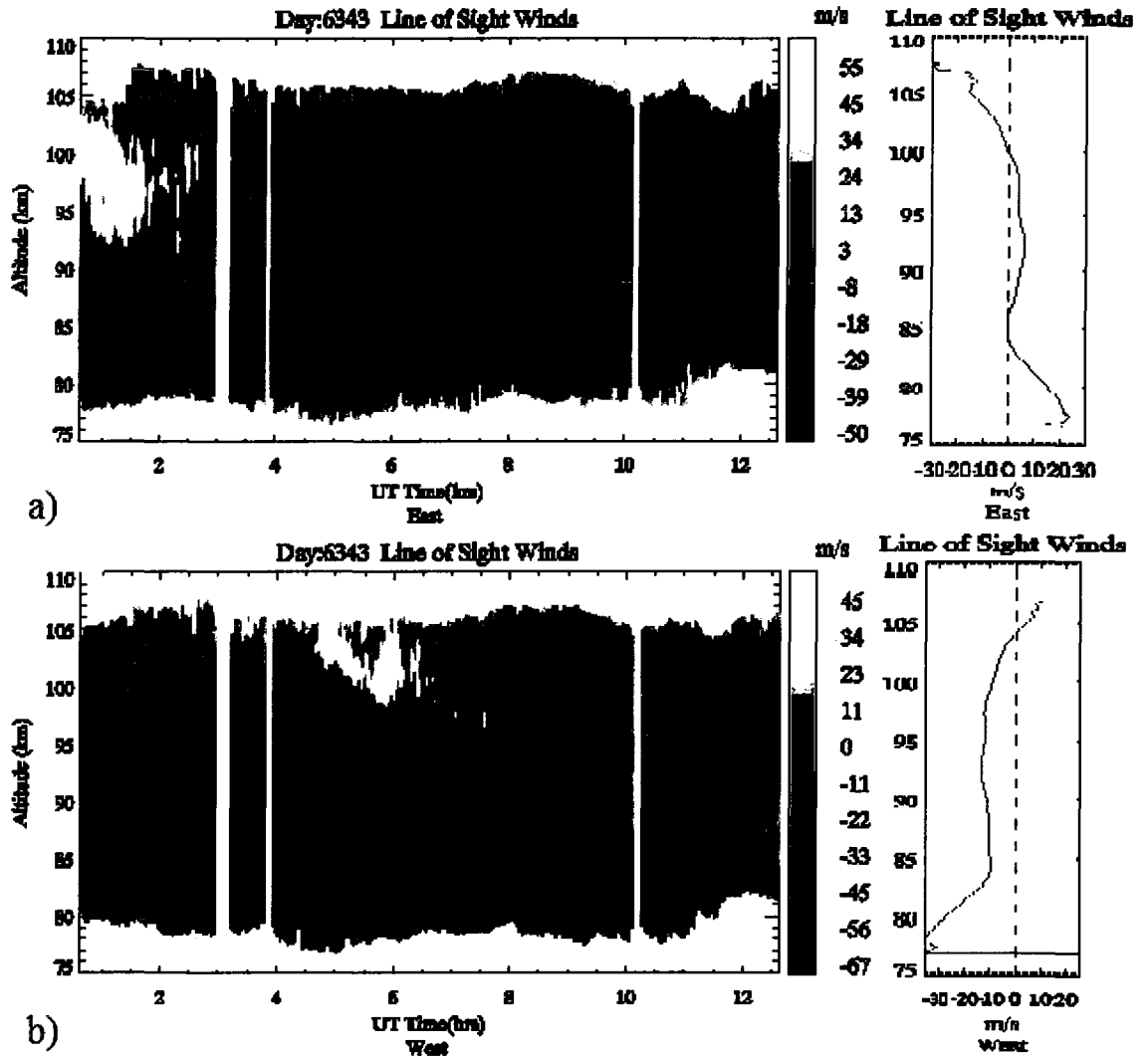


Figure 5-2. Line of sight velocities are measured with two telescopes pointing at 20° from zenith in the a) East and b) West cardinal directions. Note that the winds in each channel are approximately of the same magnitude and of opposite sign; this is due to observations at opposite angles from zenith.

5.1.1 Chirp Calculation

Doppler line-of-sight (LOS) winds were measured in the East (Figure 5-2a) and West (Figure 5-2b) cardinal directions 20° from zenith. Because the beams are pointing at different directions in the East-West plane the beams are recording opposite sign in the large-scale Doppler shifted zonal winds. Therefore, the nightly averaged LOS winds should be nearly mirror images of each other. The East and West LOS winds are averaged for the night (Figure 5-2 a and b, far right) to aid in a direct comparison. While

the shape of the averaged nightly winds are near reflections of each other, their reflection is not symmetric about 0 ms^{-1} ; therefore, the magnitudes are not equal and opposite. A transmitter frequency chirp will introduce an altitude independent fictitious Doppler shift in the LOS wind measurement in all channels that is relatively constant throughout the night. The amount of Doppler shift this chirp induces into the measurement can be quantified.

By taking a time average of the signals through the entire night it is assumed that most gravity wave perturbations between the dual beams are equally smoothed and, except for the chirp, should yield the same magnitude of winds in both channels. Equations 3.16 and 3.17 are written to include the unknown system chirp due to transmitter frequency shift (equations 5.1 and 5.2),

$$\bar{v}(\theta, R) = \bar{w}(\theta, R) \cdot \cos(\theta) + \bar{u}(\theta, R) \cdot \sin(\theta) + \overline{chirp} \quad 5.1$$

$$\bar{v}(-\theta, R) = \bar{w}(-\theta, R) \cdot \cos(-\theta) + \bar{u}(-\theta, R) \cdot \sin(-\theta) + \overline{chirp}. \quad 5.2$$

Here the average over the entire night is represented by an over bar.

By adding equations 5.1 and 5.2 the nighttime mean vertical wind plus the average system chirp is resolved (equation 5.3). By subtracting the same equations the nighttime mean zonal wind is resolved (equation 5.4).

$$\frac{\bar{v}(\theta, R) + \bar{v}(-\theta, R)}{2 \cos(\theta)} = \bar{w}(R) + \frac{chirp}{\cos(\theta)} \quad 5.3$$

$$\frac{\bar{v}(\theta, R) - \bar{v}(-\theta, R)}{2 \sin(\theta)} = \bar{u}(R) \quad 5.4$$

The vertical wind averaged over one hour or more ($\bar{w}(R)$) is expected to be near zero; therefore, the apparent wind velocity due to transmitter frequency chirp may be calculated from equation 5.3 by setting the vertical wind to zero. Averaging the entire

night of data in time and over altitudes 85 to 100 km, where the atomic sodium density is highest, an estimate of system chirp of -4.5 m/s for day 343 is obtained. Prior system performance shows that frequency chirp of the transmitter is usually ~ 3.5 m/s, experiencing small discrete changes in chirp only (< 1 m/s) when there are system transients such as a dye change in the PDA or Coherent 899 seed laser. These results compare well with the needed correction measured by chirp correction sub-system (described in section 2.2.1.2) which reports a nighttime average for day 343 of +3.6 m/s.

5.1.2 Mean Flux, Mean Wind, and Tidal Wind Definitions

Since the GWs interact with the tidal harmonics and other long-period perturbations as part of the background wind system, there is a need for clear definitions regarding the winds and fluxes resulting from various possible averages. As stated in chapter 4, the 2-hour sliding window MF/ρ is calculated every three minutes from the calculated variance of the two hours of data centered about a time associated with a specific three minute profile. If all of the MF values or winds for a night are averaged the resultant nightly average is reported in brackets with a subscript N ; for example, the nightly average of MF/ρ is reported as $\langle MF/\rho \rangle_N$, or nightly average zonal wind is reported as $\langle u \rangle_N$. Variances based on this two hour window can also be reported every 3 or 5 minutes (section 5.2), and when averaged for an entire night, they are reported as $\langle \overline{u'^2} \rangle_N$, $\langle \overline{T'^2} \rangle_N$, for zonal wind and temperature respectively. An error in the 3 minute or 5 minute mean wind or temperature of $> 10 \text{ ms}^{-1}$, $> 10 \text{ K}$, or a variance calculated from LOS winds or temperature with error $> 10 \text{ m}^2 \text{ s}^{-2}$ or $> 10 \text{ K}^2$ are discarded and the value at those times and altitudes are treated as if there were no data taken at that time.

At times it is instructive to display data as a hodograph, a plot that displays vertical profiles at sequential times, marking the progression in time of a quantity. When MF/ ρ is reported in this method, the step size of the progression is set at two hours and just the single MF/ ρ value at the step time is used with no averaging other than the initial MF/ ρ calculation. The reason for this is simple; the variance calculation, from which the MF/ ρ is calculated, is already an averaging calculation over a two hour window. However, other terms, such as zonal wind or temperature, are averaged from half the distance before and after a time step and reported as a mean value at the time step. For example, a vertical profile of the zonal wind reported at 4 UT with a step size of 2 hours would average the zonal wind from 3 UT until 5 UT and report this value as $\langle u \rangle_{2hr}$ at 4 UT.

MF/ ρ , and the related variances in section 5.2, are alternatively calculated with a method of analysis and definition of outliers that allows a direct comparison to another published long term sodium lidar MF/variance study, Gardner and Liu (2007) (G&L). First, 3 minute radial wind and temperature data with the calculated error due to photon noise larger than 10 ms^{-1} or 10 K were discarded. Data at those times and altitudes are not reported, as if no data were taken at those times and altitudes at all.

G&L, at each altitude and for each channel, subtract the linear trend (in time) of the entire night of data from their respective LOS wind and temperature data profile. G&L analyze their data in this manner in an attempt to eliminate potential biases associated with gravity waves whose periods exceed that of the individual night observation period. For example, if a night of data were 5 hours in length that would correspond to 5 hour observation period, if it were 10 hours in length that would

correspond to a 10 hour observation period, and so on. The mean of the resultant set is calculated. Perturbations in the resultant set which exceeded three standard deviations from the nightly mean were deemed as outliers and discarded. This linear fit and outlier removal process was repeated iteratively on the reduced data set until no outliers are present. The intent of this iterative procedure is to eliminate outliers and perturbations associated with gravity waves whose periods are longer than about twice the observation period. However, as noted in section 4.1, this method most likely does not remove the perturbations from the semidiurnal tide, depending on the length of an individual night of data, and defining and the removal of data three standard deviations from the mean, for no other reason, may remove valid data. Again, it is stressed that data is analyzed this way solely to allow a direct comparison to G&L. With the resulting reduced data set, the variance is calculated. This method reports one variance value, at each altitude, for an entire night of data. These values are reported in parentheses with a subscript n for example $(MF/\rho)_n$, and $(\overline{u'^2})_n$ are used for the nightly MF/ ρ and zonal variance respectively.

Our observations of temperature, zonal and meridional winds during a 24-hour interval at a given altitude, centered at the hour in question, may be fitted to the sum of a constant plus diurnal and semidiurnal harmonics as,

$$A + \sum_{i=24,12} C_i \cos\left(\frac{2\pi}{i}t\right) + S_i \sin\left(\frac{2\pi}{i}t\right) \quad 5.5$$

Equation 5.5 is stepped through the data one hour at a time, yielding a sliding mean, diurnal and semidiurnal component associated with each hour. The fit may also be expressed in terms of with the amplitude and phase (indicating the time of wave crest) of a cosine function as,

$$A + \sum_{i=24,12} A_i \cos\left(\frac{2\pi}{i}(t - \phi_i)\right). \quad 5.6$$

Five best fit parameters are generated, the 24-hr and 12-hr tidal amplitudes (A_{24} , A_{12}), 24-hr and 12-hr tidal phases (ϕ_{24} , ϕ_{12}), and the mean state (A). The diurnal and semidiurnal tidal and mean winds for a given UT day are simply the five parameters evaluated at 1200 UT of the day in question from equation 5.5, and the corresponding tidal amplitudes and phases are the transformed parameters given in equation 5.6. Due to GW and PW (planetary wave) influences, the mean state and tidal components vary in time as we perform the sliding tidal fit for each hour of the data set. A new tidal reconstruction that is performed each hour from these five changing parameters, including the mean wind, creates the daily running tides (RS); this is sometimes called the hourly sliding reconstructed tide. Therefore the daily running tidal winds in the zonal direction are expressed as U[RS]. When equations 5.5 and 5.6 are used for the entire data set, not just the 24 hours about a single hour, it is called the data set reconstructed tide (RecT). By comparing the daily running tide with the data set reconstructed tide we can see how the tide varies in time, due to GWs and PWs, with respect to the average tide of the entire data set.

5.1.3 Momentum Flux and Mean Winds

Momentum flux is analyzed for day 343, 2006 with a 2-hour sliding window (section 4.1.1). An east and west LOS wind variance is calculated every three minutes for an entire night of data. From these measured variances MF/ ρ is calculated (equation 3.25) also, every three minutes. We display the east and west variances and MF/ ρ as contour plots in Figure 5-3 top, middle and bottom, respectively. To the right are the nightly

averaged values of the data in the contour plots to the left ($\langle \overline{v_E'^2} \rangle_N$, $\langle \overline{v_W'^2} \rangle_N$, $\langle MF/\rho \rangle_N$, respectively).

The variance is off scale in the region above 97 km from ~ 2 UT until ~ 8 UT for the East beam and above 98 km and in the same time range for the West beam. An examination of the error in this region reveals that the error in the LOS wind is low and the variance is likely due to the natural variability of the atmosphere. Also of note is the large variance in the west beam at 95 km from 4 to ~ 8 UT that is not seen in the east beam. Simple theory shows that these kinds of responses in the LOS variance can occur if the phase fronts of a gravity wave packet are nearly aligned with the respective beam direction or if the GW is only observed in one of the beams. These very different variances create a dramatic increase in the apparent MF/ρ values (Figure 5-3, bottom) at these times.

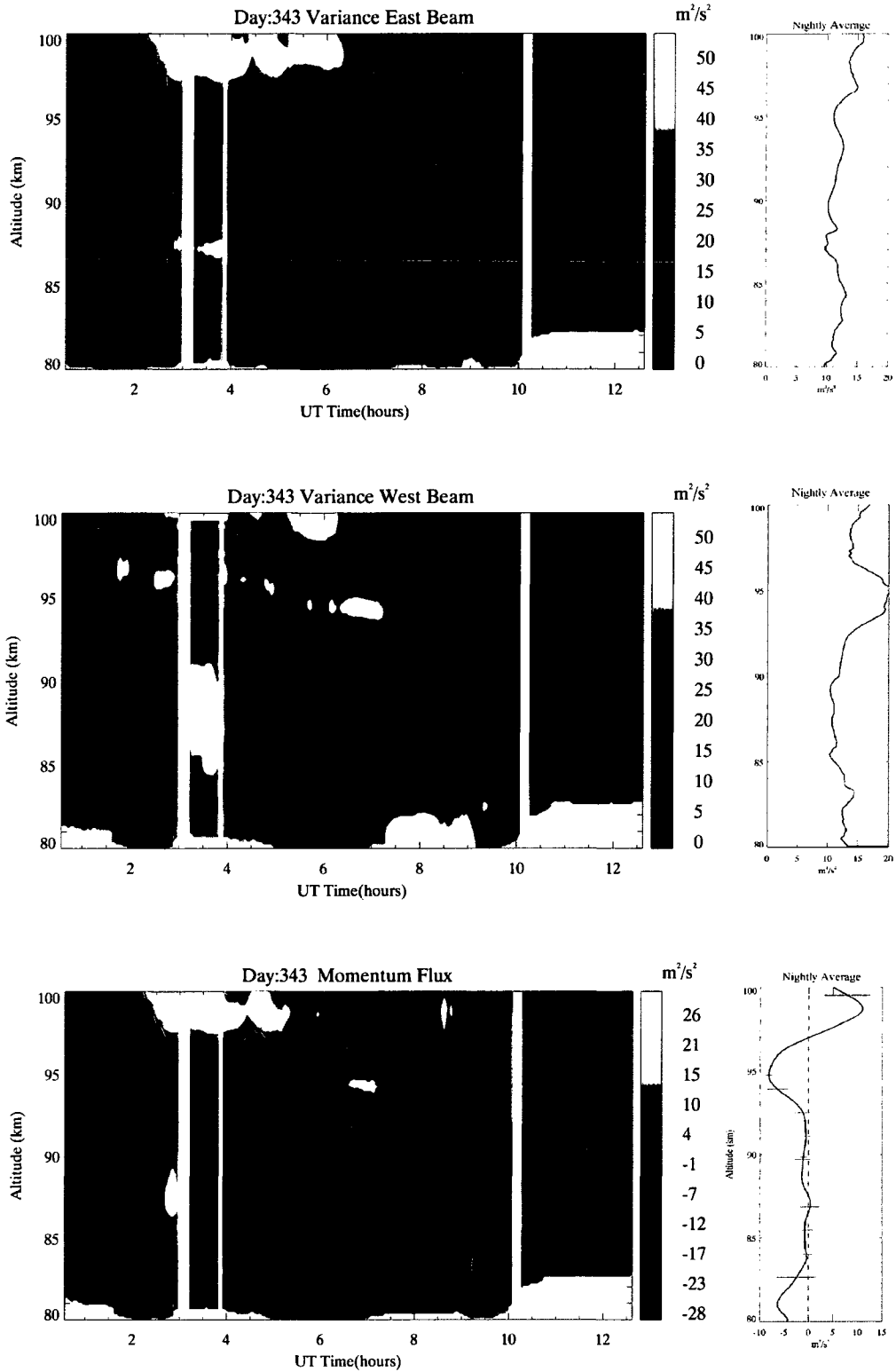


Figure 5-3. The east and west LOS wind variances and MF/ ρ for day 343 with two-hour analysis window, respectively (top), (middle), and (bottom). The zero value for MF/ ρ contour is delineated by a black line.

To further examine this event the LOS winds are filtered with two different band-pass filters. These filters pass motions with periods between 15 minutes to one hour (Figure 5-5, left) and one hour to two hours (Figure 5-5, right) and suppress the amplitudes of motions with periods outside the range. The reader is reminded of the equation for boxcar smoothing (equation 4.11),

$$R_j = \begin{cases} \frac{1}{n+1} \sum_{i=0}^n v_{i+j-\frac{n}{2}}, & j = \frac{n-1}{2}, \dots, N - \frac{n+1}{2} \\ v_j, & \text{otherwise} \end{cases} \quad 5.7$$

Where n is the window width of data points in the window. When used as a band pass filter it is the upper bound that is used for n . For example, for the 15 minute to one hour filter $n=20$ and for the one hour to two hour window $n=40$. R_j is the resulting smoothed winds. The smoothed winds are point by point subtracted from the original data set removing the slowly oscillating waves and leaving only the high frequency waves. This functions as a high pass filter, passing waves with periods less than the band pass filter upper bound and is expressed as,

$$A_j = v_j - R_j. \quad 5.8$$

Equation 5.7 is again employed to filter motions with periods less than the band pass filter lower bound.

$$W_j = \begin{cases} \frac{1}{n+1} \sum_{i=0}^n A_{i+j-\frac{n}{2}}, & j = \frac{n-1}{2}, \dots, N - \frac{n+1}{2} \\ A_j, & \text{otherwise} \end{cases} \quad 5.9$$

Where n is now the window width of data points for the lower bound of the window. For the 15 minute to one hour window $n=5$ and for the one hour to two hour window $n=20$. W_j is the resulting band pass filtered wind. This boxcar filter only weakly

dampens amplitudes outside the chosen frequency domain but it is sufficient to observe the wave activity in the stipulated observation window. Figure 5-4 is a plot of the normalized filter function generated with equations 5.7 through 5.9 for the two selected filters described above. The plot depicts the normalized amplitude of a monochromatic waveform (y-axis) of a given period (x-axis). The plot is normalized to one because the same filter is applied equally to both channels, east and west, for a qualitative comparison between the two channels.

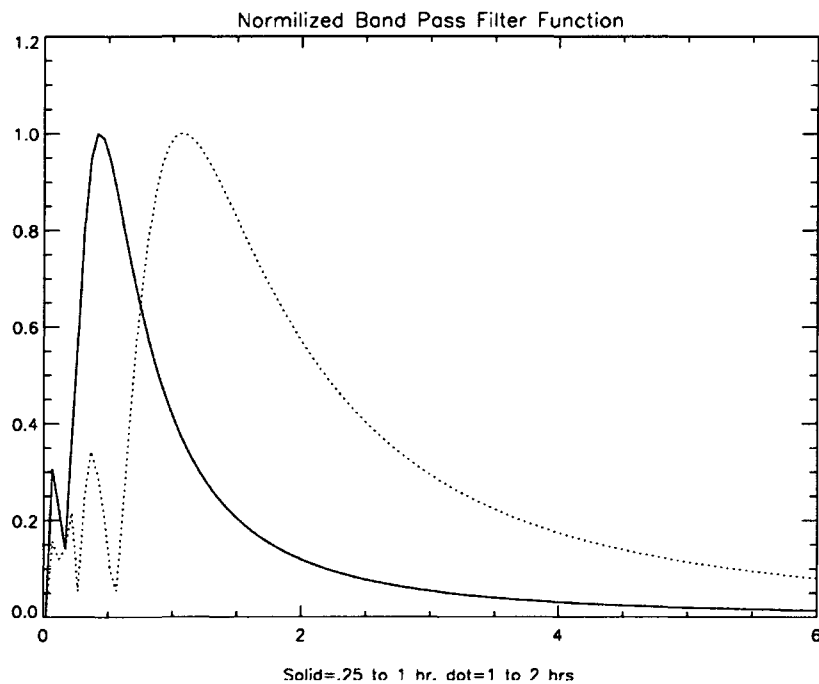


Figure 5-4. The filter function for the .25 to 1 hour filter (solid) and 1 hour to 2 hour filter (dots).

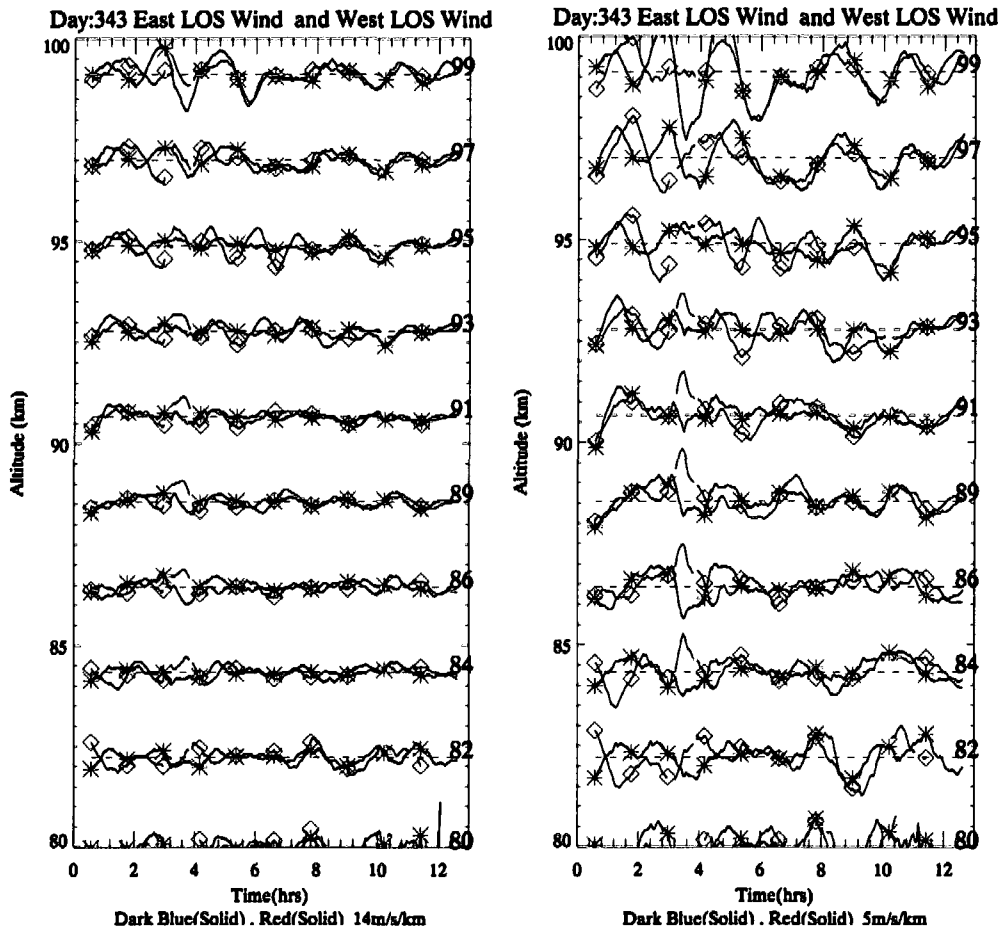


Figure 5-5. The east and west LOS winds are displayed in a time series (y-axis) at different altitudes noted on the right. To highlight the differing wave periods and amplitudes observed in each channel we plot the LOS wind after applying a band pass filter, passing motions 1/4 hour to 1 hour for the left plot and 1 hour to 2 hour motions for the right plot. East LOS wind is blue and West LOS wind is red.

In the left plot of Figure 5-5, wave-like motions with peak to peak amplitudes of ~ 10 to 15 ms^{-1} and ~ 1.5 hour period are clearly seen in the west channel (red) from ~ 2 UT until ~ 7 UT at: 93 km, 95 km and 97 km, which are not seen in the east channel (blue). Recall that in the analysis of photon files to obtain wind speeds, the smoothing in altitude is over a 2 km; therefore measurements 4 km apart share no data in smoothing and data 2 km apart share little data due to the weighting function of the Hamming window. Note that although the filter suppresses the amplitudes of periods outside the

filter width, oscillations near the cutoff period are not fully suppressed, as shown by the ~ 1.5 hour period wave seen in the $\frac{1}{4}$ hour to 1 hour filtered data.

In the right plot of Figure 5-5, at 99 km, wave-like motions with peak to peak amplitudes of ~ 20 to 25 ms^{-1} are clearly seen in the east channel (blue) from ~ 2 UT until ~ 4 UT and they are not seen in the west channel (red). This wave action in the LOS data seen in one channel but not the other is at the same altitude and same time as the noted differences in the calculated variances and resulting MF/ρ plotted in Figure 5-3.

Figure 5-6 plots vertical profiles of the 2-hour mean zonal wind (red, \times) and MF/ρ (blue, $+$) spaced at two hours apart at a given time (dotted line). To further appreciate the overall picture of the nightly interactions, the associated MF/ρ (nightly average) and zonal wind (nightly average) are plotted to the right.

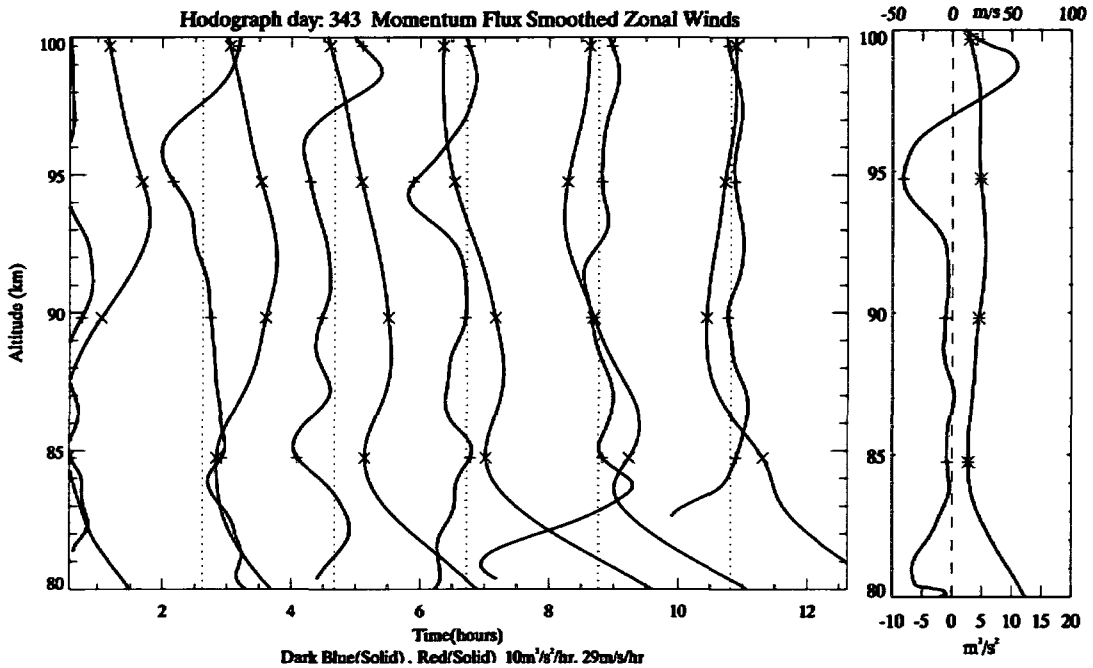


Figure 5-6. Profiles of MF/ρ (blue, $+$) is plotted every 2 hours with 2 hour average zonal winds $\langle u \rangle_{2\text{hr}}$ (red, \times). To the right is the $\langle \text{MF}/\rho \rangle_N$ and zonal wind $\langle u \rangle_N$ nightly means. The scale for the hodograph to the left is, $\text{MF}/\rho: 10 \text{ m}^2/\text{s}^2 = 1 \text{ hour}$, Zonal wind 2-hour mean: $29 \text{ m/s} = 1 \text{ hour}$. The scales for the nightly means are annotated, on the bottom for MF/ρ , and on the top for zonal wind.

Since GWs are intermittent with various sources that can cause different phase speeds, wavelengths, and group velocities, the expected negative correlation between mean state and MF does not necessarily exist throughout the entire night or through all altitudes (Holton, 1992).

If we look at the temporal evolution of MF/ ρ and 2-hour averaged zonal wind (Figure 5-6), it is apparent that MF/ ρ and the 2-hour averaged zonal wind are mostly anti-correlated. Most notable in this regard is the progression of the 2-hour averaged zonal wind from ~ 2 UT until ~ 8 UT from 90 km to 99 km and the nearly anti-correlated behavior of the MF/ ρ at the same times and altitudes (Figure 5-6).

5.1.4 Stability

In a continuation of the case study of day 343, atmospheric stability is now addressed. The study of atmospheric stability can lend to insight into possible wave breaking events. There are two types of atmospheric instability discussed here: dynamic instability and convective instability, discussed in terms of Brunt-Väisälä frequency, and Richardson number, respectively.

Recall that the Brunt-Väisälä frequency (N) is the maximum frequency at which a parcel of air can oscillate due to gravity in a stably stratified atmosphere (section 3.1).

$$N^2 = \frac{g}{T} \left(\frac{\partial T}{\partial z} + \frac{g}{c_p} \right) \quad 5.10$$

When N^2 is positive the atmosphere is assumed to be statically stable, and will support un-attenuated gravity wave propagation; when negative, the region is said to be statically unstable, and propagating waves will undergo convective overturning to become stable, and therefore, some wave energy will be dissipated and may, in turn, create turbulent eddies.

The Richardson number (Ri) is commonly (some suggest wrongly) used to gauge the dynamic stability of the atmosphere. Observations suggest that a Ri less than $\frac{1}{4}$ is a necessary but not sufficient condition for dynamic instability (Dutton, 1986). However, recent simulations in GW instability dynamics show that in atmospheric regions with a large Reynolds number, even if Richardson number is greater than $\frac{1}{4}$, the atmosphere can be dynamically unstable (Fritts, Vadas, Wan and Werne, 2006). The Reynolds number is used to characterize the relative effect of inertial forces and viscous forces (Fetter and Walecka, 1980) and Ri is defined (Holton, 1992) as,

$$Ri = \frac{N^2}{\left(\frac{\partial u}{\partial z}\right)^2 + \left(\frac{\partial v}{\partial z}\right)^2}. \quad 5.11$$

Here the zonal wind (u) is obtained by equation 5.4 and the meridional wind (v) is obtained as the projection on the meridional axis of the measured north beam that is pointing 30° north of zenith. Unlike the zonal wind measurement with 3 minute averaging, there is 15 minute temporal averaging for the meridional measurement due to smaller telescope size. Linear interpolation is used in this calculation to fill in missing data points. On day 343, the zonal and meridional winds are of similar magnitude.

It is important to note that while a low Ri and a negative N^2 do indicate a region of potential instability, the converse, large Ri and positive N , do not necessarily ensure stability. New studies (Fritts, Vadas, Wan and Werne, 2006) have revealed that wave-wave interaction and large wave amplitudes can cause instabilities and wave breaking in regions of the atmosphere that have high values of Ri (>1) and positive N^2 .

Figure 5-7 illustrates the calculated stabilities observed in the atmosphere with hodograph with a one hour separation of N^2 (lines) and Ri (dots). Regions of suspected convective instability, with a negative N^2 , show up on Figure 5-7 as red +'s (i.e. 4 UT to

10 UT at ~90 km to ~80 km). Regions where the Ri is less than $\frac{1}{4}$, indicating potential dynamic instability, show up on Figure 5-7 as yellow \times 's (i.e. ~2 UT at ~103 km).

Figure 5-7 suggests that there are more regions of convective instability than regions with Ri less than the $\frac{1}{4}$ during the observation period.

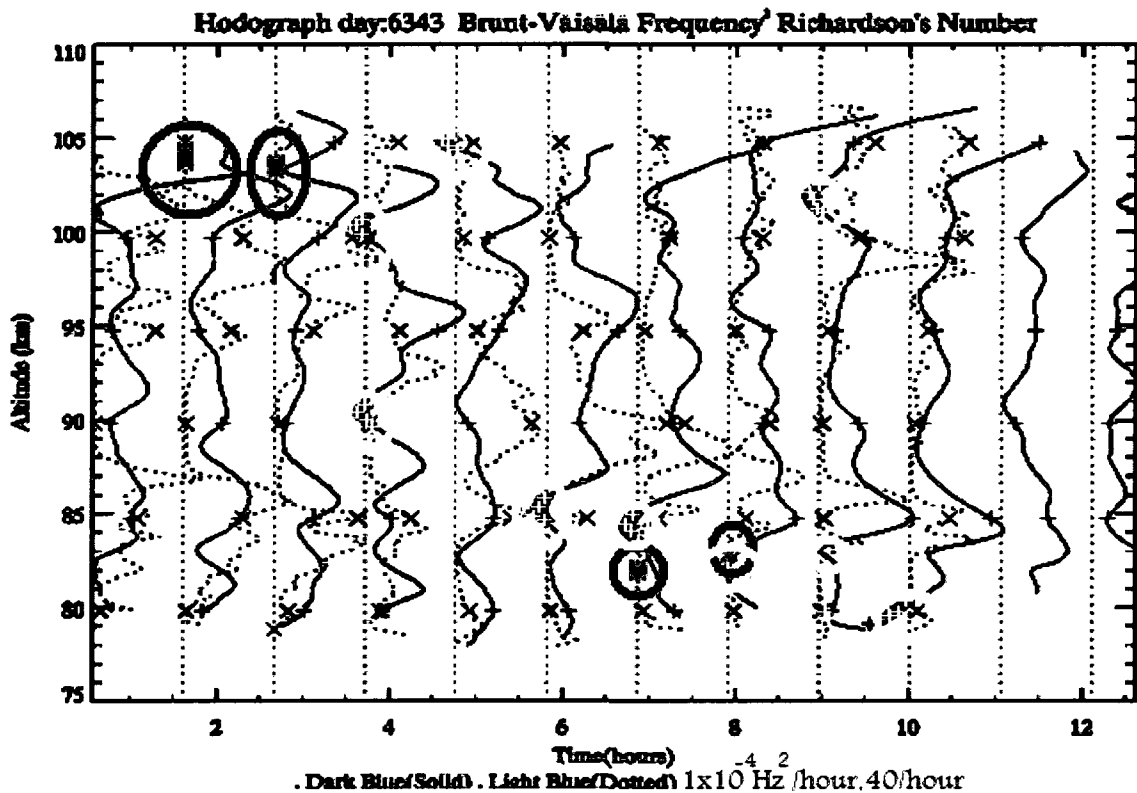


Figure 5-7. BV frequency (lines,+) and the Richardson's (dots, \times) number are plotted by use of equations 5.5 and 5.6 respectively. Both values are a measure of stability in the atmosphere. A negative N^2 (yellow + and circled in yellow) suggests a convectively unstable region, while a Ri less than $\frac{1}{4}$ (red \times and circled in red) is regarded by some as dynamically unstable. No Richardson number after 10 UT is reported due the large measurement error reported in the North channel (Figure 5-8).

Analyses on the occurrence frequencies based on year-long data sets showed comparable convective and dynamic instabilities from observations in Starfire Optical Range, NM (Zhao et al., 2003), and more dynamic instabilities from observations in Maui, HA (Li et al., 2005) and in Fort Collins, CO (Sherman and She, 2006). Note that

while these statistics depend on the atmospheric dynamics, they also depend on individual system measurement uncertainties and averaging.

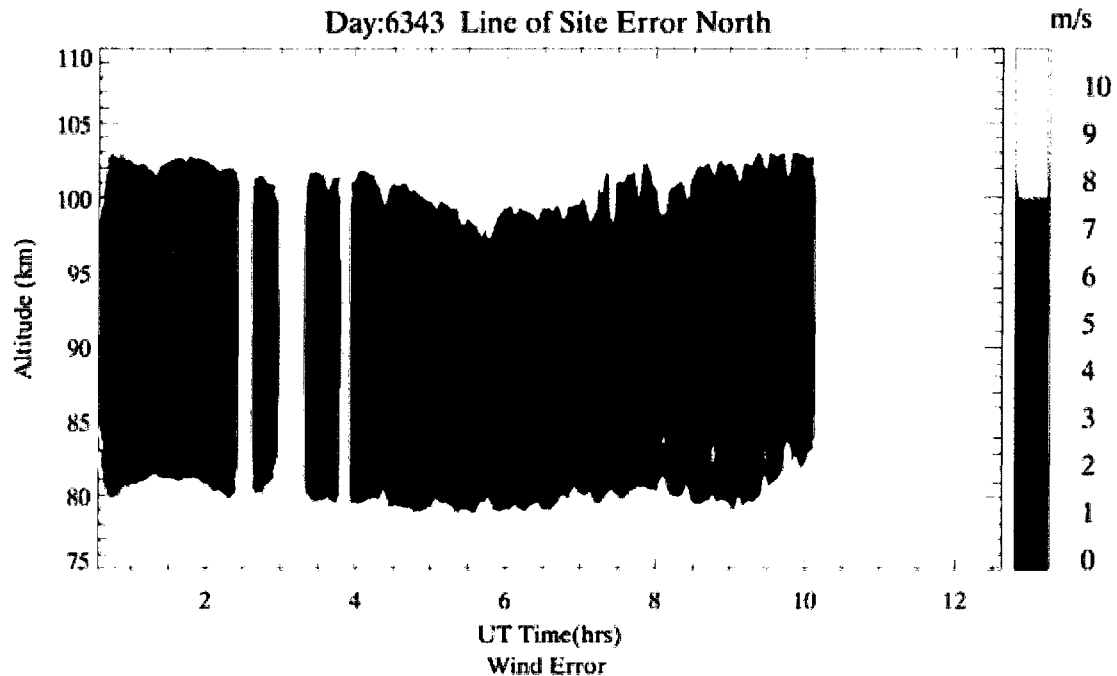


Figure 5-8. A plot of the calculated error in the line of site wind signal for the North beam shows the error near 102 km to be changing rapidly and nearing 10 m/s. Such a large error would not allow an accurate *Ri* measurement and is not considered valid.

The gradient of measurement uncertainty, due to photon noise in the North channel, is large at almost all altitudes (Figure 5-8) due to a smaller receiver area; this steep gradient in the error makes estimates of *Ri* uncertainty difficult. Averaging the LOS winds in the North channel for one hour would reduce the error of *Ri* uncertainty to <0.25 , but such averaging may be too long to make the measurement meaningful. It is highly unlikely that an unstable atmosphere would remain in a state of instability at the same altitude for greater than an hour. Even with this data, day 343 has a region of *Ri* that lasts from ~ 4 UT until ~ 10 UT but the altitude of the region changes from 90 km to ~ 80 km over the same period. An estimate of *N* uncertainty in this region is $\sim 1 \times 10^{-2}$ Hz, which is calculated by propagation of error. All instability calculations use only the east channel for their temperature measurement.

5.1.5 Nightly Averages of MF/ρ and comparison with mean and tidal winds

In addition to comparison of the nightly averaged MF/ρ ($\langle MF/\rho \rangle_N$) and the nightly averaged zonal wind ($\langle u \rangle_N$) (Figure 5-6), it is instructive to evaluate associated correlations of $(MF/\rho)_n$, the nightly average sliding tidal wind amplitude ($(A_{24})_N, (A_{12})_N$) as well as the mean wind (A_N). These comparisons will provide an overall characterization of the mean dynamical influences in the MLT region.

The reader is reminded of the distinction between the two types of nightly averages, $\langle MF/\rho \rangle_N$ and $(MF/\rho)_n$ (section 5.1.2). $(MF/\rho)_n$ is MF/ρ calculated with the repetitive process of fitting the entire night of data to a linear model and subtracting the linear fit from the initial data; this removes long period waves. After the linear fit subtraction, data three standard deviations from the mean of the resultant are removed. The resulting data is again fit to a linear model and the fit is subtracted from the data and outliers are removed. This iterative process continues until there are no more data points determined to be ‘outliers’. After the linear fit subtraction and repetitive removal of outliers, the variance is calculated for the entire night of data. This analysis allows a direct comparison of data obtained with the CSU lidar to the data obtained with the Starfire lidar (Gardner and Liu, 2007). $\langle MF/\rho \rangle_N$ is the average of the MF/ρ values calculated with a two hour window, filtering long period motions from the data.

Figure 5-9 provides a comparison between the G&L method and $\langle MF/\rho \rangle_N$ in a continuation of the case study of day 343. $(MF/\rho)_n$ contains, in addition to the momentum fluxes of waves with periods between 6 minutes and 2 hours contained in $\langle MF/\rho \rangle_N$, the contribution from motions with periods longer than 2 hours but less than

the length of the night, which was 11.5 hours for day 343. The mean length of the night for data in the yearlong study is 9.4 hours.

GWs are intermittent with various sources that can cause different phase speeds, wavelengths, and group velocities and since the atmosphere is a dynamically changing environment, the expected negative correlation between $(u)_N$ (Figure 5-9, red dash dot, \diamond) and MF/ρ does not necessarily exist throughout the entire night nor through all altitudes; but in fact, for day 343, $\langle MF/\rho \rangle_N$ (Figure 5-9, blue line, +) and $(u)_N$ do exhibit the expected negative correlation between 80 km to 97 km. Furthermore, $(u)_N$ and $(MF/\rho)_n$ (Figure 5-9, light blue dots, *) also show negative correlation through most altitudes, and when they do not (86-94 km) $\langle MF/\rho \rangle_N$ and $(u)_N$ show negative correlation. Furthermore, Figure 5-9 suggests MF/ρ , averaged over the entire night, provides a body force that reverses the zonal wind at higher altitudes (~103 km here); this is consistent with the closure of the mesospheric jet.

Also included in Figure 5-9 are semidiurnal (light green, dots, \times), and diurnal (peach, long dash, \square) tidal amplitudes, and mean winds (orange, dash dot dot, Δ) which are computed from the nightly averaged terms generated by the sliding tidal fits (equation 5.6) described in section 5.1.2. The exponential-like growth in the semidiurnal amplitude does suggest a lack of interaction between the current GW spectrum and the semidiurnal tide; however, tidal modal structure, the mean wind, diurnal tide, global waves and the state of the atmosphere below the measurement all play a role in the apparent semidiurnal tidal amplitude, thereby preventing a definitive statement about this apparent lack of interaction. Furthermore, the lack of an exponential growth in the diurnal

tides amplitude could be from GW-tidal interaction, but as with the semidiurnal tide, other factors could impact the diurnal tide amplitude.

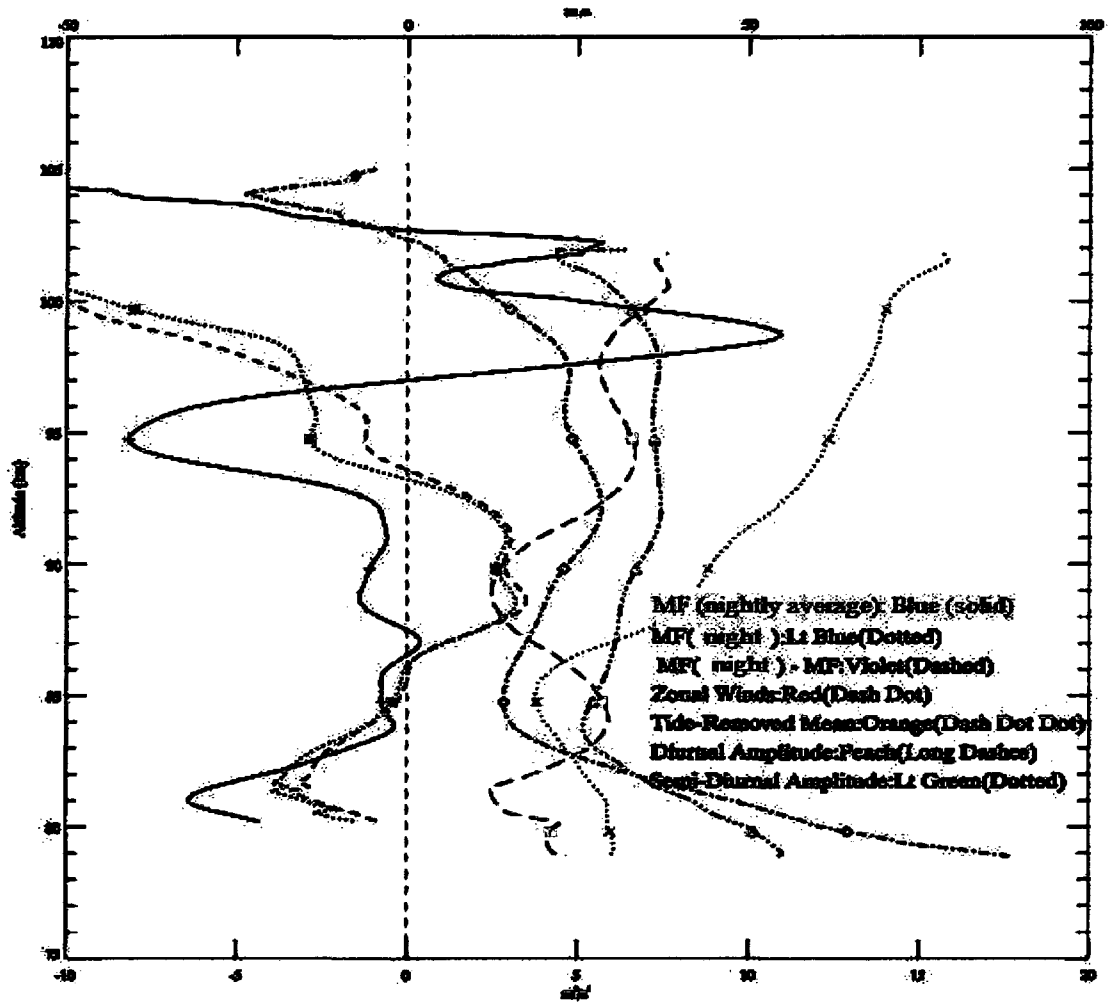


Figure 5-9. $\langle MF/\rho \rangle_N$ (Blue solid) is compared with $(MF/\rho)_n$ (Lt. Blue dots), and their difference (dots – solid = violet dash), $(u)_N$ (Red dash dot), mean wind $(A)_N$ (Orange dash dot dot), and the tidal amplitudes $((A_{24})_N, (A_{12})_N$, Peach long dash and Lt Green dots, respectively). $(A_{24})_N$ and $(A_{12})_N$, for day 343, are based on thirteen sliding tidal fit amplitudes for the 24 hr, 12 hr, tides. Note: $\langle MF/\rho \rangle_N$ uses the bottom scale (-10 to 20 m^2s^{-2}); all others use the top scale (-50 to 100 m^2s^{-2} for MF and ms^{-1} for all others).

The violet dashed line $((MF/\rho)_n - \langle MF/\rho \rangle_N)$ suggests that a significant, and sometimes dominating, contribution to $(MF/\rho)_n$ between 87 km and 93 km could be from waves with periods longer than two hours.

Figure 5-10 is a plot of the LOS winds; the left plot is filtered (section 5.1.3) to pass motions greater than 2 hours and less than 6 hours and suppress the amplitude of motions outside that range, the right plot is filtered to pass motions with periods greater than 6 hours and less than 8 hours. In the left plot two wave motions are clearly seen at 88 km and 92 km the west channel (Figure 5-10, red, \diamond) appears to be a combination of a 12 hour period wave, which we assume to be the semi diurnal tide, and a ~ 4 hour wave, while the east channel (Figure 5-10, blue, $*$) does not exhibit the ~ 4 hour period oscillation.

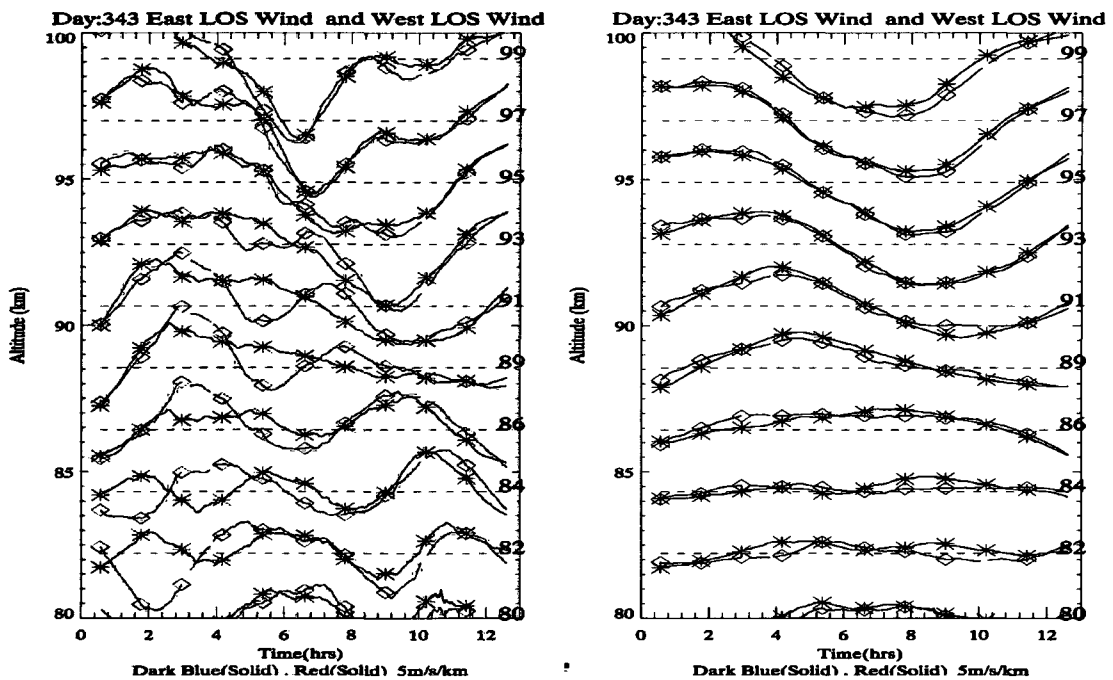


Figure 5-10. This is a plot showing the LOS wind filtered to pass motions with periods greater than 2 hours but less than 6 hours on the left and 6 to 8 hours on the right. At the 88 km and 92 km altitudes a comparison is made between the east (blue, $*$) and west (red, \diamond) LOS winds and there is a ~ 4 hour wave with an amplitude of ~ 10 m/s seen in the west channel that is not seen in the east channel; however, the right plot shows a larger amplitude in the east channel from the longer period wave seen in both channels.

However, the more wave motion seen in the west channel than the east channel on Figure 5-10 left are associated with larger negative MF (equation 4.4), and as seen in Figure 5-9, at this altitude and with this filtering the MF is more positive for the nightly

linear fit than that of the two hour sliding window; this suggests that $(MF/\rho)_n$ must be biased by an even longer period wave. When the LOS wind is analyzed to pass waves greater than 6 hours and less than 8 hours (Figure 5-10, right), we can see larger wave amplitude in the east beam than the west. This longer period wave of about a 12 hour period must overwhelm the contribution of negative MF due to the ~ 4 hour GW, and other higher frequency oscillations at 88 to 92 km. The contribution to $(MF/\rho)_n$ from this 12 hour period wave is non-negligible.

5.2 Measurement Statistics

The lidar observations were conducted at Colorado State University Foothills campus in Fort Collins, CO from late September 28th 2006 until April 29th 2007. Statistics are generated from 29 nights of observations with an average of 9.4 hours of observations per night (Table 4, p144). We report temperature variance (T'^2), zonal (u'^2) and meridional (v'^2) wind variance and momentum flux measurements. Data from September 28th, 2006 until November 8th, 2006 were obtained from photon files with a 150 m vertical binning and 2 minute integration. Data are further smoothed with a Hamming window 2 km FWHM in the vertical and 5 minute smoothing for MF, u'^2 , and T'^2 and 15 minute smoothing for the temporal resolution of v'^2 . Data obtained from November 8th, 2006 through April 29th, 2007 were obtained with a 150 m vertical binning and 1 minute integration period, and are further smoothed to 2 km and 3 minutes, and still 15 minute smoothing for v'^2 . These profiles include the perturbations associated with gravity waves having vertical wavelengths longer than 2 km and observed periods longer than 10 minutes before November 8th, 2006 and 6 minutes after in the zonal direction, and 30 minutes in the meridional direction. The data include much of the important

higher-frequency gravity waves with periods between 6 minutes and 2 hours that are thought to contribute up to $\sim 70\%$ of the momentum flux (Fritts and Vincent, 1987). All data with measurement error greater than 10 ms^{-1} in the LOS wind or 10 K in temperature are discarded for the variance and subsequent MF calculation.

To allow a direct comparison to G&L and to report values where the signal is the greatest due to a higher sodium density, all data in this section are averaged over the region 85 to 95 km. The average calculated LOS wind and temperature measurement error between 85 and 95 km is about 2.1 ms^{-1} and 3 K, respectively. The 1-mrad pointing accuracy of the lidar, which was limited by the divergence of the laser beam and the field-of-view of the detector, is much more accurate than corresponding radar observations with inherent side lobe effects.

Like the momentum flux, the wind and temperature variances are calculated similarly in two ways: in the method of G&L, 2007, described in section 5.1.5, and with a sliding two hour window, described in section 4.1.1. The former method of analysis is used to allow a direct comparison to a published long term sodium lidar variance study, G&L, 2007 and an earlier study Gardner and Yang, (1998). Only nighttime variances and MF are averaged to provide a direct comparison to the Starfire results reported by G&L. It may be helpful to the reader, and in the effort of clarity, to highlight and contrast several points about these two methods.

Both studies of G&L and Gardner and Yang were performed at the Starfire Optical Range near Albuquerque, New Mexico. The studies have one 3.5 m transceiver and point it to different directions in the sky according to a pattern. In the normal operation mode, the lidar was pointed at zenith (Z) and 10° off-zenith to the north (N),

south (S), east (E), and west (W) in the following sequence: ZNEZSW. At each position, temperature and line-of-sight (LOS) wind profiles were obtained at 500-m vertical and 90-s temporal resolution. CSU lidar constantly monitors the north (N) east (E), and west (W) directions at N 30° from zenith and the E and W beams 20° from zenith.

Colorado State University employs two .75 m transceivers pointing east and west 20° from zenith and a third .35 m transceiver pointing north 30° from zenith. These transceivers do not move from their respective pointing direction. Temperature and line-of-sight (LOS) wind profiles were obtained at 150-m vertical and 60-s temporal resolution and further smoothed to 2 km vertical and 3 minutes temporal resolution for the east and west channels and 15 minutes smoothing for the north channel. Data points with photon noise errors larger than 10 ms⁻¹ or 10 K were discarded in both methods.

G&L, in an attempt to eliminate potential biases associated with gravity waves whose periods exceed the observation period, subtract the linear trend of the entire night of data, in time and at each altitude, from their respective LOS wind and temperature data profiles. Perturbations in the resultant data, that exceeded three standard deviations from the nightly mean of the resultant data, were regarded as outliers and were discarded. This linear fitting and quality control procedure were then repeated on the reduced data set. The intent of this iterative procedure is that it eliminates outliers and perturbations associated with gravity waves whose periods are longer than about twice the observation period, where the average observation period is ~7.5 hours for G&L and ~ 9.5 hours for CSU lidar.

The repetitive removal of outliers, defined as three standard deviations from the mean, is only employed with the G&L analysis method of data, and not with windowed

analysis described in section 4.1.1. Data are deemed bad in the windowed method analysis when: LOS error $>10 \text{ ms}^{-1}$ or $>10 \text{ K}$ for an individual data point or the average LOS wind error of a 2-hour window is greater than the square root of the variance of the same 2-hour window. The second culling requirement ensures that when most of the variance of a measurement comes from photon noise, it is discarded. This rarely happens for measurements between 85 km and 95 km.

Because the windowed method calculation uses the same data point multiple times in its analysis, concerns of oversampling the data and possible biases of the result have been raised. The use of the sliding window method, and subsequent averaging of an entire night of data, appears to only filter out motions with periods longer than two hours from the data. Simulation shows that when data is only comprised of oscillations of a period shorter than the 2-hour window width, the resulting night averages from the windowed method and the method employed by G&L, converge to the same variance values.

Zonal and meridional winds are calculated by projecting the LOS wind vector on the respective plane and then their variances are calculated. Due to the smaller telescope and lower transmitter power, the meridional wind measurement requires more averaging to reduce the error due to photon noise. Data are reported once every 15 minutes.

When the monthly variances are plotted their general trend and values compare well with G&L (Figure 5-11). Figure 5-11 shows higher variances in the winter season and lower values at the equinoxes. This is consistent with current theory regarding the filtering of GWs by the mean wind (Fritts and Alexander, 2003). The month of October, for CSU data, does have an elevated variance in both the zonal and meridional

measurements, but this is only one year of data (30 nights) for CSU and values and if it were collected over four years it may look more like G&L.

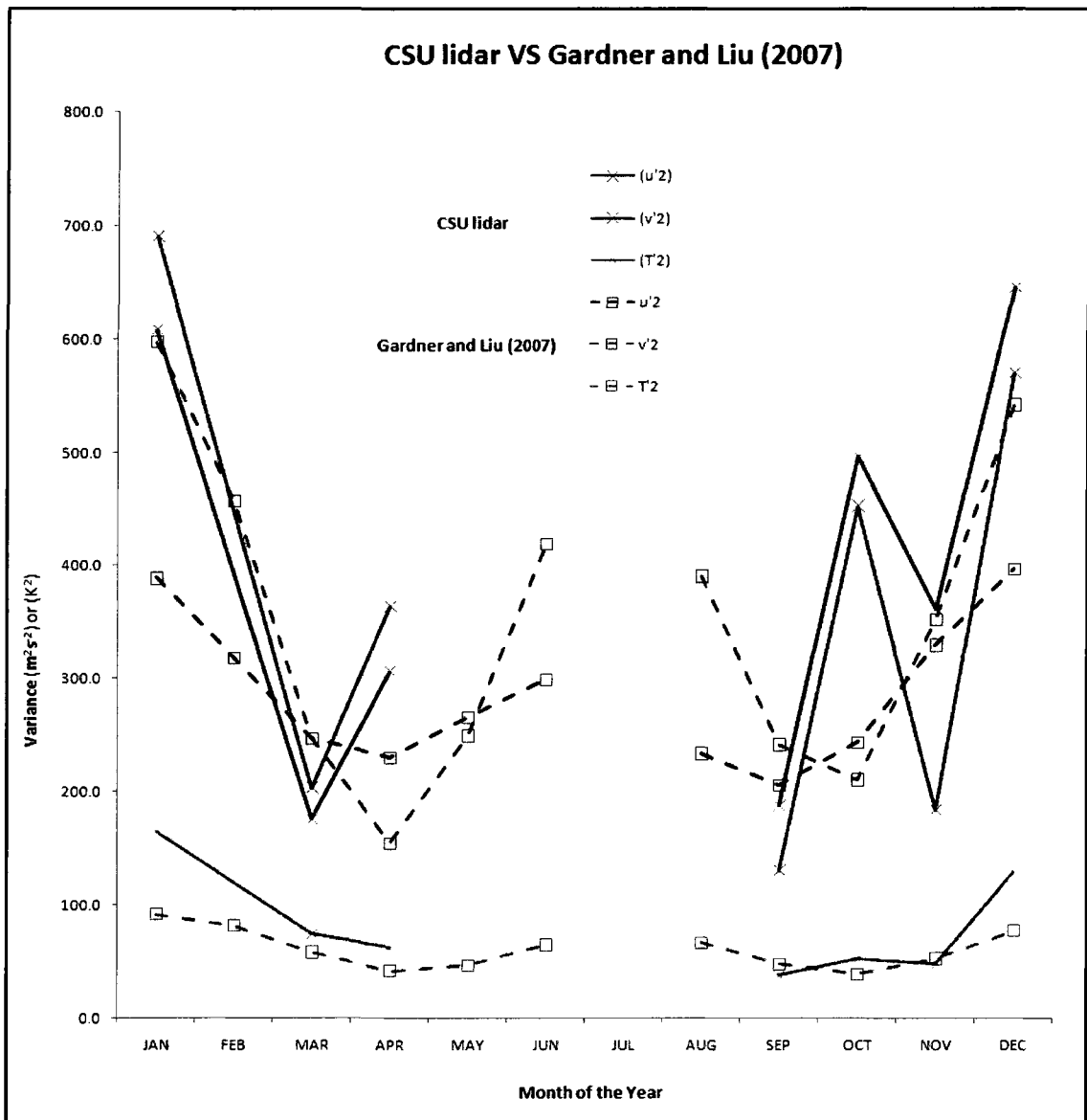


Figure 5-11. A plot breaking down variance measurements by G&L (dash, □) and CSU lidar (solid, ×) shows the generally same shape of higher wave activity in the winter months and a lowering of wave activity near the equinox. Summer data is not used due to lower sodium density causing lower signal to noise.

Both lidar systems did not collect data during July due to a low sodium density coupled with shortened nights, making Sodium lidar MF measurements impractical. CSU

lidar did not collect data in February due to poor weather, and did not collect MF/ ρ data May through August due to low sodium density and therefore low photon counts.

Table 3 details the number of observation nights (days) and observation hours (average hour) for each month during the entire study. For each month the calculated mean variance for the zonal wind $(u')^2$, meridional wind $(v')^2$, vertical wind $(w')^2$ and temperature $(T')^2$ are tabulated. The reader is reminded that that all data in this section are averaged from 85 km to 95 km in altitude. The seasonal distribution of variances in the two Gardner studies and the CSU lidar study are consistent.

The average monthly mean MF/ ρ for the CSU measurements is $-0.6 \text{ m}^2\text{s}^{-2}$ for short period motions (Table 3, top table) and $-0.7 \text{ m}^2\text{s}^{-2}$ when analyzed in the method of G&L (Table 3, second down from the top). Furthermore, the months that are negative for the windowed analysis are also negative for data analyzed in the method of G&L, suggesting consistency between analysis methods.

The G&L and CSU lidar studies are consistent with both reporting larger meridional variances than zonal variances; although the CSU results for meridional variance is only slightly larger than the reported zonal variance. If we report the results from Table 3 as a ratio of $(u')^2/(v')^2$, CSU yields a ratio ~ 1.0 and G&L is 0.79. Because of the different averaging times of 15 minutes for the meridional measurement and 5 minutes or 3 minutes for the zonal measurement, the CSU lidar may have not captured the expected variation in the meridional measurement with respect to the zonal measurement. When both the zonal and meridional winds are analyzed with the 15 minute averaging the ratio $(u')^2/(v')^2$ for CSU becomes $294 \text{ m}^2\text{s}^{-2}/372 \text{ m}^2\text{s}^{-2} = 0.79$, which is in closer agreement with G&L.

Table 3 A comparison of results from Gardner and Liu (2007), Gardner and Yang (1998) and CSU lidar extended study of MLT variance.

CSU lidar 2-hour window														
	JAN	FEB	MAR	APR	MAY	JUN	JUL	AUG	SEP	OCT	NOV	DEC	Total	Average
Number of Days	4		2	3					1	7	6	6	29	
Average Hour	12.2		10.5	8.4					8.2	8.3	8.0	10.7		9.5
Total Hour	48.8		21.0	25.3					8.2	57.9	47.9	64.4	273	39.0
MF/ρ	-0.7		0.8	0.6					-2.7	0.1	-0.8	-1.5		-0.6
(u ²)	232.7		144.9	198.1					105.1	169.7	157.3	233.7		177.4
(v ²)	231.3		54.0	174.0					121.5	157.8	111.0	172.0		145.9
(T ²) _E	28.8		21.2	25.7					18.3	14.9	13.2	24.0		20.9
(T ²) _w	24.6		18.0	28.2					19.5	14.0	13.0	24.0		20.2

CSU lidar in the method of G&L														
	JAN	FEB	MAR	APR	MAY	JUN	JUL	AUG	SEP	OCT	NOV	DEC	Total	Average
Number of Days	4		2	3					1	7	6	6	29	
Average Hour	12.2		10.5	8.4					8.2	8.3	8.0	10.7		9.5
Total Hour	48.8		21.0	25.3					8.2	57.9	47.9	64.4	273	39.0
MF/ρ	-6.1		3.5	1.9					-1.5	-1.5	-1.0	-0.1		-0.7
(u ²)	690.5		203.5	364.5					130.9	452.8	183.8	570.1		370.9
(v ²)	532.6		175.6	269.8					187.8	464.4	352.6	623.6		372.3
(T ²) _E	164.4		74.4	62.3					37.8	52.1	48.0	129.1		81.2
(T ²) _w	158.5		74.8	62.9					35.7	50.0	49.1	124.8		79.4

Gardner and Liu (2007)														
	JAN	FEB	MAR	APR	MAY	JUN	JUL	AUG	SEP	OCT	NOV	DEC	Total	Average
Number of Days	5	2	3	6	6	4		3	6	5	4	6	49	
Average Hour	9.2	8.3	7.4	6.8	6.8	6.7		5.3	6.3	8.5	6.9	8.8		7.5
Total Hour	45.9	16.6	22.3	41.0	40.9	26.7		16.0	37.5	42.4	27.7	52.6	369.7	33.6
u ²	389.0	318.0	247.0	230.0	266.0	299.0		234.0	206.0	244.0	330.0	397.0		287
v ²	597.0	457.0	247.0	155.0	250.0	419.0		391.0	242.0	211.0	353.0	542.0		363
w ²	3.2	2.6	1.6	1.8	3.7	6.2		6.1	3.7	1.9	1.8	2.7		3.5
T ²	92.0	82.0	58.3	42.0	46.9	65.0		66.8	47.7	39.2	52.7	77.8		62.2

Gardner and Yang (1998)														
	JAN	FEB	MAR	APR	MAY	JUN	JUL	AUG	SEP	OCT	NOV	DEC	Total	Average
Number of Days		3		4							1		8	2.7
w ²		5.1		4.2							2.6			3.9
T ²		47.3		117.9							28.9			64.7

A comparison of winter to equinox MF/ρ values reported in this study reveal a monthly mean value of -2.4 m²/s² for the winter months and +0.59 m²/s² during the equinox when calculated in the method of G&L, and -1.0 m²/s² for the winter months and -0.28 m²/s² during the equinox when calculated with a 2-hour window. That the G&L method yielded a difference in the magnitude of MF/ρ larger than a factor of two compared to the 2-hour window method for both seasons with the same data set suggests

that the G&L method is likely contaminated by a contribution of tidal period waves as seen in section 5.1.5. A seasonal comparison of MF/ρ with G&L is not possible as they do not break down their flux measurements in this manner. In fact, the G&L study only reports an annual mean MF/ρ ; it is more a study of heat flux and atmospheric variability than a study of MF/ρ .

Table 4 provides a summary of the MF/ρ and variance measurements obtained with CSU lidar. The sliding 2-hour linear fit (Table 4, right) reports values of two to four times lower than values obtained from G&L analysis method (Table 4, left). The error estimates are based on propagation of error due to photon counting statistics (equation 4.9) and calculated by using the standard deviation of the mean. Wind variances are in units of m^2/s^2 and temperature variances are in units of K^2 . Averages of the entire data set are noted at the bottom of the table. Statistics of MF/ρ compare well with the other reported long term study of G&L. G&L report a MF/ρ annual mean of $-1.4 \pm 0.6 m^2/s^2$; this is compared to this study's value of $-1.1 \pm 0.2 m^2/s^2$, when averaged over the same altitudes and calculated using the same method (Table 4). This study also computes MF/ρ with a sliding 2-hour window, which yields an annual mean of $-0.5 \pm 0.2 m^2/s^2$. The filtering of wind using the 2-hour sliding window analysis removes most oscillations with periods greater than two hours, including semidiurnal and terdiurnal tides, thereby concentrating on the contributions of the shorter period and higher phase speed GWs.

Table 4. A table of all momentum flux measurements, including date, number of hours of measurement, and recorded variances in winds and temperatures.

DATE	Day	Hours	CEU linear in the method of G&A (section 5.1.1)						CEU linear 2-hour window (section 4.1)													
			MF/p	err	(u^2)	err	(v^2)	err	(T^2) _e	err	(T^2) _h	err	(u^2)	err	(v^2)	err	(T^2) _w	err				
25-Sep-05	6271	8.2	-1.5	0.8	130.9	3.9	187.5	21.3	37.8	0.8	35.7	1.5	-2.7	0.6	105.1	2.8	121.5	15.1	18.3	0.3	19.5	1.9
13-Oct-06	6285	6.8	1.5	0.5	51.4	2.5	170.5	5.8	35.2	1.0	40.5	1.0	0.2	0.3	108.2	3.1	64.0	2.7	16.3	0.6	20.2	0.6
14-Oct-06	6287	9.8	-2.5	1.4	701.2	8.2	844.1	22.5	88.0	1.8	69.5	1.5	-0.6	0.8	216.0	5.3	231.9	5.0	17.2	1.4	15.2	1.2
23-Oct-06	6295	8.6	0.2	0.7	349.6	3.9	224.3	4.2	49.5	0.9	41.5	0.5	1.2	0.2	147.7	2.8	120.0	2.2	15.6	0.4	10.3	0.3
24-Oct-06	6297	9.5	1.1	1.0	586.9	5.9	248.54	8.6	56.0	1.3	56.3	1.3	1.3	0.4	201.2	4.1	212.6	4.4	14.3	0.7	15.7	0.9
27-Oct-06	6300	7.7	-0.8	1.2	701.9	6.6	348.1	7.7	22.4	0.9	26.5	0.5	-1.2	0.4	154.3	4.4	97.9	3.2	12.0	0.7	13.0	0.6
28-Oct-06	6301	5.0	-1.3	0.9	152.6	3.7	897.0	16.9	31.6	1.2	27.5	1.2	-1.3	0.5	150.8	4.9	213.4	4.6	12.2	0.7	10.5	0.7
29-Oct-06	6302	10.7	-8.8	0.9	586.3	5.2	517.5	7.6	81.9	1.3	88.3	1.3	0.5	0.4	159.8	3.6	154.5	3.1	16.4	0.6	13.5	0.5
1-Nov-06	6305	6.5	-3.3	0.5	66.4	2.1	45.0	2.7	22.9	0.9	26.5	0.5	-5.6	0.3	74.0	2.6	22.5	1.5	10.0	0.5	12.5	0.5
2-Nov-06	6305	9.4	1.9	0.5	104.2	2.5	128.1	4.3	32.9	0.9	34.4	0.5	0.5	0.5	97.8	2.9	43.2	1.8	9.6	0.7	9.0	0.6
3-Nov-06	6307	5.7	4.3	1.1	200.2	5.9	232.03	10.2	25.3	1.4	25.5	1.3	0.2	2.3	210.7	7.8	136.6	5.9	10.5	2.5	11.6	2.3
8-Nov-06	6312	8.6	-8.2	1.5	49.9	3.9	318.4	9.4	25.9	2.1	36.1	2.1	0.5	1.5	84.7	5.8	75.8	3.5	13.7	2.1	9.3	1.6
9-Nov-06	6312	7.4	-2.2	1.4	564.7	8.1	234.33	13.6	37.5	1.3	32.2	1.3	-1.3	1.3	228.8	5.1	139.7	5.4	12.8	1.5	12.3	1.7
30-Nov-06	6334	10.5	1.2	0.8	117.4	3.2	1157.5	17.6	143.7	2.5	135.6	2.3	0.1	0.5	247.6	5.7	245.4	5.6	22.3	0.8	23.1	0.8
1-Dec-05	6335	4.7	4.8	2.2	344.5	10.9	104.54	20.3	62.3	3.2	68.7	3.5	-1.6	4.1	358.5	14.8	218.8	15.6	28.8	5.9	33.8	7.8
4-Dec-05	6335	11.8	3.5	0.8	508.2	4.3	920.1	11.1	138.3	1.4	125.7	1.3	-2.1	0.3	155.5	2.9	246.5	3.8	28.9	0.5	24.3	0.6
5-Dec-05	6335	12.4	-4.3	0.7	297.5	3.5	312.7	7.5	118.1	1.5	114.7	1.5	-3.3	0.4	215.1	3.2	158.9	3.6	29.1	0.8	28.7	0.9
5-Dec-05	6342	10.2	1.0	1.1	781.4	6.3	739.3	9.3	157.1	1.9	141.6	1.7	-0.2	0.3	253.4	4.0	75.3	2.2	26.5	0.7	24.8	0.7
5-Dec-05	6342	12.1	1.7	0.9	626.5	4.7	618.3	7.4	164.1	1.6	164.5	1.5	-1.8	0.2	145.1	2.6	228.6	2.2	18.1	0.4	20.3	0.4
10-Dec-05	6344	13.3	-7.4	0.9	862.6	5.2	1046.2	9.3	134.5	1.4	125.7	1.2	0.0	0.2	153.8	2.6	150.8	2.3	12.7	0.4	12.2	0.3
16-Jan-07	7015	12.3	-4.4	0.9	399.0	4.4	216.4	5.8	110.0	1.7	99.7	1.5	-0.9	0.4	211.8	3.6	91.1	2.7	32.0	1.0	28.6	1.1
17-Jan-07	7017	12.8	-26.3	1.2	940.4	6.6	704.49	11.7	144.3	1.9	141.4	1.7	0.1	0.4	225.6	3.8	254.1	7.0	24.1	0.7	21.2	0.8
18-Jan-07	7015	12.3	0.2	1.2	591.2	6.4	880.59	15.3	157.5	2.4	141.4	1.5	0.5	0.8	253.1	4.9	350.7	5.5	25.2	1.1	21.3	1.1
19-Jan-07	7015	11.5	6.1	1.7	831.5	9.1	328.38	21.6	245.5	3.8	251.4	3.0	-2.6	1.1	240.1	5.9	259.4	12.4	24.0	2.2	27.2	2.0
4-Mar-07	7063	9.9	6.4	0.7	189.3	3.6	92.4	23.0	56.2	1.3	58.5	1.3	3.0	0.5	158.9	3.7	25.6	7.2	14.7	0.8	14.5	0.7
5-Mar-07	7064	11.2	0.6	1.3	217.8	5.0	258.5	10.0	92.5	2.3	91.0	2.4	-1.3	1.8	120.9	4.1	82.4	3.8	27.6	3.6	21.4	3.5
14-Apr-07	7104	7.5	3.3	1.5	326.2	6.9	216.1	19.0	72.5	2.1	79.2	2.1	-0.2	1.3	159.7	5.0	57.5	7.1	19.5	1.7	21.8	1.7
15-Apr-07	7105	9.4	0.0	2.3	174.9	7.2	79.13	27.7	45.7	2.5	44.5	2.5	-0.5	3.5	157.7	7.0	258.6	15.9	29.0	4.5	32.9	5.3
25-Apr-07	7115	8.5	2.4	1.8	592.3	9.3	514.2	50.5	68.6	2.3	64.7	2.4	2.4	1.8	236.9	7.0	235.8	23.0	28.6	2.5	29.9	2.9
AVG	9.4	-1.1	0.2	416.8	1.0	434.0	2.6	84.8	0.3	82.5	0.3	-0.5	0.2	158.1	3.9	154.4	1.2	20.0	0.3	19.3	0.3	

5.3 An initial study of observed gravity wave-tide interactions

As discussed in Section 3.3.1, theoretical studies have specifically addressed the influences of tidal structure on GW upward propagation and energy transport, as well as the divergence of GW momentum flux on mean and tidal winds. These studies hint at possibly important interactions and feedback, but offer no quantitative guidance. One study suggests that such interactions dampen tidal amplitudes while another suggests amplification, and still others suggest little or no impact on tidal amplitudes. More MF measurements are required to define the nature of GW-tidal interactions throughout diurnal cycles and to constrain model simulations, as well as to improve GW parameterization in general circulation models.

Full diurnal cycle observations are desired for experimental investigation of GW/tidal interactions. Prior to the observations reported in this thesis, there were no MLT lidar data in the literature that can be used for this purpose. MU (Middle and Upper atmosphere), UHF, MF and meteor radars have made 24-hour continuous wind measurement in the MLT for more than two decades, yet the number of data sets used to investigate GW/tidal interactions remain few. Observations of local wind influences on GW momentum flux may be found in recent papers Zhou and Morton, 2006 and Janches et al., 2006, for example, but also of note is Fritts and Janches (2008), which largely repudiates Zhou and Morton's findings. Dedicated studies on GW/tidal interactions are rare, and the studies in the late 1980's (Fritts and Vincent, 1987; Wang and Fritts, 1990) remain the most comprehensive.

In the study by Fritts and Vincent (1987), wind and momentum flux (via Vincent and Reid's method) were measured by radar continuously between June 9 and 17, 1984

in Australia. In analyzing the divergence of momentum flux due to high-frequency motions in the 8 consecutive days, they found a strong diurnal modulation for the last 3 days of observation. The observed modulation maximized during an 8-hour period, centered at local midnight, the accompanied by an observed momentum flux at ~ 90 km increase ~ 5 fold from the average value. Also, in the same 3 days, these authors observed the reversal of mean plus tidal wind shear at local midnight. The coherence exhibited in these observations gave a clear signal of GW-tidal interactions, which aided the authors putting forth a simple model that qualitatively accounted for the diurnal tidal amplitude decrease accompanied by 6 hour phase advancement near 90 km around local midnight, LT for the last 3 days of the campaign. Since we are not aware of any similar observations after this seminal study, we are unable to determine the frequency of occurrence of tidal/GW interaction signature of comparable quality.

5.3.1 Data used for GW/tidal interaction studies

Of the thirty nights of momentum flux observations from September 2006 to April 2007, regrettably, weather permitted only two relatively long continuous data sets. One is on days 342 to 344, 2006, consisting of ~ 60 hours of continuous observation, which we used for the case study in this chapter (Figure 5-1). The other series, consisting of ~ 100 hours of continuous observation, is on days 15 to 19, 2007. The temporal behavior of days 15 to 19, 2007 is shown in Figure 5-12 by plotting the east LOS winds, with the nighttime data boxed in green. The tidal signature and day to day variability is evident even from the contour plot.

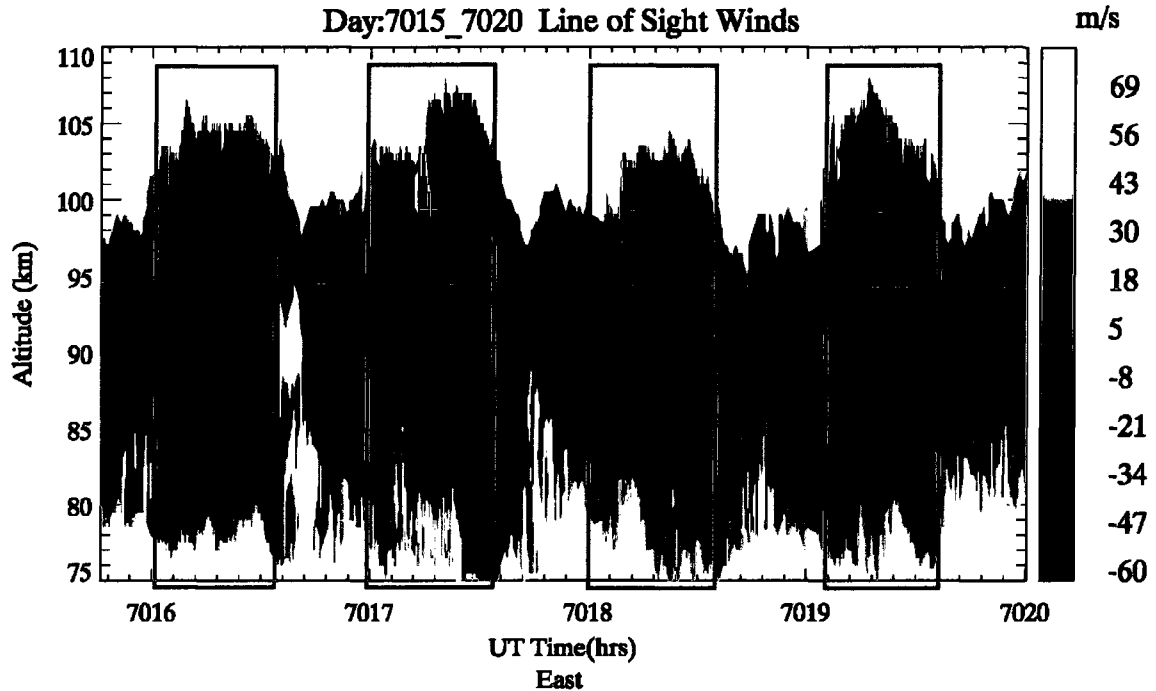


Figure 5-12. The east LOS winds for days 7015 to 7020. The data set consists of ~100 hours of nearly continuous data with brief breaks for system maintenance. The nighttime data are boxed between the green lines.

It is well known that GW activity is abundant in northern hemisphere winter. Years of nocturnal observations with the CSU lidar suggest that tidal variability and a strong wind shear often exist, though they may vary from one night to the next. To provide some insight into this variability, we show hourly mean temperature (left) and east LOS wind (right) profiles during the nights MF/ ρ were also measured; the corresponding zonal wind is about three times the east LOS wind. These profiles are shown in Figure 5-13 for the observations on days 342 to 344 and in Figure 5-14 for observations on days 15 to 19.

It is clear from these plots that strong winds and wind shears are present, though they may vary in time and altitude. For example, in Figure 5-13, a strong wind shear is present above 90 km though the direction of wind shear reverses in the night, presumably due to the semidiurnal tide. In the first two nights the semidiurnal tidal amplitude

increases nearly exponentially with increase in altitude; however during the third night, 344, the semidiurnal tidal wind amplitude does not appear to grow in amplitude above 90 km.

6342



6343

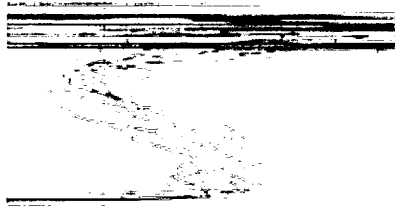


6344



Figure 5-13. The hourly mean temperature and east LOS wind profiles during the nights of 6342 to 6344.

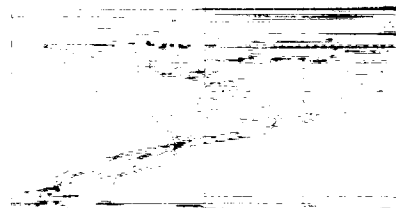
7016



7017



7018



7019

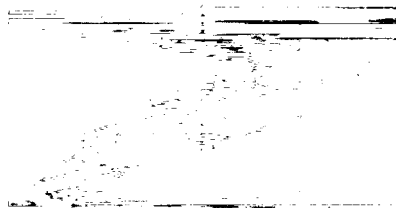


Figure 5-14. The hourly mean temperature and east LOS wind profiles during the nights of 7016 to 7019.

A larger negative mean wind in the lower altitudes during days 15 to 19 tends to create a large positive gradient during most nights (Figure 5-14). The tidal modulation of the wind is apparent in the nights of day 16, 18, 342 and 343 where a growth in tidal amplitude with increasing altitude is evident. A large shear is still present in the data, but it occurs at lower altitudes. For instance, day 16 exhibits large shear near 85 km that changes direction throughout the night.

5.3.2 Observed correlations between momentum flux and tides

The negative divergence of GW flux provides a body force that accelerates the background wind (equation 3.17). GWs interact with the tidal harmonics as part of the background wind system, depending on the time scale of interest. Since we are interested in the tidal influence, we interpret the background wind in this analysis as a superposition of diurnal, semidiurnal tides and a mean wind (equation 5.6). In order to increase the signal to noise of MF/ρ to facilitate the observation of correlations with tides, we plot MF/ρ smoothed by a running boxcar average of a 3 hour width, the zonal daily running tidal wind ($U[RS]$, section 5.1.2), every 4 km (Figure 5-16 through Figure 5-20, left). Note the zonal daily running tidal wind contains the diurnal, semidiurnal tides as well as the mean winds. Furthermore, we plot the convergence of the smoothed MF/ρ ($\partial(-MF/\rho)/\partial z$) with $U[RS]$ diurnal and semidiurnal amplitudes, also every 4 km (Figure 5-16 through Figure 5-20, right). The 3 hour smoothing is accomplished with the aid of the IDL SMOOTH function with set to a width of 61-three minute (~ 3 hours) files.

We remind the reader of equation 3.18

$$\frac{\partial \bar{u}}{\partial t} \approx -\frac{1}{\rho} \frac{\partial \overline{\rho u' w'}}{\partial z}, \quad 5.12$$

where the convergence of MF is shown to provide a force to the background wind. For consistency our plots do not include the density terms in the derivative nor in the numerator outside the derivative. Because the altitude over which we perform our observations is relatively small (~two scale heights), including or not including the density term makes little difference in the qualitative result (Figure 5-15).

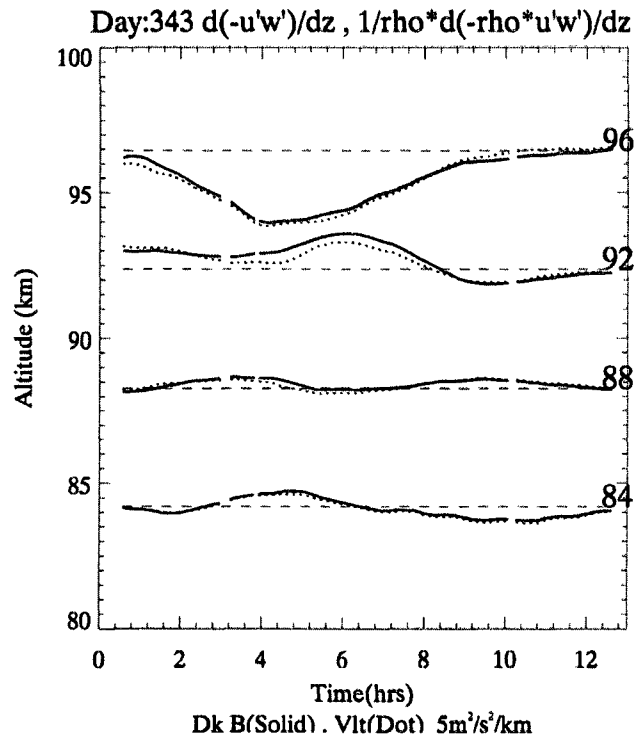


Figure 5-15. The dark blue solid line is the convergence of (MF/ρ) and the violet dotted line is the convergence of $(MF)/\rho$. Both lines are the same units; the scale is $(5 \text{ m}^2\text{s}^{-2}\text{km}^{-1})$ per km in altitude.

Starting with day 343 at 84 km (Figure 5-16, left), there appears to be a modulation of MF/ρ that has nearly the same period as the diurnal tide. At this altitude the diurnal tide is the larger component in the background wind, this is shown in the right plot of Figure 5-16 with mean diurnal amplitude of 29 ms^{-1} and semidiurnal amplitude of 20 ms^{-1} . At the same altitude, the daily running diurnal tides amplitude (dots) and the convergence of the MF/ρ (solid) appear to be anti-correlated (Figure 5-16, right), while

the semidiurnal tide (dash) appears to be correlated between 2 and 9 hr. With an increase in altitude the amplitude of the diurnal tide decreases to 13 ms^{-1} while the amplitude of the semidiurnal tide has grown to 40 ms^{-1} at $\sim 88 \text{ km}$, and the period of the apparent modulation in the MF/ ρ now clearly has changed to an apparent 12 hour period (Figure 5-16, left). Because the major component of the background wind at these altitudes is the semidiurnal tide, there is an apparent interaction between the semidiurnal tide and the flux produced by the GW spectrum. Above 92 km this anti-correlation relationship diminishes, and the MF/ ρ and tidal phases are nearly in quadrature (~ 3 hour phase difference), suggesting that the GW spectrum, filtered in the mid-altitudes (84 km to 88 km), is no longer directly interacting with the tides. The result is that the phase of MF/ ρ appears unchanged from 88 km to 96 km. Furthermore, at 88 km there is anti-correlation between the convergence of the MF/ ρ and the diurnal and semidiurnal tidal amplitudes. This anti-correlation between the convergence of the MF/ ρ and the diurnal tidal amplitude is consistent at all altitudes (84 km to 96 km) during the observation period. The convergence of the flux and the semidiurnal tide amplitude moves from anti-correlated at 88 km to correlated at 92 km which is also the altitudes that the modulation of the MF/ ρ moves from anti-correlated to leading the tide in quadrature.

Strong anti-correlation between the zonal daily running tide and smoothed MF/ ρ suggests interaction between the background wind and the GWs producing the MF/ ρ . Furthermore, the anti-correlation between the convergence of the MF/ ρ and the diurnal tidal amplitude coupled with its lack of exponential growth in amplitude (Figure 5-9) suggests that the amplitude of the diurnal tide is suppressed by the convergence of the flux created by the short period GWs.

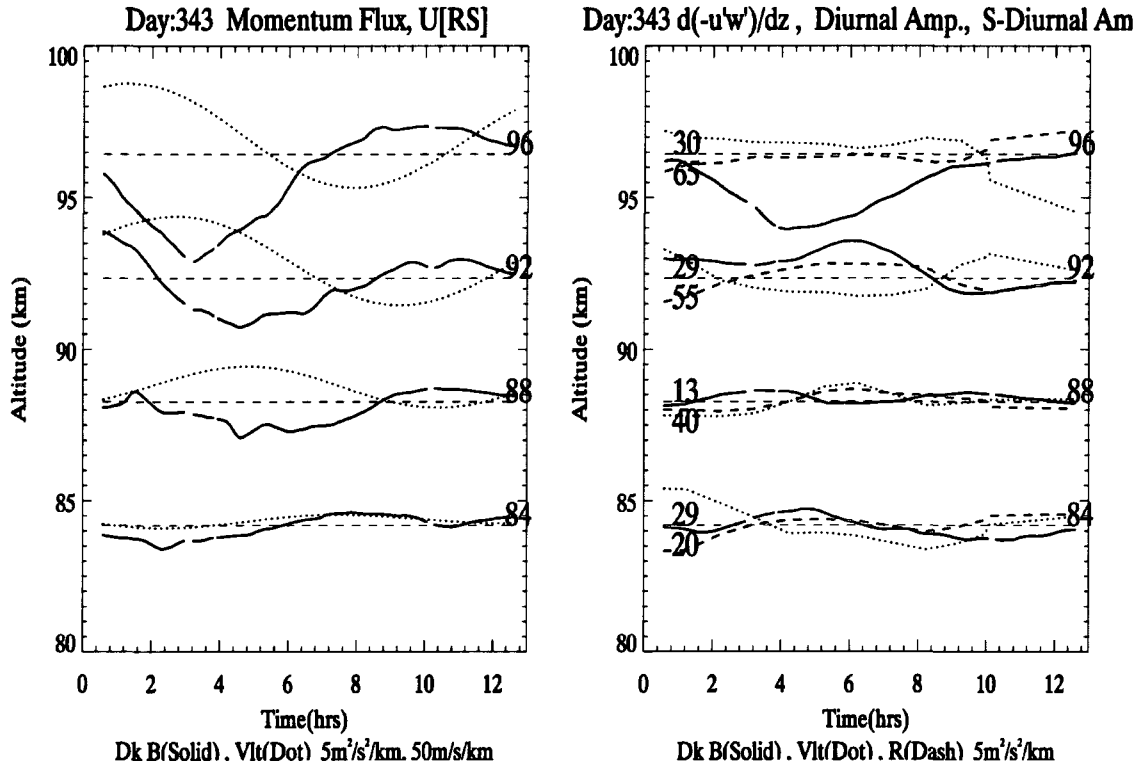


Figure 5-16. The left plot is the smoothed MF/ρ (solid, blue, scale = $5 \text{ m}^2\text{s}^{-2}$ per km) and the zonal daily running tide ($U[RS]$) (dots, violet, scale = 50 ms^{-1} per km) of day 343, 2006. The right plot is the convergence of the smoothed MF/ρ ($\partial(-MF/\rho)/\partial z$), solid, blue, scale = $5 \text{ m}^2\text{s}^{-2} \text{ km}^{-1}$ per km) with $U[RS]$ diurnal (dots, violet, scale = 5 ms^{-1} per km) and semidiurnal amplitudes (dash, red, scale = 5 ms^{-1} per km). The altitudes are noted to the right. The averaged tidal amplitude for the given altitude is plotted on the left, with diurnal above and semidiurnal below the straight black dashes that represents the altitude and the mean amplitudes.

In contrast to day 343, data from days 16 to 19 already have large amplitude in the modulation of the smoothed MF/ρ measurements at the lower altitudes. However, this apparent modulation is not anti-correlated with the tides, suggesting some interaction or an influencing source on the GW spectrum due to the environment at lower altitudes that is not due only to tidal filtering or modulation. While day 343 above 95 km the MF/ρ appears to be leading the tidal phase in quadrature, the MF/ρ in days 16 to 19 appears to be lagging the tidal phase in quadrature in the altitudes below 84 km.

Day 16 has large mean winds in the lower altitudes (up to 80 ms^{-1}) which dominate the background winds at lower altitudes. Not until the mean winds diminish in

magnitude does a relatively weak tidal amplitude become large enough to dominate the mean wind and cause a reversal in the direction of the background wind (~ 92 km, 7 UT, Figure 5-17, left). At 84 km the smoothed MF/ρ is modulated with what appears to be 12 hour period and peak-to-peak amplitude of $\sim 20 \text{ m}^2\text{s}^{-2}$. The oscillating amplitude of the MF/ρ diminishes with increasing altitude until ~ 92 km to $\sim 5 \text{ m}^2\text{s}^{-2}$, where the mean winds have decreased and a relatively weak tide changes the direction of the background wind. The phase of the smoothed MF/ρ is lagging the daily running tide by $\sim 90^\circ$ at 84 km, and at 92 km the flux appears to be anti-correlated with the tidal wind (Figure 5-17, left). It is not clear that the tides are interacting with the flux, or vice versa, until this reversal in the direction of the background wind (and some may argue that it is still not clear at this altitude!). However, at 92 km there is a modulation of the convergence of the momentum flux (Figure 5-17, right) that appears to be anti-correlated with the daily running tidal phase (Figure 5-17, left) with ~ 12 hour period.

Unfortunately day 16 does not have sufficient data to allow an accurate determination of the daily running tide amplitudes before 7UT. The daily running tide results (Figure 5-17, left) utilize interpolation to fill in the missing tidal data points before the seventh hour. While interpolation used for reconstructing the daily running tide is accurate enough to understand the background winds it does not allow an accurate enough determination of the tidal amplitudes to complete Figure 5-17's plot on the right.

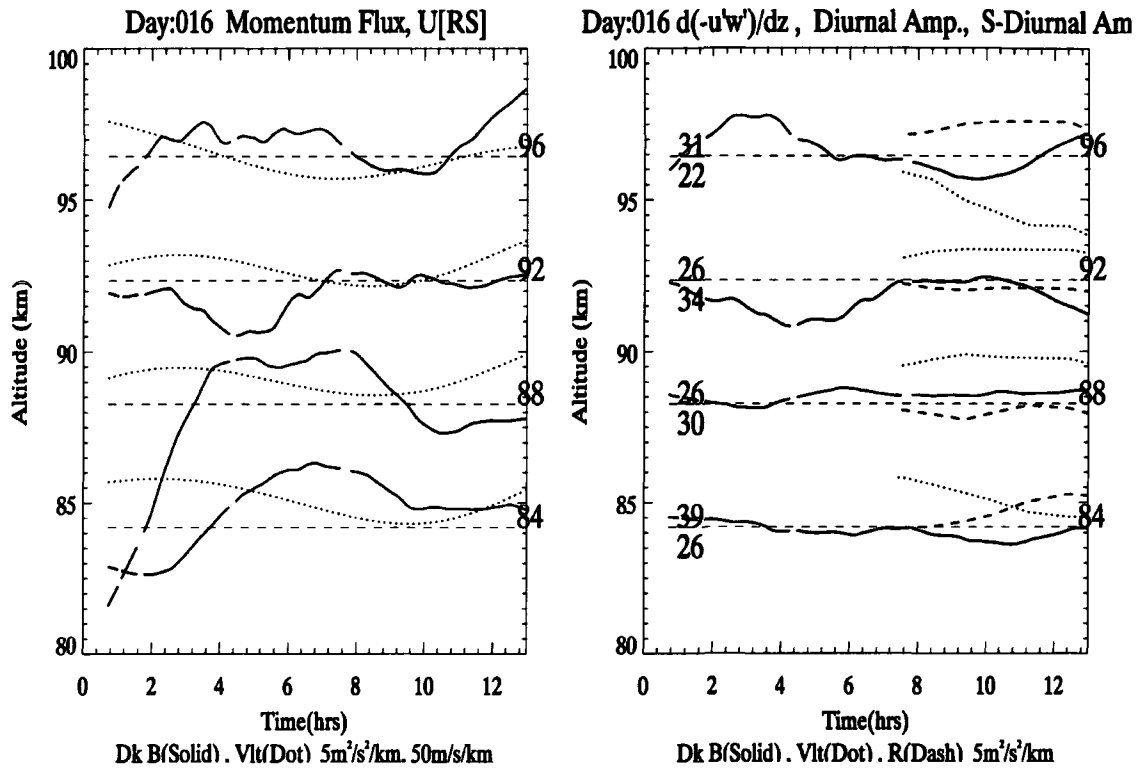


Figure 5-17. The left plot is the smoothed MF/ρ (solid, blue, scale = $5 \text{ m}^2\text{s}^{-2}$ per km) and the zonal daily running tide (U[RS]) (dots, violet, scale = 50 ms^{-1} per km) of day 16, 2007. The left plot is the convergence of the smoothed MF/ρ ($\partial(-MF/\rho)/\partial z$), solid, blue, scale = $5 \text{ m}^2\text{s}^{-2} \text{ km}^{-1}$ per km) with U[RS] diurnal (dots, violet, scale = 5 ms^{-1} per km) and semidiurnal amplitudes (dash, red, scale = 5 ms^{-1} per km). The altitudes are noted to the right. The averaged tidal amplitude for the given altitude is plotted on the left, with diurnal above and semidiurnal below the straight black dashes that represents the altitude and the mean amplitudes.

Day 17 (Figure 5-18) has a large amplitude oscillation of MF/ρ that occurs at altitudes below 92 km, which is similar to day 16, however the MF/ρ oscillations seem to be leading the tide in quadrature unlike day 16 where the oscillations are lagging the tide. Strong mean winds and weak tidal amplitudes persist in day 17, preventing the background wind, the wind field in which the GWs propagate, from crossing 0 ms^{-1} until 92 km. At 92 km, increasing tidal amplitude (Figure 5-18, right, mean diurnal 40 ms^{-1} and mean semidiurnal 38 ms^{-1}) combine with a decreasing mean wind causing a reversal in the background wind ~ 4 UT. As the tidal amplitudes increase and the mean winds diminish above 92 km (Figure 5-18) anti-correlation between the tide and MF/ρ occurs.

Day 17 is similar to day 16 except at higher altitudes, where day 16 has the flux lagging the semidiurnal tide in quadrature and day 17 has the flux leading the semidiurnal tide in quadrature; this is more similar to day 343, where the flux also appears to be leading in quadrature. Furthermore, the modulation of the flux changes in altitude, suggesting that the GW spectrum is interacting with different tidal components. The dominating tidal contributor to the background wind transitions from diurnal tide with a mean amplitude of 40 ms^{-1} at 92 km to semidiurnal tide with a mean amplitude of 62 ms^{-1} at 96 km (Figure 5-18, right), and the apparent period of the flux modulation reflects this change. For instance, the flux modulation at 92 km (Figure 5-18, left) has an approximate modulation period of ~ 12 hours, while the apparent modulation at 84 km is closer to the diurnal tidal period.

The convergence of the flux at 84 km, and to a lesser extent at 88 km, appears to be correlated with diurnal amplitude yet at 96 km the diurnal amplitude appears to be anti-correlated with the convergence of the flux (Figure 5-18). Examination of the mean tidal amplitudes (Figure 5-18, right) show increasing diurnal tidal amplitude from 84 km to 88 km (35 ms^{-1} and 39 ms^{-1} respectively) and decreasing amplitude from 92 km to 96 km (40 ms^{-1} and 17 ms^{-1} respectively). The anti-correlation of flux convergence with the diurnal tide amplitude coupled with decreasing diurnal tide amplitude suggests that the MF/ρ may be suppressing the diurnal tidal amplitude growth at the higher altitudes and may not be suppressing it in the lower altitudes.

The semidiurnal tidal amplitude is loosely anti-correlated with the convergence of the flux at 84 km and 88 km, but is correlated at 92 km and 96 km (Figure 5-18, right). Examination of the mean semidiurnal tidal amplitudes show a non-growing semidiurnal

tidal amplitude from 84 km to 88 km (21 ms^{-1} and 22 ms^{-1} respectively) and growing amplitude from 92 km to 96 km (38 ms^{-1} and 62 ms^{-1} respectively). The anti-correlation of the flux convergence with the local semidiurnal tidal amplitude is coupled with a non-growing semidiurnal tide; this suggests a possible dampening of the local semidiurnal tides amplitude in the lower observed altitudes by the MF from short period GWs. Furthermore, the correlation of the flux convergence with the local semidiurnal tidal amplitude coupled with growing amplitude in the semidiurnal tide suggests that the convergence of the MF is no longer dampening the semidiurnal tides amplitude in the higher observed altitudes.

Figure 5-18 (day 17) suggests filtering of the GW spectrum at the lower altitudes by the diurnal tide, and the suppression of the semidiurnal tides amplitude by the MF/ ρ generated by the diurnal tide filtered GWs. At higher altitudes the opposite effect takes place. The GW spectrum at the higher altitudes appears to be filtered by the semidiurnal tide which in turn the MF/ ρ generated by the semidiurnal tide filtered GWs suppresses diurnal tide amplitude.

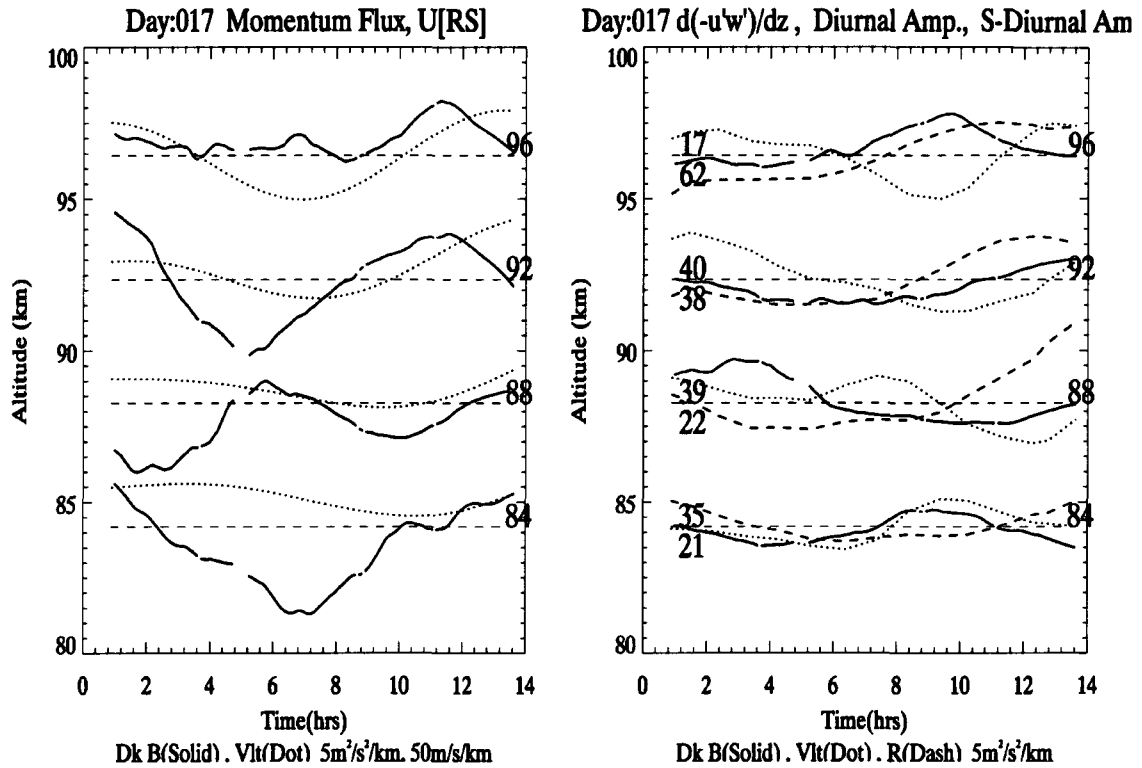


Figure 5-18. The left plot is the smoothed MF/ρ (solid, blue, scale = $5 \text{ m}^2\text{s}^{-2}$ per km) and the zonal daily running tide ($U[RS]$) (dots, violet, scale = 50 ms^{-1} per km) of day 17, 2007. The left plot is the convergence of the smoothed MF/ρ ($\partial(-MF/\rho)/\partial z$), solid, blue, scale = $5 \text{ m}^2\text{s}^{-2} \text{ km}^{-1}$ per km) with $U[RS]$ diurnal (dots, violet, scale = 5 ms^{-1} per km) and semidiurnal amplitudes (dash, red, scale = 5 ms^{-1} per km). The altitudes are noted to the right. The averaged tidal amplitude for the given altitude is plotted on the left, with diurnal above and semidiurnal below the straight black dashes that represents the altitude and the mean amplitudes.

Again the reader is reminded that since GWs are intermittent with various sources that can cause different phase speeds, wavelengths, and group velocities, the expected negative correlation between background wind and MF/ρ does not necessarily exist throughout the entire night or through all altitudes (Holton, 1992). Furthermore, tidal effects in the atmosphere are complex and varied. Migrating and non-migrating tides as well as different tidal modes complicate the observed picture.

Days 18 and 19 do not contain as clean a picture as days 343 and 17. With the exception of the large modulation of the flux at lower altitudes, days 18 and 19 are more similar to day 343 than day 16. Near 88 km, for both days, the flux is anti-correlated with

the background winds, with a transition to flux leading the tide in quadrature at the higher altitudes. For day 18 the convergence of the MF (Figure 5-19, right) appears to be loosely anti-correlated with diurnal amplitude and loosely correlated with the semidiurnal tide at most altitudes. The diurnal tide does not grow in amplitude with increase in altitude while the semidiurnal tide does grow in amplitude with increase in altitude, suggesting a possible dampening of the diurnal tide and non-dampening of the semidiurnal tide

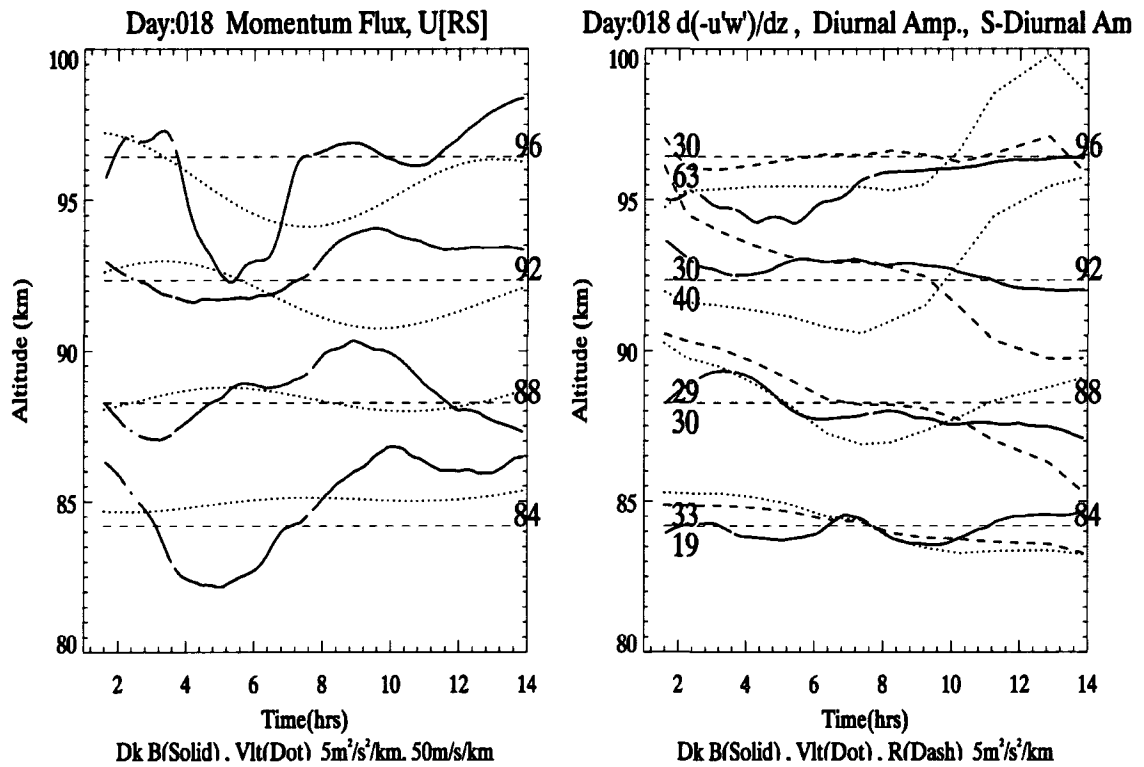


Figure 5-19. The left plot is the smoothed MF/ρ (solid, blue, scale = $5 \text{ m}^2\text{s}^{-2}$ per km) and the zonal daily running tide ($U[RS]$) (dots, violet, scale = 50 ms^{-1} per km) of day 18, 2007. The left plot is the convergence of the smoothed MF/ρ ($\partial(-MF/\rho)/\partial z$), solid, blue, scale = $5 \text{ m}^2\text{s}^{-2} \text{ km}^{-1}$ per km) with $U[RS]$ diurnal (dots, violet, scale = 5 ms^{-1} per km) and semidiurnal amplitudes (dash, red, scale = 5 ms^{-1} per km). The altitudes are noted to the right. The averaged tidal amplitude for the given altitude is plotted on the left, with diurnal above and semidiurnal below the straight black dashes that represents the altitude and the mean amplitudes.

Unfortunately day 19 does not have sufficient data after it ends to allow an accurate determination of the daily running tide amplitudes after 7UT, however modulation of the MF, similar to the modulation seen in days 18 and 343, is also seen in

day 19 (Figure 5-20). Day 19 does exhibit unusually high diurnal tidal mean amplitudes at 88 km and 92 km, suggesting possible issues with the tidal fit and the resulting amplitudes.

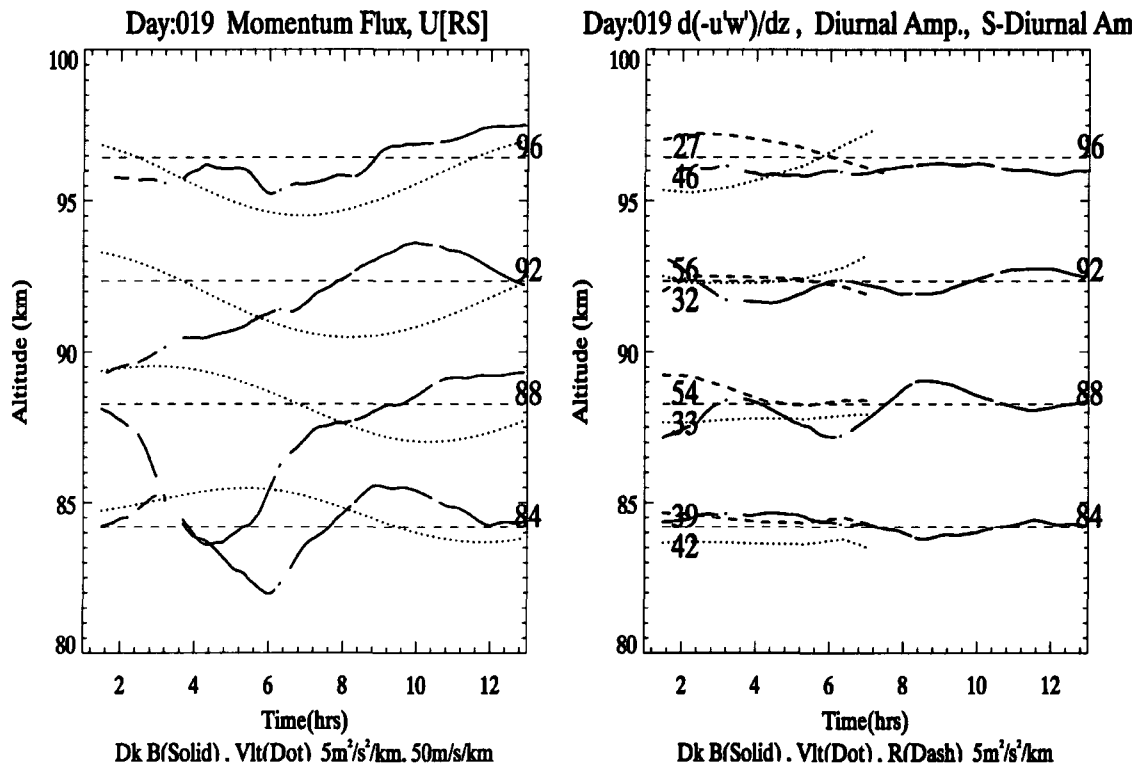


Figure 5-20. The left plot is the smoothed MF/ρ (solid, blue, scale = $5 \text{ m}^2\text{s}^{-2}$ per km) and the zonal daily running tide ($U[RS]$) (dots, violet, scale = 50 ms^{-1} per km) of day 19, 2007. The left plot is the convergence of the smoothed MF/ρ ($\partial(-MF/\rho)/\partial z$), solid, blue, scale = $5 \text{ m}^2\text{s}^{-2} \text{ km}^{-1}$ per km) with $U[RS]$ diurnal (dots, violet, scale = 5 ms^{-1} per km) and semidiurnal amplitudes (dash, red, scale = 5 ms^{-1} per km). The altitudes are noted to the right. The averaged tidal amplitude for the given altitude is plotted on the left, with diurnal above and semidiurnal below the straight black dashes that represents the altitude and the mean amplitudes.

The impact of MF/ρ convergence on tidal phase was explored with this method, but no clear phase jump was found. Further measurements are needed to allow a statistical comparison of tidal amplitudes and phases to MF/ρ amplitudes and phases to better understand how they are affected by the MF/ρ convergence. A continuation of this MF/ρ study, coupled with concurrent tidal study, should allow this examination.

In summary, this chapter has presented the data acquired. First, a case study of day 343, 2006, describes, and displays, the analysis that is typically performed on the data including: chirp analysis, a study of stability, and MF/ ρ calculations. The LOS wind data is shown and filtered to afford an examination of the oscillations in the wind that, when analyzed, provides the variance for subsequent MF/ ρ calculations. Second, the statistical results of the yearlong study are presented. These statistics of variances and MF/ ρ values are compared with a similar study by Gardner and Liu (2007). The comparison of the two studies at two different longitudes provides strikingly very similar results. However, the shorter and varied data length in individual nights in the study of Gardner and Liu (2007) prevented them from being able to perform linear background subtraction that consistently removes the contamination of longer period perturbations. Finally, MF/ ρ and tidal interaction is examined. For the data analyzed, there is observed anti-correlation between the daily running tide and smoothed MF/ ρ at the middle altitudes in the observation, suggesting a filtering of the GWs by the local tides. The phase relationship between the smoothed MF/ ρ and the daily running tide changes with altitude, suggesting that the GWs, filtered at a lower altitude are no longer filtered by the tide at the higher altitudes.

The convergence of the MF/ ρ appears to be anti-correlated and correlated with the tidal amplitudes depending upon the altitude and the day of the measurement. When clear anti-correlation between the convergence of flux and diurnal tidal amplitude is observed, such as day 343, the growth of diurnal tidal amplitude is damped; suggesting that tidal energy is partially transferred into the short period GWs.

Chapter 6 will provide conclusions and a projection of further work.

References:

- Dutton, J. A. *The Ceaseless Wind*, Dover, 1986.
- Fetter, A. L., and J. D. Walecka, *Theoretical Mechanics of Particles and Continua*, McGraw-Hill Book Company, 1985.
- Fritts, D. C., and D. Janches, Dual-beam measurements of gravity waves over Arecibo: Reevaluation of wave structure, dynamics, and momentum fluxes, *J. Geophys. Res.*, **113**, D05112, doi:10.1029/2007JD008896, 2008.
- Fritts, D. C., and M. J. Alexander, Gravity dynamics and effects in the middle atmosphere, *Rev. Geophys.*, **41**, doi:10.1029/2001RG000106, 2003.
- Fritts, D. C., S. L. Vadas, K. Wan and J. A. Werne, Mean and variable forcing of the middle atmosphere by gravity waves, *J. Atmos. Sci.*, **68**, pp.247-265, 2006.
- Fritts, D. C., and R. A. Vincent, Mesospheric momentum flux studies at Adelaide, Australia: Observations and a gravity wave/tidal interaction model, *J. Atmos. Sci.*, **44**, pp.605-619, 1987.
- Gardner, C. S., and A. Z. Liu, Seasonal variations of the vertical fluxes of heat and horizontal momentum in the mesopause region at Starfire Optical Range, New Mexico, *J. Geophys. Res.*, **112**, D09113, 2007.
- Gardner, C. S., and W. Yang, Measurements of the dynamical cooling rate associated with the vertical transport of heat by dissipating gravity waves in the mesopause region at the Starfire Optical Range, New Mexico, *J. Geophys. Res.*, **103**, 16,909–916,926, 1998.
- Holton, J. R., *An Introduction to Dynamic Meteorology*, International Geophysics Series, Volume **48**, Elsevier Science (USA), Academic Press, 1992.
- Janches, D., D. C. Fritts, D. M. Riggin, M. P. Sulzer, and S. Gonzalez, Gravity waves and momentum fluxes in the mesosphere and lower thermosphere using 430 MHz dual-beam measurements at Arecibo: 1. Measurements, methods, and gravity waves, *J. Geophys. Res.*, **111**, D18107, doi:10.1029/2005JD006882., 2006.
- Li, F., Liu, A. Z., Swenson, G. R., Characteristics of instabilities in the mesopause region over Maui, Hawaii. *Journal of Geophysical Research*, **110**, D09S12. 2005.
- Li, T., C. Y. She, B. P. Williams, T. Yuan, R. L. Collins, L. M. Kieffaber and A. W. Peterson, Concurrent OH imager and sodium temperature/wind lidar observation of localized ripples over Northern Colorado, *J. Geophys. Res.* **110**, D13110, doi:10.1029/2004JD004885, 2005.
- Lindzen, R. S., Turbulence and stress owing to gravity wave and tidal breakdown, *J. Geophys. Res.*, **86**, pp. 9707-9714, 1981.

- Sherman, J. P., and C.Y. She, Seasonal variation of mesopause region wind shears, convective and dynamic instabilities above Fort Collins, CO: A statistical study, *J. Atmo. Solar-Terr. Physics*, **68**, 1061-1074, 2006.
- Yuan, T., H. *Schmidt*, C. Y. She, D. A. Krueger, and S. Reising, Seasonal variations of semidiurnal tidal perturbations in mesopause region temperature, zonal and meridional winds above Fort Collins, CO (40.6°N, 105.1°W), preprint.
- Vincent, R. A. and I. M. Reid, HF Doppler measurements of mesospheric gravity wave momentum fluxes, *J. Atmos. Sci.*, **40**, 1321-1333, 1983
- Wang, D.-Y., and D. C. Fritts, Mesospheric momentum fluxes observed by the MST radar at Poker Flat, Alaska, *J. Atmos. Sci.*, **47**, pp.1511-1521, 1990.
- Zhou, Q., and Morton, Y. T., A case study of mesospheric gravity wave momentum flux and dynamical instability using the Arecibo dual beam incoherent scatter radar, *Geophys. Res. Lett.*, **33**, L10802, 2006

Chapter 6: **Conclusions and Further Work**

Since system upgrades to the Colorado State University Sodium Lidar in September 2006, over 300 hours of nighttime three-beam observations have been made with co-planar beams 20° east and 20° west from zenith and a third beam 30° north from zenith. This geometry has allowed the determination of nighttime gravity wave zonal momentum flux profile with simultaneous 24-hour measurements of the mean and tidal fields of the mesopause region temperature and zonal and meridional winds. This also allows a quantitative estimate of the accompanying GW-tidal interactions.

6.1 Conclusions

This dissertation begins by describing the basic theory of sodium fluorescence lidar; this is followed by a description of the sodium lidar system, and the changes made to the system to perform co-planar beam, MF measurements. After a discussion of the measurement procedure, the basic atmospheric theory is discussed with an emphasis on wave theory and its role in the MLT dynamics. Chapter 4 is a detailed discussion of MF data analysis and the error estimate. Chapter 5 presents the data and analysis techniques used for the data set, by using day 343, 2006, as a case study. Statistics of the yearlong study are presented using the previously described analysis techniques, and the results are compared with Gardner and Liu 2007. And to conclude, the MF-tidal interaction results are presented and discussed using day 343, 2006 (Figure 5-15) and days 16 to 19, 2007 (Figures 5-16 through 5-19).

6.1.1 Chirp

Vertical winds, averaged over a night of data, are expected to be very small. By setting this vertical wind to zero, an estimate of transmitter chirp (which leads to frequency and wind bias) is calculated (Equation 5.3) and used for verification of the chirp correction sub-system. The chirp sub-system corrects the LOS wind to within 0.9 ms^{-1} , which is sufficient for wind and temperature measurements (Section 5.1.1). Note that because differences in signal are involved in MF measurements, chirp correction does not play a role. The variance calculation subtracts the mean of the set window size (equation 4.2), and any slowly changing signal, such as the chirp, will be removed. Additional suppression of any effect of chirp comes because the variance would be seen in both beams equally, and would be removed in the subsequent MF calculation.

6.1.2 Momentum Flux and Mean Winds

The variance for the east and west radial winds is calculated and plotted (Figure 5-3). A comparison of with the filtered radial wind reveals wave motion during the times and at the altitudes that large values for variance are reported. This comparison of the radial wind and the calculated variance increases the confidence of the data, showing that large variances do in fact reflect GW propagation through the observation channels. The calculated MF/ρ at two hour intervals is compared with the 2-hour mean zonal wind, with the aid of a hodographic plot, revealing anti-correlation for most of the night and most of the altitudes; this is consistent with current GW theory (Section 5.1.3).

Nightly averaged zonal winds, tidal amplitudes, and fluxes are given.

Examination of the fluxes due to, a GW spectrum of only short period waves (< 2 hours), and a GW spectrum that includes longer period waves (< 12 hours), reveals that GWs of

longer periods (2 to 8 hour periods), at times, can have a dominating effect on the nightly mean MF. Radial winds are filtered to pass longer period waves and suppress the amplitude of short period waves. These plots clearly show long period oscillations in the LOS wind signal that significantly contribute to the variances in the respective channels. The contribution of longer period GWs to the MF measurement is further reflected in the statistics of the entire data set with the difference between the annual mean MF/ ρ reported for waves with periods < 2 hours and waves with periods < total hours in a night of observations (Section 5.1.5). Although longer period waves do have an impact on the measured MF for night of 343 the statistics of the entire data set show a mean monthly MF/ ρ of $-0.6 \text{ m}^2\text{s}^{-2}$ when analyzed with a two hour window and $-0.7 \text{ m}^2\text{s}^{-2}$ when analyzed in the method of G&L (Table 3), suggesting greater contribution to flux from short period waves. And when the MF/ ρ is not broken down into monthly averages but averaged over the entire data set, the mean MF/ ρ is $-0.5 \text{ m}^2\text{s}^{-2}$ when analyzed with a two hour window and $-1.1 \text{ m}^2\text{s}^{-2}$ when analyzed in the method of G&L (Table 4).

6.1.3 Stability

Atmospheric stability is examined by using measured temperatures and winds using the conventional stability criteria. More regions of potential convective instability are observed in day 343 than in previous studies; it is hypothesized that this is due to a shorter period of temporal averaging in this study, 3 minutes in this study compared to 30 minutes for the previous studies. If there were a region of atmospheric stability, it could 'correct' itself and become stable in a short period of time, roughly in about the period of the waves that propagate through the region. Over long periods, regions of atmospheric

instability could become unstable and then stable in the averaging period, thereby masking the instability (Section 5.1.4).

6.1.4 Statistics

Statistics of MF/ρ and zonal, meridional wind and temperature variances are calculated in two ways for the entire year; first, by filtering oscillations with periods longer than 2 hours and second, by filtering only periods longer than the night's observation period. The variances are further broken down into monthly means to allow the results to be compared with other reported sodium lidar studies, Gardner and Liu (2007), and Gardner and Yang (1998). A comparison of G&L and CSU lidar monthly variances shows consistent results in the annual average of the monthly means and in the distribution of monthly averages between winter and equinox. A discrepancy is noted in ratios of zonal and meridional variances in the CSU lidar measurements compared to G&L. This difference in monthly annual mean is attributed to a difference in temporal averaging between the zonal data (3 minutes) and the meridional data (15 minutes) (Section 5.2).

G&L report an annual mean MF/ρ of $-1.4 \pm 0.6 \text{ m}^2\text{s}^{-2}$. This is compared to the current study's value of $-1.1 \pm 0.2 \text{ m}^2\text{s}^{-2}$, when averaged over the same altitudes and analyzed using the same method. This study also computes MF/ρ , by filtering motions greater than a 2-hour period, which captures the flux due to GWs with higher vertical velocities and horizontal phase speed (periods shorter than 2 hrs), and results in an annual mean of $-0.5 \pm 0.2 \text{ m}^2\text{s}^{-2}$ (Table 4).

A comparison of winter to equinox MF/ρ values reported in this study reveal a monthly mean value of $-2.4 \text{ m}^2/\text{s}^2$ for the winter months (November, December, January)

and $+0.59 \text{ m}^2/\text{s}^2$ for the months more nearest the two equinoxes (March, April, September, October) when calculated in the method of G&L, and $-1.0 \text{ m}^2/\text{s}^2$ for the winter months and $-0.28 \text{ m}^2/\text{s}^2$ during the equinox when calculated with a 2-hour window. A seasonal comparison of MF/ ρ with G&L is not possible, as they do not break down their flux measurements in this manner.

6.1.5 MF/ ρ – Tidal Interaction

Finally, MF/ ρ and tidal interaction is examined (Section 5.3). For the data analyzed, there is anti-correlation between the reconstructed tide and smoothed MF/ ρ (Figures 5-15 through 5-19). This anti-correlation suggests interaction between the tides and the high phase speed GWs inducing the MF/ ρ . At higher altitudes this anti-correlation relationship evolves to near quadrature, suggesting that the GW spectrum, already filtered by the tides, is no longer directly interacting with the tides. The convergence of the MF/ ρ is examined and appears to be anti-correlated or correlated with the tidal amplitudes depending upon the altitude and the day of the measurement. Where clear anti-correlation between the convergence of flux and diurnal tidal amplitude is observed, such as days 343 and 17, the growth of diurnal tidal amplitude is damped; suggesting that tidal energy is partially transferred into the short period GWs.

6.2 Further Work

This study, and the ongoing work, has made a convincing link between the modulation of MF, induced by short period GWs, and the atmospheric tide. The dampening of the diurnal tide by high phase speed short period GWs is suggested. Further work on this subject will probably take years. The surface has just been scratched with the analysis this data allows.

The dulcet tones of Joe She calling for more data are epic to his graduate students, and never more prudent than now. Further measurements are needed to allow a statistical comparison of tidal phases to MF/ ρ convergence. It is anticipated that a continuation of this MF/ ρ study, coupled with the ongoing tidal study, will allow this statistical examination of how the MF/ ρ convergence will affect tidal phases.

Nighttime summer and full 24-hour MF/ ρ measurements during the winter are desirable because they would fill in gaps in the data set and hopefully provide greater insight into the seasonal MF/ ρ and MF/ ρ -tidal interaction. At the onset of this study it was thought that winter daytime and nighttime summer measurements of MF/ ρ with sodium lidar were improbable at best, however comparisons of the signal-to-noise ratio (SNR) show that an increase in the SNR by a factor of ~ 4 would allow MF/ ρ measurements during the winter days and summer nights with error levels similar to that presented in this study; to obtain the same measurement error in summer daytime there would have to be an increase in the SNR of ~ 8 . There are several ways to increase the SNR by modifying the lidar system: increasing the efficiency, transmitting more photons, and so on, but here we only address increasing the receiver size. Increasing the receiver radius by a factor of four could be obtained by increasing the diameter of the telescopes primary mirror to 3 m, which is very expensive, or by obtaining four additional telescopes and the subsequent receiver subsystem, which is relatively inexpensive. Quadrupling the number of receivers and adding the associated fibers, optics, PMTs and counting card would cost $\sim \$120,000$. Adding four additional channels is a technically simple modification to the current lidar system. The geometry of the telescope layout in

the observatory hall must be considered as well as how to accurately co-align four telescopes to one beam.

Further work on the current data can be made by use of the Monte Carlo simulation described in section 4.2.2. The simulation has promise for a greater understanding of uncertainty in the MF/ ρ measurement and the bias discussed in section 4.2.2. The bias in the MF measurement can be further quantified in relation to the wind, temperature and photon levels. While the expected value of this bias is small, MF/ ρ values are also small, and this bias should be better understood.

On a final note, the lidar-atmosphere simulation that is used in the Monte Carlo analysis shows promise of being employed, in conjunction with wavelet analysis, in a further study of the gravity wave spectrum above Fort Collins. In Appendix I Correlation and Wavelet Analysis, Figure I-1 shows the same lidar-atmosphere simulation being used to simulate gravity waves of known wavelength and phase speeds. These gravity waves propagate through a simulated lidar system and a resultant MF value is measured. By simulating gravity waves where all the wave components are known and comparing the simulation results to actual results, further insight can be developed about the gravity wave spectrum and the ability of the current lidar system to measure it and its effects above Fort Collins.

References:

Gardner, C. S., and A. Z. Liu, Seasonal variations of the vertical fluxes of heat and horizontal momentum in the mesopause region at Starfire Optical Range, New Mexico, *J. Geophys. Res.*, **112**, D09113, 2007.

Gardner, C. S., and W. Yang, Measurements of the dynamical cooling rate associated with the vertical transport of heat by dissipating gravity waves in the mesopause region at the Starfire Optical Range, New Mexico, *J. Geophys. Res.*, **103**, 16,909–916,926, 1998.

Appendix I. Correlation and Wavelet Analysis

Wavelet analysis is not used in main body of this dissertation in preference to a more traditional spectral analysis, the fast Fourier transform, but wavelets were employed during the course of study of gravity waves and the associated momentum fluxes.

Wavelets have advantages over traditional Fourier methods in analyzing physical situations where signal discontinuities are at issue. They are mathematical functions that cut data into differing frequency components, and then study each component with a resolution matched to its scale. Wavelets, developed independently in the fields of mathematics, quantum physics, electrical engineering, and seismic geology (Graps, 1995), and are employed here in the study atmospheric gravity waves.

To display how the wavelet analysis represents a spectrum of gravity waves, a spectrum of simultaneous six gravity waves are simulated with given periods of {20, 30, 40, 50, 60, 120} minutes and given respective horizontal wavelengths of {20, 30, 60, 90, 100, 200} km. The waves are started at 70 km with amplitudes of 5 m/s and allowed to propagate upward in the atmosphere using basic GW theory. The waves are measured by a simulated lidar system with the same Vincent and Reid geometry as the current CSU lidar system. A contour plot is made of the simulated data set observed in the Eastward pointing beam (Figure I-1. top). The simulated gravity waves are seen propagating through the channel with the expected downward phase propagation and gravity wave amplitudes grow with increase in altitude, as predicted by theory. For the same data a Morlet-amplitude wavelet analysis is performed exploring the GW spectrum and relative amplitudes near 95 km (Figure I-1).

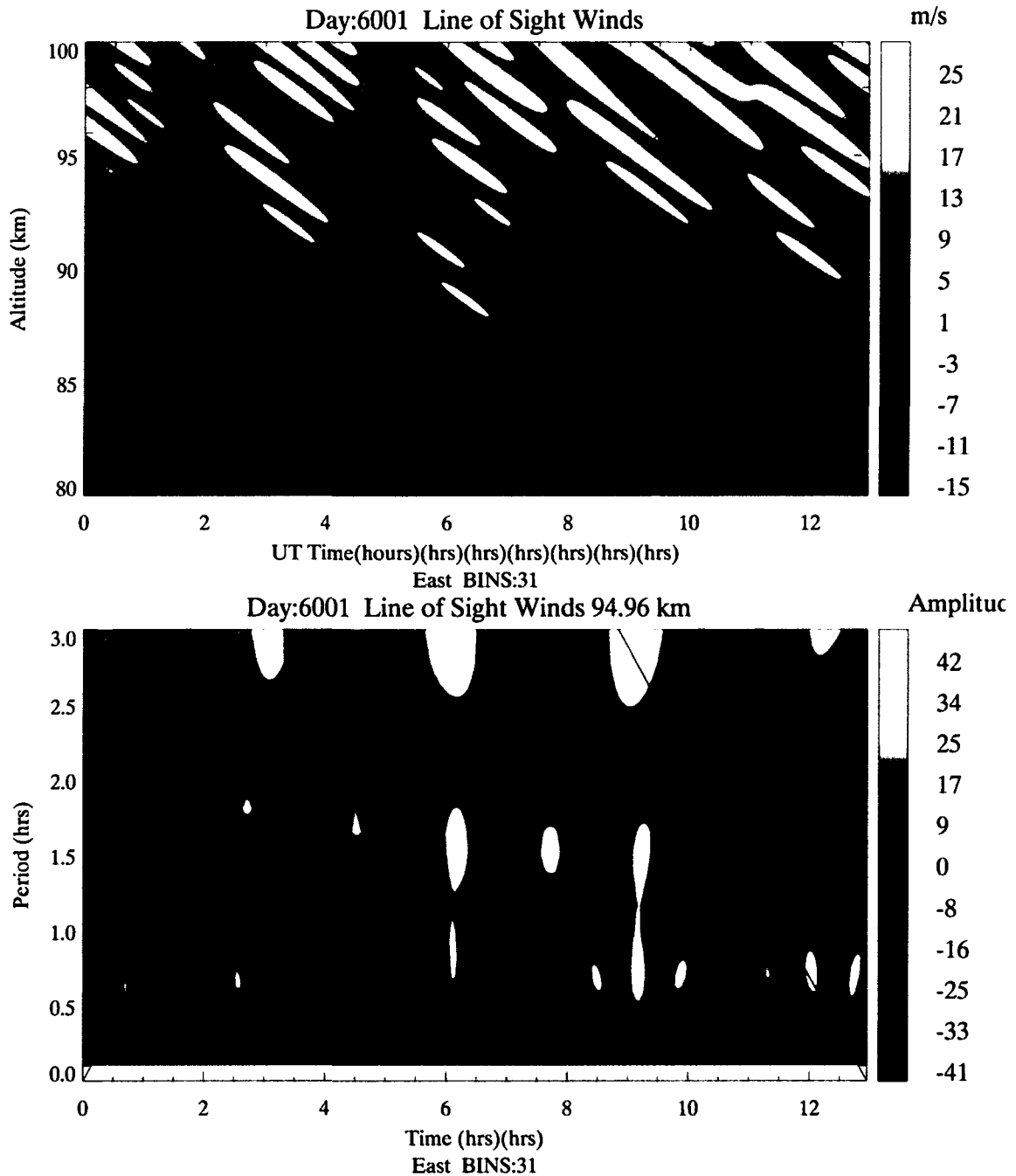


Figure I-1. A gravity wave spectrum simulated with six waves of differing periods (see main body for wave description) and plotted with time along the x-axis and altitude along the y-axis. The data is then analyzed using a Morlet-amplitude wavelet (bottom).

Wavelet analysis allows the exploration of the GW spectrum via comparison of relative amplitudes. This wavelet analysis is performed on the array of data points at one altitude but two dimensional wavelet analyses is possible and could lend a valuable

insight into gravity wave vertical wavelengths. There are many types of wavelets with each their own advantages and disadvantages. It is the inexperience that the author has in the use of wavelets that precludes their inclusion in this dissertation and not the wavelet analysis itself. Use of wavelets can yield qualitative and quantitative results (Torrence, C., and G.P. Compo), but it is that inexperience that has relegated the wavelet analysis to an appendix and only qualitative results are addressed here.

The all plots show the west (left/color) and east (right/lines) LOS high-pass box car (Chapter 4 section 4.2) filtered winds. The top two plots employs a filter with a cutoff period of two hours the middle two plots and the bottom plot employ that with a cutoff period of one hour. Because wavelet analysis magnifies the wavelet amplitude of longer period waves (Torrence, C., and G.P. Compo) the amplitudes of the longer period waves are more pronounced in the colors displayed. The middle two plots show the same LOS winds filtered with a one hour cutoff period allowing shorter period waves to be seen by adjusting the maximum and minimum values permissible on the color bar. Note that the same waves appear in the plots with the one hour cut off as the plots with the two hour cut off, only their amplitudes are suppressed by the shorter filter cutoff period. The bottom most plot shows a combination of the two plots directly above to compare relative phase. The west beam is represented with the color and the east beam is represented with the lines. The lines are marked with amplitudes on the plot. White lines signify negative values while black lines signify positive values. Note: the beams are pointing in opposite directions in the zonal plane; hence same values of zonal wind would be expressed as the color contour and the line contour 180° out of phase (Figure I-2).

Wavelet analysis suggests that GWs of many different periods are present during the observation period. Both signals record a + 3 hour wave well correlated between signals, with a positive peak of maximum amplitude at ~6.5 hours in the west signal about same time a negative peak of maximum amplitude appears in the east signal. Shorter period waves occur at periods of ~1.5 hours and ~ 1.0 hours. In the west channel plot (left) a ~1.0 hour GW is strong and persistent while a ~1.5 hour GW is very weak if not non-existent; the opposite can be seen in the east channel plot (right), a ~1.5 hour GW is strong and persistent while a ~1.0 hour GW is very weak if not non-existent. GW simulation of suggests that both waves may be present in both beams.

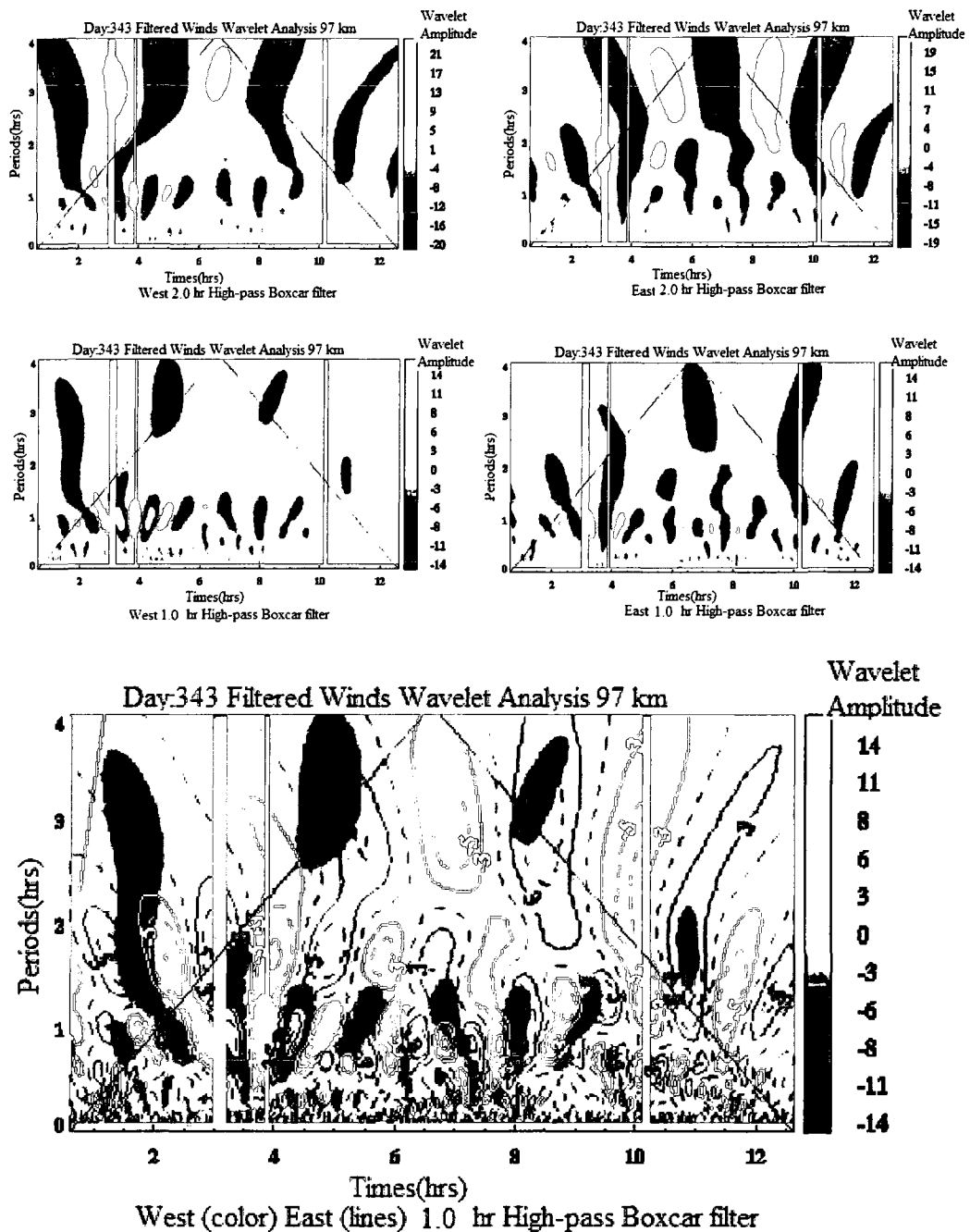


Figure I-2. Wavelet analysis is performed at 97 km with differing cutoff periods. The top plots show the west (left) and east (right) high-pass boxcar filtered LOS winds with a 2 hour cutoff period. The filter diminishes the amplitudes of waveforms periods longer than 2 hours but does not completely remove observed waves. The middle plots employ the same filter with a 1 hour cutoff period to suppress longer period waves and allow better observation of wave with a period less than 2 hours. The bottom plot shows the phase relations between the two channels, showing the wave forms in both beams mostly anti-correlated.

The bottom most plot is a combination of the two plots directly above. The plot illustrates the relative phase and amplitude of the signals observed in the west and east channels. Most of the waveforms that fall into a one to two hour period, where the complement signal is present, are 180° out of phase. This suggests that either the horizontal wavelengths of these waves are much larger than the spatial separation of the regions sampled or there are an integral number of waves between the two sampled regions. The second point can be tested by looking at the same plot at different altitudes. The separation of the two observed regions range from 61-72km at altitudes 85-100km. Furthermore is not likely due to the randomness of the atmosphere. Shorter period GWs, less than a one hour period, are faintly seen at the very bottom of the plot. In order to resolve these shorter period GWs a more stringent filter, with a cutoff of 0.25 hours, is employed.

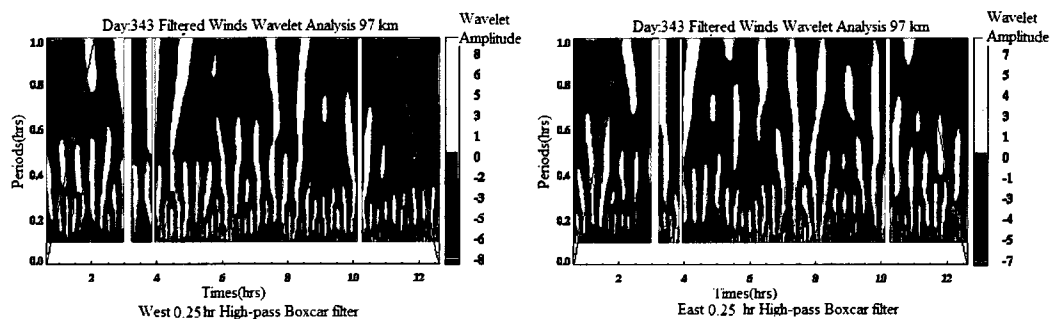


Figure I-3. Wavelet analysis performed at 97km with a 0.25 hour cutoff period. GW bursts of 1 to 2 hours in duration prevail for the shorter period GWs.

Figure I-3 show shorter period waves at 97 km by employing a filter with a 0.25 hour cutoff. First the wavelet analysis of periods less than 1.0 hour suggests that GWs of this period in this dataset, occur in bursts of activity, and are not coherent in time throughout an entire night of observations. Furthermore, GW theory developed in chapter 3 suggests that shorter period waves would tend to have shorter horizontal wavelengths.

In Figure I-3 it is difficult to see direct correlation between the signals of the west and east channels. This could mean a short horizontal wavelength gravity wave may be seen in one channel at one altitude and then another at a different time and/or altitude. This possible behavior was probed unsuccessfully with cross-correlation analysis techniques modifying equation I.1 to allow a myriad of altitude offsets and time lags. The suggested behavior was not observed in analysis results. This is possibly due to the many apparent waves propagating through the region and the inability of the cross-correlation techniques employed to pull out a specific spectral signature

1.1 Correlation of Radial Measurements

It is especially noteworthy that the dual co-planar beam measurements of momentum flux do not require any knowledge of the horizontal scales of the wave or eddy motions involved. Information about the gravity wave scales is important if current theories of wave transport are to be tested and improved. The scales can be estimated by measuring the time displacements between the fluctuating motions measured in complement beams (Vincent and Reid, 1983).

If the observed LOS wind was perfect, meaning there was no error in the wind measurement, there would still be error in the reported MF value due to not sampling the same volume of atmosphere and the differing wavelengths of gravity waves. The Vincent-Reid co-planar beam method presupposes that the oscillations in one channel are the same oscillations we see in the other, and only differ in amplitude due to the relationship of the phase angle of the GW and the probing transmitter beam. GWs of comparable or shorter wavelengths than the horizontal separation of the two beams can have differing phases of the oscillating GW observed in each channel. Differences in a

gravity wave's phase, seen in the measured LOS winds, could cause signal beating in an instantaneous MF calculation. When the analysis window is taken of sufficient duration as to allow a full 2π cycle of the phase differences the beating smooths out in the MF measurement. The current analysis window spans two hours centered on a reported value. In order to gauge if the zonal wavelength of the observed gravity waves are much larger than the spatial separation of regions of observation, the cross correlation of the east and west LOS temperatures are calculated for the filtered and non-filtered data.

The linear fit is applied to the data inside the sliding window as described in section 4.1.1. At each altitude z there are N data points representing all times during the observation period, and they are given the index t . Every time t has n data points associated with it composing an analysis window of two hour duration centered on t . At the ends of the entire data set the window is truncated. These n data points of wind or temperature measurements are least-squares fit to the form $A + Bt$. This best fit result is then subtracted from the original data set, leaving a set of n linear filtered data points associated with the point t . The sliding cross-correlation is then calculated with n data points centered at time t . The formula for the cross-correlation of the east (x) and west (y) LOS temperatures at time t is,

$$CR_{xy}(L)_t = \frac{\sum_{k=t-\frac{n}{2}}^{t+\frac{n}{2}-L} (x_{(k+L)} - \bar{x}_t)(y_k - \bar{y}_t)}{\sqrt{\left[\sum_{k=t-\frac{n}{2}}^{t+\frac{n}{2}-L} (x_k - \bar{x}_t)^2 \right] \left[\sum_{k=t-\frac{n}{2}}^{t+\frac{n}{2}-L} (y_k - \bar{y}_t)^2 \right]}} \quad 1.1$$

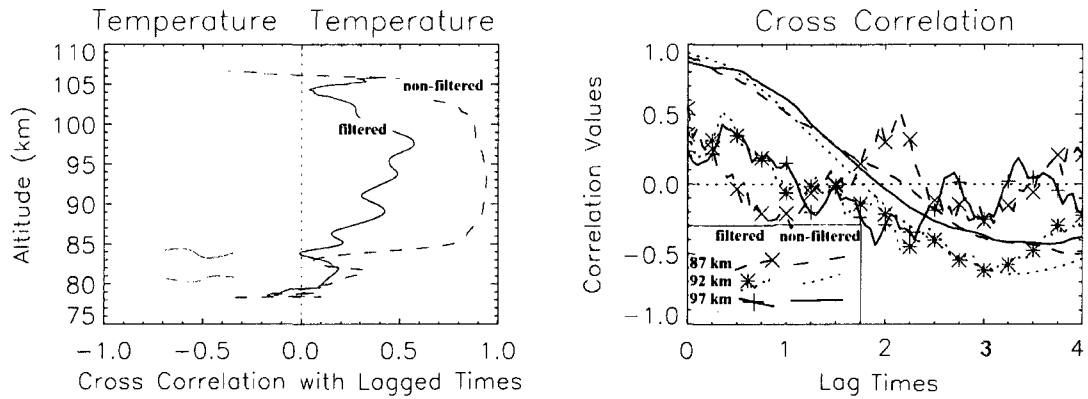


Figure I-4. Cross Correlation of linear filtered and non-filtered LOS temperatures. Linear fit filtered correlations are performed with all data points associated with a 2 hour data analysis window. The cross-correlation versus altitude (left) at a time lag of 0 minutes. To the right is the cross correlation of the two LOS temperatures (y-axis) at three different altitudes vs. different lag values (x-axis) where the lag is 3 minutes per increment on plot. The top three smoother lines are the non-filtered values.

Figure I-4 (left) illustrates the correlation of the line of sight wind for the East and West channels on December 9th, 2006 (day 6343). CR_t 's are then averaged for the entire night of N measurements to produce one point at one altitude for the entire night. This procedure is repeated for all z 's to produce the solid line in Figure I-4a. The cross correlation of the non-filtered line of sight temperatures is calculated with the array of N data points of the east and west beams at times t and this is represented with the dashed line (Figure I-4a, left). L is the lag in the cross correlation function. By shifting the lag value a temporal phase shift is introduced in the correlation between the two channels. This shift may detect a phase shift in the signal between the two channels due to short horizontal wavelength gravity waves (Figure I-4b). The data for the non-filtered temperatures is well correlated between the east and west beams for most altitudes 85km to 100 km for a non-shifted phase difference (Figure I-4b, right solid lines near 1.0). The filtered temperature is also positively correlated, but not as strongly correlated as the non-filtered signal suggesting the waves with the shorter periods have shorter wavelengths.

With normalized correlation values of ~ 0.5 the filtered signal is correlated for altitudes 87 km to 100 km with a lag time of 0.0 minutes. Of note is a peak near 2 hours lag time for altitudes 87 km, but not at 92 and 97 km. This peak suggests that a shorter wavelength gravity wave may exist at the lower altitudes, and the absence of the same peak at 92 km and 97 km suggests the gravity wave did not propagate to 92 km and further 97 km.

Eight plots (Figure I-5) show the progression of waves in altitude through observations made with the west channel. Starting at 85 km a wavelet amplitude contour is made analysis every 2 km. The LOS wind data is originally analyzed with a 3minute 2km resolution, therefore points selected 2km or greater apart are considered independent data points. The plots maintain the same color bar scale to aid comparison of plots. First, note the amplitude of the ~ 1.5 hour period wave progressing from 85km (bottom right) to 99km (top on left). A notable cyclical behavior of the ~ 1.5 hour period waveform is seen propagating through the data. Note that the 95-93km phase of the one hour wave is 180° out of phase with the same wave form at 89km. and 99km suggesting a repeating waveform over ~ 10 km.

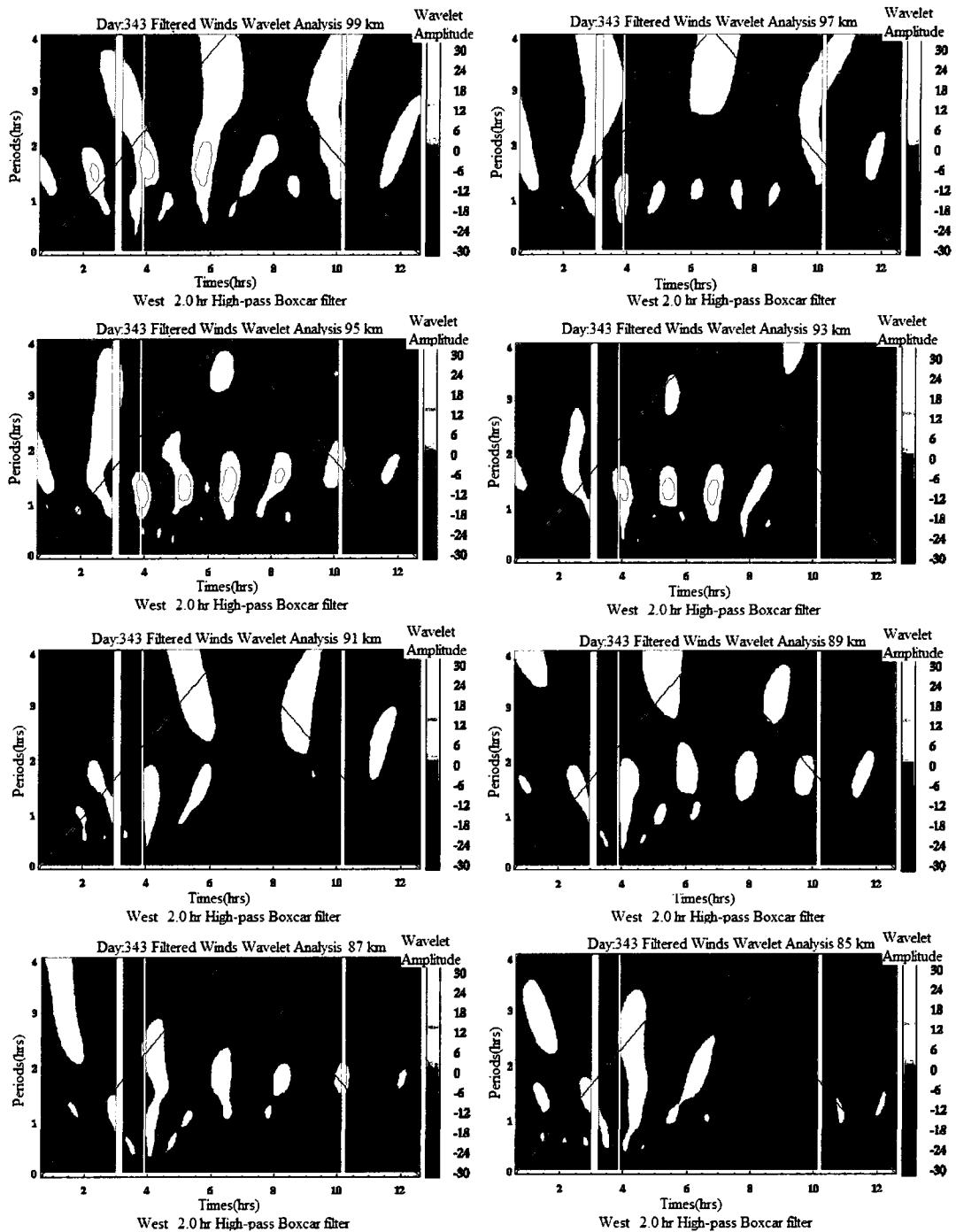


Figure I-5. A series of wavelet plots from 85-99km every 2km. All plots use the same scale to allow the reader see the increase in amplitude of the waves as they travel +z in altitude. Altitudes are noted in the title line starting at 85km in the bottom right and increasing every 2km until 99km in the top left.

References:

Graps, A., *An Introduction to Wavelets*, IEEE Computational Science and Engineering, Summer 1995, IEEE Computer Society, **2**(2), 1995

Torrence, C., and G.P. Compo, A Practical Guide to Wavelet Analysis. *Bull. Amer. Meteor. Soc.*, **79**, 61–78, 1998.

Vincent, R. A. and I. M. Reid, HF Doppler measurements of mesospheric gravity wave momentum fluxes, *J. Atmos. Sci.*, **40**, 1321-1333, 1983.

Appendix II. Electronics

A 50 Hz pulsed laser emits light which interacts with the atmosphere with some of the light collected by the telescopes. Returning photons are counted by photomultiplier tubes in $1\mu\text{s}$ bins for the region of interest. The time of flight is known so the distance where the interaction takes place is known within ~ 150 m. Data is integrated for one (two) minutes to yield 3000 (6000) total shots after which the data is stored.

The CSU lidar electronics subsystem is more complicated than this due to the shifting between three frequencies in order to obtain R_T and R_V ratios (2.1.4.1). The light is shifted via acoustic optic (AO) modulation (2.2.1.2) and must be in sync with the AO chopper wheel, the receiver chopper wheel, and the firing of the pulsed YAG laser. The electronics must also allow for two data acquisition cards to count and record returning photons with respect to time of flight of the laser pulse. The system must also bin these returned photon counts with respect to which frequency the light pulse is transmitted. In addition to these timing requirements, signals to the YAG and the counting cards must be conditioned for impedance matching. All of these requirements are met with a simple clock, one-shots, digital logic, and current supplies (Figure II-1).

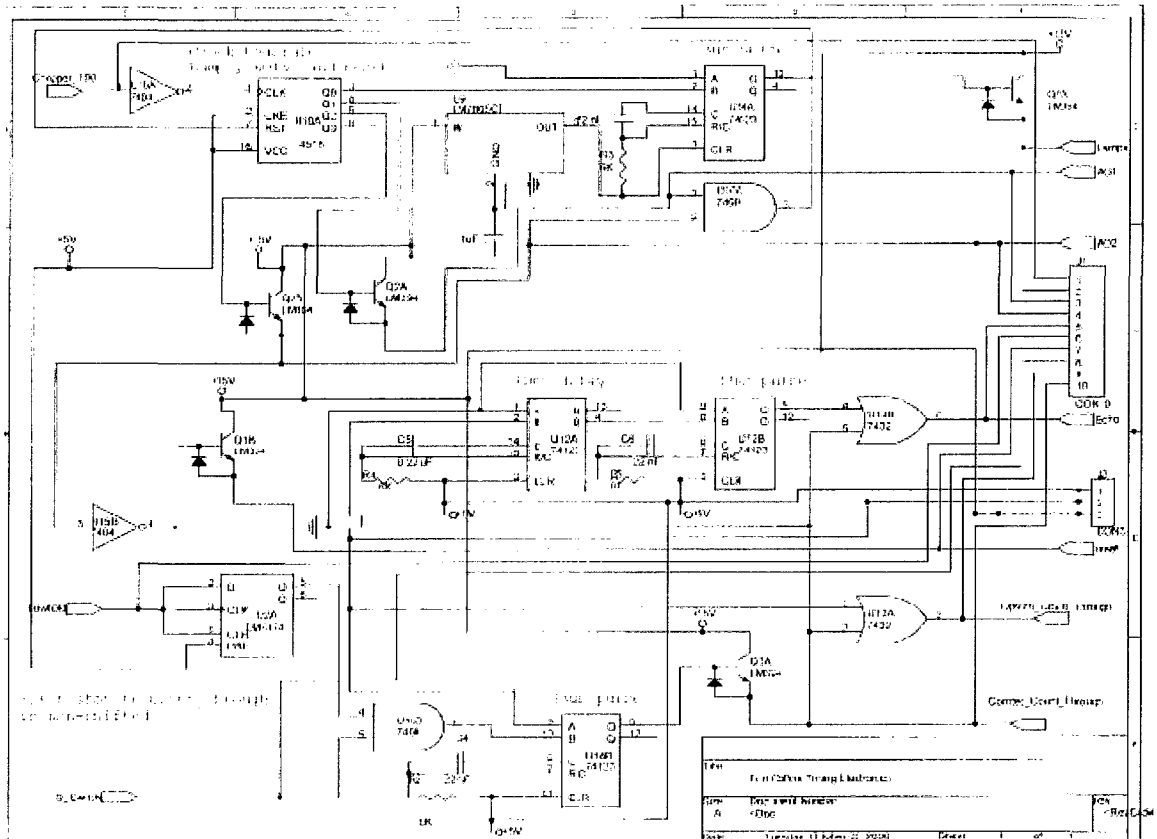


Figure II-1. A schematic of the timing electronics starting in the top left with Chopper 100, which is a 100Hz TTL signal that dictates the timing of the circuit. This signal is divided by a clock to shift the frequency of the transmitted pulses, time the transmitted pulses, and allow for proper binning of the sequence of the returning photon pulses. Q_Switch, at the bottom left, is a signal from the YAG laser indicating when the laser has fired. This provides an accurate time of flight measurement for counted photons.

II.1 System Timing

During nighttime measurements, three beams are sent into the sky and are collected by telescopes, directed into fibers, and then counted by photomultiplier tubes (PMT). The telescope pointed north is a 14" diameter Celestron telescope. Due to the north beams transmitted power being cut to 20% of the total power, the return counts are expected to drop to 40% of previous values. In order to raise counts in this channel, a new PMT was purchased from Hamamatsu with 40% quantum efficiency (QE) at 589nm while of our older PMTs are closer to 15% QE. This raise in QE returned the underpowered north channel to near the previously recorded counts, but with a price. The

old PMTs contain an integrated circuit that will allow the voltages of the first two dynodes to be switched for a short time (50us). The 'blanking circuit' prevents the Rayleigh return from lower altitudes (under 15km) from saturating the PMT and possible damage. The new 40% Hamamatsu PMT does not have this blanking capability, requiring optically chopping the beam to prevent saturation and damage of the PMT anode. The system timing is most easily described by explanation of the different inputs and outputs to the timing circuit.

Chopper_100 - This 100Hz signal is inverted and put into a digital counter (Figure 2-4, Chopper_100). The four bit counter counts to six: 0001, 0010, 0011, 0100, 0101, and 0110. When six is reached, bits two and three are high; and an AND gate connected to both provides a +5 V high signal to the counter reset, causing the counter to immediately reset to '0000'. This reset causes the AND to return to 0 V, and the counter is ready to count again. Each counter output bit controls a different timing function.

One (0001): Laser shot triggers the YAG and a pulse of light is sent into the air.

Two (0010): The AO1 crystal transducer is turned on, which shifts the PDA seed beam +630MHz, the COMTEC counter card DIG_IO0 goes high tagging the counted spectrum as (+).

Three (0011): Laser shot triggers the YAG.

Four (0100): The AO1 transducer is turned off. The AO2 crystal transducer is turned on, which shifts the seed beam -630MHz, the COMTEC counter card DIG_IO1 goes high tagging the counted spectrum as (-).

Five (0101): Laser shot triggers the YAG.

Six (0110): Bits two and three are inputs into an AND gate; and, when both are high, the AND gate output is high. The AND gate output goes to the counter reset which resets the counter to zero (0000). When the counter resets to zero, the AND gate output goes low; and the counter is ready to count to six again.

Laser shot - . The first counter bit, after it is conditioned, triggers the YAG electronics at 50Hz. The YAG requires a pulse width of 10-100us, a pulse height of 2.4 to 6v and a current capable of driving a 50 Ohm load. The 50Hz signal used to trigger the YAG is conditioned by: a 74123 (monostable multivibrator, one-shot) to provide a 33us width pulse, a LM394 transistor to provide enough current capable of driving a 50 Ohm load with a 4.6 V pulse height.

AO1&2 – Bits two and three, after conditioning, shift the AO crystals and provide information about the state of the crystals to the COMTEC counting card for spectral tagging. The digital counter starts at zero (0000) with 10ms between each successive number in the count.

Reset - Reset is AO2 inverted. It is used to synchronize the AO chopper wheel phase with the signals for AO1&2 and the pulse of the YAG. The AO chopper wheel uses a 300Synch Chopper Synchronizer manufactured by Boston Electronics to synchronize the phase of the wheel with the needed light path for the shifting crystal.

Lowhold – After the YAG has fired 3000(6000) shots, the software that operates the counting cards stop counting and stores the data acquired. During this time the locking software for the ring laser scans the Doppler Free Lamb dip, to allow operator verification of the lock on the correct spectral feature and re-acquires lock on the Lamb Dip. The storing of saved data is much faster (~150ms) than the scanning of the Lamb

Dip (~4s); this allows the data card to be ready to take more data before active locking on the D_{2a} Lamb dip. Lowhold is generated by the counting card when it is saving data. This Lowhold signal is intercepted by the ring laser locking program and is used to identify when to scan the ring laser as well as when to begin to generate the computer program Lowhold signal to prevent the data card from acquiring data when the ring is not locked. Currently the Optech card is generating Lowhold that is the input to the computer.

II.2 Counting Cards

There are two types of counting cards use in the CSU lidar--the Optech fdc700m card and the Comtec P7882 card. The Optech card has been used for over 10 years in the CSU lidar system, and its operation has been described in previous dissertations (White, 1999; Li, 2005). Due to the age of the Optec card it is desirable to have a verifiable substitute that can be integrated into the current system with minor modifications. Also the Optec card can only sample two channels and the current experiment required three beam operations. The Comtec card (Figure 2-18) was recently installed and allows two channel inputs with an adjustable bin width down to 200 ns in dual input mode, with counting rates in excess of 350 MHz, far faster than individual pulse resolution of our PMTs.

Count_through is connected to TRG(START)/SAMPLE IN. The signals from the PMTs are sampled with COUNT(STOP)1 IN and COUNT(STOP)2 IN. The 15 pin connector is used for digital tagging: DIG_IO 0 (pin 1) and DIG_IO 1 (pin 11) for AO1 and AO2 respectively. When the signal is high (>+2.3V) turning on either transducer for the AOM shifted light, it also turns on the associated Comtec signal channel, thus enabling the digital tagging to sort out the received signal into storage channels with

respect to transmitted frequency, 00 for ν_0 , 10 for ν_+ , and 01 for ν_- . The 'GO'-LINE is used if the Comtec board is used to generate Low Hold. Low Hold is currently generated by the Optech card due to the Comtec card being shut down during daytime operations.

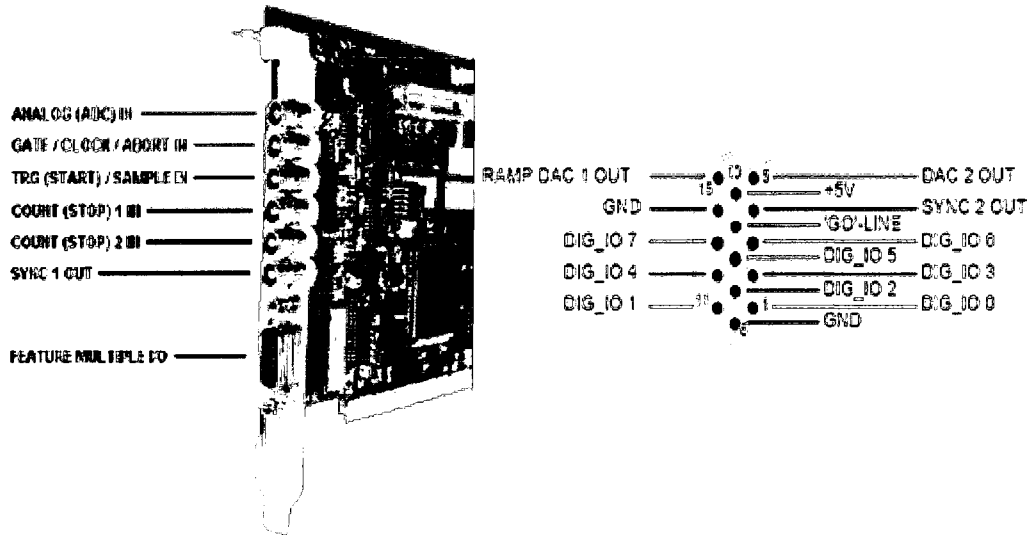


Figure II-2. This is a picture of the Comtec card with the access ports annotated and the 15-pin connector to the right. Timing of when the laser is fired (count_through) is input into TRG (START) and returned photons (PMT pulses) are counted with COUNT (STOP) 1 and 2 IN. DIG_IO 0 and 1 are used for spectral tagging.

The Comtec board has been operational for over three years.